HEMODYNAMIC WALL SHEAR STRESS IN MODELS OF ATHEROSCLEROTIC PLAQUES USING PHASE CONTRAST MAGNETIC RESONANCE VELOCIMETRY AND COMPUTATIONAL FLUID DYNAMICS

A Thesis
Presented to
The Academic Faculty

by

Daniel Roberts Karolyi

In Partial Fulfillment
of the Requirements for the Degree
Doctor of Philosophy
from the
Wallace H. Coulter School of Biomedical Engineering

Georgia Institute of Technology
March 2002

HEMODYNAMIC WALL SHEAR STRESS IN MODELS OF ATHEROSCLEROTIC PLAQUES USING PHASE CONTRAST MAGNETIC RESONANCE VELOCIMETRY AND COMPUTATIONAL FLUID DYNAMICS

APPROVED:

Don P. Giddens, PhD Co-Chairman

John N. Oshinski, PhD Co-Chairman

David G. Harrison, MD

Jennifer S. Pollock, PhD

W. Robert Taylor, MD, PhD

Ajit P. [illegible], PhD

Data Approved by Chairman: 3/29/02

This work is dedicated to my parents, Glenn and Mary.

ACKNOWLEDGEMENTS

I would like to thank my advisor, Don P. Giddens, for guiding my professional growth throughout my graduate studies. Dr. Giddens has provided a research environment that has allowed me to pursue several different research projects culminating in a set of skills that will allow me to perform engineering and/or medical research of the highest quality in any field or specialty. I have also observed and attempted to emulate Dr. Giddens attention to detail and interpersonal relationship skills, which will undoubtedly help not only my professional career but also my interactions with future patients.

I would also like to thank my co-advisor, John N. Oshinski, for assisting me in my final research project, which is the topic of this thesis. Dr. Oshinski's can-do attitude and encouragement were essential driving forces behind the development and implementation of this research. His ability to encourage students facing adversity makes him a truly excellent teacher and extraordinary research advisor.

I would also like to thank the members of my thesis committee for their guidance and encouragement: David G. Harrison, Jennifer S. Pollock, W. Robert Taylor, and Ajit P. Yoganathan.

Since 1994, David G. Harrison has been my mentor in both scientific research and the practice of medicine. He is responsible for a great deal of what I have accomplished and will accomplish in the future. I was truly fortunate to stumble into his lab eight years ago and I look forward to seeking his advise for several years to come.

I would also like to thank Robert Schlant for his guidance and support of my medical and academic pursuits. I am very grateful for his insight with regards to the advantages of a career in academic medicine and the skills needed to succeed in the future.

I would like to thank Robert M. Nerem for allowing me work in his lab as an undergraduate student at Georgia Tech and for his interest in my progress as a graduate student. My positive undergraduate research experience in his lab was the most important factor in my decision to return to Georgia Tech to pursue my graduate degree in engineering.

Colleen Brophy was my co-advisor for my first two years during my graduate studies. I greatly appreciate her support while working at the Augusta Veterans Administration hospital as well as the biomedical engineering department at Georgia Tech.

I would like to thank Jim Goldenring for his support as the director of the University System of Georgia MD/PhD program. He is truly a student advocate with a desire to see that every Medical College of Georgia MD/PhD student succeeds.

I am grateful to the other members of Dr. Giddens' lab for their friendship and comic relief: Jimmy Costello, Cecilia Curry, Suo Jin, David Ting, Amanda Wake, and Annica Wayman. I would especially like to thank Puneet Sharma for his assistance with the operation of the MRI scanner and Chris Conrad for showing me the basics of FIDAP 8.0.

I thank Jim McEntee of J.M. Machining for manufacturing the molds used in this project. I would also like to express my appreciation to Harry Rudd, Wayne Springfield,

and Harold Meyer of the Georgia Tech Aerospace Engineering machine shop for their assistance and workmanship. I also thank the Georgia Tech administrative staff including Patricia Thomas, Gail Jefferson, Joanne Wheatley, Rachael Arnold, Pat Fowler, and Shuana Durham as well as Becky Click at the Medical College of Georgia for all of their support.

I especially thank my family for their support and understanding during my entire educational career. I thank my Grandmothers, Helen Wright and Ethel Karolyi, for their love and support as well as their kind company. Finally, I would like to express thanks to my parents Glenn and Mary for their love and understanding.

TABLE OF CONTENTS

CHAPTER

LIST OF TABLES

Page

LIST OF FIGURES

Page

LIST OF SYMBOLS, ABBREVIATIONS, NOMENCLATURE, GLOSSARY

BC	Boundary condition
B_o	External magnetic field
CABG	Coronary artery bypass surgery
CFD	Computational fluid dynamics
f_i	Body forces
I	Signal intensity
LDL	Low density lipoprotein
M_o	Net magnetization of a proton
MRI	Magnetic resonance imaging
M_{xy}	Net transverse magnetization vector of a proton
M_z	Net longitudinal magnetization vector of a proton
N	Vector normal to the phantom/arterial wall
P	Pressure
PC-MRI	Phase contrast magnetic resonance imaging
PTCA	Percutaneous transluminal coronary angioplasty
PVA	Polyvinyl alcohol
Q	Volumetric flow rate
Re	Reynolds number
RF	Radio frequency
U	Velocity vector
WSS	Wall shear stress

ϕ	Phase shift
ρ	Density
μ	Dynamic viscosity
ν	Kinematic viscosity
ω_w	Wall vorticity
τ_w	Wall shear stress
ω_o	Larmor frequency
γ	Gyromagnetic frequency
σ_{ij}	Stress tensor
τ_{ij}	Deviatoric stress tensor
δ_{ij}	Kronecker delta
s_{ij}	Strain rate tensor

Cylindrical coordinates

z = axial coordinate

θ = angular coordinate

r = radial coordinate

SUMMARY

Arterial wall shear stress (WSS) is thought to be a factor that determines locations in the vasculature where atherosclerotic plaques are formed. Providing patient specific WSS data may increase the potential for early detection and treatment before serious clinical complications occur. Phase contrast magnetic resonance imaging (PC-MRI) offers a non-invasive method for determining blood velocity profiles. However, the limited resolution of this technique restricts the accuracy of the near-wall velocity data that are needed to calculate WSS. The purpose of this research was to determine if improved WSS calculations from current magnetic resonance imaging technologies could be developed.

PC-MRI data were obtained for anatomically scaled phantoms representing blood vessels with and without symmetric stenoses under average and peak steady flow conditions. WSS values were calculated by two methods: (1) directly from PC-MRI velocity profiles and (2) from computational fluid dynamic (CFD) simulations with MRI defined geometries and inlet boundary conditions. The accuracy of both methods was determined by comparing the results to gold standard WSS data derived from CFD simulations using ideal geometries and boundary conditions.

Both methodologies resulted in data with large variations in WSS values between adjacent axial and angular locations. The direct calculation of WSS from PC-MRI data yielded large underestimations of the maximum WSS values present within the stenosis geometries. These errors were related to the low resolution of the velocity data obtained from PC-MRI as well as the inability to accurately detect the phantom wall location due to partial volume errors and low signal-to-noise ratios. The CFD simulations yielded moderate underestimations of WSS within the stenoses. The MRI derived computational geometries and the underestimation of the flow rates used for the inlet boundary

conditions were found to cause the greatest errors for the average and peak flow rate simulations, respectively.

It was determined that WSS values derived from the CFD simulations are more accurate compared to the direct calculation of WSS from PC-MRI data. To improve upon these CFD methodologies, more studies are required to optimize geometry smoothing and reconstruction in order to reduce WSS errors while maintaining physiologically relevant geometries.

CHAPTER I

BACKGROUND

Atherosclerosis

Atherosclerosis is a pathological inflammatory syndrome that occurs within large arteries of the human body and is the cause of most cardiovascular disease. Cardiovascular disease from all causes accounts for 29% of deaths worldwide, ranking second only to infectious and parasitic diseases (WHO, 1997). In the United States, atherosclerosis affects one in four people, causing approximately 42% of all deaths. Approximately half of these are due to atherosclerotic coronary heart disease (CDC, 1999; AHA, 2000; CDC, 1997). Once thought to be a disease of the Western World, atherosclerosis now threatens developing countries as well, reflecting greater exposure to certain risk factors with rising standards of living (Reddy and Yusuf, 1998). The early detection of atherosclerosis could significantly reduce the morbidity and mortality of cardiovascular related diseases.

Atherosclerosis is a progressive disease characterized by the accumulation of lipids and fibrous materials within the walls of large arteries. Within the first decade of life, the initial lesions of atherosclerosis can be seen on the walls of the aorta. These lesions can also be seen in most human coronary arteries by the second decade and in the cerebral arteries by the third or fourth decades of life. These initial lesions are characterized by the accumulation of "foam cells" within the sub-endothelial layer. Foam cells are derived from monocytes found within the circulating blood that are recruited to the arterial wall by the expression of ligand molecules on the endoluminal

surface of endothelial cells. The expression of these ligands is regulated by chemotactic signals received from the surrounding cellular environment. For example, oxidized low-density lipoprotein (LDL) is known to promote the endothelial expression of adhesion molecules and growth factors such as macrophage colony-stimulating factor (M-CSF). Once the monocytes are recruited into the arterial wall, they become macrophages. In an attempt to prevent the progression of pathological processes caused by oxidizing agents, the macrophages engulf oxidized LDL molecules. The interaction between LDL molecules and the molecular chemistry of the macrophages results in a change in the cells' phenotypes resulting in a transformation to foam cells. Therefore, atherosclerosis can be viewed as a response to injury with oxidized-LDL as the noxious agent.

The foam cells recruit other cells into the lesion by secreting chemokine and cytokine signals. The initial build-up of sub-endothelial foam cells leads to a non-clinically significant lesion called a fatty streak that can be observed in gross specimens. These lesions are the precursors of more advanced lesions characterized by the accumulation of lipid-rich necrotic debris and extracellular fibrous material. The chemical signals expressed by the foam cells can also recruit smooth muscle cells from the tunica media of the arterial wall. These cells can also engulf LDL molecules thereby changing phenotypes to become foam cells. The recruited smooth muscle cells also produce and secrete the fibrous material found within more advanced lesions. These cellular events lead to the formation of an advanced plaque with the ability to cause arterial lumen obstruction.

The recruitment of macrophages and smooth muscle cells and the secretion of fibrous materials cause the initial lesion to grow in size. Initially, the circumference of

the artery increases to maintain a constant diameter (Glagov et al., 1987). However, eventually the lesion becomes large enough to encroach upon the lumen. Cells within the center of the lesion can die due to lack of oxygen and nutrients and contribute their lipid-filled contents to form a necrotic core. A fibrous cap made of extracellular components and smooth muscle cells covers the necrotic core. These complex plaques can progress further, leading to calcification, ulceration at the luminal surface, and hemorrhage due to small blood vessels that grow into the lesion from the adventitial side of the arterial wall.

Clinical problems caused by these lesions can be the result of several mechanisms. First, the encroachment of the lesion into the lumen increases the resistance of the blood vessel to blood flow. Since the human vascular system is composed of several arterial conduits in parallel, this increase in arterial resistance causes the blood to flow preferentially into arteries with lower resistances. Therefore, the volumetric blood flow rate through these diseased arteries is decreased and the amount of oxygen available to organs, tissues, and cells served by these arteries diminishes. This can cause congestive heart failure or angina in the case of diseased coronary arteries, transient ischemic attacks in the case of diseased carotid or cerebral arteries, and claudication of the legs in the case of diseased femoral or popliteal arteries. Moreover, if the arterial lesion decreases the blood flow capacity of the artery to the extent that the end organs cannot receive enough oxygen to survive, infarction will occur. In the case of the coronary artery this will lead to myocardial infarction and in the case of the carotid or cerebral arteries it will lead to stroke. The growth of the plaque causes a slow and gradual reduction in blood flow. Under these circumstances, collateral blood vessels can grow around the occlusion and provide alternate blood supply to distal tissues in the case

of arterial occlusion. Moreover, the gradual onset may cause clinical symptoms of ischemia to become evident allowing for the potential of medical or surgical intervention before permanent damage can occur.

Rupture of a vulnerable atherosclerotic plaque can also cause ischemia and infarction. The lipid-filled necrotic core is not as mechanically stable as other parts of the lesion due to the lack of fibrous material. This mechanical instability can cause the fibrous cap to be sheared away from the lesion and the arterial wall when acted on by hemodynamic forces. The chemical composition of the exposed necrotic core can promote thrombus formation. As the thrombus grows, it can further reduce or completely occlude the arterial lumen causing acute onset ischemic events. The rupture of the vulnerable atherosclerotic plaque can occur with even moderately sized lesions. Therefore, people suffering from this pathological process may have no prior symptoms of ischemic disease and are therefore at a higher risk for sudden cardiac death.

Risk factors for atherosclerosis include dyslipidemia, hypertension, diabetes, smoking, obesity, sedentary lifestyle, and family history. Current therapy for the occlusion of coronary arteries includes thrombolytic pharmaceutical therapy, percutaneous transluminal coronary angioplasty (PTCA), and coronary artery bypass surgery (CABG). Treatment for diseased carotid arteries can also include carotid endarterectomy. In all cases, the early detection of disease leads to lower morbidity and mortality rates.

Arterial Wall Shear Stress

Although the measurement of atherosclerosis risk factors can determine the relative risk of having a cardiovascular related disease, it cannot be used to determine the location of the lesion. Atherosclerosis is commonly found in specific large arteries. The abdominal aorta, carotid, coronary, iliac, femoral, and popliteal arteries are commonly affected, whereas the mammary, pulmonary, renal, and mesenteric vessels are largely spared. Moreover, plaques are more likely to occur at specific locations within these disease prone arteries. For example, the outer walls of the carotid bifurcation, the posterior wall of the abdominal aorta, and the myocardial surface of the left anterior descending coronary artery are more common regions of atherosclerosis plaque formation. The frequent occurrence of atherosclerotic lesions in specific arteries, together with the focal distribution in regions of curvature, bifurcations, and arterial branches, suggests that vessel geometry and fluid dynamics may play a role in the localization of plaques.

Arterial wall shear stress (WSS) is derived from the frictional force created as blood flows over the arterial wall. For a Newtonian fluid (a fluid with a linear relationship between the shear rate and the strain rate), the WSS is calculated as the dynamic viscosity multiplied by the strain rate of the fluid at the wall. It has been suggested that this hemodynamic property plays an important role in determining the size of the arterial lumen. Several studies have used animal models to examine this effect.

Surgical, unilateral arteriovenous fistulas have been created in canine carotid arteries in order to increase the volumetric flow rate (Kamiya and Togawa, 1980). Six months post-operative evaluation of the arteries showed an enlarged lumen of the artery

associated with the fistula. Calculation of the mean WSS using Poiseuille assumptions (fully developed parabolic flow profile, smooth cylindrical geometry, and Newtonian fluid) showed that the mean WSS in both the normal artery and the artery with the fistula were approximately equal. High flow rate arterial fistulas have also been created in the iliac arteries of Cynomolgus monkeys (Zarins et al., 1987). Again, the artery associated with the fistula showed a twofold increase in diameter. Using the Poiseuille assumptions to calculate the mean wall shear stress showed that both the normal artery and the artery with the fistula had values approximately equal to 15 dynes/cm^2. Wall shear stress measured in the abdominal aorta of these monkeys was calculated in a similar manner and found to be 12 dynes/cm^2 (Zarins et al., 1987). In order to examine the effects of reduced blood flow, observations of rabbit common carotid artery diameters have been made distal to surgically created arterial constrictions (Languille, et al., 1986). The arterial diameter was found to decrease on the side of the arterial constriction compared to the contralateral control artery. This study also demonstrated the dependence of this effect on the presence of endothelial cells. These studies taken together suggest that endothelial-dependent arterial remodeling takes place in response to hemodynamic stimulus to re-establish arterial wall shear stress levels in the range of 10 – 20 dynes/cm^2.

In addition to regulation of arterial diameter, the location of atherosclerotic plaque formation may also be related to WSS. Using scaled up models of the human carotid artery bifurcation, correlation studies were performed between hemodynamic parameters and atherosclerosis patterns studied in cadavers (Zarins et al., 1983; Ku et al., 1985). Laser Doppler velocimetry (LDV) was employed to measure the velocity profiles throughout the models, which were used to compute WSS. Along the outer wall of the

sinus, an area of flow separation was observed. In this region, the WSS vector magnitudes were low, whereas the vector directions oscillated during the cardiac cycle. Correlations with cadaver carotid bifurcations found that the outer wall of the sinus was also associated with intimal thickening and plaque formation. These data coupled with the propensity for arteries to remodel to maintain WSS values within a narrow range led to the conclusion that, "Early atherosclerotic plaque localization may be an unstable extension of the otherwise physiologic response of arteries to remodel so as to decrease diameter if the wall shear stress is below that range required for homeostasis." (Giddens et al., 1987; Giddens et al., 1990).

Further evidence for the relationship between arterial WSS and atherosclerosis is associated with how the artery remodels during the early stages of plaque build-up. Studies of human coronary arteries have shown that as a plaque encroaches upon the lumen of an artery, the artery will dilate. In doing so, the diameter of the arterial lumen remains constant, and therefore the arterial resistance, volumetric flow rate, and WSS values remain unchanged. The mechanism causing the dilation of the artery may be related to the higher WSS values that would result from narrowing the lumen (Glagov et al., 1987). Eventually, the artery is no longer able to use this mechanism to compensate and the plaque grows, impinging upon the arterial diameter. In doing so, the resistance of the artery increases causing an exponential decrease in the volumetric flow rate through the artery, leading to ischemia.

The effects of WSS on endothelial cell biology have also been examined in cell culture systems. After exposure to WSS, the cytoskeleton of these cells aligns with the direction of the fluid velocity vector (Sato et al., 1987). These cells also have a lower cell

growth rate when exposed to WSS due to inhibition of entry into the S-phase of mitosis (Levesque et al., 1990). The secretion of the potent vasodilator nitric oxide is increased with increased WSS (Taylor et al., 1991). Nitric oxide has been shown to be chronically released when exposed to high WSS values for an extended period of time. This suggests that the mechanotransduction can also affect the mRNA transcription of the enzyme nitric oxide synthase that is required to produce nitric oxide from L-arginine (Uematsu et al., 1996). Other molecules involved in signaling and cell physiology such as platelet derived growth factor, endothelial transforming growth factor beta-1, intercellular adhesion molecule-1, endothelin-1, tissue plasminogen activator, monocyte chemotactic protein-1, thrombomodulin, prostaglandin I_2, vascular cell adhesion molecule-1, and Cu/Zn superoxide dismutase have also been found to be regulated by WSS (Hsieh et al., 1992; Ohno et al., 1995; Nagel et al., 1994; Malek et al., 1993; Diamond et al., 1989; Shyy et al., 1994; Malek et al., 1994; Frangos et al., 1985; Chappell et al., 1995; Varner et al., 1997; Inoue et al., 1996). Therefore, several mechanisms exist such that low and oscillatory WSS values can alter the endothelial cell physiology making the arterial wall more susceptible to LDL molecule attraction and oxidation as well as monocyte recruitment.

The ability to non-invasively determine the WSS values in arteries susceptible to atherosclerosis could be a valuable tool when combined with the information gained from other tests to determine risk factors. In this manner, the relative risk of plaque formation and the location in the arterial systems most likely to be affected could be used to guide clinical therapy.

Fluid Dynamics in Stenosis Geometries

The fluid dynamics associated with flow through a stenosis are affected by several parameters. The Reynolds number, pulsatile character of the flow, percent area reduction, and length and shape of the stenosis all influence the resulting flow patterns in the system. In steady flow studies, the maximum WSS has been found to occur slightly upstream of the point of maximum stenosis and is much greater than that predicted assuming a parabolic profile (Lee et al., 1970). Flow separation has been observed just distal to the point of maximum stenosis and occurs at both low and high values of the Reynolds number (Deshpande et al., 1977).

The dimensionless pressure drop across the stenosis increases with increasing Reynolds number. The pressure drop is caused by viscous effects at lower Reynolds numbers and primarily by turbulent energy losses at larger Reynolds numbers. The pressure drop values were greater than predicted using Poiseuille's law for flow through a straight tube. The pressure decreases in the stenosis and reaches its minimum value slightly downstream from the throat of the constriction followed by a gradual recovery. The recirculation area was found to increase as the Reynolds number was increased for laminar flow conditions and is also a function of the stenosis geometry. For steady flow, it was found that a specific symmetric stenosis causing a 56% reduction in the cross-sectional area exhibited transitional flow at Re = 300±20 and fully turbulent flow at Re = 500±50 at a location just distal to the maximum stenosis (Young and Tsai., 1973a). An asymmetric stenosis with the same area reduction exhibited transitional flow at Re = 1340±40 and turbulent flow at Re = 2050±50 just distal to the maximum stenosis. These results suggest that the streamlines will depart from laminar behavior for relatively low

Reynolds Numbers. These critical Reynolds numbers were found to be higher for pulsatile flow through the same stenosis geometries (Young and Tsai., 1973b).

Studies by Lieber (1985) found that only flow disturbances and not fully developed turbulence occurred in pulsatile studies with 50% and 75% symmetric stenosis models over a range of Reynolds numbers (200 – 1000). These core flow transitional phenomena of starting structures and puff formations were found to affect the WSS values. Steady flow studies by Ahmed (1981) in the same models found that the interaction of the main jet from the stenosis with the shear layer created regions of high disturbance levels which migrated toward the centerline until uniform turbulence was achieved or the disturbances decayed. This depended on the upstream flow conditions and the stenosis geometry. For a 50% area reduction, only vortex shedding from the recirculation region was observed for Re = 500 to 1000. For a 75% area reduction stenosis, large scale periodic instabilities were observed in the core post-stenotic flow for $Re > 500$.

These data taken together suggest that the potential for transitional and turbulent flow exists for stenosis geometries that reduce the cross-sectional area greater than 50%. However, the extent to which these disturbance structures contribute to the flow field and affect the WSS values depends upon the Reynolds number and the specific geometry of the stenosis.

Magnetic Resonance Imaging

Basic Principles

Magnetic resonance imaging is based on the nuclear magnetic moment of nuclei. Atoms having nuclei with odd atomic numbers and/or odd atomic weights will possess magnetic moments which when combined are referred to as the "spin." The value of the spin is limited by the principles of quantum mechanics to zero, half-integral values, and integral values. As the nucleus spins, the positively charged protons move through space creating an electrical current. This electrical current also induces a magnetic field around the nucleus, which after vector summation can be represented as the net magnetization vector of the nucleus (M_o). The orientation of this net magnetic vector and how it changes due to the experimental manipulations that the nucleus undergoes provide the basis for the MR signal.

The magnetic poles found in human tissue atoms are randomly oriented in all directions (Figure 1.1a). However, when placed in an external magnetic field (B_0), some of these protons will align with B_0 (parallel orientation) and some will align against B_0 (anti-parallel orientation) and begin to precess about the net magnetic vector at a given resonance frequency (Figure 1.1b).

The frequency is a function of an inherent property associated with the protons, called the gyromagnetic ratio (42.58 MHz/T for hydrogen), and the external magnetic field as stated in the Larmor equation:

$$\omega_o = \gamma * B_o / 2\pi$$

where ω_o is the Larmor frequency, γ is the gyromagnetic ration, and B_o is the external magnetic field.

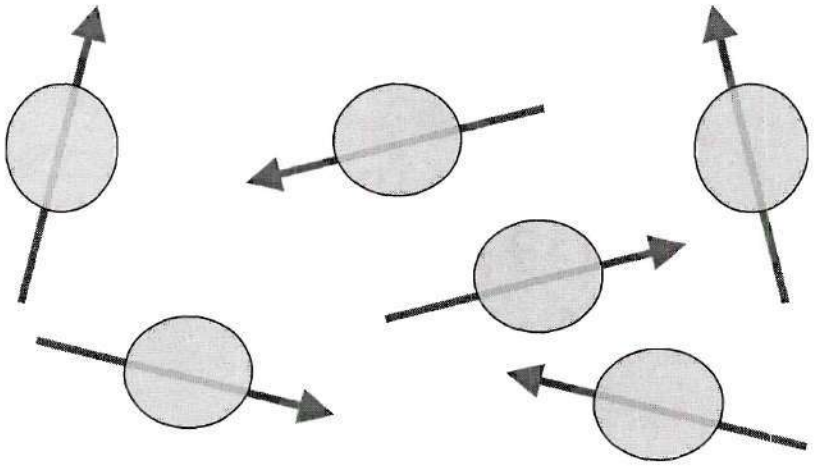

Figure 1.1a: Proton magnetic poles randomly oriented in space when not under the influence of an external magnetic force.

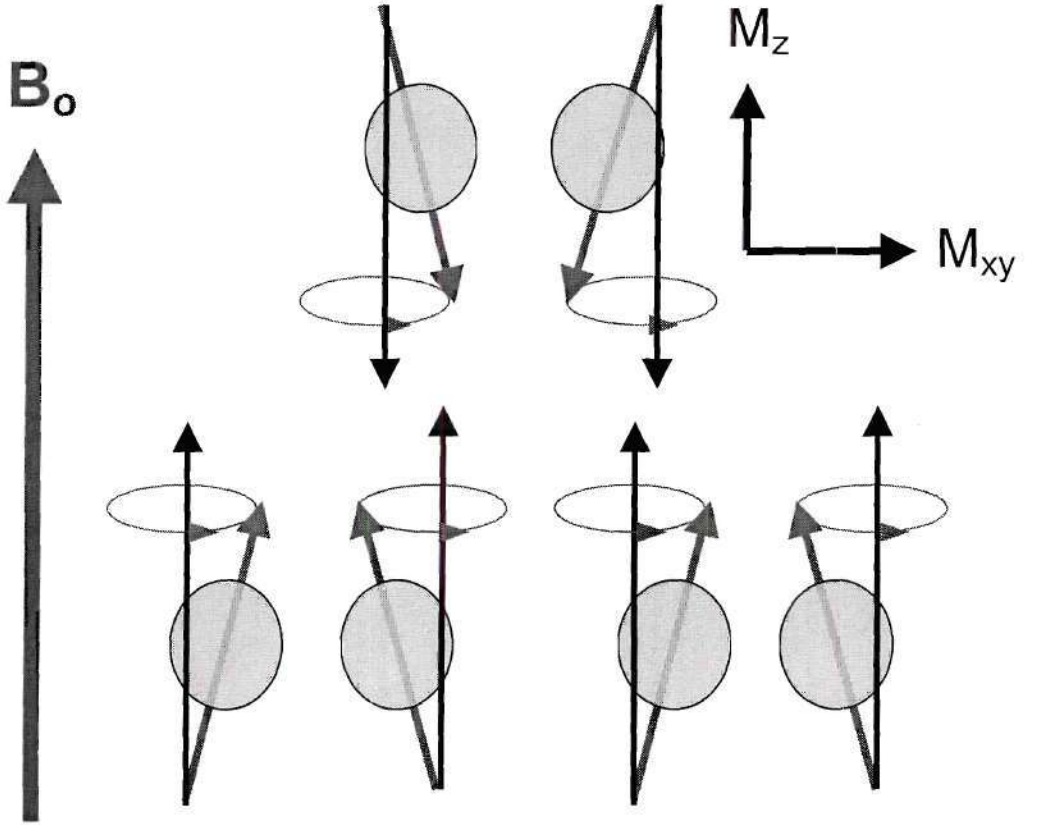

Figure 1.1b: Proton magnetic poles aligning parallel or anti-parallel to the external magnetic field B_o and precessing around the net magnetic vector.

The protons can be excited to higher energy levels by an external radio frequency (RF) pulse applied perpendicular to B_0 and at the protons' Larmor frequency. This reduces the net longitudinal (aligned parallel to B_o) magnetization (M_{xy}) of the protons. The RF pulse also causes the protons to precess in synchronization producing a net transverse (not parallel to B_o) magnetization. When the external RF is turned off, the net longitudinal and transverse magnetic vectors of the protons recover to their original positions. As this occurs, the protons emit an RF signal at the Larmor frequency, which is used to reconstruct magnetic resonance images. The amplitude of the emitted signal is proportional to the physical properties (density, lattice, structure, etc.) and motion (velocity, acceleration, etc.) of the nuclei as they return to their original position.

The physical properties of the material and its environment affect the signal by changing the recovery times. The net magnetization, caused by the spinning protons, is originally aligned with B_0 in a longitudinal direction. After being excited by the RF pulse, the net magnetization direction changes as the longitudinal magnetization decreases and the transverse magnetization increases. Each component recovers independently of the other component and at different rates. The time required for the longitudinal component to recover to 63% of the original value is referred to as the T_1 relaxation time (Figure 1.2). Similarly, the time required for the transverse component to decay 37% from the excited value is referred to as the T_2 relaxation time (Figure 1.3). Several gradient sequences have been designed to create contrast between tissues with different relaxation properties.

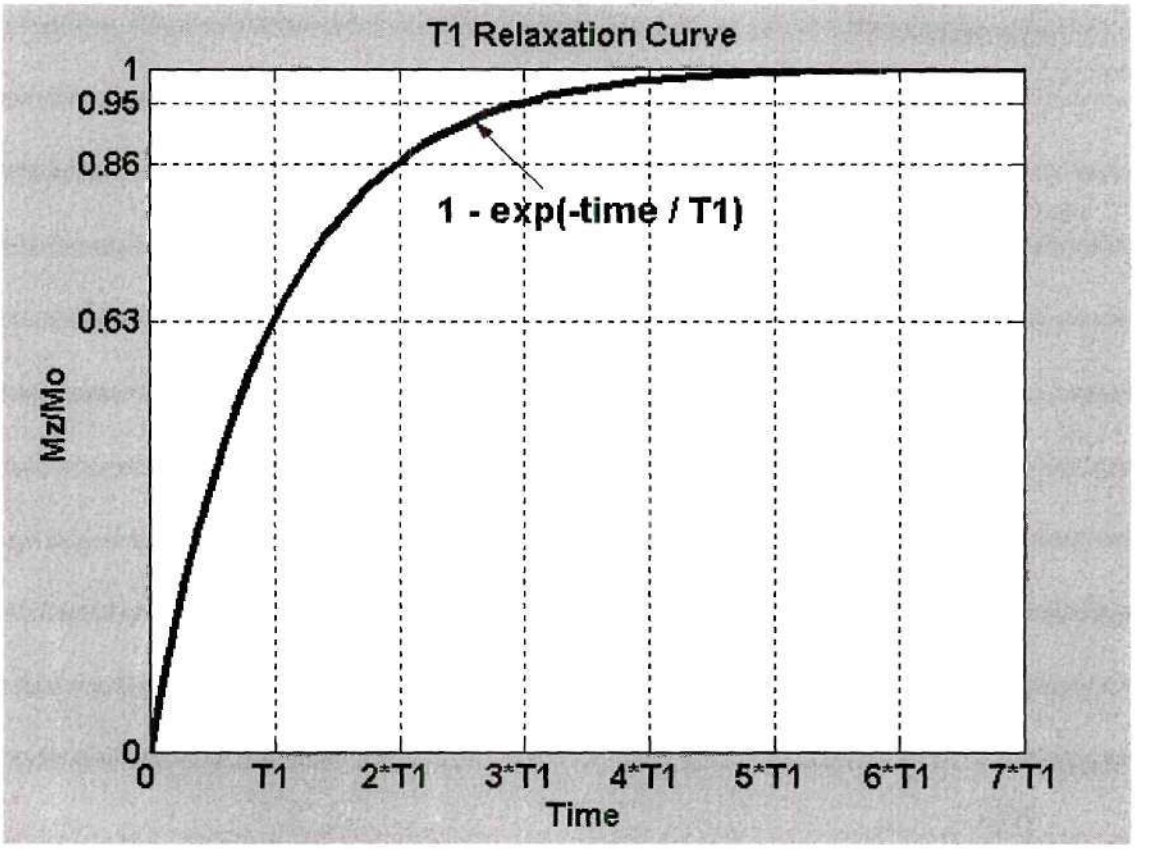

Figure 1.2: Following a 90° pulse, no longitudinal magnetization is present. As protons release their energy through T1 relaxation, the longitudinal magnetization (M_z) is gradually re-established to it pre-excitation level (M_o). The change of M_z/M_o with time follows an exponential growth process. The time constant of this exponential function is referred to as the T1 relaxation time or the spin-lattice relaxation time and is the time when M_z has returned to approximately 63% of its original value M_o.

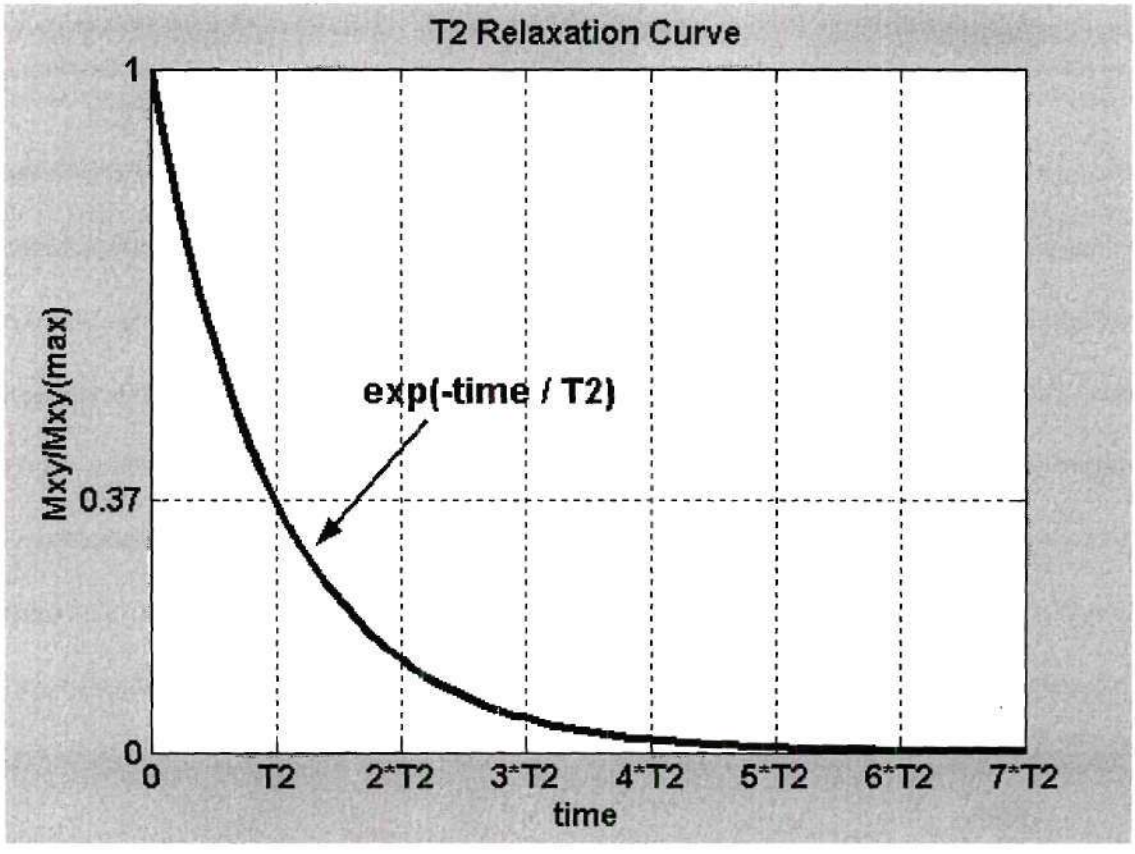

Figure 1.3: Following a 90° pulse, the maximum transverse magnetization is present. As protons release their energy through T2 relaxation, the transverse magnetization (M_{xy}) gradually decays to it pre-excitation level of zero. The change of $M_{xy}/M_{xy(max)}$ with time follows an exponential decay process. The time constant of this exponential function is referred to as the T2 relaxation time or the spin-spin relaxation time and is the time when M_{xy} has returned to approximately 37% of its original value.

Spatial Encoding and Image Reconstruction

In order to determine the location of the protons creating the RF signal, magnetic field gradients are used to make the RF signal characteristics dependent upon its location. To create 2D MRI images, slice selection is used to select which portion of the three dimensional object will be imaged. The excitation RF pulses are chosen so that only the portion of the object within the corresponding region of the magnetic gradient with the same Larmor frequency will respond.

To determine the location of the signals within the plane, frequency and phase encodings are used. The frequency encoding is accomplished by imposing a magnetic gradient at the echo time. The phase encoding is accomplished by varying the gradient waveform over several acquisitions in one direction. Each view causes the phase of the echo signal to change according to its location along that direction. By using phase encoding in a plane perpendicular to the frequency encoding and the slice encoding, the spatial location of the RF signal can be determined.

Imaging Sequences

Two main imaging sequences are used to obtain images with different contrast properties. Gradient echo sequences use gradient waveforms to dephase and rephase the protons after the initial RF excitation pulse (Figure 1.4). Gradient echo images are very fast but the echo signal intensity may be of lower quality due to inhomogeneities in the magnetic fields. Spin echo pulse applies a second RF pulse to rephase the protons (Figure 1.5). This sequence usually takes longer but the signal is not as largely affected by the magnetic field inhomogeneities. A variation on the spin echo is the inversion

recovery scheme which uses a 180° pulse applied prior to the initial excitation phase (Figure 1.6). This method enhances the T1 sensitivity at the time of the excitation pulse. Clinically, this sequence is used to suppress signal generated from protons in fat.

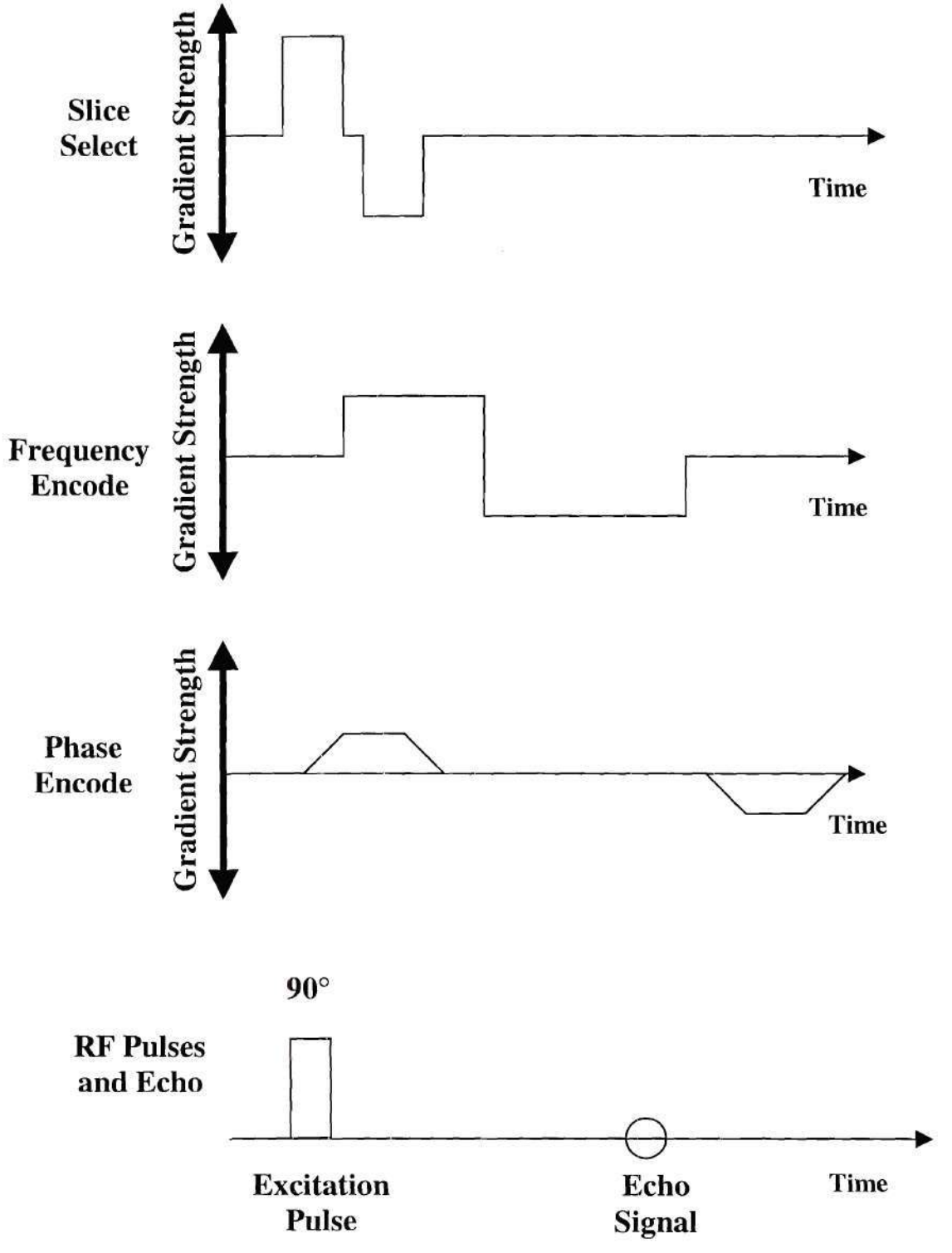

Figure 1.4: Basic Gradient Echo Sequence

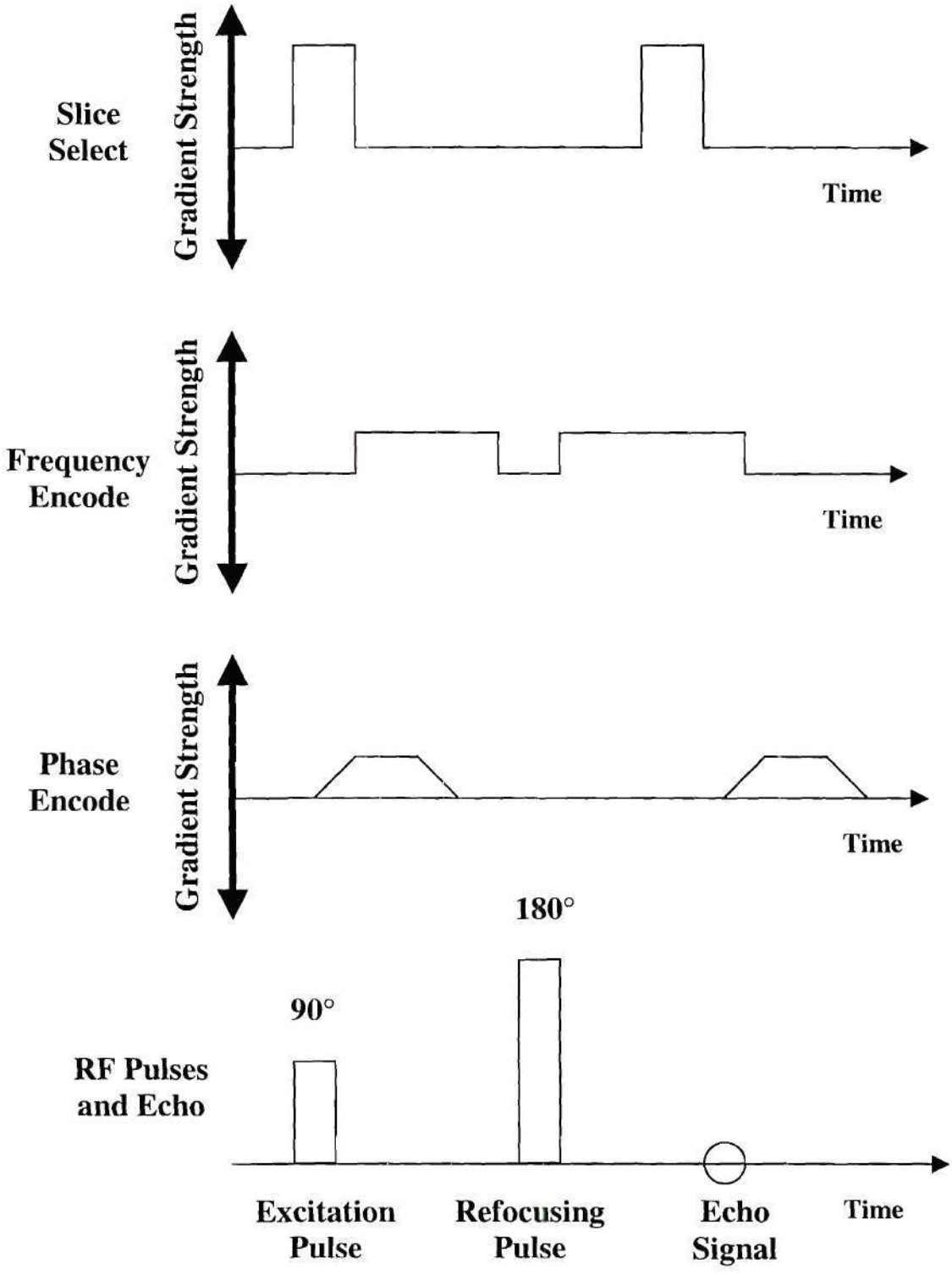

Figure 1.5: Basic Spin Echo Sequence

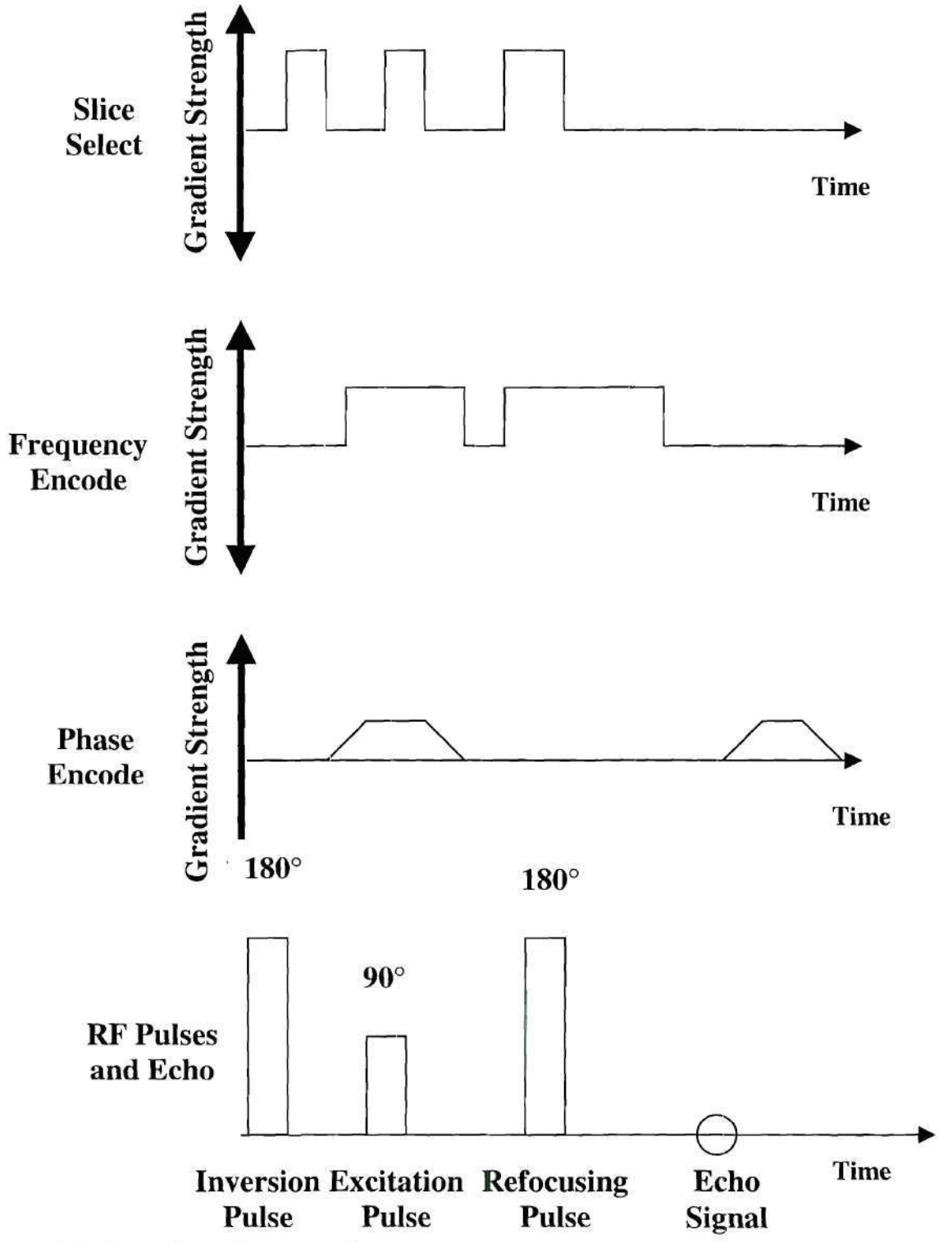

Figure 1.6: Inversion – Recovery Sequence

Phase Contrast Magnetic Resonance

PC-MRI is based on the observation that spinning protons move with a velocity along a magnetic field gradient, acquiring a shift in their angular position relative to stationary spins. This spin phase shift is proportional to the velocity of the spinning protons. Given the strength of the magnetic gradient and the time that the spinning protons were exposed to the gradient, a grayscale image can be produced that is encoded with the velocity values.

Each MR raw data set represents the transverse magnetization in each voxel as a vector quantity having both magnitude and direction (phase angle). The magnitude of the magnetization contributes to the image intensity while the phase provides information about the motion. The quantitative analysis of the relationship between the flow-related phase shift ϕ and the spins moving velocity V_x is expressed as

$$\phi(t) = \gamma \int x(t) \bullet G_x(t) dt$$

where $\phi(t)$ is the phase shift of the spin at time t, γ is the gyromagnetic ratio, x(t) is the location of the spin at time t, and $G_x(t)$ is the strength of the magnetic field gradient as a function of time.

Two equal pulses of opposite polarity (gradient pulse) are used to encode proton velocity as a change of phase. The phase shift induced by this two-pulse sequence is expressed as

$$\phi(t) = \gamma \int_0^{T_G} x(t) \bullet G_x(t) dt + \gamma \int_T^{T+T_G} x(t) \bullet G_x(t) dt$$

where T_G is the duration of each pulse. In this equation, $G_X(T+t) = - G_x(t)$, if M1 is the first moment of the gradient waveform $G_x(t)$ evaluated at the echo delay time (TE), and

$M1 = \int_0^{T_G} G_x(t)dt$, yielding the equation for a constant velocity

$$\phi = \gamma V_x T M1$$

This equation provides for stationary protons ($V_x = 0$) having a phase shift equal to zero. If the pulse sequence is repeated with the inverted flow encoding gradients, the signal intensity I obtained from complex subtraction of the two acquired data sets will be

$$I = 2 k \sin\phi$$

where k is a proportionality factor that includes spin population and instrument sensitivity. The resulting grayscale image is representative of the velocity fields present during the scan where the minimum possible velocity is represented as 0 and the maximum possible velocity is assigned a value of 1. The velocities are represented as quantized grayscale quantities linearly scaled between the maximum and minimum possible encoded velocities. The step size between quantized velocity values is a function of the total range of velocities possible and the size of the data storage used (8 bit, 16 bit, etc.) (Long et al., 1998).

Phase Contrast MRI Velocimetry

Displacement artifacts are caused by spins that move during the MR imaging sequence. These displacements can either be considered spatial/oblique or acceleration/velocity displacement artifacts. Spatial artifacts are a result of the time delay between different spatial encodings. During this time, the spins are displaced proportional to their velocity causing the artifact. The acceleration artifacts are a result of the spins changing velocity during the time delays caused by magnetic gradient spatial

encoding. These accelerations can be in the form of temporal or convective acceleration and have been investigated using an end-to-side anastomosis phantom with a diameter of 6.8mm (Steinmann et al., 1997). The steady flow velocities were recorded using a 0.5mm in plane resolution and a 3.4mm slice thickness. It was found that spatial displacement artifacts mapped the correct velocity field to incorrect spatial locations. Moreover, velocity displacement artifacts assigned incorrect velocities to correct spatial locations. Therefore, velocities near the center of arteries, which are usually higher than at the wall, can be expected to contain more of these errors.

Ku et al. (1990) have previously studied the accuracy of PC-MRI in determining the steady flow velocity profiles for several complex geometries. One-inch (25.4mm) diameter models of a straight tube, a curved tube, a smooth 90% area stenosis, and a 90% area orifice were studied. The in-plane resolution was 2mm and the slice thickness was 10mm. The MRI velocity data were able to detect forward and reverse flow associated with the two area reduction models. Skewed velocity profiles in the curved tube caused by secondary flows were also detected. The MRI velocity values at moderate levels of turbulence were realistic. However, as the turbulence intensities approached 100 percent, the MRI velocity data became unreasonable. It is thought that the random fluctuations associated with turbulence decrease the ability of a microscopic group of protons to remain coherent and return a homogenous signal (Bradley et al. 1984). It was also reported that phase images of velocity profiles were frequently disrupted at the boundary of the tube wall and that these disruptions were worse for the silicone and acrylic models as compared to the glass models (Ku et al., 1990).

Additional studies with this 25.4mm diameter 90% area stenosis model were performed to further characterize the accuracy of PC-MRI. As in the previous study, the stenosis had a minimum diameter of 8.128mm and occurred over a length of 76.2mm. In these studies, a 1mm in-plane resolution and 3mm slice thickness were used. Over estimations of velocities were measured when convective accelerations were present and under estimations of velocities were made when convective decelerations were present in the flow field. These were thought to be due to convective acceleration terms augmenting the velocity induced phase shifts. As the number of signals averaged was reduced from 12 to 1, the signal-to-noise ratio dropped significantly and the velocity values were underestimated. As the slice thickness was increased from 3 to 20mm, a dramatic decrease in the flow rate error was observed. This was thought to be due to a linear increase in the signal-to-noise ratio, a decrease in the echo time (time between signal excitation and detection over which the spins develop their phase value), and a decrease in the net acceleration and deceleration due to the greater number of velocity vectors averaged per voxel. The article also points out that when these methodologies were used in smaller sized arteries, a decrease in the resolution would be inherent due to the limitations of in-plane resolution and that a wider range of velocities contained within each voxel would decrease the signal-to-noise ratio. The overall findings of this study concluded that smaller voxels and longer echo times caused more inaccurate velocity measurements compared to shorter echo times and lower resolution measurements (Siegel et al., 1994). Further studies suggested that phantom experiments should not use scaled models or fluids with different viscosities. Scaled models may distort the signal

loss pattern and produce different results than would be seen in the *in vivo* case. (Oshinski et al., 1995)

Studies have also been performed comparing phantom models and *in vivo* data. Good qualitative agreement was found between these values tested in an abdominal aortic geometry using a 1mm in plane resolution and 2mm slice thickness. Areas of recirculation were found in both the phantom model and the volunteers at the posterior wall of the aorta and at the lateral walls of the aortic bifurcation. However, the magnitudes of the velocities did not agree due to the inability to match the waveform used in the phantom model to the actual waveforms present in the volunteers (Moore et al., 1994, Apr).

Good agreement has also been found for one-dimensional pulsatile flow phantom studies. Using a 9.5 mm diameter straight tube, PC-MRI data were obtained with a 0.5mm in-plane resolution and a 5mm slice thickness. The major limitation associated with this study was the relatively simple geometry utilized that only produced one-dimensional flow patterns (Frayne et al., 1995).

The studies cited state that there was generally good agreement between the PC-MRI velocity data and gold standard values with both steady and pulsatile flow in simple and complex geometries. Furthermore, good agreement with velocity values has also been found with data collected from human volunteers. However, inherent errors associated with obtaining PC-MRI data from flows with convective and temporal accelerations do exist. The best data are obtained when a large number of protons are used to obtain the signal (low in-plane resolution and high slice thickness) and with lower

echo times. It is also suggested that the phantoms and flow parameters used not be scaled and that the phantom material be selected to minimize the fluid-wall velocity disruptions.

Direct Calculation of WSS from MRI Velocity Profiles

Several experimental studies using human subjects and phantom arterial models to estimate WSS from phase contrast MRI velocity data have been performed. In all of these studies, some assumption regarding the shape of the near-wall velocity profile was used to fit curves to near-wall velocity data. These curves were then used to estimate the near-wall fluid shear rate by calculating the slope of the curve as it approached the wall. Oshinski et al. (1995) calculated the WSS in the abdominal aortas of eight volunteers. A 1.5T ACS scanner was used with the following parameters: field of view = 190mm; acquisition matrix = 256X256; pixel resolution = 0.74X0.74mm; slice thickness = 3-5mm; flip angle = 35°; repetition time = 17msec; echo time = 8msec; signal averages = 2. The velocity data from the edge pixel (V_1) and the adjacent intraluminal pixel (V_2) were used to estimate the wall location. Once the wall location had been determined, the average velocity of the two pixels ($V_h = (V_1 + V_2) / 2$) was used to calculate the near-wall shear rate using the following formula:

$$\Delta v / \Delta r = V_h / x$$

where x represented the distance from the interface of the two pixles to the calculated wall location. The calculated shear rate values were compared to theoretical velocity profiles derived from Womersley solutions using similar blood flow waveforms and straight geometries with uniform diameters approximately equal to the average diameters of the abdominal aortas of the human subjects.

Using this comparison technique, errors ranging from –45% (negative error refers to underestimations of shear rate) to 32% were recorded with the mean error equal to –12%. Overall, the study reported that larger WSS values were found on the posterior aspect of the suprarenal abdominal aorta when compared to the anterior wall. In the infrarenal aorta, negative WSS values were calculated, illustrating the ability of this technique to detect retrograde flow when applied to these geometries. In contrast to the suprarenal aorta, the posterior wall of the infrarenal aorta displayed a significantly lower mean WSS compared to the anterior wall. These same suprarenal abdominal aorta WSS patterns were also obtained by another reasearch group using the same techniques (Oyre et al., 1997; Pederson et al., 1999).

Masaryk et al. (1999) calculated WSS using three different methods: (1) linear interpolation (2) linear interpolation with wall location estimation (via the Oshinski method) and (3) quadratic interpolation with wall location estimation. These experiments were carried out using a 6.4mm cylindrical agar phantom with an MRI in-plane resolution of 0.7mm and a 10mm slice thickness. For steady flow experiments, the linear interpolation was found to over estimate the WSS values while the linear interpolation with wall location estimation was found to under estimate the WSS values. The quadratic interpolation method yielded the best results, which calculated the wall shear rate to be within $5.0sec^{-1}$ of the theoretical value. However, this would be expected since the theoretical solution of the velocity profile for fully developed flow in a straight tube is a quadratic function. For pulsatile flow, the wall strain rate estimations were significantly different than the theoretical values predicted by the Womersley equation. The root mean square errors showed that the linear interpolation method with wall

location estimation was the best method in this case. However, this method had a 17% error between the root mean square differences and the Womersley derived time-averaged wall shear rate values. Due to the straight geometry model, experiments testing the ability to detect high axial WSS gradients could not be accomplished for either the steady or the pulsatile flow experiments.

Moore et al. (1994) used linear and quadratic least squares PC-MRI velocity profile interpolation for WSS calculation on abdominal aorta phantoms. For these studies, the areas calculated to have low magnitudes and high oscillations of WSS correlated well, in a qualitative sense, with areas of plaque formation observed in post mortem examination of *in vivo* abdominal aortas. WSS calculations in the suprarenal aorta were compared to theoretical solutions of the Womersley problem for a straight tube having a similar internal diameter. The differences for the mean, maximum, and minimum WSS values were 2%, 3%, and 10%, respectively. Due to large changes in magnetic properties over a small distance near the phantom wall (Gibbs artifacts), the near-wall velocity data were found to fluctuate more than the velocity measurements in the center of the model. Therefore, although larger MRI resolution increases the accuracy of velocity profile curve fitting, this technique can also increase the inherent error associated with collecting the near-wall velocity data. This study also points out that as the Womersley parameter increases, the changes associated with the shape of the velocity profile are largely confined to the near-wall regions. This illustrates that flow conditions (specifically the Reynolds number and Womersley parameter) will affect the accuracy of near-wall curve fitting techniques to estimate the near-wall strain rates even within the same geometry (Moore et al., 1994).

A Fourier-encoded velocity imaging technique was also attempted in order to obtain sub-pixel velocity data (Frayne et al., 1995). A 0.64cm diameter straight tube phantom made from agar material was used in this study. This method was able to predict the location of the arterial wall and obtain sub-pixel velocity values for strain rate calculation. However, this method took two hours of imaging to obtain the velocity data for steady flow through a cylindrical phantom.

Oyre et al.(1998a,1998b, 1998c; Kozerke, 1999; Stokholm, 2000) have developed a multi-sectored 3D paraboloid method to calculate WSS. This method fits a 3D paraboloid to the pixels within a ring close to the wall. The edge pixels and the pixels at the center of the vessel are not used in this procedure. This method was tested on an 8mm diameter cylindrical phantom under steady flow conditions, imaged with a 0.7mm in-plane resolution and a 10mm slice thickness. The calculated WSS values agreed well with the theoretical values for steady flow through a cylinder.

In the first study reported by Oyre (1998a), manganese chloride doped water was used as the working fluid at flow rates corresponding to Reynolds numbers of 695 and 1027. For each flow rate, ten measurements were made moving the glass tube model to different in-plane positions between each scan. The preliminary edge of the model was determined by manually placing two points at opposite sides of the MRI images where the edge was visually determined. A circle was drawn between these points which represented the initial approximation of the edge location. The velocity data associated with the edge pixels were then discarded, and the adjacent intraluminal pixels comprising a 1mm band of velocity data were used to approximate the velocity profile. It is important to note that since ten scans were performed for each flow rate and axial

position, ten times as many data points were available for curve fitting. The time required to take the addition scans was not reported. A three dimensional paraboloid was fitted to the data points extracted. This surface was then extrapolated to zero velocity. The location where the extrapolated paraboloid was equal to zero was then defined as the true edge location. The near-wall strain rate was then taken as the derivative of the paraboloid at the wall.

The results reported WSS values of 0.81 ± 0.1 dynes/cm^2 and 1.36 ± 0.1 dynes/cm^2 for the lower and higher Reynolds numbers tested, respectively. From a hemodynamics stand point, due to the lower viscosity of doped water compared to blood, the corresponding velocities required to match the Reynolds numbers were also lower than physiological values. Although the fluid dynamics of the system should be similar due to the similarity properties of Reynolds number matching, the MRI images will not be the same. The slower velocities allow for less phase dispersement in the axial direction and therefore result in higher signal-to-noise ratios that cannot be matched clinically.

This study also used the paraboloid methodology to calculate the WSS in the common carotid arteries of human volunteers. The data calculated 25.6 dynes/cm^2 for the peak systole WSS and 6.3 dynes/cm^2 for the end diastole WSS. Negative values of WSS were not calculated using this method in the phantom or in the human subjects. Although negative velocities were not expected to be present in the phantom experiments, this technique limits the possibility of detecting recirculation regions. Since the edge detection methodology ultimately depends upon the extrapolation of velocity data to zero velocities, negative velocities could only be detected if (1) the nearest wall

pixel considered in the study was negative and (2) the 3D paraboloid fitted to the data was negative at that position. Due to the smoothing effects of the least squares velocity fitting techniques and the data averaging caused by inclusion of several velocity points along the circumference of the geometry, it is possible that negative near-wall WSS data points could go undetected due to data analysis techniques.

The ability to validate the *in vivo* experiments using *in vitro* phantoms in these studies is limited. The previously mentioned problems associated with the lower viscosity and velocities used in the phantom models would lead to the conclusion that errors for the *in vivo* studies will be inherently higher. Another dissimilarity is the discrepancy of wall shear stresses measured in the two experiments. The phantom studies measured WSS in the range of 0.81 - 1.36 dynes/cm^2 whereas the *in vivo* studies recorded WSS values of 6.3 - 25.6 dynes/cm^2. The viscosity of the blood was approximately four times greater than the viscosity of the manganese doped water. However, the strain rate associated with the *in vivo* studies is still greater by factors ranging from 2X to 5X even when the discrepancies in viscosity are considered. Thus, phantom studies testing the ability of this methodology to accurately detect more realistic strain rates were not performed.

One study has compared the WSS values derived from direct calculation to CFD data for two arterial bifurcation geometries (Köhler et al., 2001). Idealized geometries of a 60 degree symmetric bifurcation and an idealized carotid bifurcation were both examined under steady flow conditions. The phase contrast imaging parameters were 0.5mm in-plane resolution and a 1.0mm slice thickness. To provide detailed geometric data, a gradient echo sequence was performed under no flow conditions with a 0.8mm

slice thickness. The velocity profiles were determined by fitting a three-dimensional fifth order polynomial to the velocity data derived from PC-MRI. The fitting was carried out on a moving subset of five consecutive slices. The fitting was considered necessary to prevent poor estimates of WSS due to noisy experimental data. The CFD was carried out using 57,000 node models with the nearest wall node being 0.18mm from the wall. The inlet boundary conditions were determined from PC-MRI velocity data.

For the sixty-degree idealized symmetric bifurcation, WSS values were compared at three axial locations: proximal to the bifurcation, just distal to the bifurcation (bilaterally), and more distal to the bifurcation (bilaterally). Immediately distal to the bifurcation, the MRI velocity profile derived WSS values were determined to be very poor. Large negative WSS values were calculated and were thought to be caused by signal noise which was much larger than the near-wall velocities. The expected large velocities at the flow divider were not detected due to the inability of the fifth order polynomial to capture the high velocity gradients.

Further downstream, the MRI and CFD values were in better qualitative agreement. However, the MRI derived WSS values were 40% lower compared to the CFD values (6.0 dynes/cm^2 compared to 10.2 dynes/cm^2). This was thought to be due to a partial volume effect at the walls. There were also significant differences between the two symmetrical branch vessels which could not be explained by the 49/51 flow split ratio measured from the PC-MRI data.

In the inflow region, a Poiseulle flow theoretical WSS value of 15.4 dynes/cm^2 was calculated. Both the MRI and the CFD WSS methods overestimated this value by 20%. When the CFD was run with an idealistic inlet velocity profile, the WSS was

calculated at 16.2 dynes/cm^2. The difference was thought to be caused by an underestimation of the reconstructed vessel diameter.

Similar problems were also present in the carotid phantom tested. When the geometry was determined by extrapolating velocity vectors to zero, a false wall was detected along the flow separation area where forward and backward velocities intersected. Similar larger errors were also found at the outer wall of the carotid bulb due to the low velocity values and the relatively high signal noise. The study concluded that the use of small surface coils and long TR times (to reduce T1 saturation effects) yielded the best MRI data sets. However, using small spatial coils reduced the area of coverage that can be imaged and the longer TR times lead to total scan times that are unrealistic for the clinical setting. The conclusion of this study was that fitting fifth order polynomials to the available velocity data reduced the large errors associated with determining WSS values while still retaining the ability to detect non-parabolic velocity profiles. Furthermore, the WSS values derived from the CFD simulations were more accurate especially in areas of recirculation and low velocities.

The studies for MRI velocimetry and WSS calculation all used slice thicknesses of 1 to 10mm. Furthermore, all but one of the quantitative comparisons were done with straight cylindrical models that produce only one-dimensional steady or pulsatile flow fields. The current research examines the accuracy of PC-MRI WSS calculations on non-cylindrical geometries that change over short distances (stenoses). These geometries represent pathological states encountered clinically. WSS information obtained from these geometries could be used to study plaque growth and rupture. This information may be useful for guiding clinical therapy and intervention. For acute stenosis

geometries, a large slice thickness would be expected to essentially average out the different 3D flow elements created by the stenoses. These types of geometries will also create velocity profiles that cannot be fit to polynomial curves. This essentially makes the velocity data at the center of the tube ineffective for near-wall velocity interpolation and differentiation. The shape of the near-wall velocity profile will also change from position to position and therefore errors associated with curve fitting techniques will also be a function of spatial location.

Computational Fluid Dynamics

Basic Principles and Numerical Theory

Computational fluid dynamics (CFD) is a technique used to solve the Navier-Stokes equations using numerical methods and iterative techniques. For an incompressible Newtonian fluid, the continuity equation can be written

$$\partial\rho/\partial t + (\rho u_j)_{,j} = 0 \qquad (1.1)$$

where ρ is the density and u_j is the velocity

The momentum equation can then be written as

$$\rho(\partial u_j/\partial t + u_j u_{i,j}) = \sigma_{ij,j} + \rho f_i \qquad (1.2)$$

where σ_{ij} is a stress tensor and f_i represents the body force per unit mass. The stress tensor can further be defined by

$$\sigma_{ij} = -P\delta_{ij} + \tau_{ij} \qquad (1.3)$$

where P is the pressure, τ_{ij} is the deviatoric stress tensor, and δ_{ij} is the Kronecker delta operator. The material properties of the fluid determine the constitutive relation between the deviatoric stress tensor and the strain rate tensor, s_{ij}

$$s_{ij} = 0.5(u_{i,j} + u_{j,i}) \tag{1.4}$$

For viscous incompressible fluids, the dynamic viscosity is the only fluid property required to define this relationship

$$\tau_{ij} = 2\,\mu\, s_{ij} \tag{1.5}$$

By combining the equations for the conservation of linear momentum (1.2), the total stress tensor (1.3), the strain rate tensor (1.4), and the deviatoric stress tensor (1.5), the stress divergence form of the linear momentum equation can be written

$$\rho(\partial u_i/\partial t + u_j u_{i,j}) = -P_{,i} + [\mu(u_{i,j} - u_{j,i})]_{,j} + \rho f_i \tag{1.6}$$

Applying incompressibility and constant viscosity constraints, equation 1.6 can be further simplified to the Navier Stokes form of the momentum equation

$$\rho(\partial u_i/\partial t + u_j u_{i,j}) = -P_{,i} + [\mu\, u_{i,j}]_{,j} + \rho f_i \tag{1.7}$$

Since the simulations for these studies will be considered isothermal, there is no temperature or species dependence. Therefore, the energy equation, the species equations, and the buoyancy term in the momentum equation are not required.

The objective of finite element simulations is to reduce the continuum problem (with an infinite number of degrees of freedom) to a discrete problem (with a finite number of degrees of freedom) described by a system of algebraic equations. For each geometry to be solved using this methodology, the computational domain must be discretized into elements whose shapes are defined by nodal points. Within each element, the dependent variables u_i and P are interpolated by functions of compatible order (determined by the set of nodal points comprising the element). Within each element, the velocity and pressure are approximated by the functions

$$U_i(x,t) = \phi^T u_i(t) \tag{1.8}$$

$$P(x,t) = \psi^T P(t) \tag{1.9}$$

where U_i and P are column vectors of element nodal points and ϕ and ψ are column vectors of the interpolation functions

$$\text{Mass: } f_1(\phi, U_i) = R1 \tag{1.10}$$

$$\text{Momentum: } f_2(\phi, \psi, U_i, P) = R2 \tag{1.11}$$

where R1 and R2 are residuals (errors) resulting from the use of approximation equations. The Galerkin method of weighted residuals format of finite elements analysis seeks to reduce these errors to zero, in a weighted sense, by making the residuals orthogonal to the interpolation function of each element.

This methodology iteratively solves the Navier Stokes equations (1.7) over the discretized geometric domain given the boundary condition definitions to create a unique computational problem. If the computational approach achieves a convergent solution, the values for the velocity and pressure variables can be used to define the flow field as well as calculate other fluid dynamic variables such as wall shear stress.

Calculation of WSS from CFD Simulations

The three steps in applying CFD simulations to MRI derived data are (1) obtaining geometry and boundary condition images using PC-MRI, (2) image segmentation and geometry/grid construction, and (3) applying the MRI derived boundary conditions to the computational model and executing the code until a convergent solution is reached. Geometry creation is the most time consuming and difficult step in the process. Given the limited resolution of MRI images, the segmentation of images and subsequent reconstruction of three-dimensional geometries require significant smoothing to create an

acceptable geometry. However, the smoothing functions often average out unique geometry shapes, which could potentially affect the flow field and wall shear stress distributions both locally and globally.

Studies comparing the reconstructed geometries of rabbits' aortoiliac bifurcations to intraluminal casts have examined the accuracy of these methodologies (Moore, 1999a). Large differences were seen between the two methods. The bifurcation angle was larger in the casts than in the reconstructed computational geometry. Although the computational model was able to replicate the overall vessel geometry, the vascular casting technique was found to better capture detailed vessel cross-sectional dimensions and shape.

These same geometry reconstruction techniques have been used to run CFD simulations through idealized carotid artery phantom models (Moore et al., 1999b). Ultimately, the reconstructed geometries showed good agreement with the gold standard phantom geometries. However, the initial MRI images and resulting geometries were unacceptably noisy unless a two-step smoothing process was performed. First, the segmented cross-sectional arterial lumen boundaries were smoothed using a B-spline fitted through discrete surface points. The three-dimensional geometry was smoothed further by fitting a surface spline to the arterial lumen boundaries. These studies were carried out using acrylic phantoms, which produce MRI images with very distinct fluid-wall intersections. These edge locations were only affected by the resolution of the MRI images and the resulting partial-volume errors. CFD simulations through these models yielded a mean error of approximately 15% between the computer wall shear stress fields for the MRI derived geometry and the idealized CFD geometry.

A study designed to determine the lower bounds of errors associated with image segmentation, model construction, and finite element discretization was performed on a

straight tube model (Moore et al., 1998). The ultimate finding of the study was that using geometries based on unsmoothed MRI data can lead to large errors in computed wall shear stress values, even if mean errors in contour dimensions are fairly small. These errors were attributed mostly to image segmentation and model reconstruction since wall shear stress errors from finite element discrimination and governing equation solution were on the order of 6-8% of the mean wall shear stress values. Since the wall shear stress is inversely related to the cube of the radius for fully developed steady flow through a straight tube, small errors in arterial dimensions can result in large wall shear stress errors. Furthermore, errors in the three-dimensional geometry can create errors that are even larger than predicted using the cubic relationship. This occurred when two edge contours with different dimensions were located adjacent to one another leading to errors up to 40% of the mean wall shear stress.

Using these same reconstruction techniques, CFD results based on MRI derived carotid artery geometries from volunteers were compared to idealized carotid artery phantom geometries (Milner et al., 1998). Differences were observed in the bifurcation branch angle, bulb size and length, and the overall curvature of all three arteries. Qualitative differences in WSS patterns were also observed. In particular, secondary helical flow patterns were found to be an important determinant in the resulting WSS patterns and magnitudes. The use of *in vivo* flow rate patterns was also found to affect the WSS values, but to a lesser extent.

Other groups studying the carotid bifurcation have observed the same conclusions. The reconstructed geometries differed from the idealized models by having helical curvature and out-of-plane curvature. These geometrical features resulted in flow

patterns and WSS values that were significantly different compared to the idealized results. Comparisons between the CFD predicted flow patterns and those observed from the MRI images were reported as having good qualitative agreement (Long et al., 2000a). However, WSS values were not calculated in these studies. The same procedures were tested on the aortoiliac bifurcation. 2D cine phase contrast measurements were used to provide the pulsatile inlet boundary condition. Large differences were observed between the wall shear stress values from the MRI generated geometries and the idealized bifurcation. As in the carotid bifurcation model, good qualitative agreement was found between the CFD predicted flow patterns and those observed in the MRI images (Long et al., 2000b).

Other CFD studies in an 180° bend (Weston et al., 1998), an end-to-side anastomosis model (Steinman et al., 1996), and in the descending aorta (Wood et al., 2001) have also been studied. In all of the studies cited, the re-creation of the arterial geometry is the major factor influencing the WSS distribution and error. Issues associated with smoothing the geometry to reduce errors created by low MRI resolution and partial volume effects have been studied. However, a consequence of smoothing computational geometries is that high gradient anatomical geometries that actually exist can be eliminated. These features may cause important flow field patterns that can affect the WSS values locally as well as farther downstream. To date, no consensus exists with regard to how CFD geometries should be smoothed.

Summary

Taken together, this information suggests that vessel geometry and local hemodynamics contribute significantly to the initiation and growth of atherosclerotic plaques. Local hemodynamic forces create favorable sites for oxidized LDL formation and monocyte recruitment. These same forces are also involved in the advanced stages of atherosclerotic disease contributing to plaque rupture, thrombus formation, and arterial occlusion. Therefore, patient specific WSS data could be used to determine areas in the vasculature where atherosclerosis is most likely to occur. Furthermore, knowing the maximum shearing stresses acting on a plaque as well as its chemical make-up (from MR spectroscopy) could enable physicians to better predict when plaque rupture events may occur. The ability to determine WSS values in patients requires knowledge of (1) arterial wall location and (2) near-wall velocity profiles. MRI offers a non-invasive method of determining these parameters through manipulation of proton spin recovery times using various magnetic gradient and RF energy sequences. Arterial WSS can then be determined through direct calculation based on wall location and near-wall fluid strain rates or CFD simulations. However, errors associated with obtaining arterial wall location and blood velocity information using MRI (such as resolution, noise, and inherent phase contrast errors) can cause subsequent errors in the WSS calculations.

Only one study cited has compared the results from calculating WSS values from the MRI derived velocity profiles to the results derived from CFD simulations (Köhler et al., 2001). In that study, large values of WSS occurring at the flow divider of the bifurcation could not be captured using either method. In other attempts to calculate WSS values directly from MRI derived velocity profiles, simple straight tube geometries

have been employed. The flow patterns in these geometries are predictable, and therefore data analysis techniques can be specified to reduce errors under these controlled conditions. Furthermore, the MRI scan parameters were set to reduce noise levels by increasing the slice thickness and, effectively, the voxel dimensions. In this manner, the ability of the MRI images to capture acute geometric or velocity changes was decreased due to the large variation in proton signal averaged over such large pixels. None of the experiments to date have evaluated the ability of PC-MRI to capture large WSS gradients using physiologically scaled models with MRI relaxation properties similar to arterial wall tissue.

The purpose of this study is to determine which method, direct calculation from PC-MRI velocity data or CFD simulation, will produce more accurate WSS values through symmetric stenosis geometries and to suggest techniques to improve this accuracy. The symmetric stenosis geometry was chosen so that the ability of these two methodologies to capture large WSS gradients could be assessed. This information, in addition to other clinical parameters, could be used for earlier detection of atherosclerotic arterial disease and intervention.

CHAPTER II

METHODS AND MATERIALS

Experimental Approach

The experimental approach utilized three models to assess the accuracy of wall shear stress values derived from PC-MRI data. The first model was a straight tube that represented a non-diseased artery. This model was chosen since theoretical solutions are known for well-developed steady flow conditions. The other models were straight tubes with symmetric stenoses representing 52.7% and 75.0% area reductions. These models were chosen to represent different degrees of arterial disease and blood flow disruption.

The models for PC-MRI studies were manufactured to be of a size typical of the human common carotid artery to recreate the MRI resolution expected clinically. These models were made from polyvinyl alcohol, which mimics the MRI relaxation times of *in-vivo* arterial wall tissue. Data obtained from PC-MRI was used to calculate WSS in two ways. First, the velocity profiles from the MRI images were used to directly calculate WSS. Second, the geometry and inlet boundary conditions were used to create computational fluid dynamic simulations. The velocity distributions from these simulations were then used to calculate the WSS values. Scaled up models were also created for flow visualization studies.

Gold standard WSS values were assumed to be determined from CFD simulations. In these studies, the ideal geometries were taken from the cast used to make the polyvinyl alcohol (PVA) models. The volumetric flow rate was measured directly from the MRI flow loop using ultrasonic flow probes. This information was used to

create the inlet boundary condition using the Poiseuille assumption of a fully developed parabolic velocity profile.

Flow Visualization

Optically clear models of the 0.0%, 52.7%, and 75.0% stenosis geometries were manufactured using a silicon-based elastomer molded around polished aluminum models. The diameter of the aluminum models in the non-stenotic regions was 2.54cm (1.0 inches). The diameters at the point of maximum stenosis were 1.75cm (11/16 inches) and 1.27cm (1/2 inches) for the 52.7% and 75.0% stenosis models, respectively. The stenosis was manufactured in the shape of the cosine function with the entire stenosis occurring over a 2.54cm length in the center of the model. The equation describing the stenoses is:

$$\text{Radius}(Z) = R_{max} - ((R_o - R_{min})/2)*(1+\cos(\pi*Z/Z_o))$$

where R_{max} = maximum radius

R_{min} = minium radius (at maximum stenosis)

Z = axial location

Z_o = one-half of the stenosis length

and $-Z_o \leq Z \leq Z_o$

The models were assembled in two halves that were connected at the point of maximum stenosis by a screw and centered in a Plexiglas box (5.08cm x 5.08cm x 27.94cm).

A silicon based elastomer (Sylgard 184, Dow Corning Corporation, Midland, MI) was created by combining ten parts of the base material with one part of the polymerization catalyst and mixing thoroughly. The elastomer was then exposed to a

vacuum of approximately 70 kPa to extract the dissolved gases from the solution. This prepared material was then poured into the Plexiglas mold being cautious to discourage the entrapment of air into the model. The elastomer was allowed to cure for seven days in a dust free environment after which the polished aluminum model was removed leaving the final mold.

The model was placed in a flow loop powered by a centrifugal pump (Little Giant Pump Company, Oklahoma City, OK), which provided steady flow rates that were adjusted by varying the downstream resistance (Figure 2.1). The pump was submerged in ice water to keep the temperature of the working fluid constant. A glycerin/water solution was used in the flow loop to match the refractive properties of the Sylgard model and provide a viscous fluid for easier Reynolds number matching. This solution was initially mixed as a 58/42% glycerin to water solution. The exact composition of the mixture was then adjusted to create a solution with a refractive index matching the Sylgard models (1.41) which was measured with an Extech refractometer (model 2192). The viscosity of the final solution was then measured using a Cannon Fenske routine viscometer (size 100, Fisher Scientific, Pittsburgh, PA). The average kinematic viscosity measured was 0.076 Stokes.

In order to replicate the same flow conditions that were used in the PC-MRI flow loop, the principle of Reynolds number similarity was utilized to calculate the flow rates used in the model. Using these techniques, the average flow rate used in the system was approximately 2.22 L/min and the peak flow rate used in the system was approximately 6.50 L/min. The actual flow rates used were based upon the viscosity, measured prior to each experiment, which fluctuated slightly due to variations in room temperature. A

transit time ultrasonic flow probe (H16XL) connected to a flow meter (T110, Transonics Inc., Ithica, NY) was used to measure the flow rate. The glycerin/water solution was seeded with Amberlyst A-21 particles (Sigma Chemical Co., St. Louis, MO). The particles were sieved with a RO TAP (model RX-29, W.S. Tyler, Mentor, OH) mechanical sieving device using U.S.A. Standard Testing Sieves numbers 35 and 40 yielded particles with diameters ranging from 425 – 500μm. These particles were added to the glycerin/water solution in sufficient quantities to adequately image the flow patterns during flow visualization.

Sheets of laser light were created using glass capillary tubes to diffract the laser beam produced by two helium-neon 10mW lasers (Class IIIb, Aerotech, Pittsburgh, PA). These laser sheets were positioned to illuminate the particles in the center plane of the optically clear models. The particle streamlines were photographed using ASA 400 speed film, an F-stop of 5.6, and a shutter speed of 1.0 second.

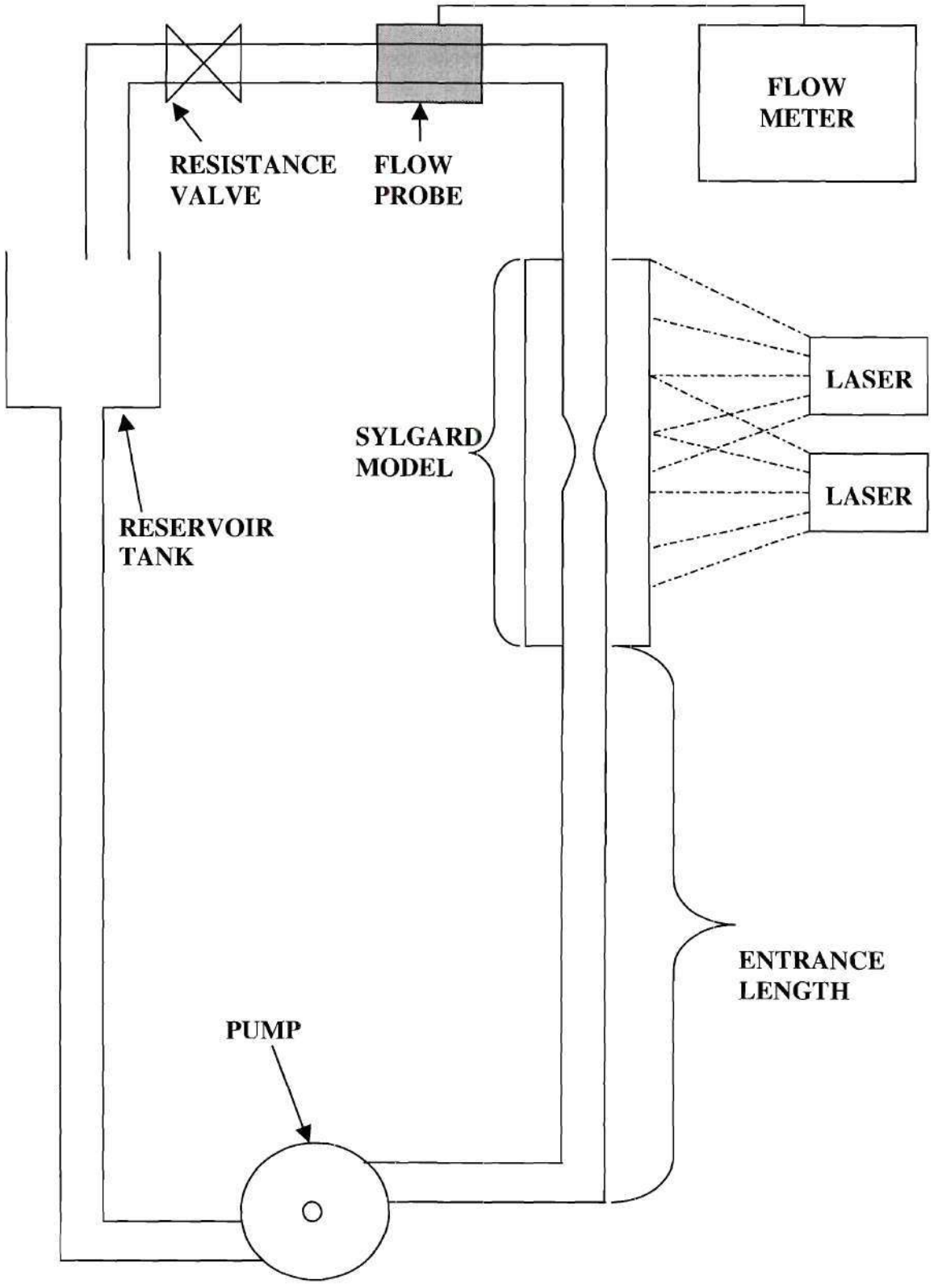

Figure 2.1: Flow visualization flow loop.

Phase Contrast Magnetic Resonance Imaging

Physiologically scaled models, with the same geometric shape used for the flow visualization studies, were manufactured from polyvinyl alcohol (Av Mol Wt = 70,000 – 100,000, Sigma Chemical Company, St. Louis, MO). The maximum diameter of the models was 0.635cm. The minimum diameters occurring at the point of maximum stenosis were 0.449cm and 0.318cm for the 52.7% stenosis and the 75.0% stenosis models, respectively. Polyvinyl alcohol is a material that can be prepared as a hydrogel or a cryogel based on manufacturing techniques. This material has similar T1 and T2 relaxation signals compared to arterial wall tissue and was used in this study to replicate the ambiguity of the blood-artery wall interface (Rickey et al, 1995; Chu et al., 1997; Mano et al., 1986).

The PVA powder was added to a 50/50 mixture of glycerin and water. This ratio was found to create the most stable osmotic pressure when placed in the MRI flow loop with the 40/60 glycerin/water solution. The PVA powder was dissolved in the glycerin/water mixture by autoclaving for 15 minutes at 121°C. Polished aluminum models with the geometries described above were manufactured on a computer-controlled lathe (J.M. Machining, Lawrenceville, GA). These models were centered in 1.27cm (0.5 inches) internal diameter Plexiglas tubes using O-rings at both ends. The PVA was poured into the tube and around the model. The entire apparatus was placed in a -70°C freezer for 24 hours after which the cured PVA mold and the polished aluminum were removed from the Plexiglas tube. The polished aluminum model was then removed leaving the PVA mold of the stenosis geometries.

The PVA model was positioned in a flow loop illustrated in Figure 2.2 and was placed within a 1.27cm (0.5 inches) Plexiglas tube. The entrance and exit tubes (0.635cm ID, 0.953cm OD) were also made of Plexiglas and centered within the larger 1.27cm tube using O-rings (Figure 2.3). The entrance tube was approximately 90.0cm long to assure a fully developed velocity profile at the entrance to the PVA model. A centrifugal pump (Little Giant Pump Company, Oklahoma City, OK) provided steady flow rates that were adjusted by varying the upstream resistance. The pump was submerged in ice water to keep the temperature of the glycerin/water solution constant and kept at a sufficient distance to assure the magnetic field from the MRI scanner would not affect its static disposition. The system resistance was placed upstream of the model since the junction of the entrance length tubing and the PVA model could not tolerate high fluid pressures. However, any fluid flow disturbances caused by the resistance would have dissipated by the time the fluid entered the PVA model due to the sufficiently long entrance tubing. A rotometer was used to roughly set the flow rate, and the graduated cylinder/stopwatch technique was used for fine measurements. The average flow rate was set at 0.635 cm^3/min (Re = 244) and the peak flow rate was set at 0.790 cm^3/min (Re = 714).

The solution used in the flow loop was approximately a 40/60 glycerin/water mixture. The final composition of the solution was adjusted to match the kinematic viscosity of blood (0.037 Stokes) as measured using a Cannon Fenske routine viscometer (size 100, Fisher Scientific, Pittsburgh, PA). A large reservoir of the solution was used in the flow loop in order to further assure the temperature of the solution remained constant.

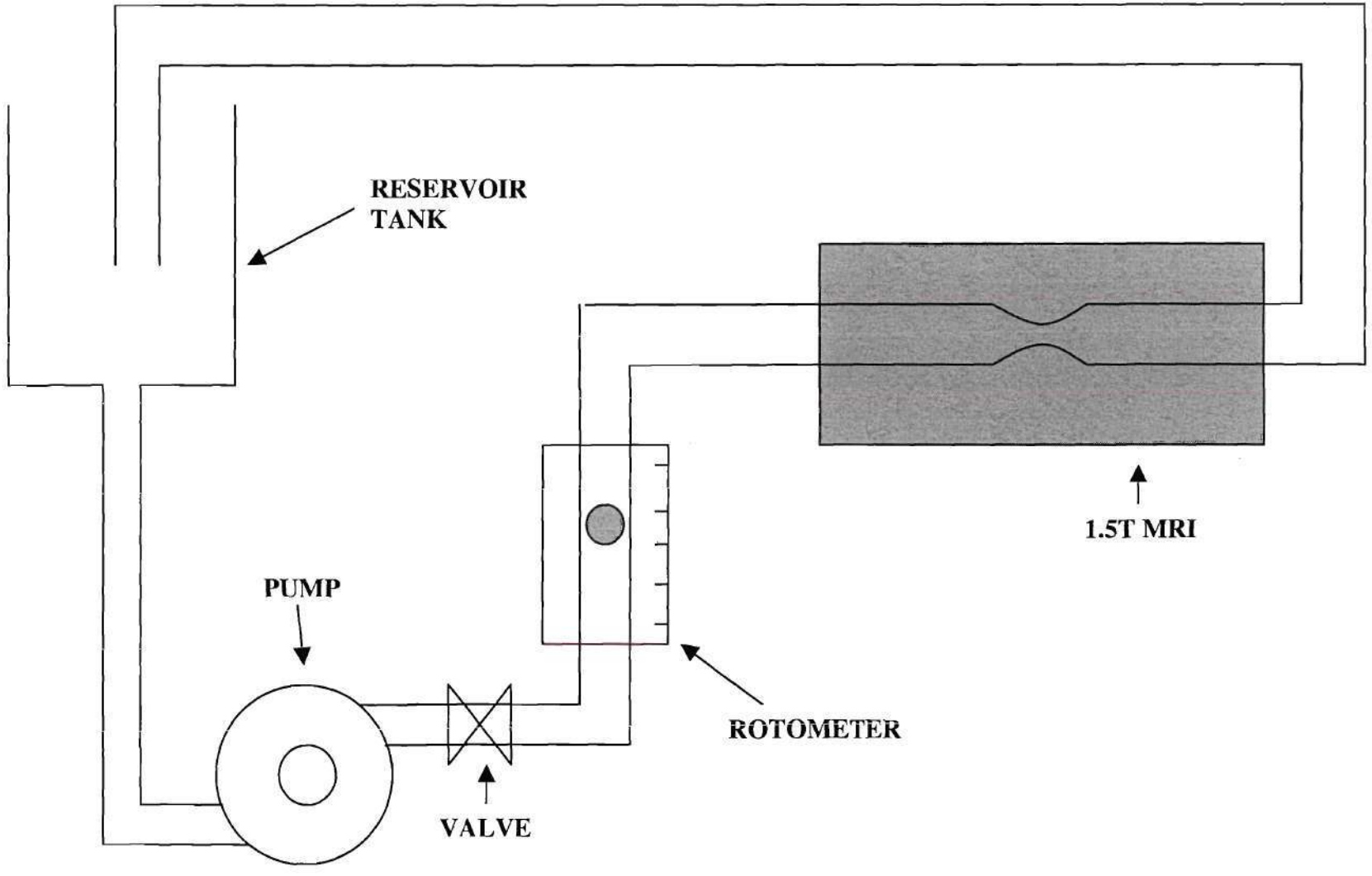

Figure 2.2: Phase contrast MRI flow loop.

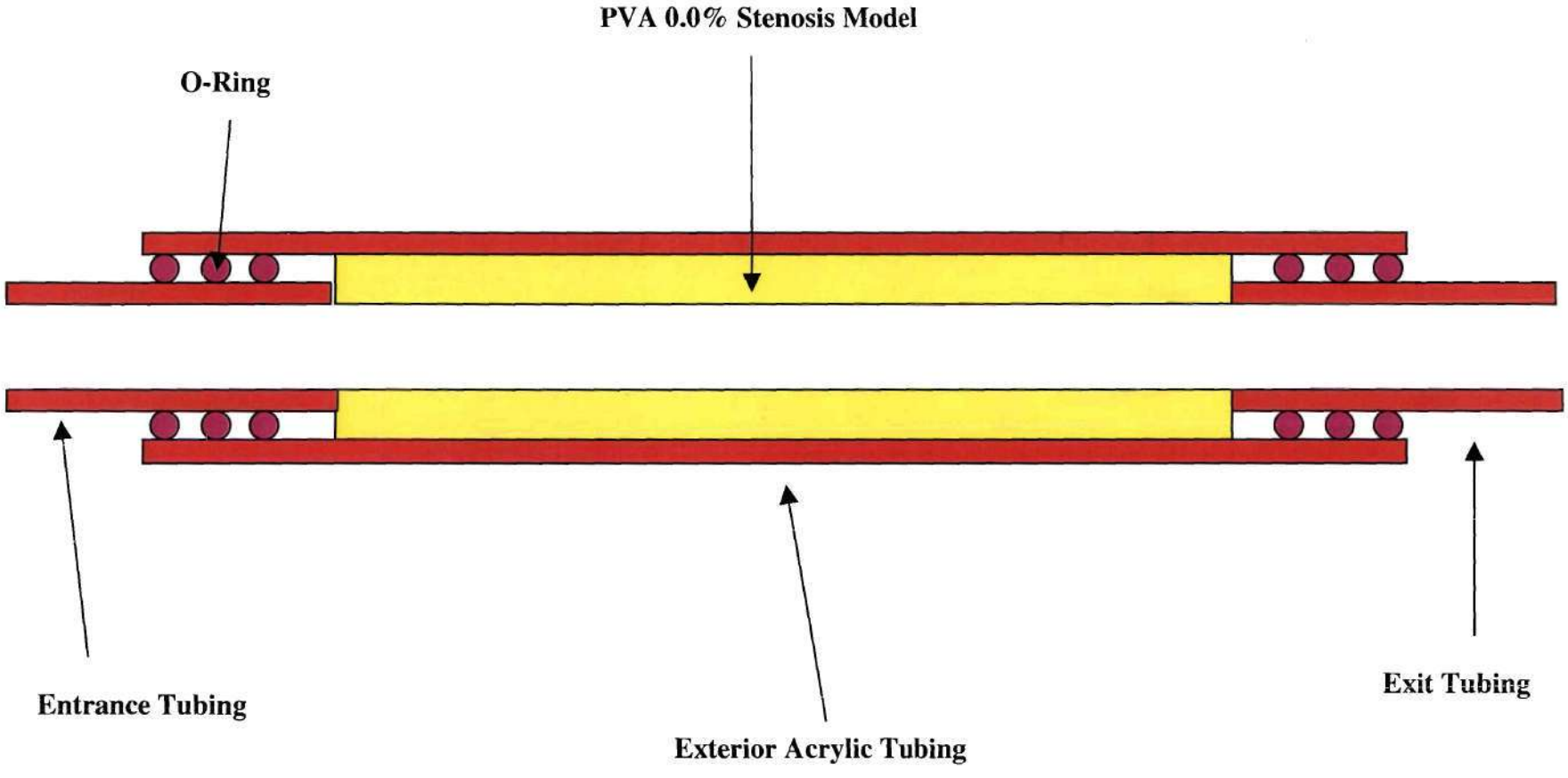

Figure 2.3: PVA flow apparatus. A TMJ coil was placed over the PVA model in the MRI scanner.

Phase contrast MRI velocity data were collected for each geometry and both the average and peak flow rates at thirteen axial locations (Figures 2.4 and 2.5). The imaging parameters used were: field of view = 128 mm, scan matrix = 256 x 256, TR = 20 msec, TE = 6 msec, flip angle = 40 degrees, slice thickness = 2mm, and 8 signal averages. In order to obtain higher quality images for edge detection purposes, an inversion-recovery MRI sequence was used at the same axial locations. For these images, the pump was turned off and the data were collected under zero flow conditions. This was necessary due to flow-induced artifacts that were present in other imaging sequences attempted. However, it is believed that similar quality images could be collected for *in vivo* pulsatile flow conditions using a black blood imaging sequence. This technique could not be used in the current study since steady flow was utilized. In these cases, areas of recirculating fluid were not cleared between the time of excitation and read-back, and therefore yielded errors suggesting the area of recirculating fluid was a part of the wall. The MRI image files collected were converted to a 256 x 256 unsigned 16-bit format using an in house program (Marijn Brummer, Ph.D., Emory University Department of Radiology).

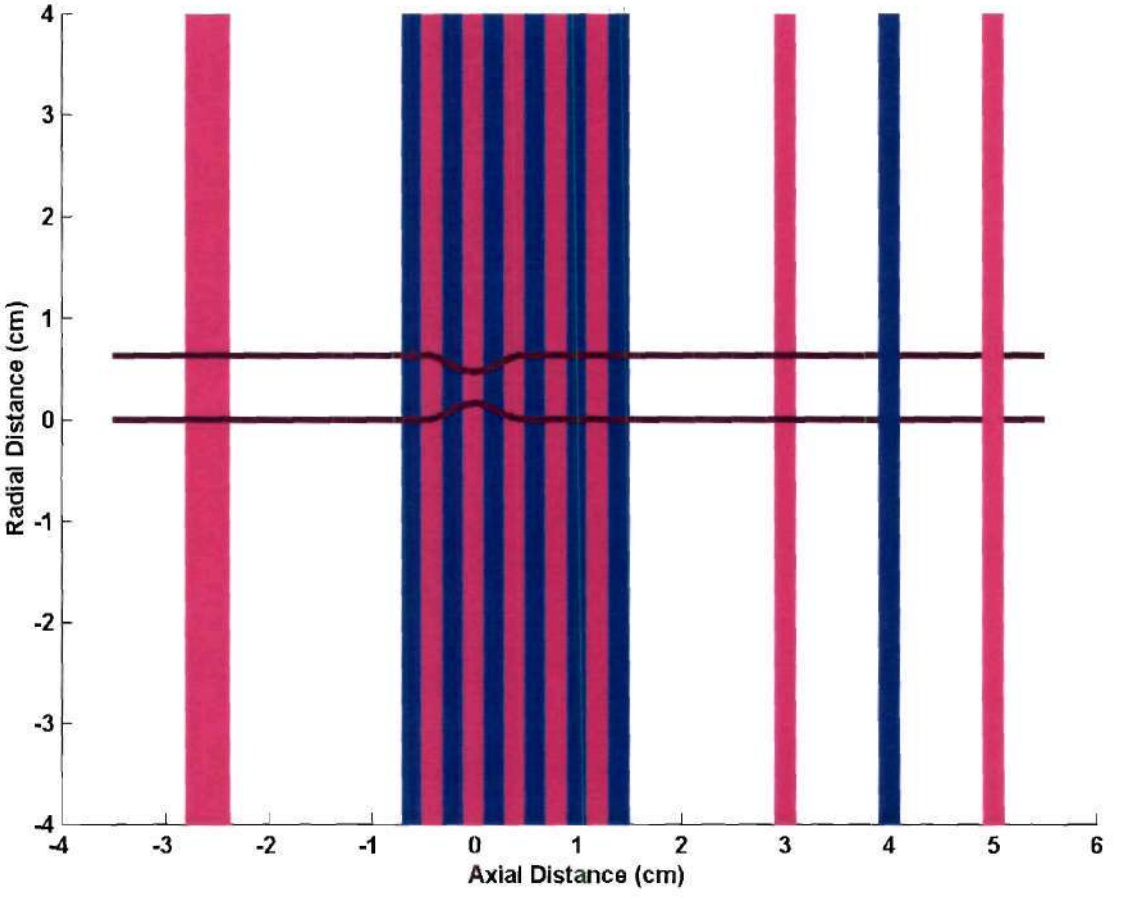

Figure 2.4: 75.0% stenosis model (black). The alternating purple and blue lines represent MRI slices obtained for all models. The first up-stream slice (furthest to left) is 5mm thick. All other slices are 2mm thick. The first slice is larger to capture an inlet velocity profile with less noise for CFD simulations.

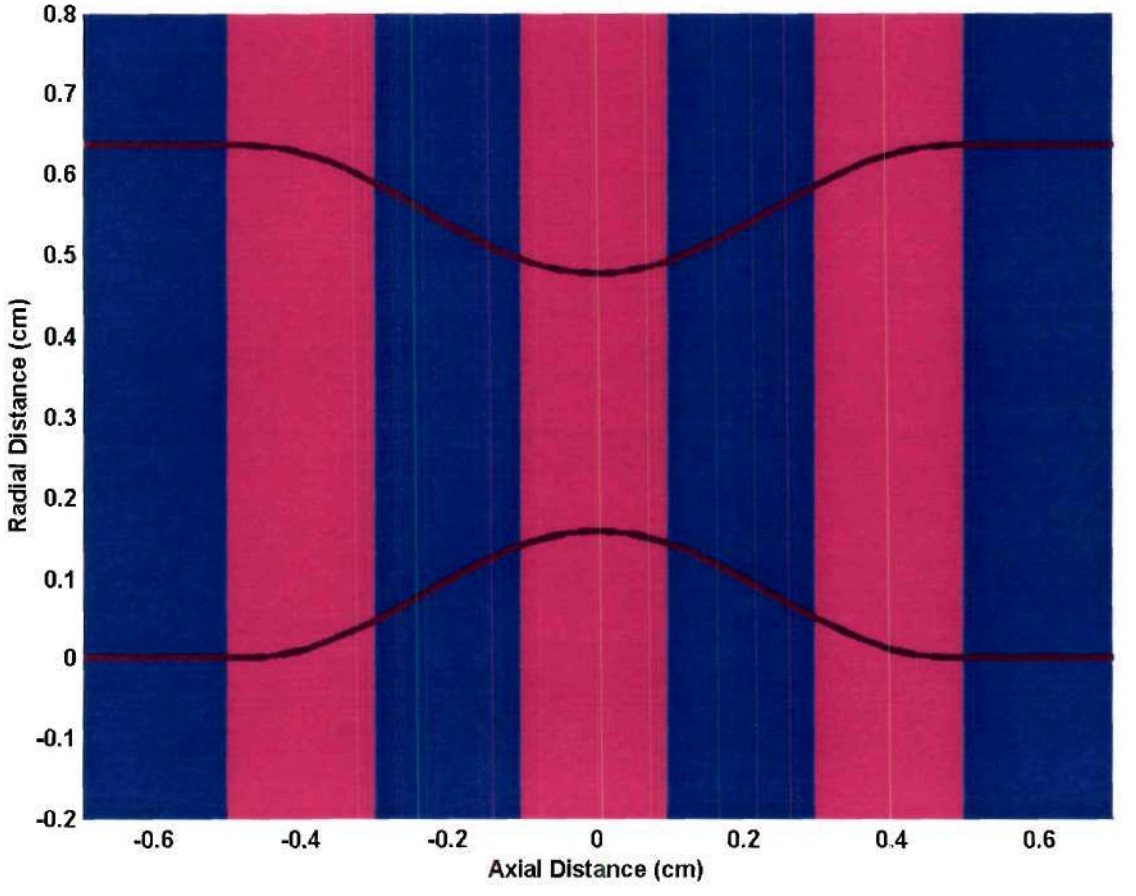

Figure 2.5: A closer view of the stenosis in Figure 2.4.

Direct Calculation of WSS from MRI Data

The wall location was determined by thresholding the inversion-recovery images: all pixels having a value above 0.4 were given a value of 1, and a value of 0 was assigned to all other pixels (program MRIWSSMAIN, see appendix) (see Figure 2.6). This created a binary image with the PVA model represented as the white entity. Erroneous pixels along the edges were then converted to their correct values using a binary dilation and erosion procedure. The initial edge approximation was determined by fitting a contour line to the resulting binary image (function EDGEDETECT, see appendix). This line was then smoothed by reassigning points along the curve to new values based on the averages of three points (each point and one point on either side). This procedure was executed five times for each image resulting in a smooth line interpretation of the edge location (function SMOOTHFIL, see appendix).

The edge derived from the inversion-recovery sequences was then transferred to the phase contrast images so velocity data could be extracted. Four velocity profiles were interpolated from each image at 45 degree intervals. The velocity data for the profiles were derived from the phase contrast images and recorded at each edge location and at each pixel located between the edge points (functions WSSBOUNDARYPNTS and VELPROFILE, see appendix). To determine the wall shear stress, linear and quadratic least square approximate curves were fitted to the one and/or two points nearest to the edge and to the edge velocity points to determined the near-wall velocity profile. For the quadratic curve fitting, three points were required. For the linear curve fitting, two points and three points were used to obtain two near-wall velocity profile approximations. For each curve fitting, two near-wall velocity profiles were created by (1) allowing the data

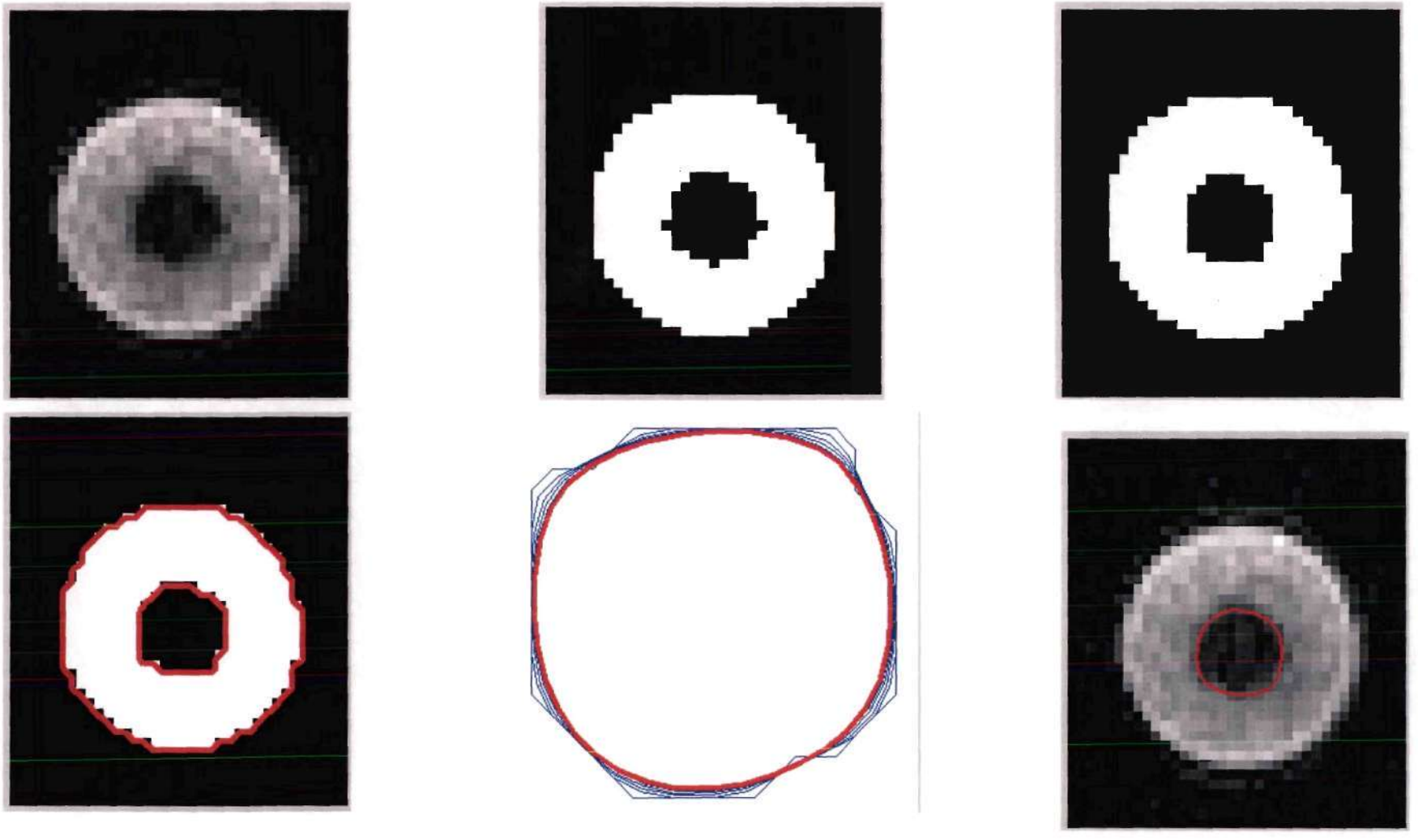

Figure 2.6: Edge detection algorithm. Top row left to right: Original image; thresholded image; after dilation/erosion procedure. Bottom row left to right: Fitted contour lines; smoothing of inner contour line; final edge representation superimposed over original MRI image.

point at the wall to equal the velocity recorded from the phase contrast data and (2) by forcing the data points at the wall to zero velocity be enforcing a no slip boundary condition. For all least square curves calculated, the WSS values were determined by taking the derivative of the polynomials at the location of the wall and multiplying by the dynamic viscosity (0.04 Poise) of the glycerin/water solution used in the flow loop (function WSSCALC, see appendix).

For each slice evaluated, the eight WSS values were evaluated separately and together by calculating the average WSS and standard deviation for each axial location. Since the geometries used in the flow loop were axi-symmetrical and the entrance boundary conditions were assumed to be well developed and symmetrical, the WSS values at each axial location would be expected to be independent of angular location within that image.

Computational Fluid Dynamics

The wall curves used for the direct calculation of WSS were also used to create the three dimensional geometries in the preprocessor software GAMBIT (Fluent, Lebanon, NH) (program MRICONTMAIN, see appendix). Spline functions were used to connect the curves creating a wire frame of the arterial model. The computational mesh was created by defining the boundary layer parameters and allowing GAMBIT to create the internal mesh using finite tetrahedral elements. The distance from the wall to the first node, the growth rate from one tetrahedral to the next, and the number of rows of nodes were the parameters required to define the boundary condition.

To determine the appropriate grid parameters, grid sensitivity studies were performed on the 75.0% stenosis model at the average flow rate. Twelve different simulations were run on the same wire-frame geometry derived from the MRI data but with different grid spacing and boundary layer parameters (see Table 2.1 below).

Simulation Name	Grid Spacing	Boundary Layer First Row (cm)	Boundary Layer Growth Rate	Boundary Layer Number of Rows	Number of Nodes	Number of Elements
st75_01	0.04	0.001	1.5	8	137984	131820
st75_02	0.04	0.0005	1.5	9	150528	144300
st75_03	0.04	0.00025	1.5	11	169540	163215
st75_04	0.035	0.001	1.5	8	187650	179048
st75_05	0.035	0.0005	1.5	9	219150	211008
st75_06	0.035	0.00025	1.5	11	230625	222432
st75_07	0.03	0.001	1.5	8	278506	267786
st75_08	0.03	0.0005	1.5	9	281619	292392
st75_09	0.03	0.00025	1.5	11	331430	320508
st75_10	0.025	0.001	1.5	7	392121	377300
st75_11	0.025	0.0005	1.5	9	444960	429968
st75_12	0.025	0.00025	1.5	11	502434	487256

Table 2.1: Grid Sensitivity/Independence Test Cases

The plots of axial location versus WSS were used to determine the minimum requirements to define a mesh independent solution. It was determined that the best grid parameters to use were a grid spacing of 0.03 with a boundary layer first row location of 0.00025cm from the wall. This grid scheme was used for all other CFD simulations. Further information about choosing the appropriate grid density and configuration can be found in the results section.

All models were executed with a no-slip boundary condition at the walls and a zero traction boundary condition at the outlet. Two inlet boundary conditions were used

for each geometry and flow rate combination. First, an idealized boundary condition was used with a volumetric flow rate equal to the flow rate measured from the flow loop. The parabolic velocity profile was created so the maximum velocity was equal to twice the average velocity. Each inlet node axial velocity was determined by linearly interpolating the parabolic velocity profile to each node location (program IDEALBC, see appendix). Due to the irregularity of the inlet boundary, the idealized parabolic velocity profile was also irregular. The nodes located on the wall of the inlet geometry were then set to zero to satisfy the no-slip boundary condition. All of the non-axial inlet velocity components were set to zero.

The second boundary condition was derived from the phase contrast velocity profiles. Again, each inlet node velocity was determined by linearly interpolating the phase contrast data for the inlet slice geometry (program INELEMENT, see appendix). The nodes located on the wall of the inlet geometry were then set to zero to satisfy the no-slip boundary condition. The inlet non-axial velocity components were set to zero.

The simulation parameters were three dimensional non-moving geometry, incompressible Newtonian fluid, steady flow rate, laminar flow conditions, non-linear Navier-Stokes equations (convective terms present in the momentum equations), and isothermal. The fluid dynamic viscosity and density were set to 0.04 Poise and 1.081 g/cm^3 respectively. A segregated iterative method was used to obtain the nonlinear steady solution. The convergence criteria for all simulations were a decrease of four orders of magnitude of the pressure and all three components of velocity. For the segregated solver, the norm is calculated for each degree of freedom at each node after

every iteration. The solution was considered converged when the norms for all degrees of freedom at all nodes were less than the prescribed convergence tolerance.

$$ABS((Ui - Ui\text{-}1) / Ui) <= Tolerance$$

After each simulation, the geometry velocity vectors and pressure at each node were written to a file for post processing. The WSS values were also calculated by the FIDAP program by first calculating total fluid stresses and then decomposing the stresses into viscous/pressure and normal/tangential direction. The WSS vectors were defined by the tangential viscous stresses taken at the wall. Ten degrees of freedom (node x-location, node y-location, node z-location, u-velocity, v-velocity, z-velocity, u-WSS, v-WSS, z-WSS, and pressure) were then converted into a file format readable by the post processing software Tecplot 9.0 (Amtec Engineering, Bellevue, WA) (program FDP2TP2, see appendix).

Gold Standard Velocity and WSS Values

Gold standard flow field parameters were determined from CFD simulations. For these studies, the three dimensional geometries were taken directly from the CAD files used to make the polished aluminum models used in the PVA model construction. The boundary conditions were the same as those described for the MRI derived geometries. The inlet boundary condition was described by a parabolic velocity profile having the same volumetric flow rate as measured from the flow loop. Since the inlet boundary shape was idealized, the parabolic shape was exactly the same as the inlet geometry boundaries. Therefore, the near-wall errors present in the fitting of the parabola to the

MRI inlet geometry did not occur in these simulations. The meshing properties and post processing data handling were the same as previously described.

CFD simulations were also performed with the MRI derived inlet boundary conditions and the idealized geometries. For these studies, the PC-MRI derived velocity components were assigned to the inlet nodes by linear interpolation (program MRIBC, see appendix).

In all, four CFD simulations were executed for each geometry and boundary condition pair:

Geometry	Boundary Condition	Significance
Ideal	Ideal	Taken as gold standard.
Ideal	MRI	Isolated errors derived from PC-MRI inlet boundary conditions from errors associated with the MRI derived geometry
MRI	Ideal	Isolated errors derived from the MRI geometry from errors associated with the PC-MRI derived inlet boundary conditions
MRI	MRI	Represented data expected to obtain clinically.

Table 2.2: Summary of computational models.

CFD Code Validation

In order to validate the CFD code FIDAP, the symmetric stenosis model used by Deshpande (1977) was created in three-dimensions in the pre-processor code GAMBIT. The initial diameter of the model was 5.08cm (2.0 inches). The stenosis reduced the lumen by 75% at the point of maximum stenosis and followed the shape of the cosine function. The stenosis occurred over a length of 1.5 diameters unlike the experimental models where the stenosis occurred over a length of 1.0 diameters. The computational

grid was set to have the same relative dimensions as those determined from the grid sensitivity/independence studies. The dynamic viscosity was set to 0.12972 Poise. The steady flow entrance boundary condition was a parabolic profile having a mean velocity of 4.72 cm/sec and a maximum velocity of 9.45 cm/sec corresponding to a Reynolds number of 200. A no-slip boundary condition was applied to the walls of the model, and the exit boundary condition was set to zero traction. The CFD code was executed until a convergent solution was reached using the same convergence criteria described for the previous models. Since the subject of this work was to examine the WSS values, the WSS values were compared to those reported by Deshpande for the same geometry and boundary conditions.

CHAPTER III

RESULTS

Flow Visualization

The results of the flow visualization experiments are shown in Figures 3.1 through 3.4. The 52.7% stenosis model under average flow rate (Re = 244) conditions showed streaklines representative of recirculation regions (Figures 3.1a and 3.1b). Areas of recirculation were also observed for the 52.7% stenosis model under peak flow rate (Re = 714) conditions (Figures 3.2a and 3.2b). Clear streaklines could be visualized where particles exiting the stenosis were seen colliding with the wall of the model further downstream.

Clear recirculation patterns were observed for the 75.0% stenosis model under average flow rate (Re = 244) conditions (Figure 3.3a and 3.3b). The recirculation regions appeared to extend 2 or 3 diameter lengths downfield of the stenosis. No signs of transitional or turbulent flow patterns were observed. However, these patterns were observed for the 75.0% stenosis model at the peak flow rate (Re = 714) (Figure 3.4a and 3.4b). These patterns could be observed in both the expanding post-stenotic jet as well as the recirculation region (Figure 3.4b). The reattachment point was difficult to determine due to the turbulent flow patterns; however, the reattachment point appeared to be approximately two diameter lengths downstream of the stenosis. Therefore, it was observed that the recirculation area was shorter for the peak flow conditions compared to the average flow conditions for the 75.0% stenosis model.

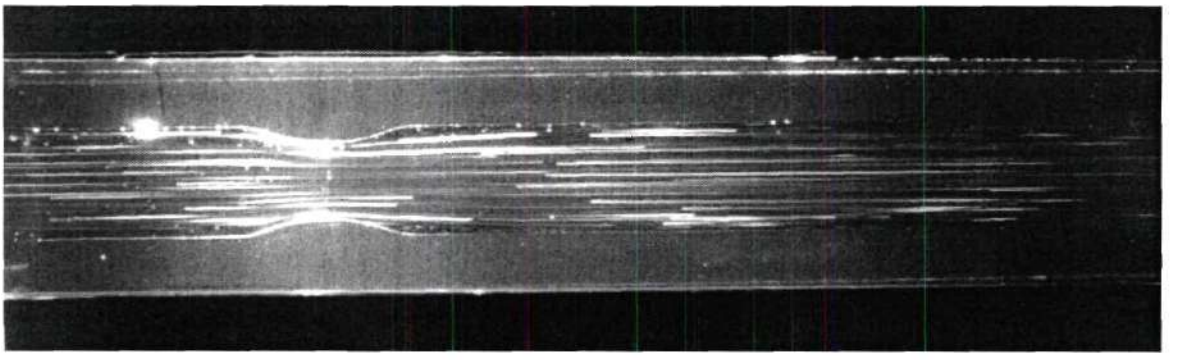

Figure 3.1a: Flow Visualization of the 52.7% stenosis model under average flow rate conditions (Re = 244).

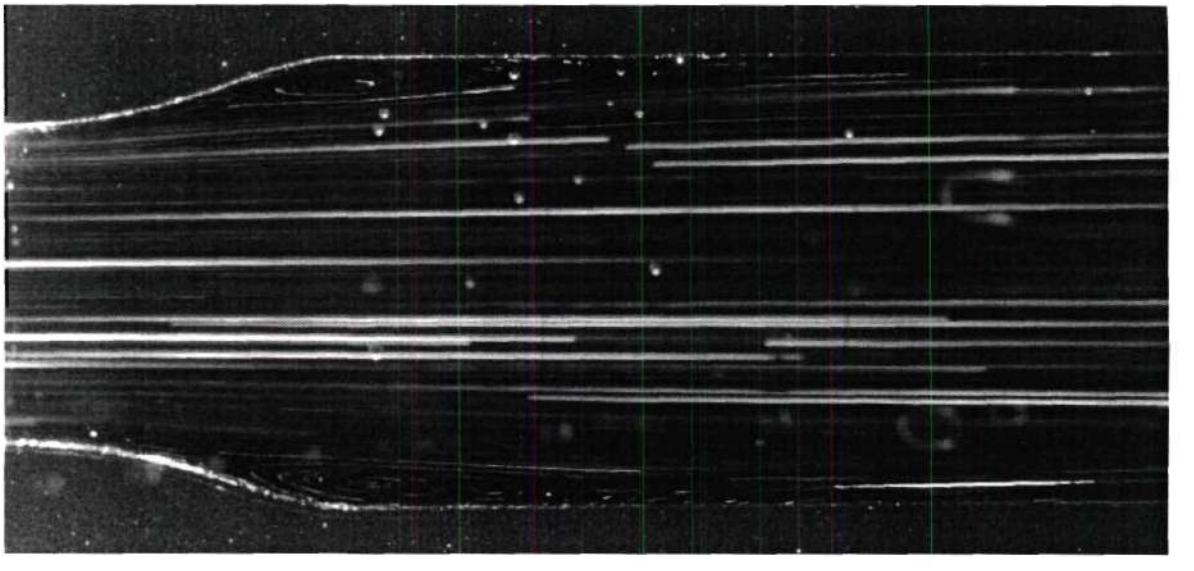

Figure 3.1b: Flow Visualization of the post-stenosis 52.7% stenosis model under average flow rate conditions (Re = 244).

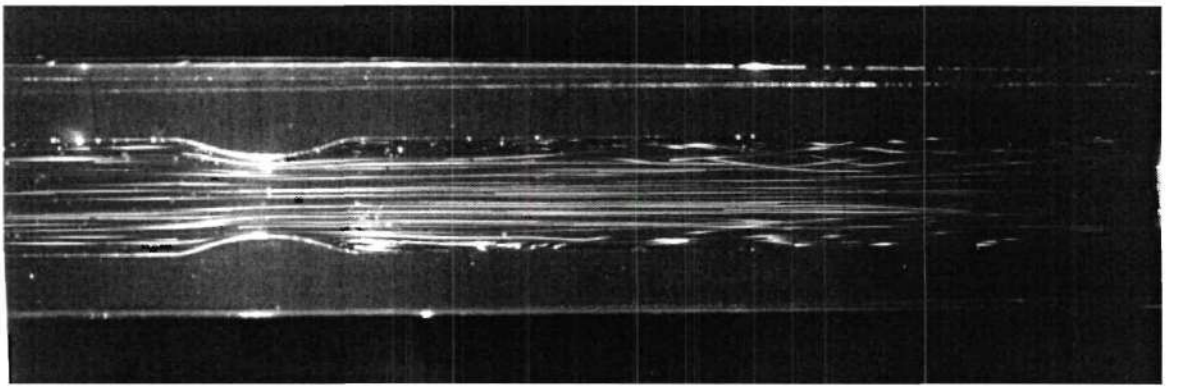

Figure 3.2a: Flow Visualization of the 52.7% stenosis model under peak flow rate conditions (Re = 714).

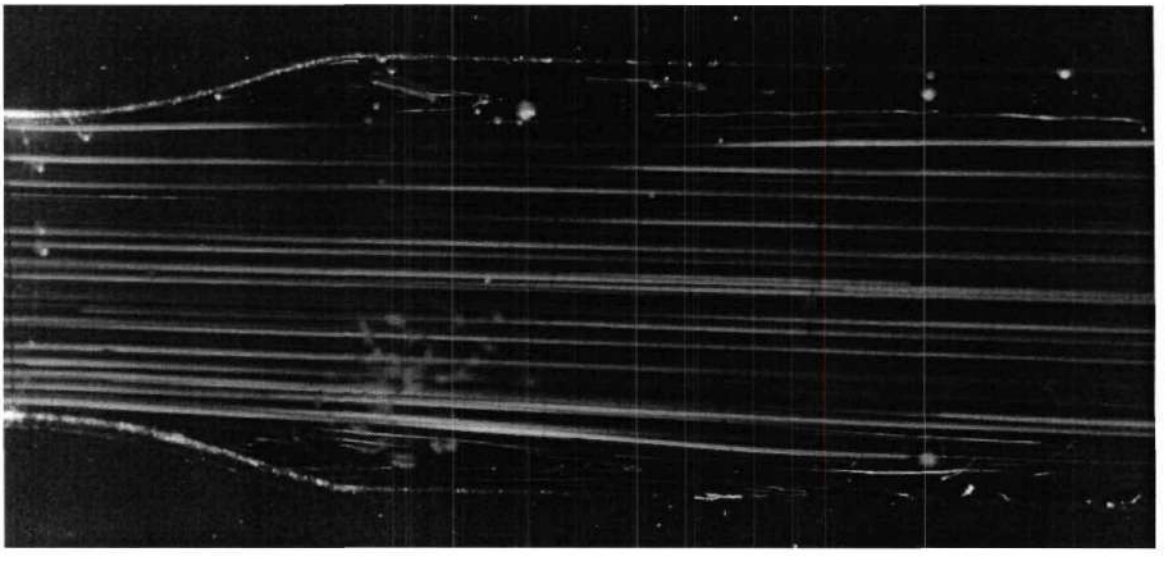

Figure 3.2b: Flow Visualization of the post-stenosis 52.7% stenosis model under peak flow rate conditions (Re = 714).

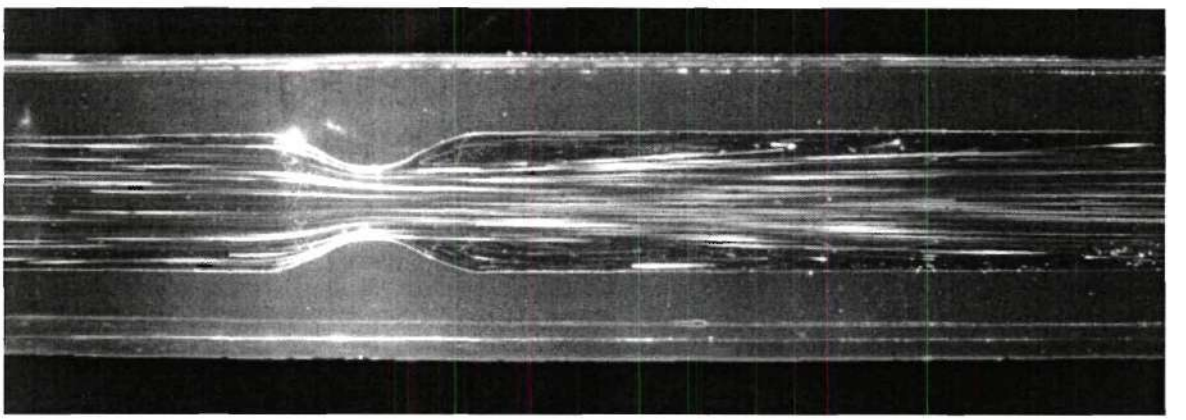

Figure 3.3a: Flow Visualization of the 75.0% stenosis model under average flow rate conditions (Re = 244).

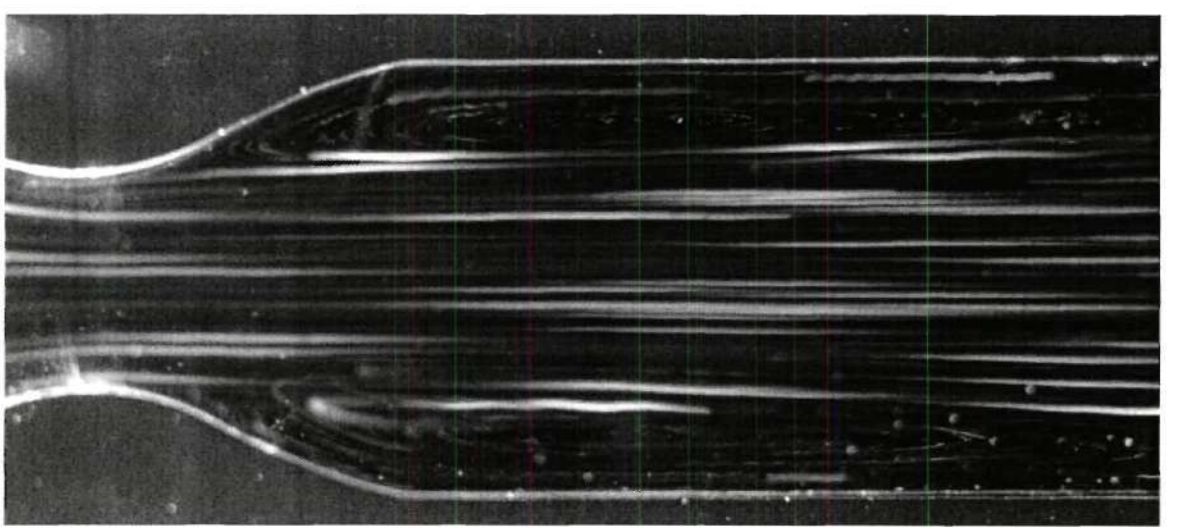

Figure 3.3b: Flow Visualization of the post-stenosis 75.0% stenosis model under average flow rate conditions (Re = 244).

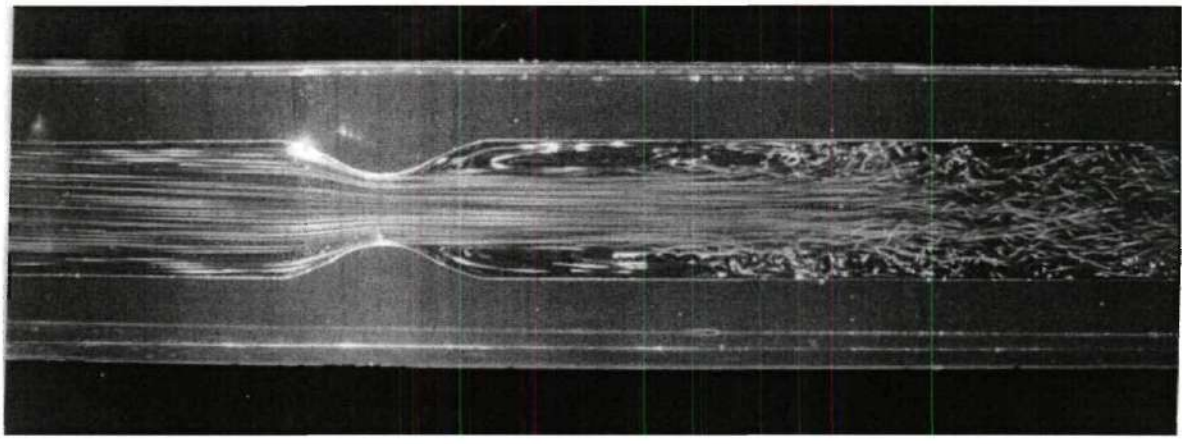

Figure 3.4a: Flow Visualization of the 75.0% stenosis model under peak flow rate conditions (Re = 714).

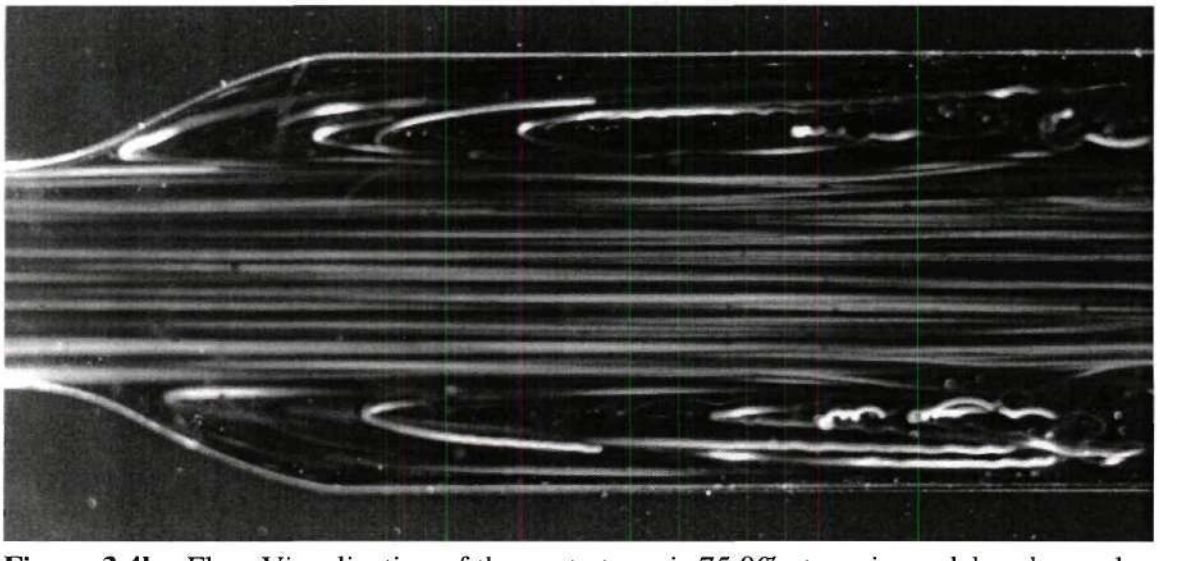

Figure 3.4b: Flow Visualization of the post-stenosis 75.0% stenosis model under peak flow rate conditions (Re = 714).

Magnetic Resonance Images

0.0% Stenosis Geometry / Average and Peak Flow Rates

Representative MRI images are shown in Figures 3.5 and 3.6 for the average and peak flow rates, respectively. The inversion-recovery scanning parameters were set to obtain the greatest differentiation between the PVA and the glycerin/water solution. However, there was still some ambiguity with regards to the actual vessel wall location. Positive and negative velocity values were obtained from the PVA using the phase contrast scanning sequence. The areas outside of the PVA model (which represented the acrylic tubing the PVA was contained within) displayed no signal for inversion/recovery or the phase contrast images.

Representative two dimensional velocity profiles derived from the phase contrast images are displayed in Figures 3.7 (average flow rate, Re = 244) and 3.9 (peak flow rate, Re = 714). The theoretical solution for steady flow through a straight tube yielded a theoretical maximum velocity of 28.4cm/sec for the average flow rate and 83.2 cm/sec for the peak flow rate. The maximum velocities recorded in Figures 3.7a and 3.7b are approximately 30cm/sec. The maximum velocities recorded in Figures 3.9a and 3.9b are approximately 70cm/sec and 80cm/sec, respectively. The shape of the velocity profiles was parabolic which was expected from the theoretical solution. The internal diameter of the lumen of the 0.0% stenosis PVA phantom was 0.635cm, and the external diameter was 1.27cm yielding a PVA wall thickness of 0.318cm. The first and last 0.318cm of the velocity profiles therefore represented the PVA phantom wall, which should register a zero velocity. However, widely varying velocity values were observed which represented noise from the PC-MRI image. The noise was larger for the peak flow rate

case, which was thought to explain the difference in the peak flow rates recorded (70cm/sec versus 80 cm/sec).

Representative three dimensional velocity profiles are shown in Figure 3.8 (average flow rate, Re = 244) and Figure 3.10 (peak flow rate, Re = 714). All of these figures show a parabolic profile surrounded by noise related to the PVA phantom. The noise observed in Figure 3.10a was predominately negative. Larger errors were also observed at the PVA-acrylic tube interface in all of the 3D velocity profiles.

52.7% Stenosis Geometry / Average Flow Rate

Representative MRI images for the 52.7% stenosis geometry under average flow rate conditions (Re = 244) are shown in Figure 3.11. The same ambiguity in wall location and noise from the PVA material as seen in the 0.0% stenosis model was observed. The diameter of the lumen of the geometry images at the point of maximum stenosis (Figure 3.11b) was smaller compared to images proximal and distal to the stenosis (Figure 3.11a, c, and d). Two dimensional velocity profiles are shown in Figures 3.12 and 3.13. The maximum velocity observed proximal to the stenosis was approximately 27.0cm/sec, which was slightly less than the 28.4cm/sec theoretical entrance maximum velocity. The maximum velocity increased at the point of maximum stenosis and remained elevated just distal of the stenosis. This was representative of the laminar jet observed in flow visualization. Negative velocities were observed near the PVA/fluid interface. However, the noise observed in the PVA material prevented the definitive observation of flow reversal distal to the stenosis. Furthermore, negative velocities were also observed far downfield of the stenosis, which was also attributed to

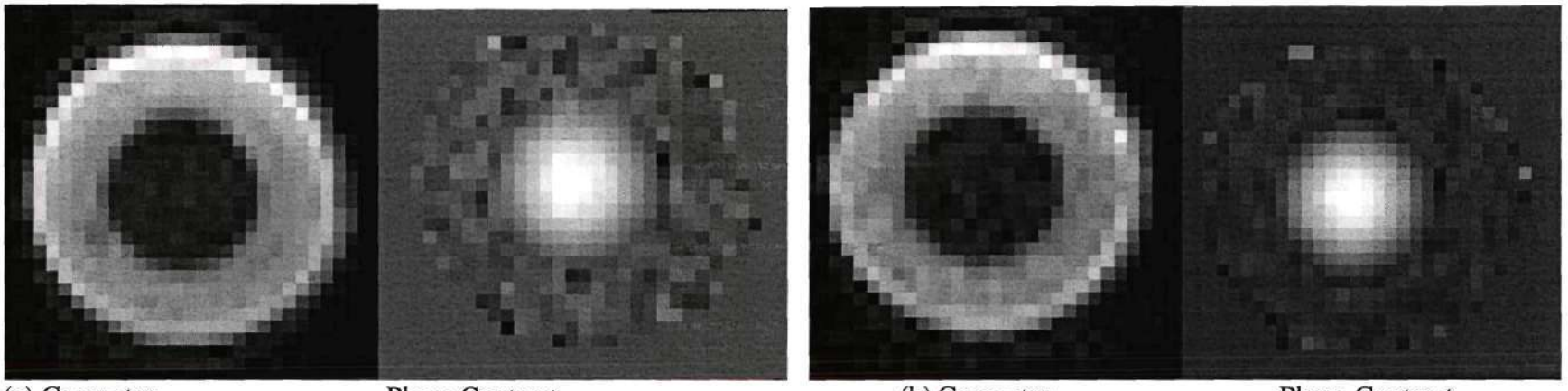

(a) Geometry Phase Contrast (b) Geometry Phase Contrast

Figure 3.5: Geometry and phase contrast MRI images at (a)upfield and (b)downfield locations in the 0.0% stenosis model at the average flow rate (Re = 244).

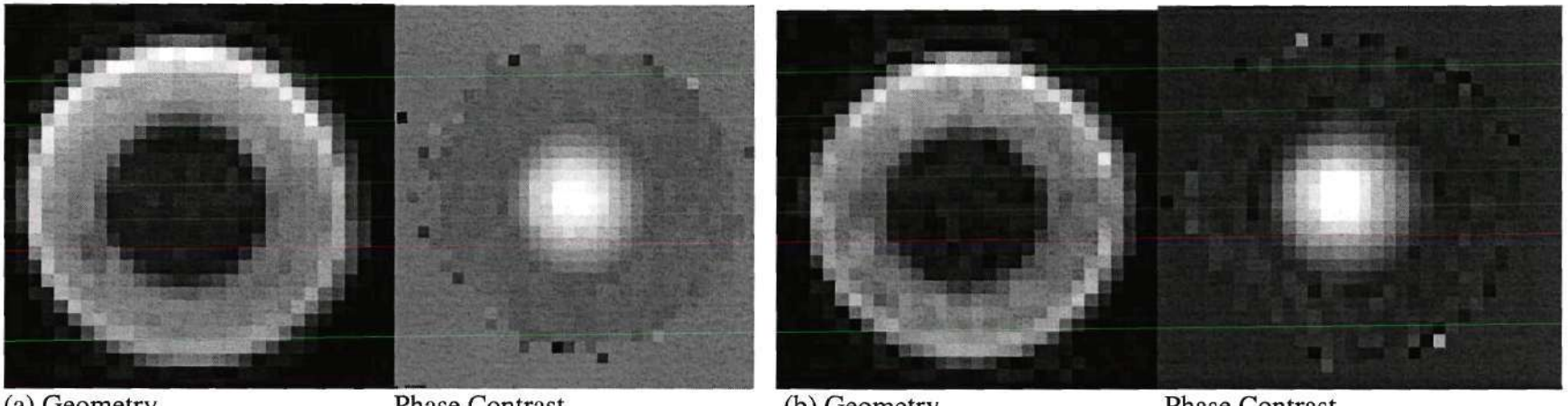

(a) Geometry Phase Contrast (b) Geometry Phase Contrast

Figure 3.6: Geometry and phase contrast MRI images at (a)upfield and (b)downfield locations in the 0.0% stenosis model at the peak flow rate (Re = 714).

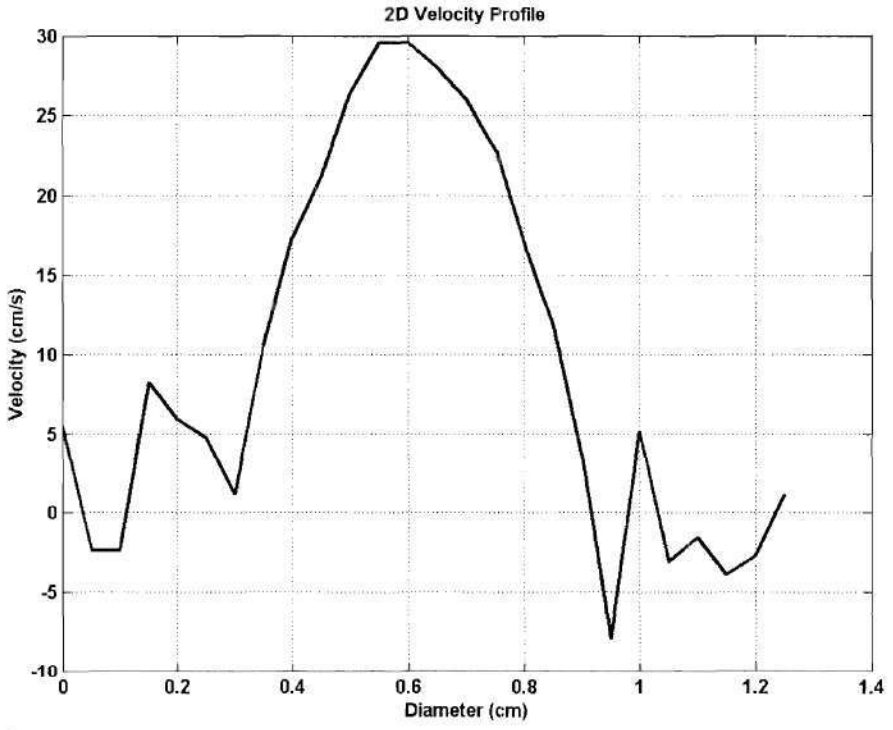

(a) upstream location

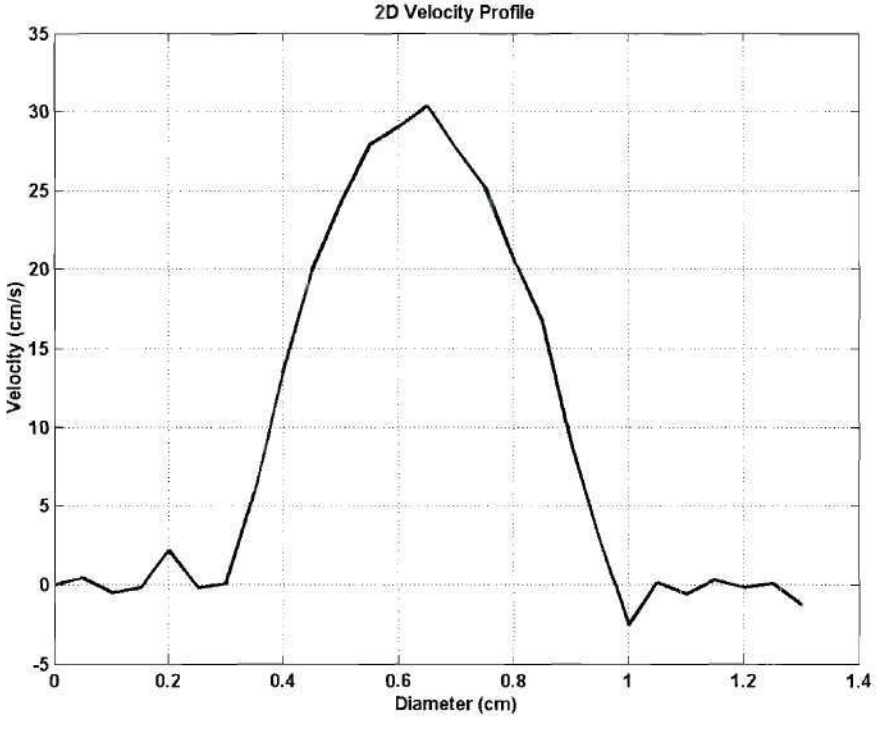

(b) downstream location

Figure 3.7: 2D velocity profiles for the 0.0% stenosis model at the average flow rate (Re = 244) at (a) upstream and (b) downstream locations.

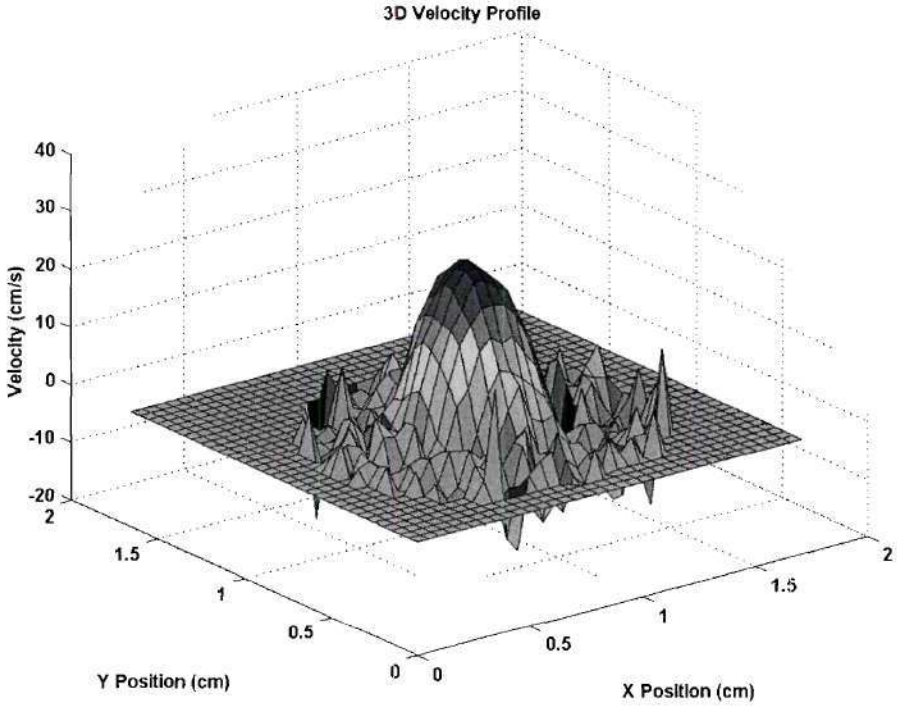

(a) upstream location

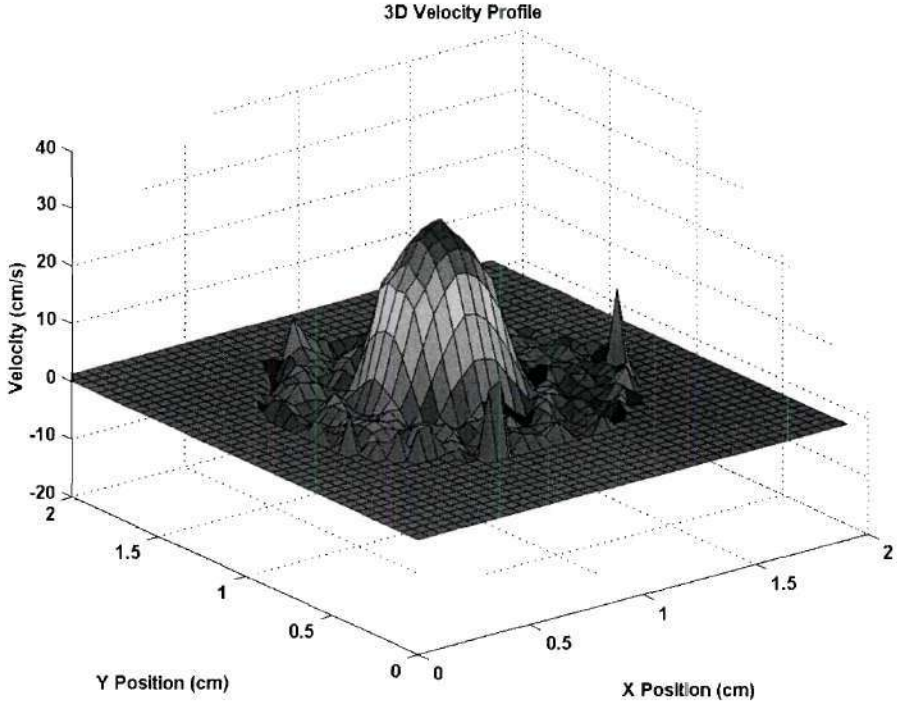

(b) downstream location

Figure 3.8: 3D velocity profiles for the 0.0% stenosis model at the average flow rate (Re = 244) at (a) upstream and (b) downstream locations.

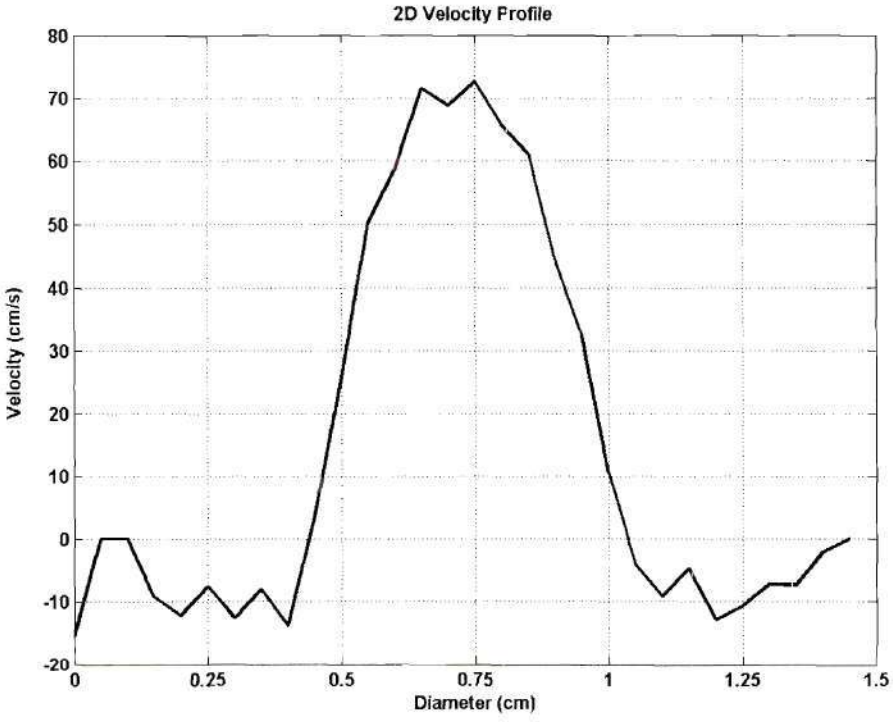

(a) upstream location

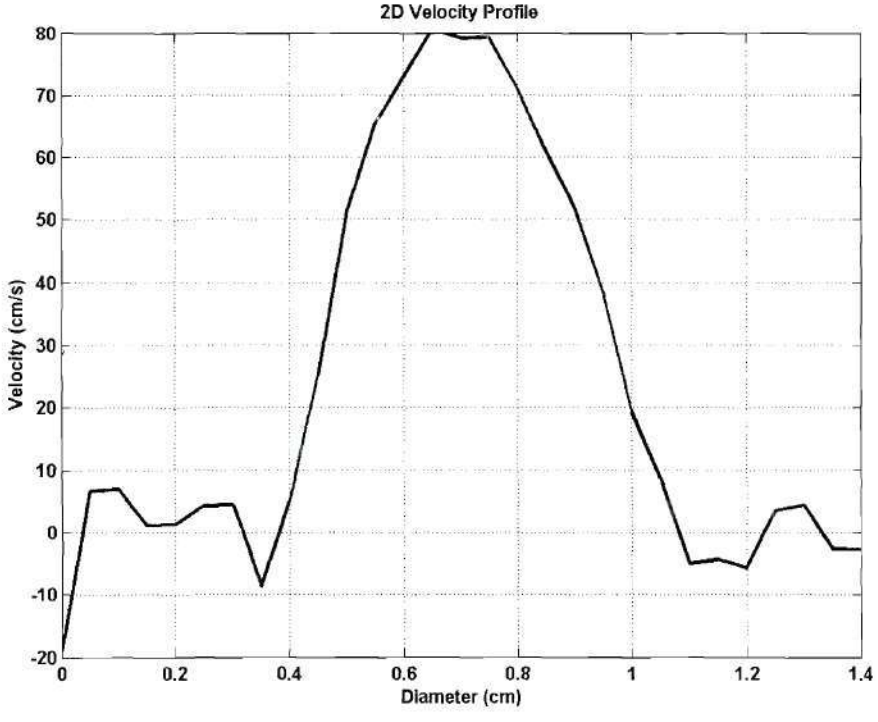

(b) downstream location

Figure 3.9: 2D velocity profiles for the 0.0% stenosis model at the peak flow rate (Re = 714) at (a) upstream and (b) downstream locations.

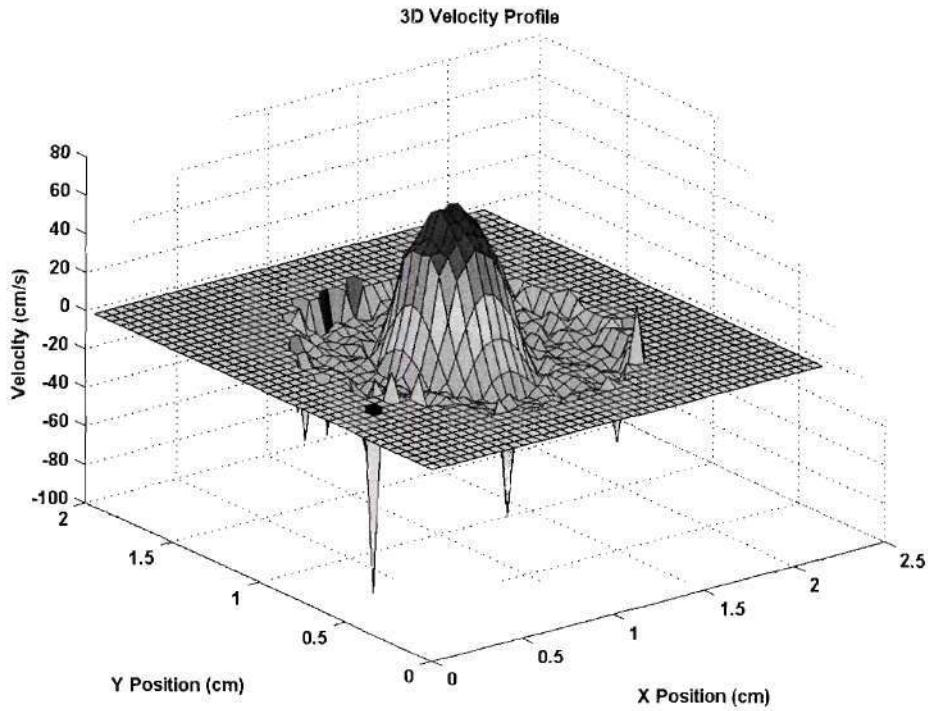

(a) upstream location

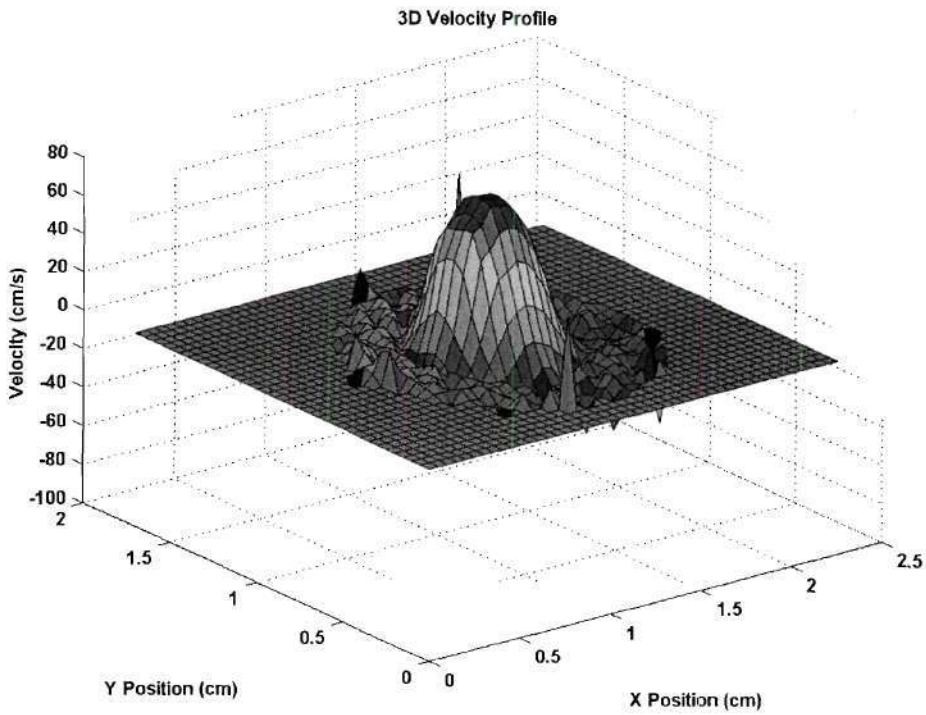

(b) downstream location

Figure 3.10: 3D velocity profiles for the 0.0% stenosis model at the peak flow rate (Re = 714) at (a) upstream and (b) downstream locations.

noise. The maximum velocity far downfield of the stenosis was observed to decrease from the values observed at, and just distal to the stenosis, which was suggestive of jet expansion and dissipation as well as reestablishment of the pre-stenosis entrance velocity profile.

The same observations were made with the three dimensional velocity profiles shown in Figures 3.14 and 3.15. Noise was observed at all locations surrounding the lumen (representative of the PVA model). Larger levels of noise were observed at the PVA-acrylic tube interfaces.

52.7% Stenosis Geometry / Peak Flow Rate

Representative MRI images for the 52.7% stenosis geometry under peak flow rate conditions (Re = 714) are shown in Figure 3.16. The same ambiguity in wall location and noise from the PVA material as seen in the 0.0% stenosis model were observed. The diameter of the lumen of the geometry images at the point of maximum stenosis (Figure 3.16b) was smaller compared to images proximal and distal to the stenosis (Figures 3.16a, c, and d). Signs of signal loss were observed in Figures 3.16b and 3.16c. Areas of minimum and maximum pixel values are illustrated as completely black and completely white pixels, respectively. This was thought to be caused by transitional flow patterns that developed as the fluid passed through the stenosis and formed the corresponding jet.

Two dimensional velocity profiles are shown in Figures 3.17 and 3.18. The maximum velocity observed proximal to the stenosis was approximately 77.0 cm/sec, which is less than the 83.2cm/sec theoretical entrance maximum velocity. The maximum

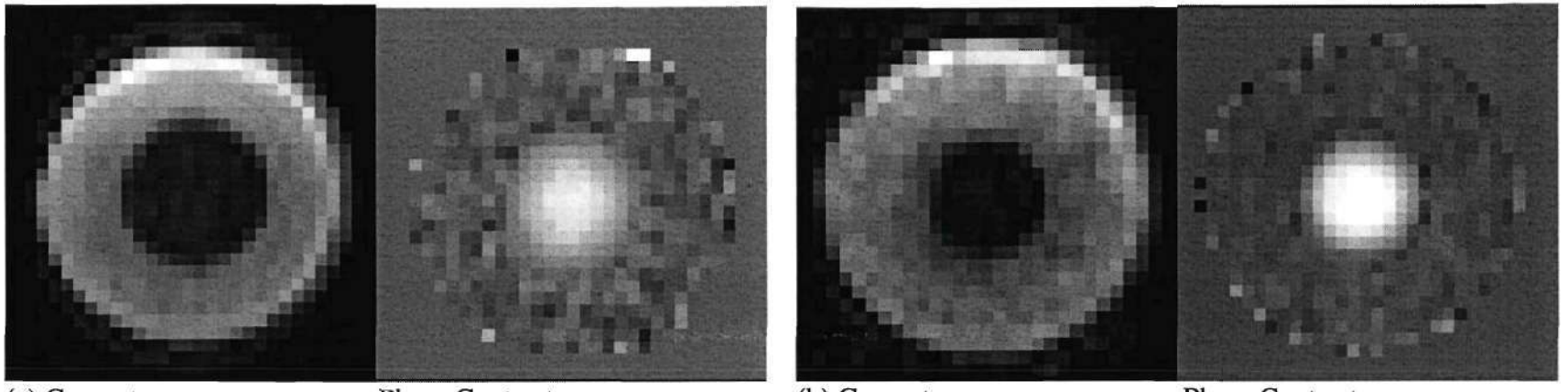

(a) Geometry Phase Contrast (b) Geometry Phase Contrast

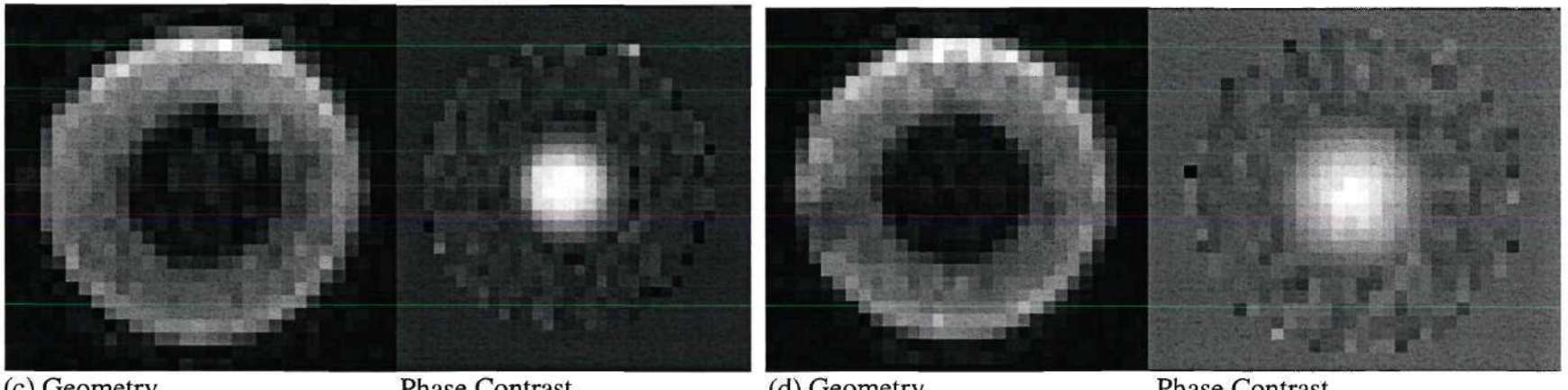

(c) Geometry Phase Contrast (d) Geometry Phase Contrast

Figure 3.11: Geometry and phase contrast MRI images (a) proximal to stenosis (b) at maximum stenosis (c) just distal of stenosis and (d) far down-field of stenosis for the 52.7% stenosis model at the average flow rate (Re = 244).

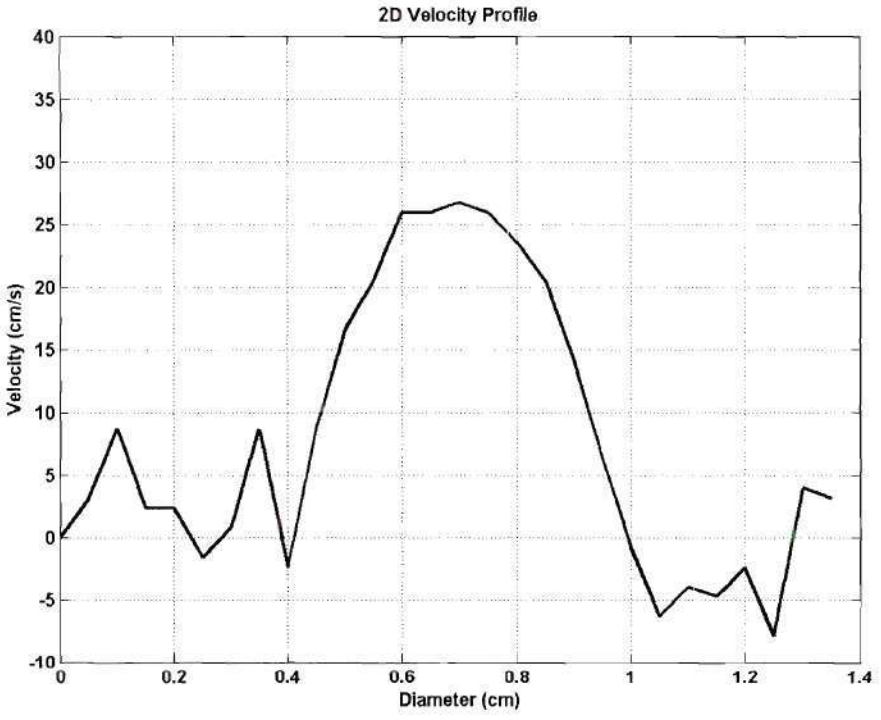

(a) proximal to stenosis

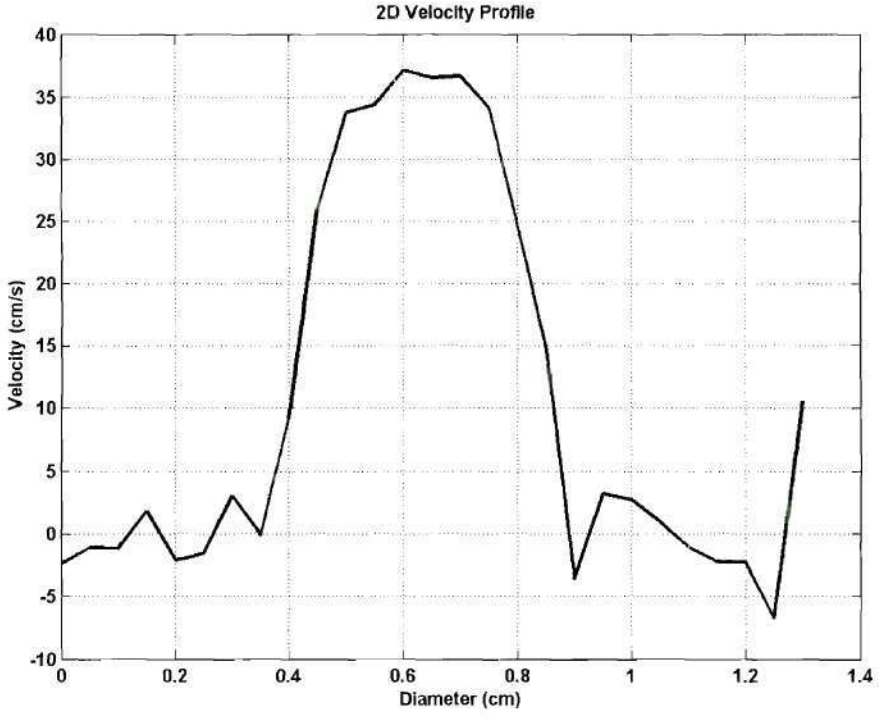

(b) at point of maximum stenosis

Figure 3.12: 2D velocity profiles for the 52.7% stenosis model at the average flow rate (Re = 244) (a) proximal to stenosis and (b) at point of maximum stenosis.

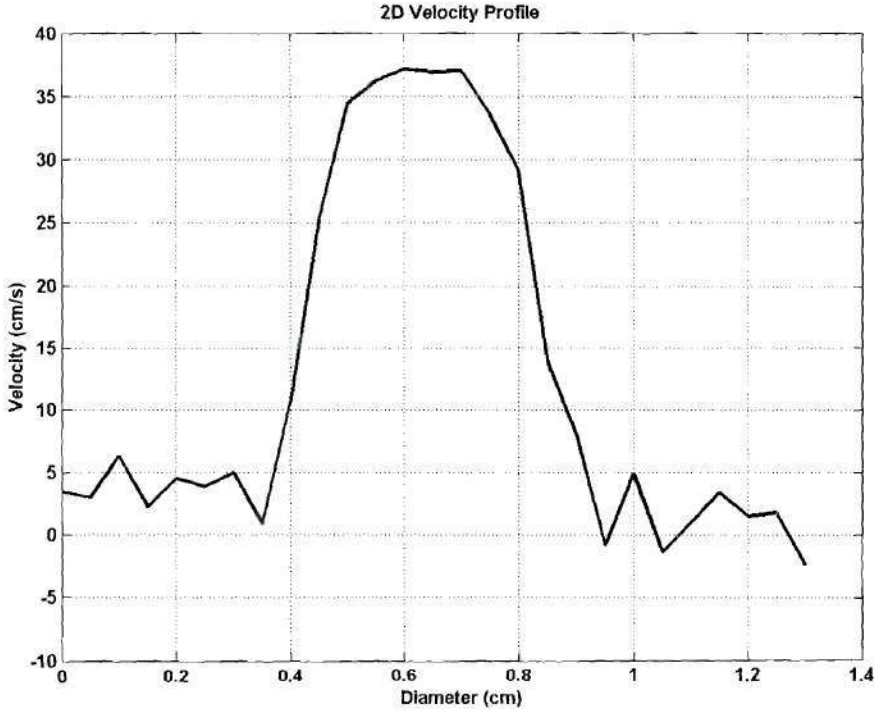

(a) just distal to stenosis

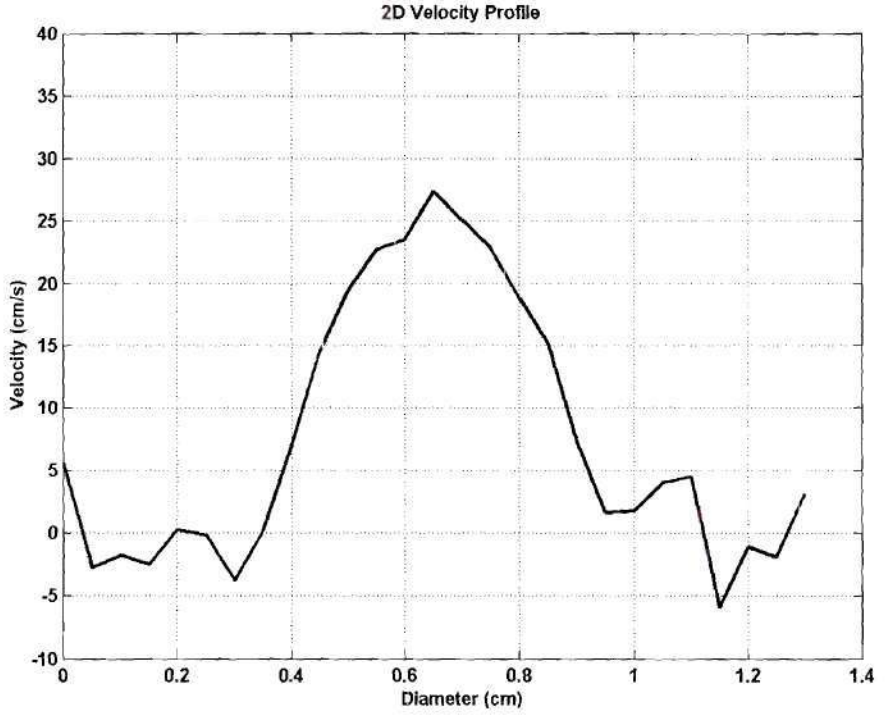

(b) far downstream of stenosis

Figure 3.13: 2D velocity profiles for the 52.7% stenosis model at the average flow rate (Re = 244) (a) just distal to stenosis and (b) far downstream of stenosis.

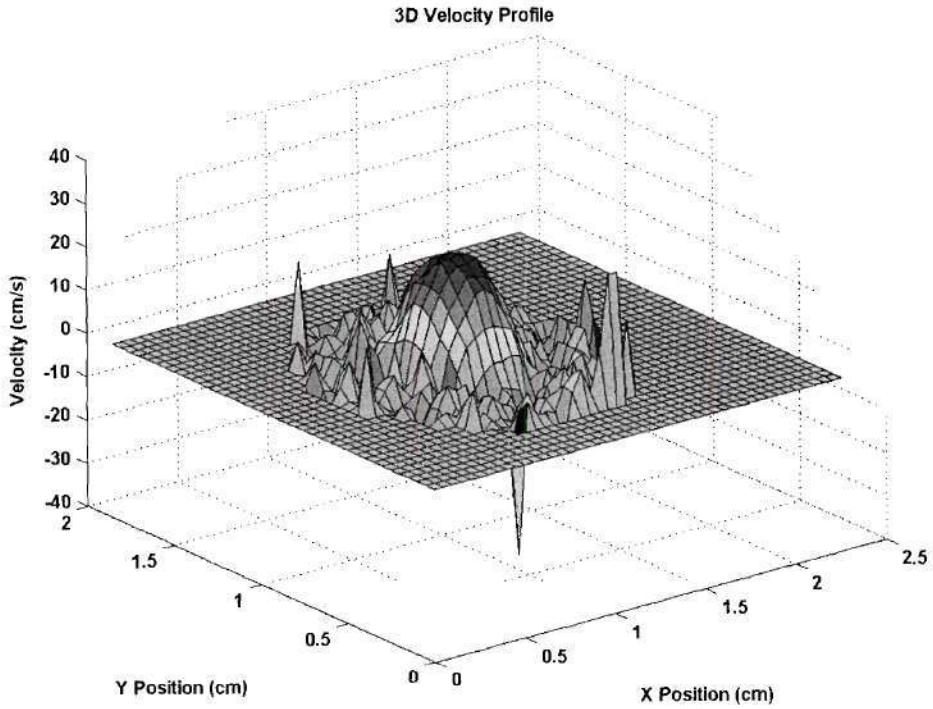

(a) proximal to stenosis

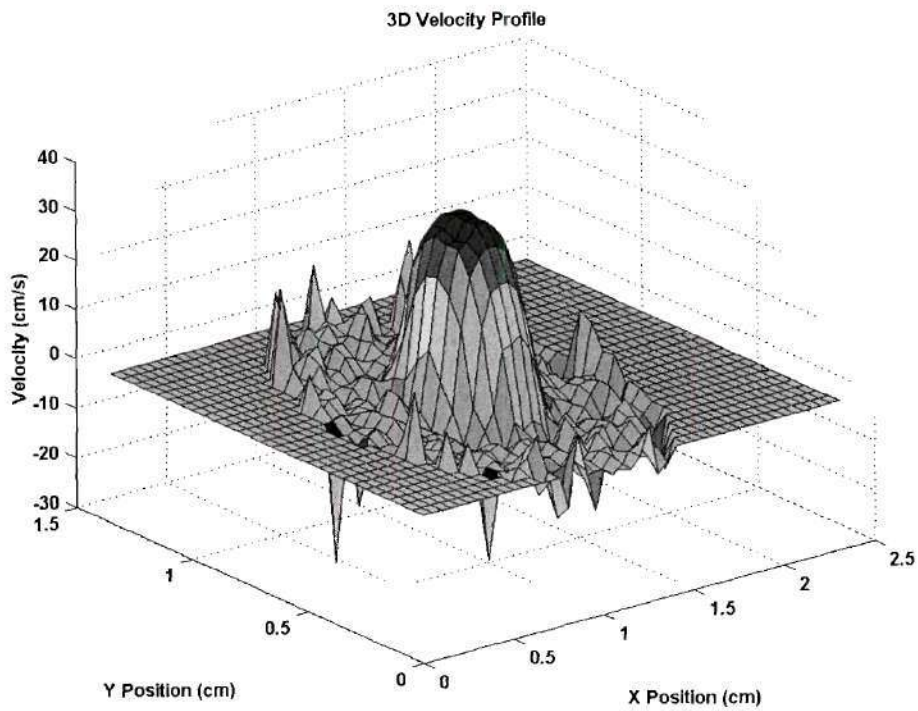

(b) at point of maximum stenosis

Figure 3.14: 3D velocity profiles for the 52.7% stenosis model at the average flow rate (Re = 244) (a) proximal to stenosis and (b) at point of maximum stenosis.

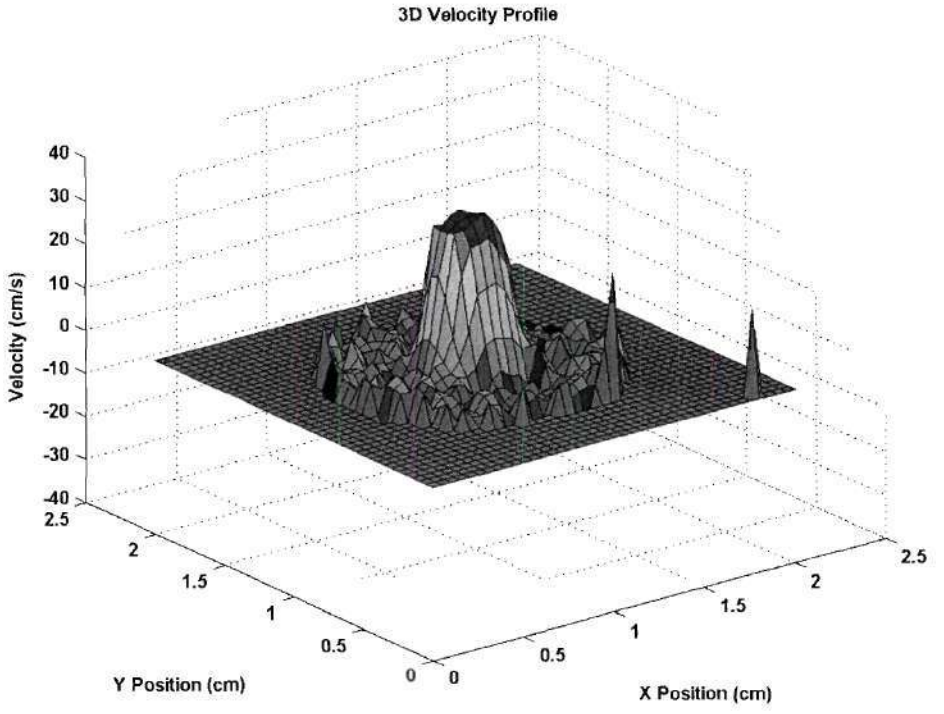

(a) just distal to stenosis

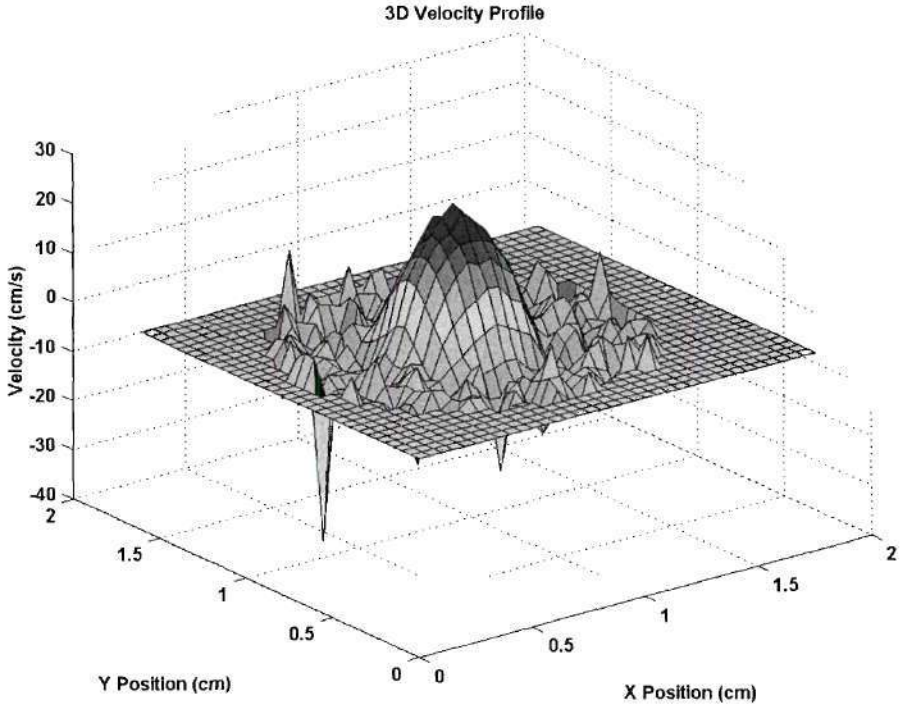

(b) far downstream of stenosis

Figure 3.15: 3D velocity profiles for the 52.7% stenosis model at the average flow rate (Re = 244) (a) just distal to stenosis and (b) far downstream of stenosis.

velocity increased at the point of maximum stenosis and remained elevated just distal of the stenosis. This was representative of the laminar jet observed in flow visualization.

Additional noise was observed at the middle of the lumen in Figures 3.17b and 3.18a. This was attributed to flow acceleration that can produce errors in the phase contrast data. Negative velocities were observed near the PVA/fluid interface. However, the noise observed in the PVA material prevented the definitive observation of flow reversal distal to the stenosis. Furthermore, negative velocities were also observed far downfield of the stenosis (Figure 3.20b), which could also represent flow recirculation, noise, or a combination of both flow reversal and noise.. The maximum velocity far downfield of the stenosis was observed to decrease from the values observed at, and just distal to the stenosis, which was suggestive of jet expansion and dissipation as well as reestablishment of the pre-stenosis entrance velocity profile.

The same observations were made with the three dimensional velocity profiles shown in Figures 3.19 and 3.20. Noise was observed at all locations surrounding the lumen (representative of the PVA model). Larger levels of noise were observed at the PVA-acrylic tube interfaces. The PVA material registered largely negative velocity values in the images proximal to the stenosis (Figure 3.19a).

75.0% Stenosis Geometry / Average Flow Rate

Representative MRI images for the 75.0% stenosis geometry under average flow rate conditions (Re = 244) are shown in Figure 3.21. The same ambiguity in wall location and noise from the PVA material as seen in the other stenosis models was observed. The diameter of the lumen of the geometry images at the point of maximum

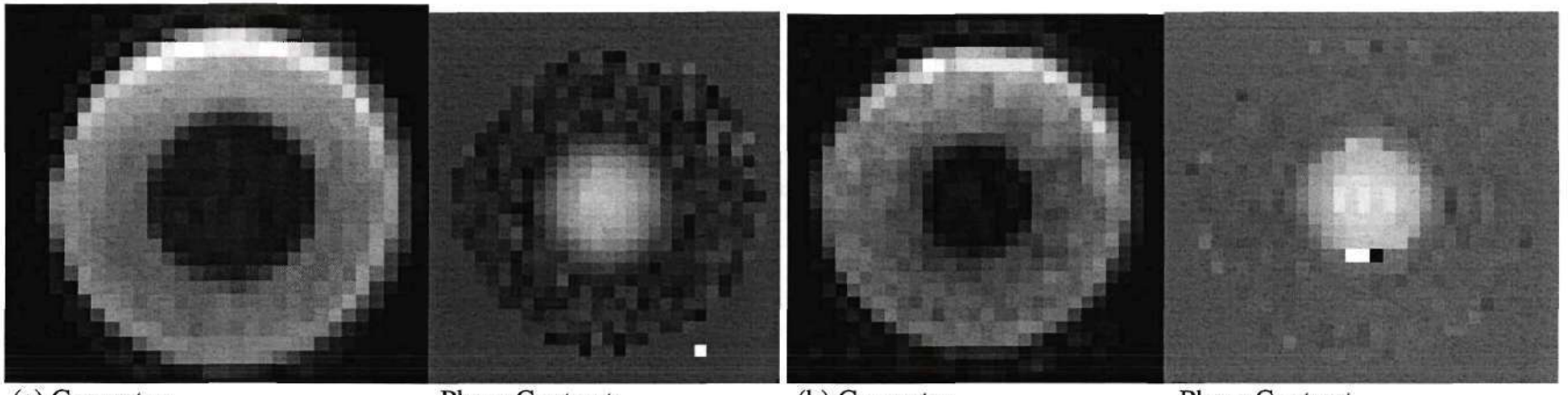

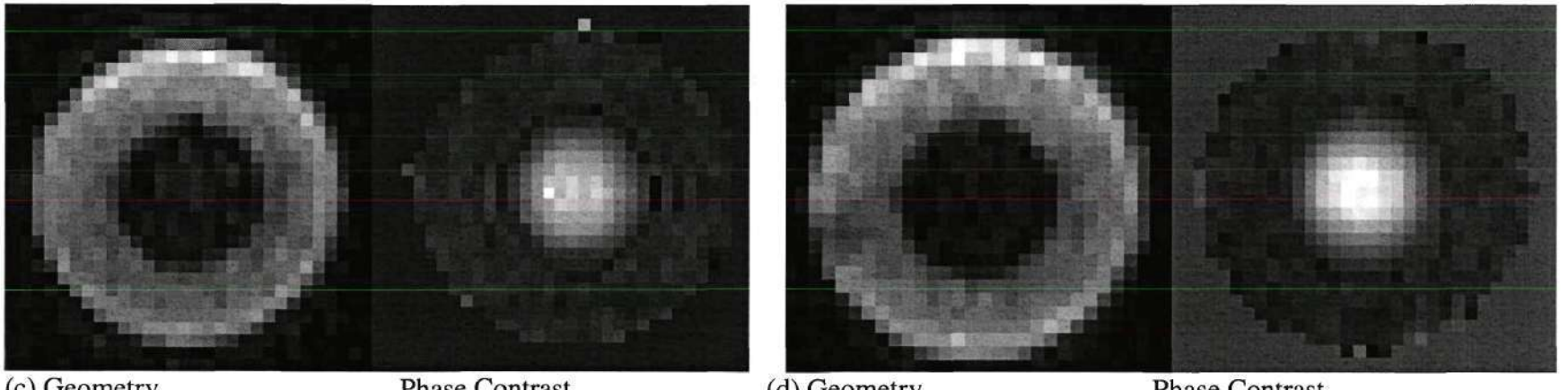

Figure 3.16: Geometry and phase contrast MRI images (a) proximal to stenosis (b) at maximum stenosis (c) just distal of stenosis and (d) far down-field of stenosis for the 52.7% stenosis model at the peak flow rate (Re = 714).

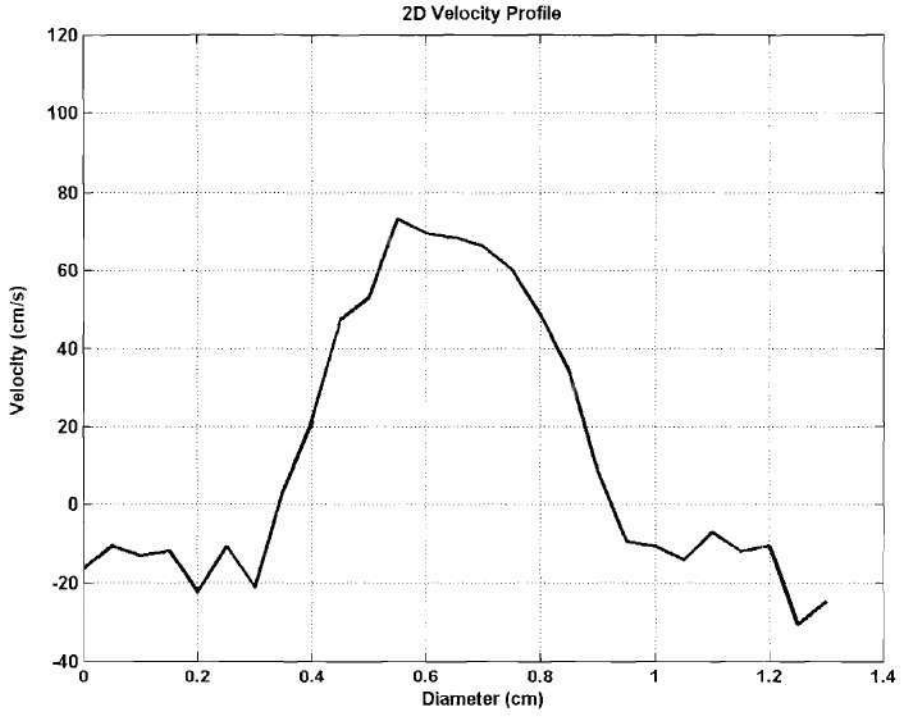

(a) proximal to stenosis

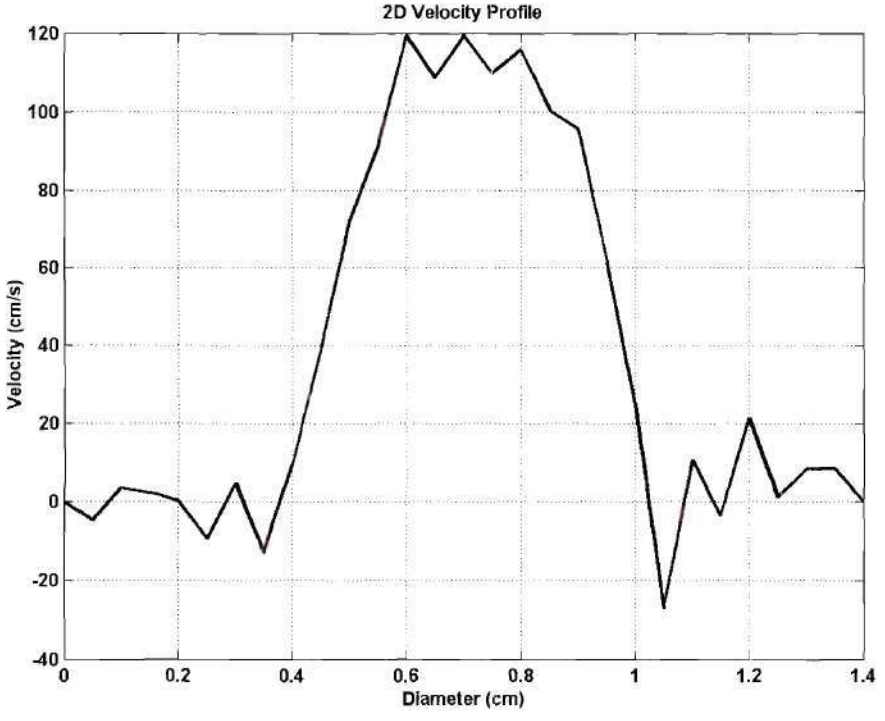

(b) at point of maximum stenosis

Figure 3.17: 2D velocity profiles for the 52.7% stenosis model at the peak flow rate (Re = 714) (a) proximal to stenosis and (b) at point of maximum stenosis.

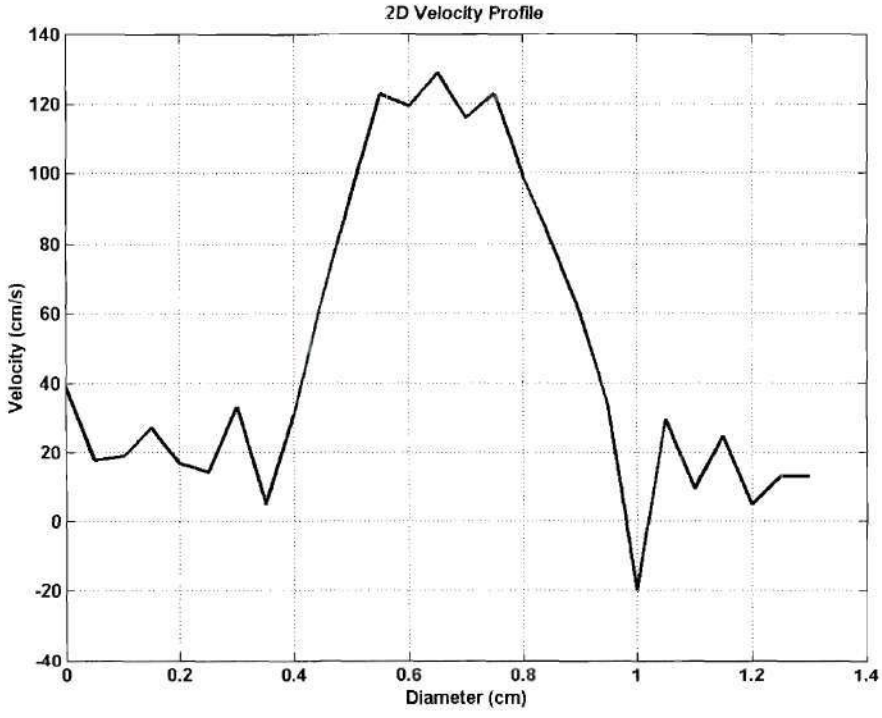

(a) just distal to stenosis

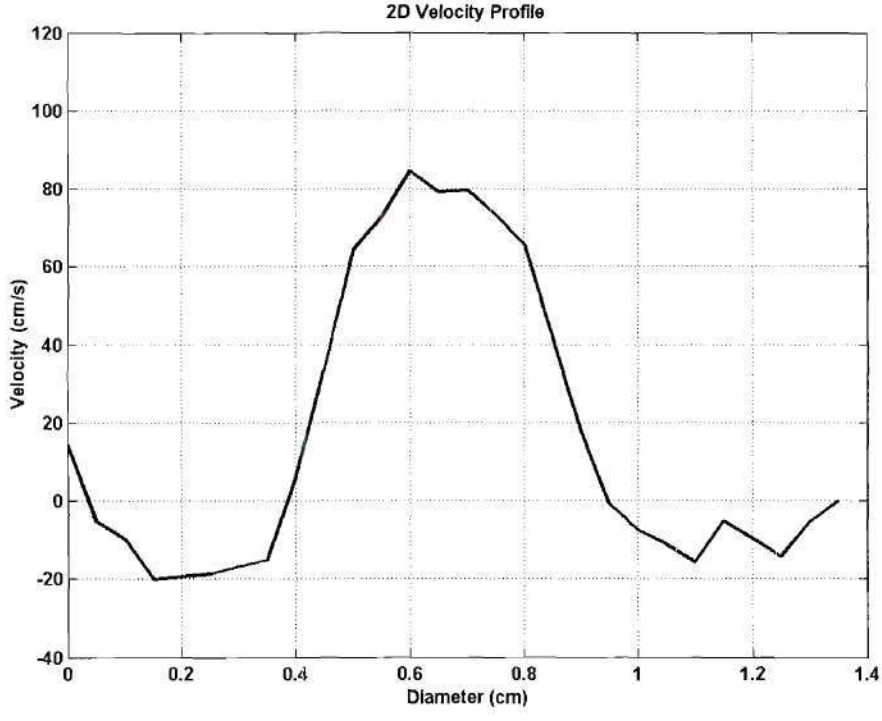

(b) far downstream of stenosis

Figure 3.18: 2D velocity profiles for the 52.7% stenosis model at the peak flow rate (Re = 714) (a) just distal to stenosis and (b) far downstream of stenosis.

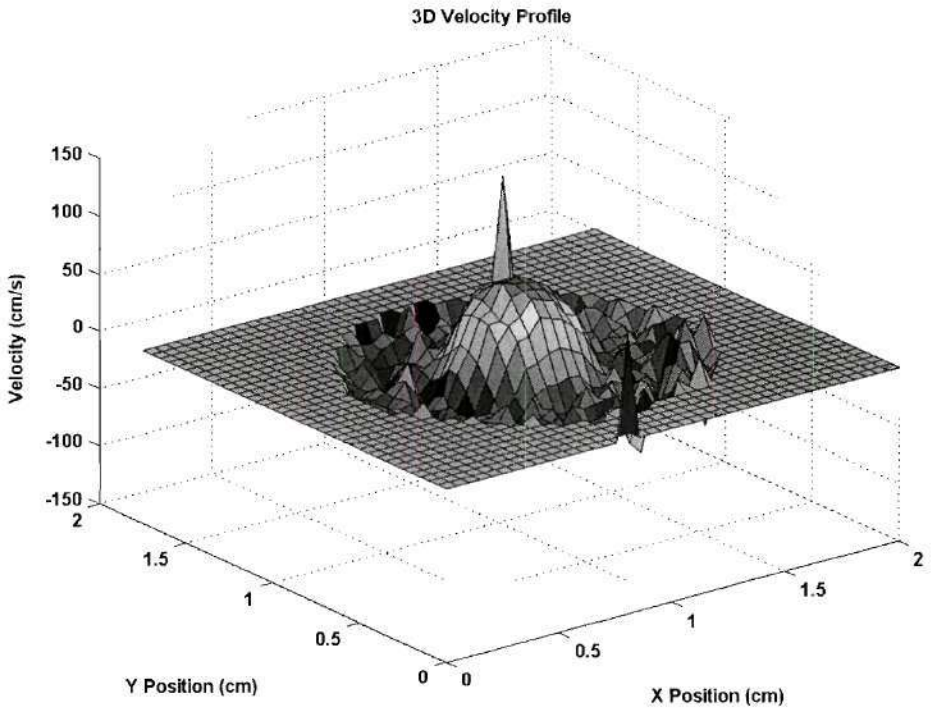

(a) proximal to stenosis

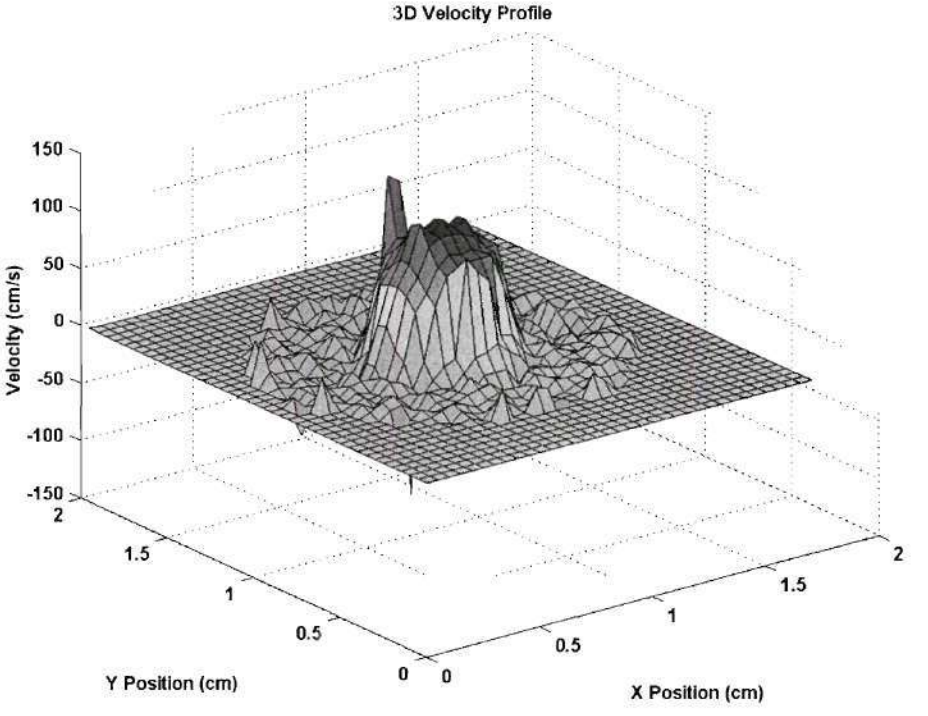

(b) at point of maximum stenosis

Figure 3.19: 3D velocity profiles for the 52.7% stenosis model at the peak flow rate (Re = 714) (a) proximal to stenosis and (b) at point of maximum stenosis.

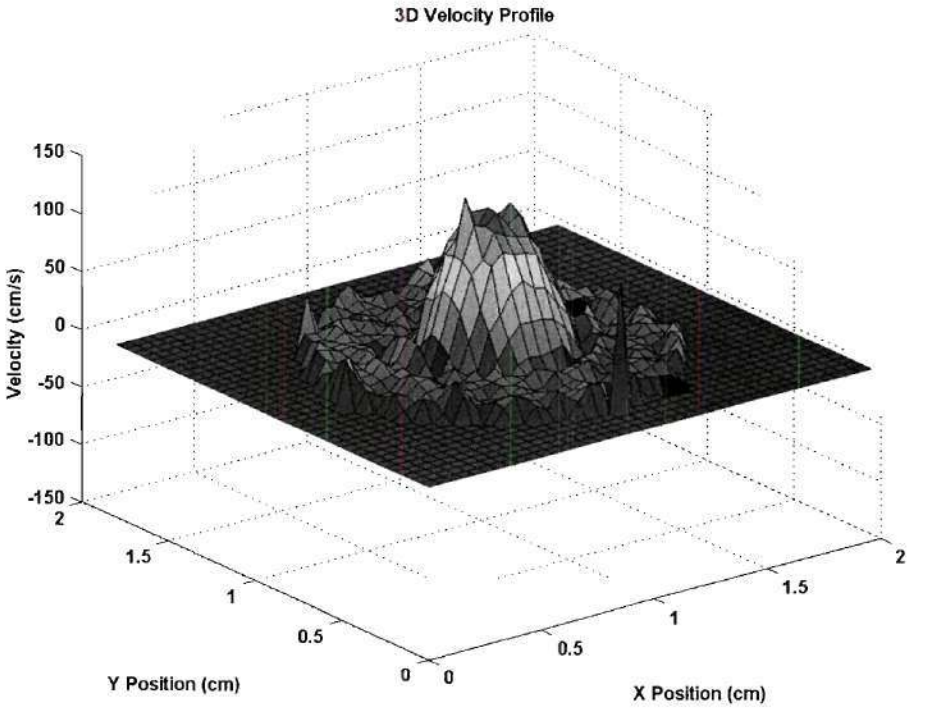

(a) just distal to stenosis

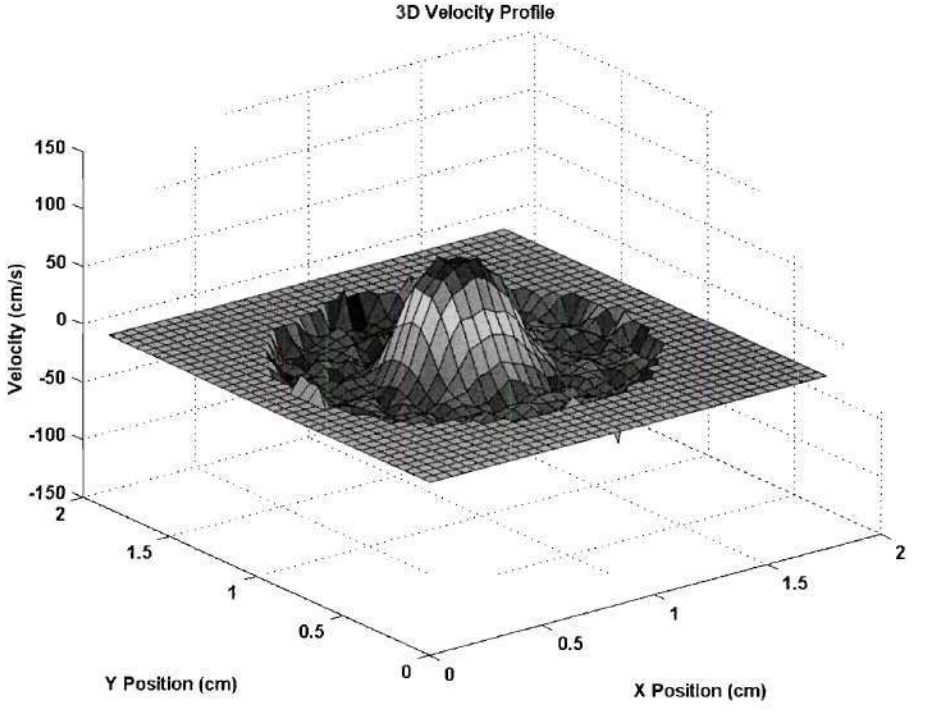

(b) far downstream of stenosis

Figure 3.20: 3D velocity profiles for the 52.7% stenosis model at the peak flow rate (Re = 714) (a) just distal to stenosis and (b) far downstream of stenosis.

stenosis (Figure 3.21b) was smaller compared to images proximal and distal to the stenosis (Figures 3.21a, c, and d).

Two dimensional velocity profiles are shown in Figures 3.22 and 3.23. The maximum velocity observed proximal to the stenosis was approximately 27.0 cm/sec, which is slightly less than the 28.4 cm/sec theoretical entrance maximum velocity. The maximum velocity increased at the point of maximum stenosis and remained elevated just distal of the stenosis. This is representative of the laminar jet observed in flow visualization. Additional noise was observed at the middle of the lumen in Figures 3.22b and 3.23a. This was attributed to flow acceleration that can produce errors in the phase contrast data. Negative velocities were observed near the PVA/fluid interface just distal and far downfield of the stenosis. However, the noise observed in the PVA material prevented the definitive observation of flow reversal distal to the stenosis. The maximum velocity far downfield of the stenosis was observed to decrease from the values observed at, and just distal to the stenosis, which was suggestive of jet expansion and dissipation as well as reestablishment of the pre-stenosis entrance velocity profile. The same observations were made with the three dimensional velocity profiles shown in Figures 3.24 and 3.25. Noise was observed at all locations surrounding the lumen (representative of the PVA model). Larger levels of noise were observed at the PVA-acrylic tube interfaces.

75.0% Stenosis Geometry / Peak Flow Rate

Representative MRI images for the 75.0% stenosis geometry under peak flow rate conditions (Re = 714) are shown in Figure 3.26. The same ambiguity in wall location

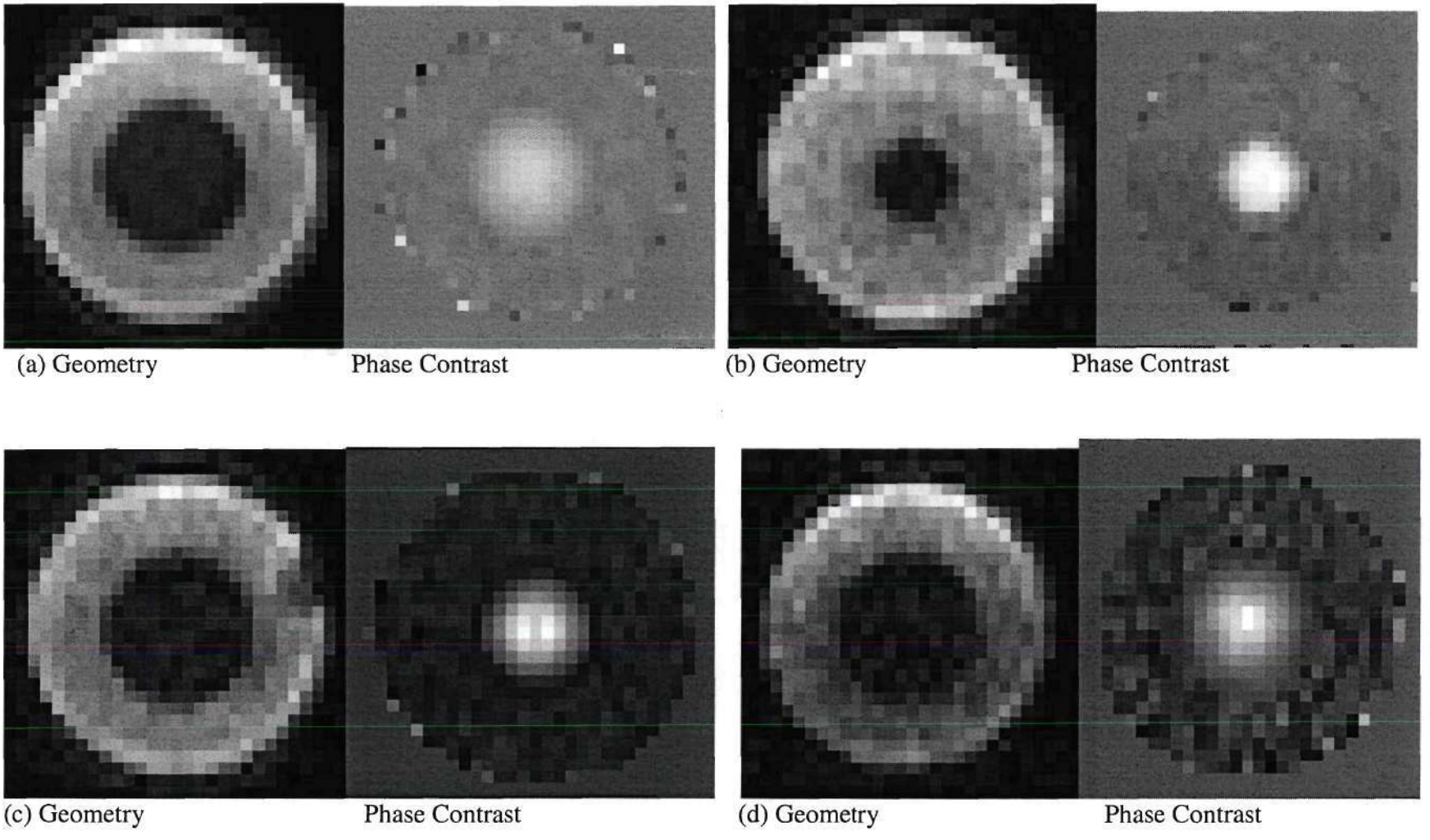

Figure 3.21: Geometry and phase contrast MRI images (a) proximal to stenosis (b) at maximum stenosis (c) just distal of stenosis and (d) far down-field of stenosis for the 75.0% stenosis model at the average flow rate (Re = 244).

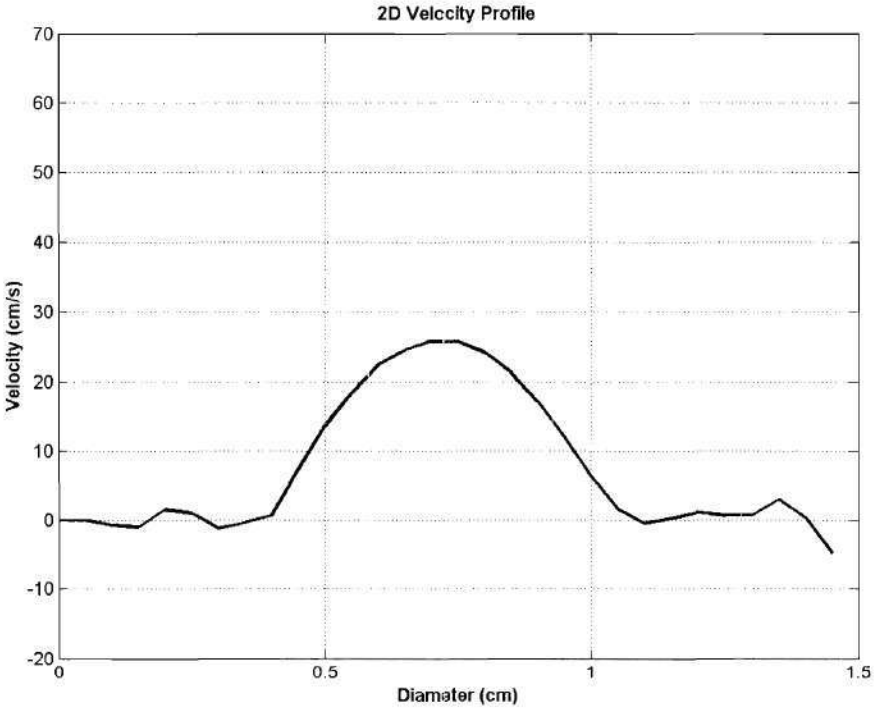

(a) proximal to stenosis

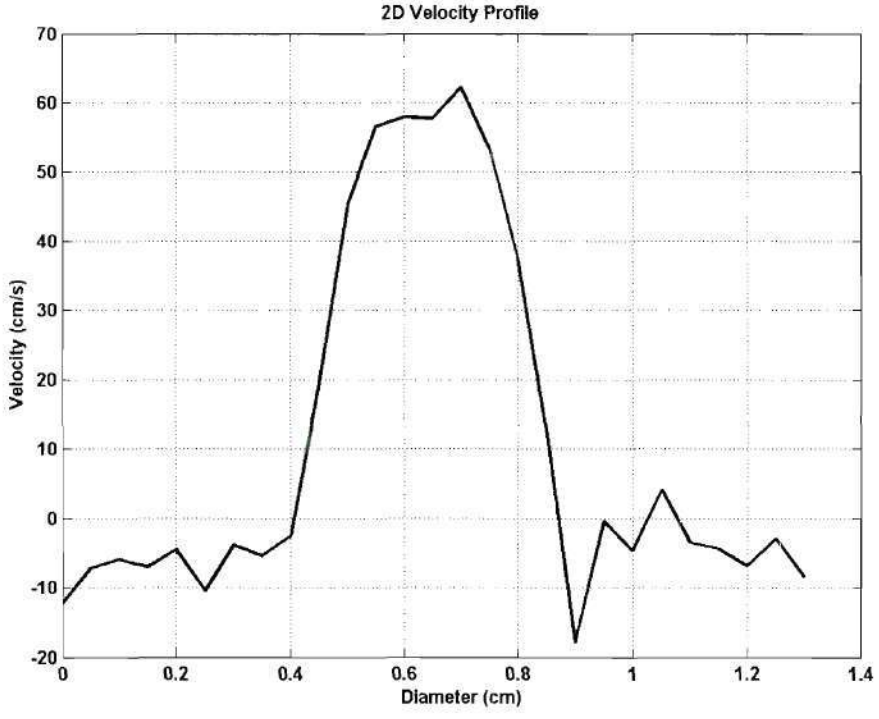

(b) at point of maximum stenosis

Figure 3.22: 2D velocity profiles for the 75.0% stenosis model at the average flow rate (Re = 244) (a) proximal to stenosis and (b) at point of maximum stenosis.

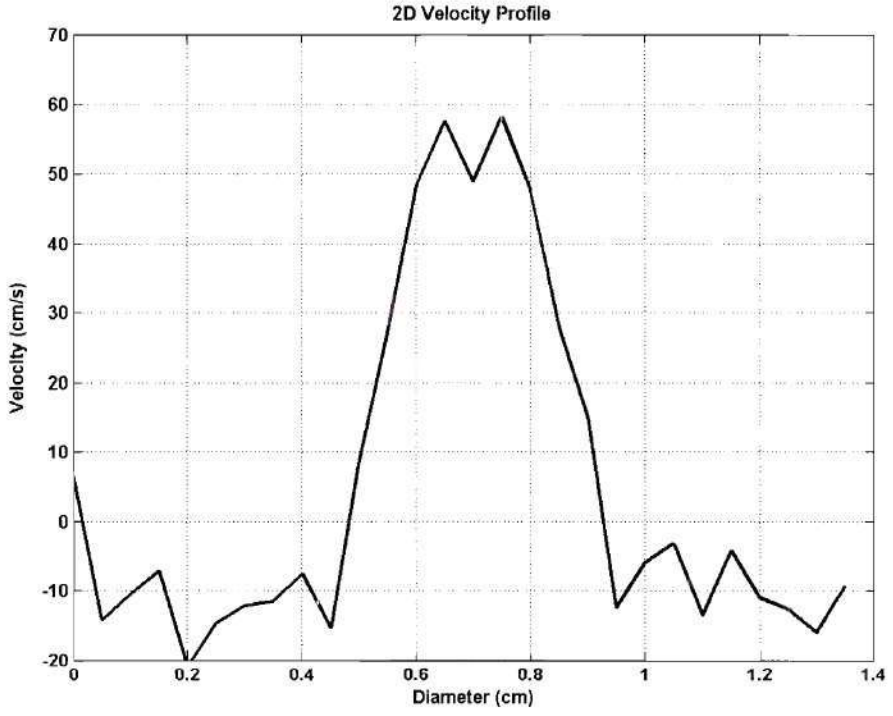

(a) just distal to stenosis

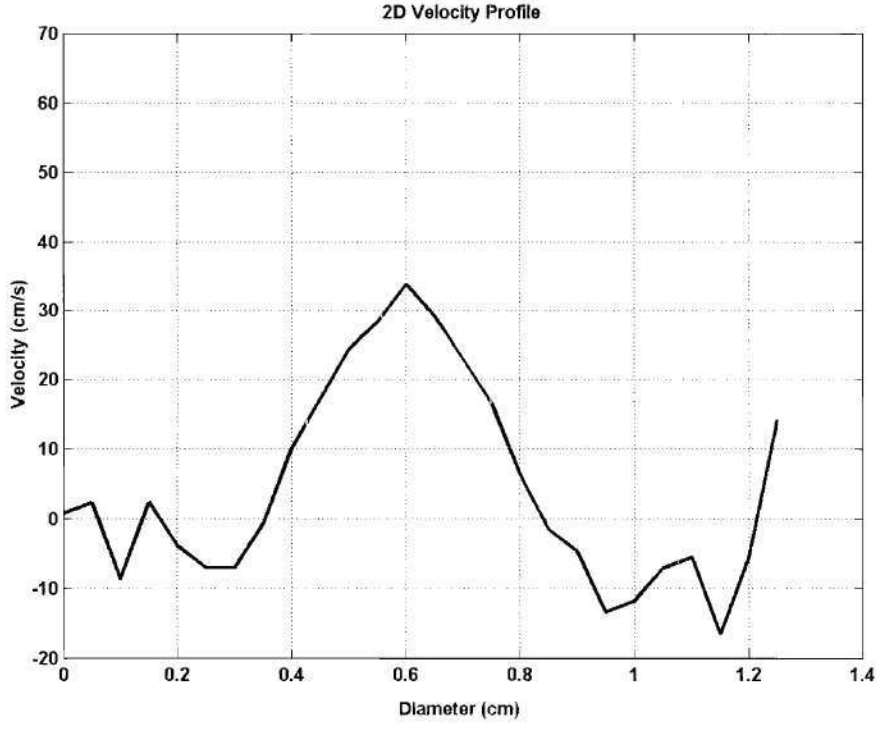

(b) far downstream of stenosis

Figure 3.23: 2D velocity profiles for the 75.0% stenosis model at the average flow rate (Re = 244) (a) just distal to stenosis and (b) far downstream of stenosis.

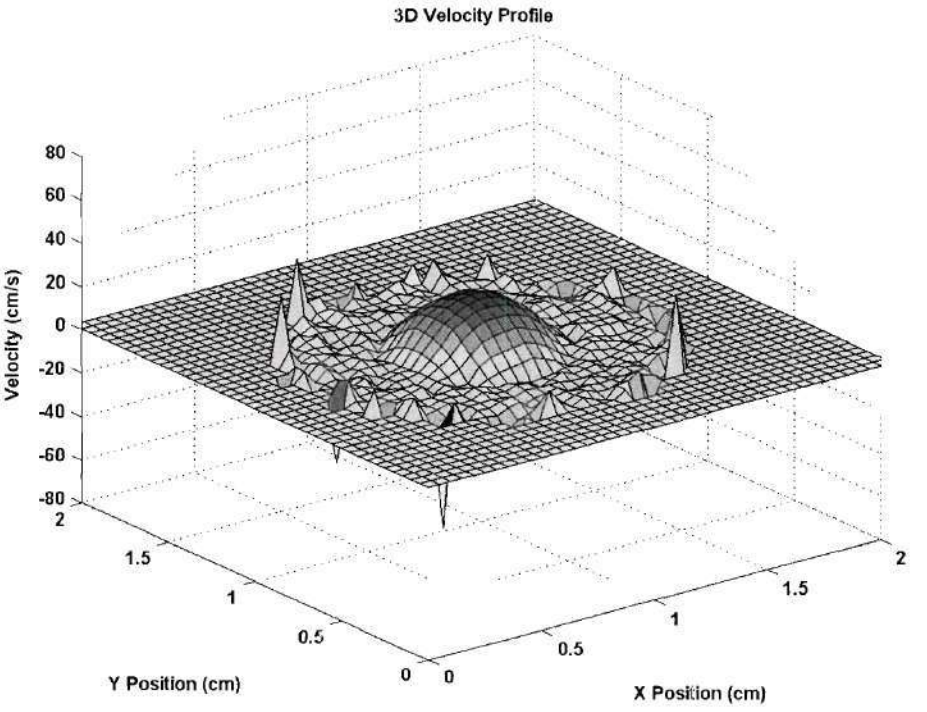

(a) proximal to stenosis

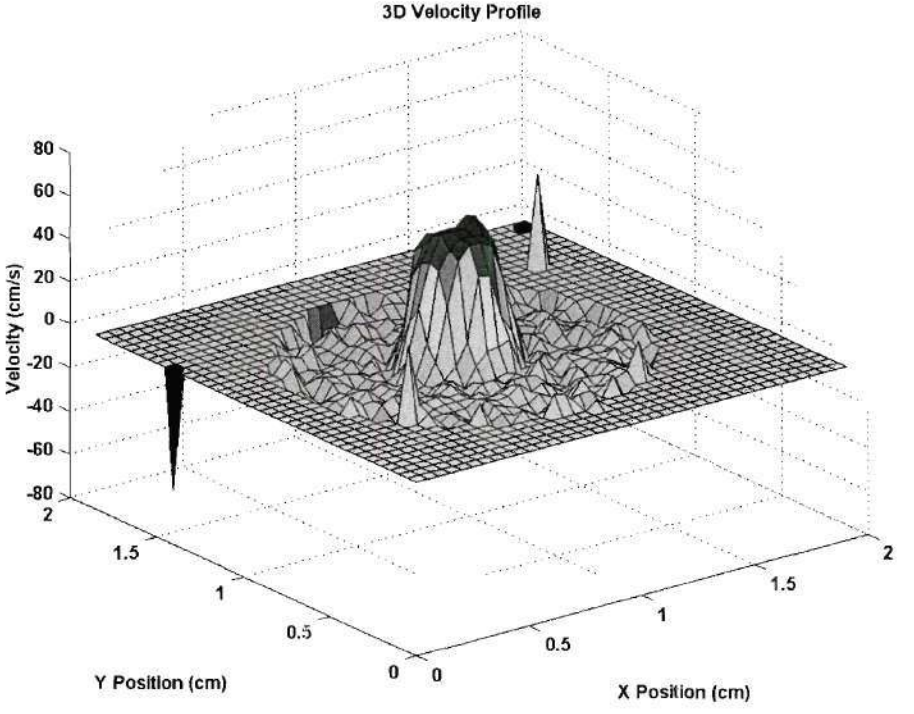

(b) at point of maximum stenosis

Figure 3.24: 3D velocity profiles for the 75.0% stenosis model at the average flow rate (Re = 244) (a) proximal to stenosis and (b) at point of maximum stenosis.

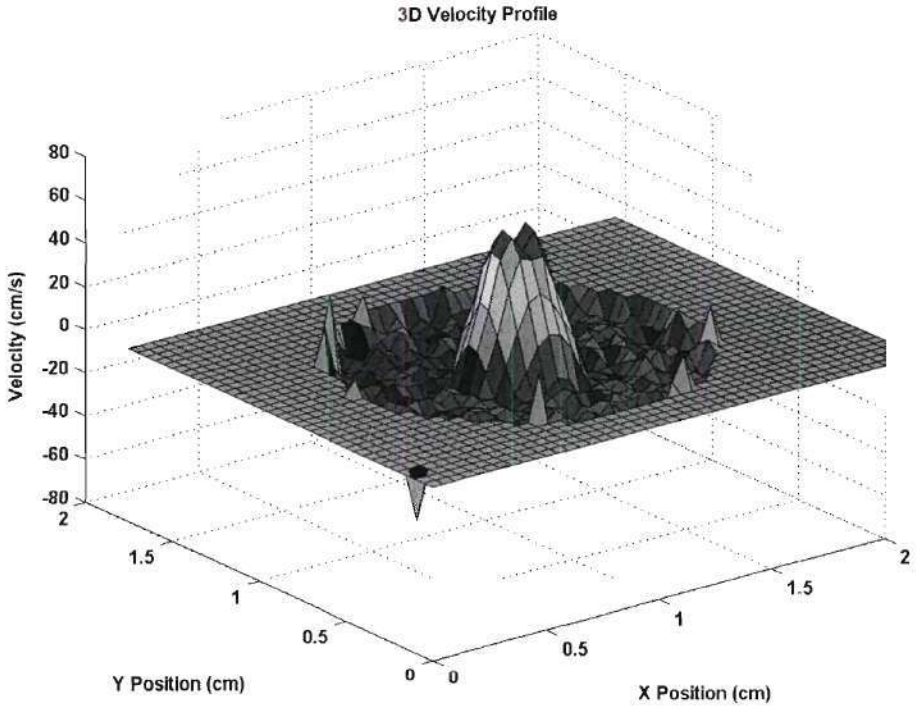

(a) just distal to stenosis

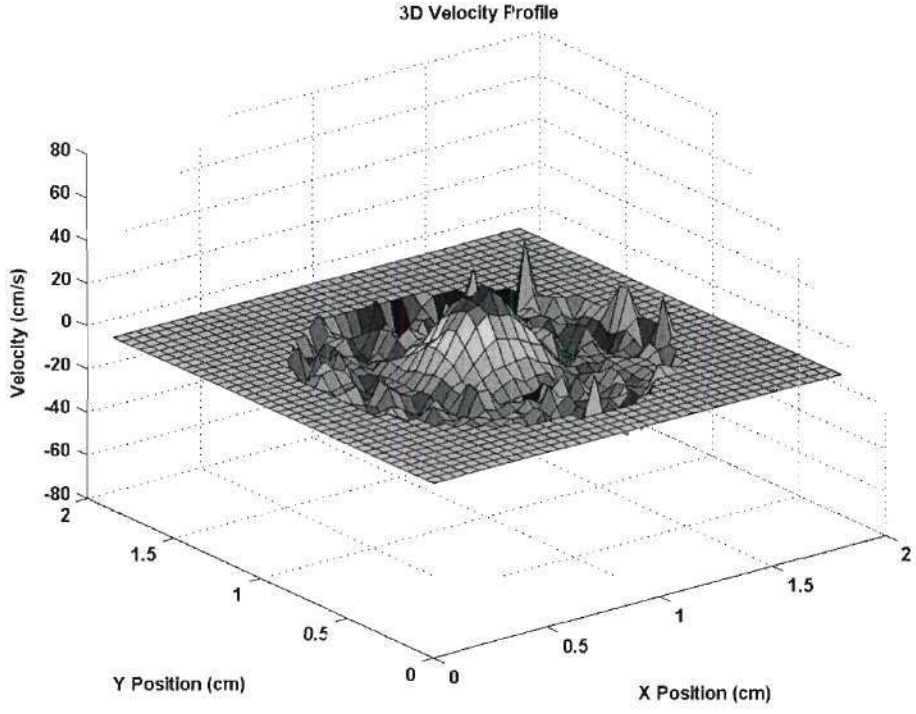

(b) far downstream of stenosis

Figure 3.25: 3D velocity profiles for the 75.0% stenosis model at the average flow rate (Re = 244) (a) just distal to stenosis and (b) far downstream of stenosis.

and noise from the PVA material as seen in the other stenosis models were observed. The diameter of the lumen of the geometry images at the point of maximum stenosis (Figure 3.26b) was smaller compared to images proximal and distal to the stenosis (Figures 3.26a, c, and d). Signs of signal loss were observed at the point of maximum stenosis (Figure 3.26b) and just distal to the stenosis (Figure 3.26c). Complete signal loss was observed downstream of the stenosis (Figure 3.26d). This area corresponded with the fully turbulent flow fields observed in the flow visualization studies (Figure 3.4).

Two dimensional velocity profiles are shown in Figures 3.27 and 3.28. The maximum velocity observed proximal to the stenosis was approximately 100.0cm/sec, which was greater than the 83.2cm/sec theoretical entrance maximum velocity. The maximum velocity increased at the point of maximum stenosis and remained elevated just distal of the stenosis. This was representative of the laminar jet observed in flow visualization. Additional noise was observed at the middle of the lumen in Figures 3.27b and 3.28a. This was attributed to flow acceleration that can produce errors in the phase contrast data. Far downstream of the stenosis only noise was observed (Figure 3.28b) due to the turbulent flow patterns. Unlike the previous models, negative velocities were only observed at finite regions of the PVA models. In the three-dimensional figures (Figures 3.29 and 3.30), random noise was seen at all axial locations.

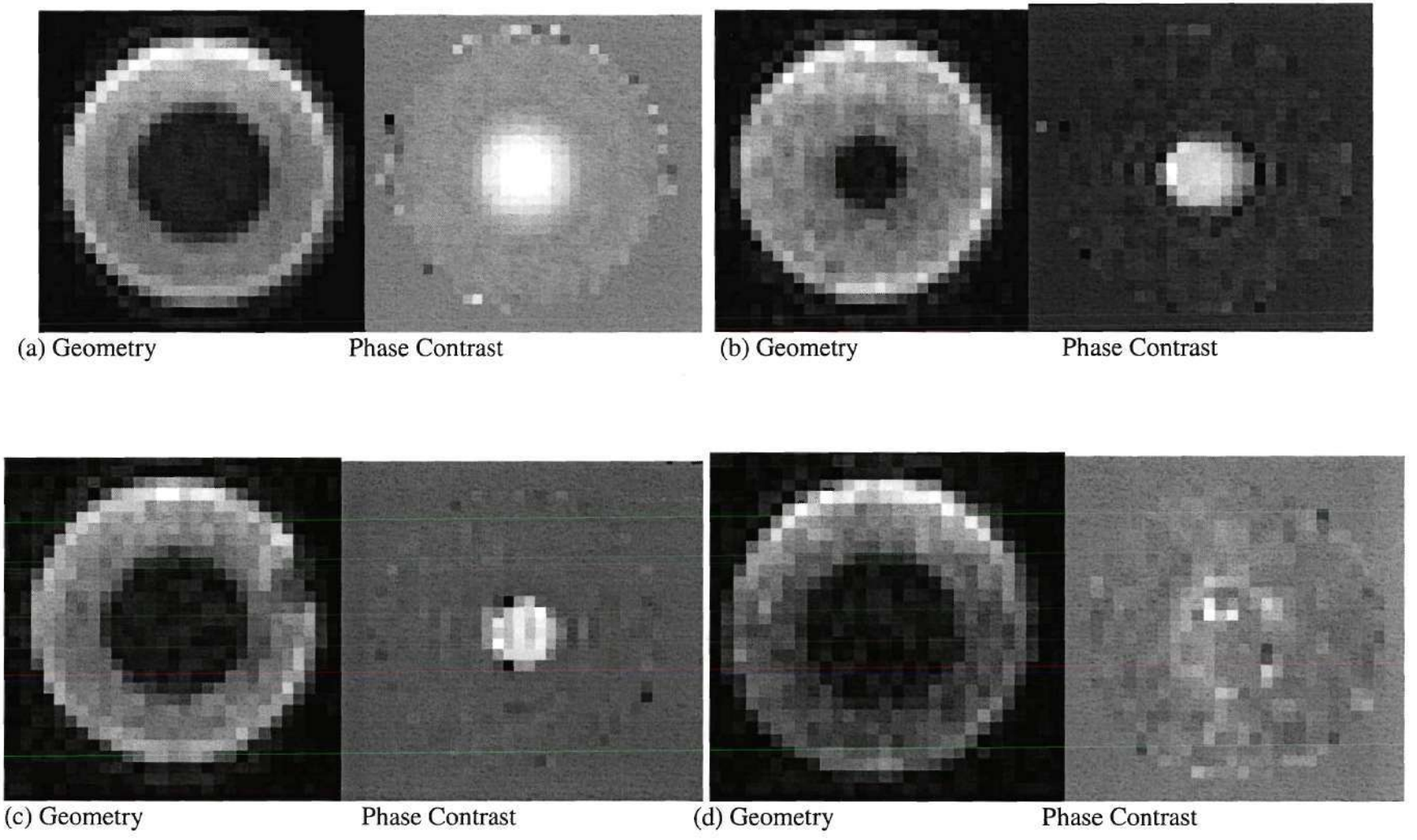

Figure 3.26: Geometry and phase contrast MRI images (a) proximal to stenosis (b) at maximum stenosis (c) just distal of stenosis and (d) far down-field of stenosis for the 75.0% stenosis model at the peak flow rate (Re = 714).

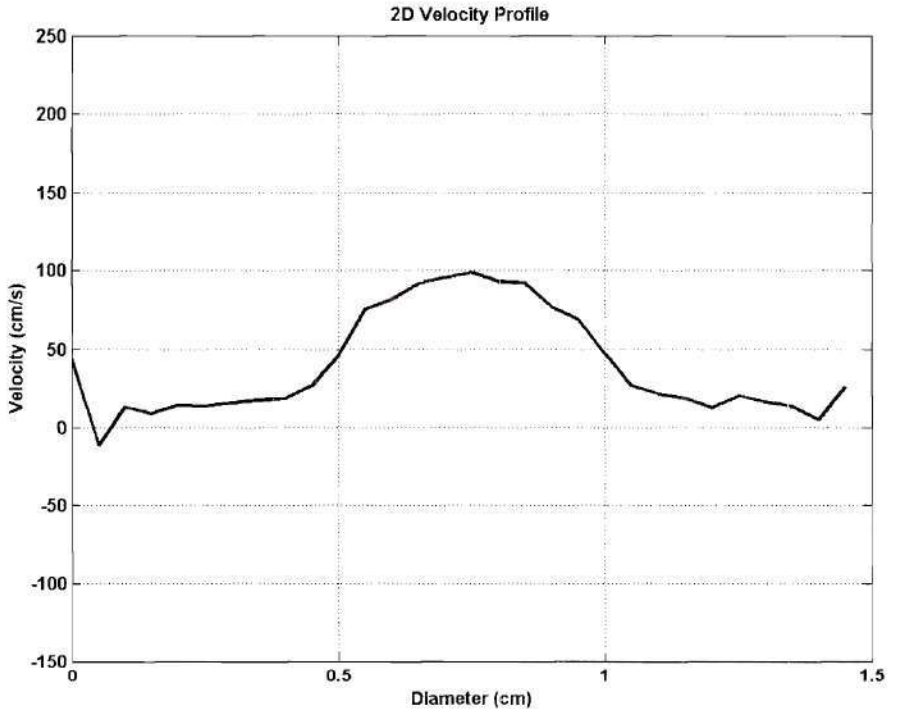

(a) proximal to stenosis

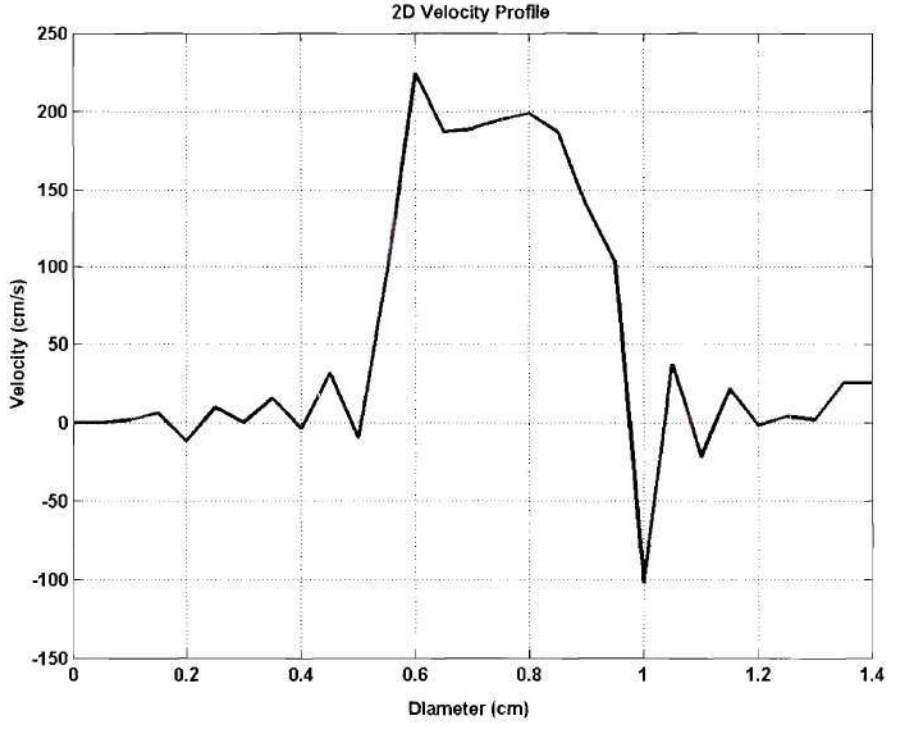

(b) at point of maximum stenosis

Figure 3.27: 2D velocity profiles for the 75.0% stenosis model at the peak flow rate (Re = 714) (a) proximal to stenosis and (b) at point of maximum stenosis.

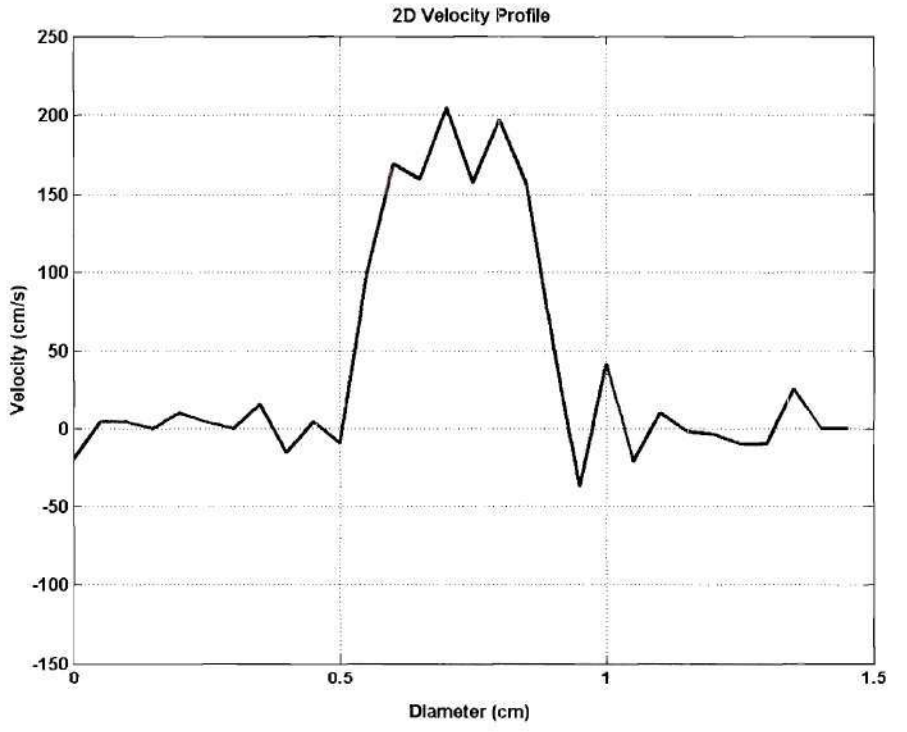

(a) just distal to stenosis

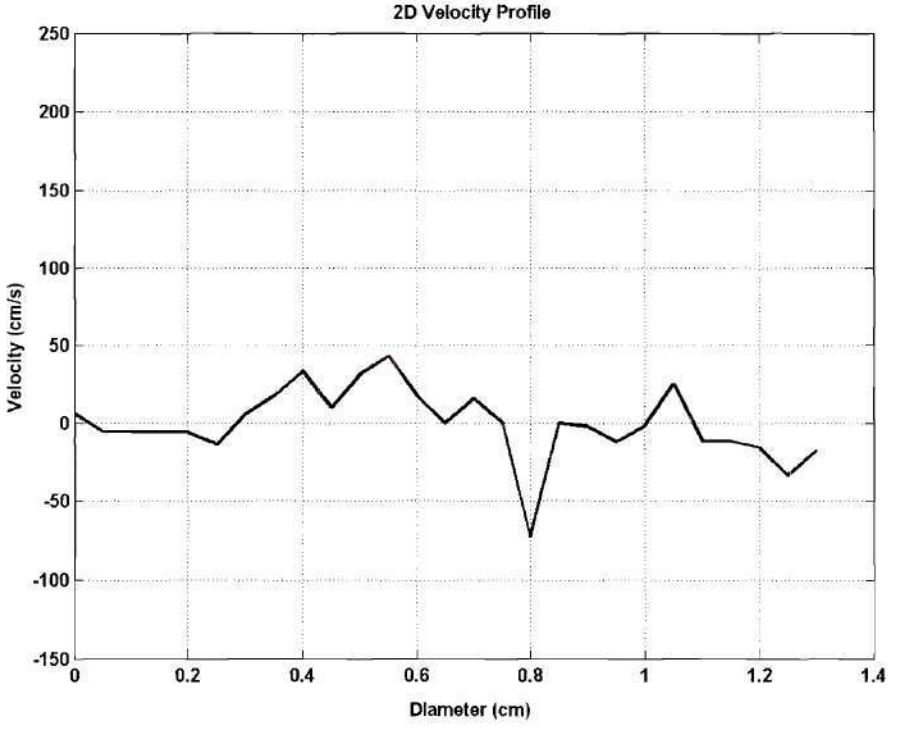

(b) far downstream of stenosis

Figure 3.28: 2D velocity profiles for the 75.0% stenosis model at the peak flow rate (Re = 714) (a) just distal to stenosis and (b) far downstream of stenosis.

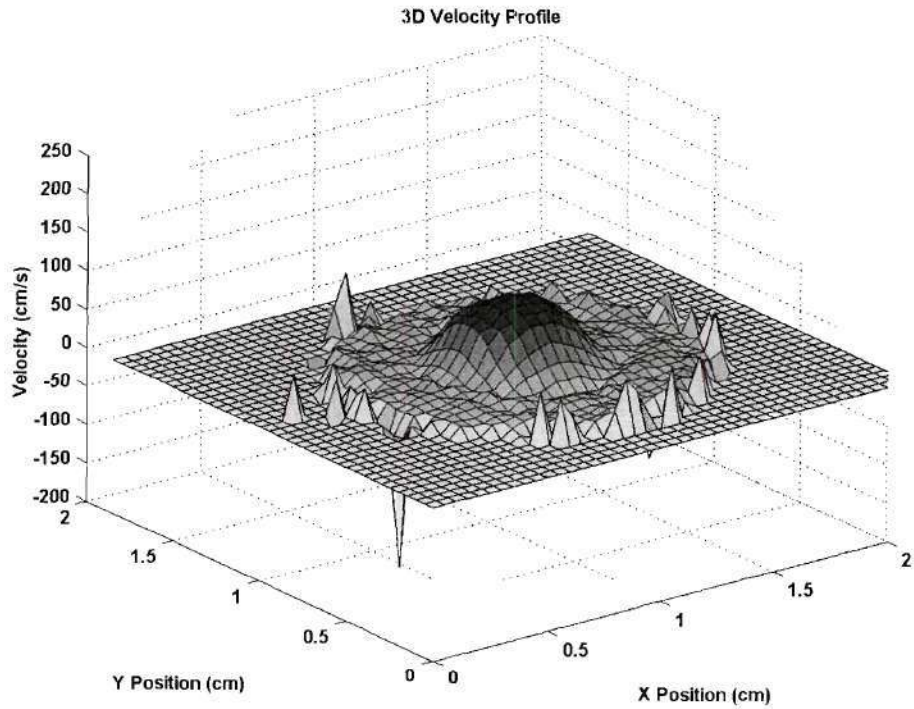

(a) proximal to stenosis

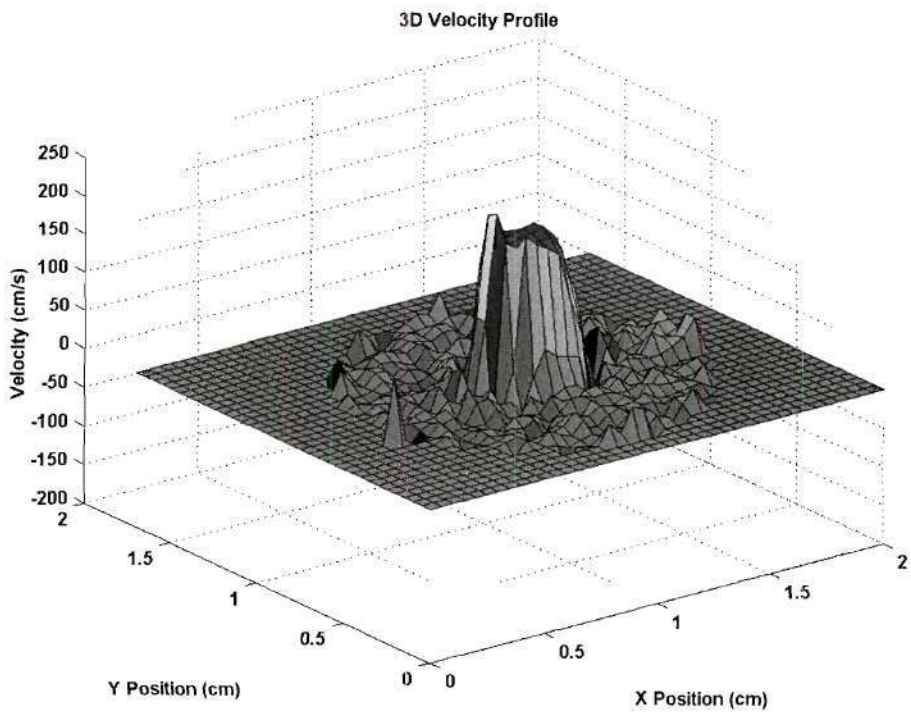

(b) at point of maximum stenosis

Figure 3.29: 3D velocity profiles for the 75.0% stenosis model at the peak flow rate (Re = 714) (a) proximal to stenosis and (b) at point of maximum stenosis.

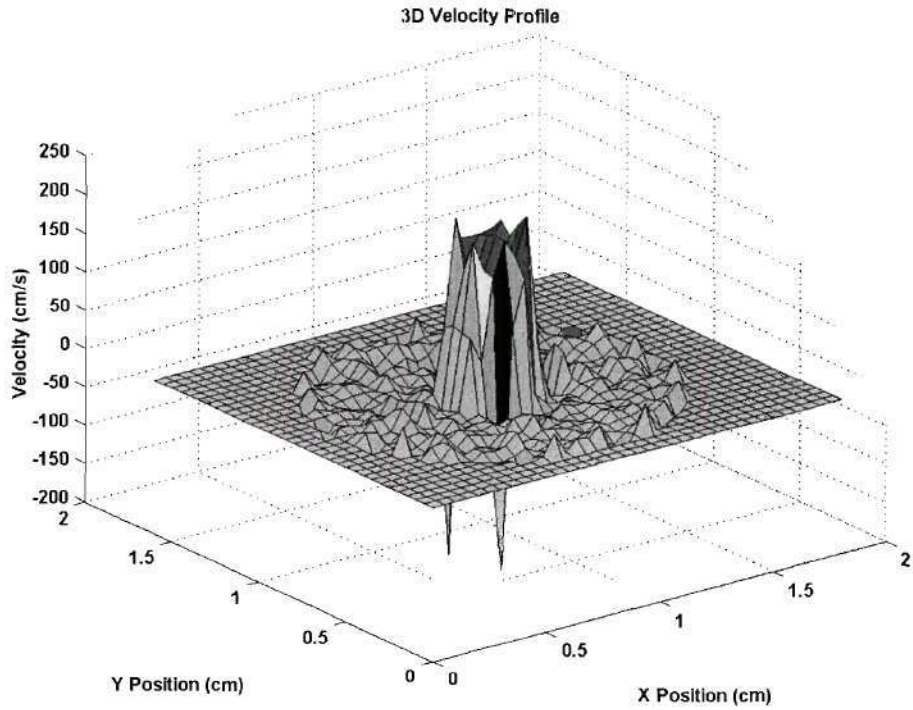

(a) just distal to stenosis

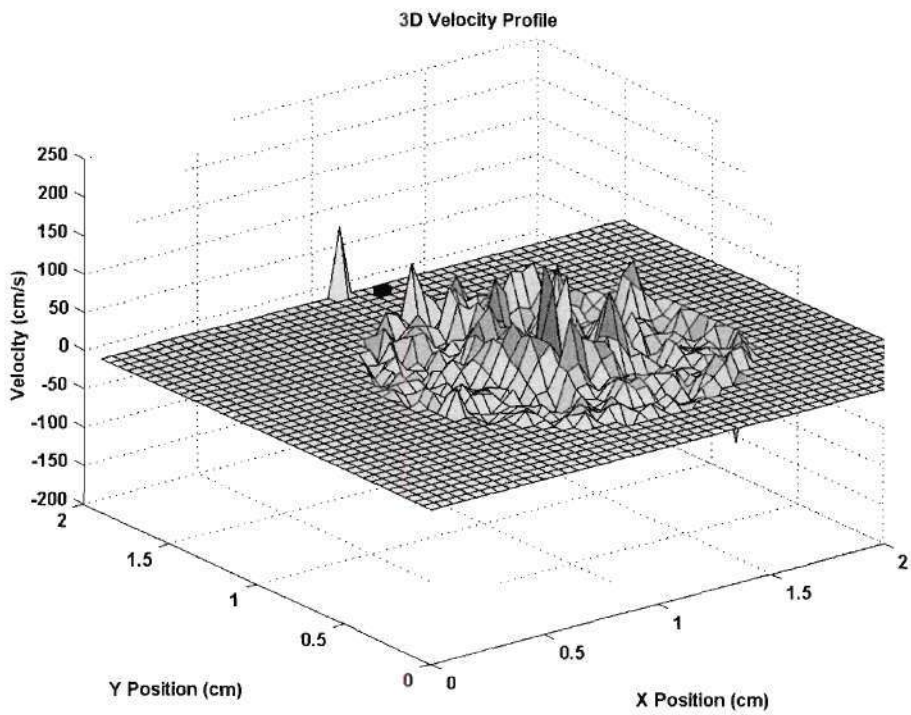

(b) far downstream of stenosis

Figure 3.30: 3D velocity profiles for the 75.0% stenosis model at the peak flow rate (Re = 714) (a) just distal to stenosis and (b) far downstream of stenosis.

CFD Validation

The wall shear stress distributions derived from the CFD simulation are shown in Figure 3.31. In order to compare the WSS results from the FIDAP simulation, the results had to be converted to wall vorticity values. The relationship is described by the following formula:

$$\omega_w = (\tau_w * a_0) / (\mu * U_{max}) \qquad (3.1)$$

where ω_w = wall vorticity

τ_w = wall shear stress

a_0 = radius of entrance vessel = 2.54cm

μ = dynamic viscosity = 0.12 Poise

U_{max} = maximum velocity on the axis far removed from the stenosis = 9.40 cm/sec

The results are shown in Figure 32a. For comparison, the results from Deshpande's analysis are shown in Figure 32b (Deshpande, 1977). Good agreement in wall vorticity pattern, maximum wall vorticity, and minimum wall vorticity were observed.

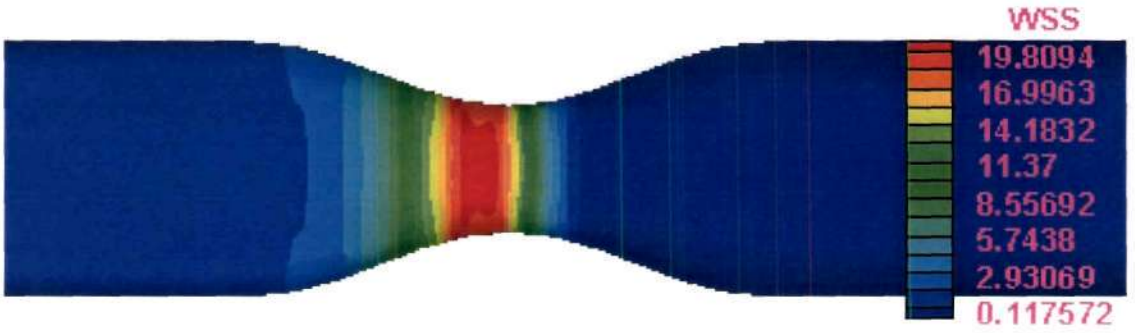

(a) CFD validation geometry and resulting wall shear stress contour plot.

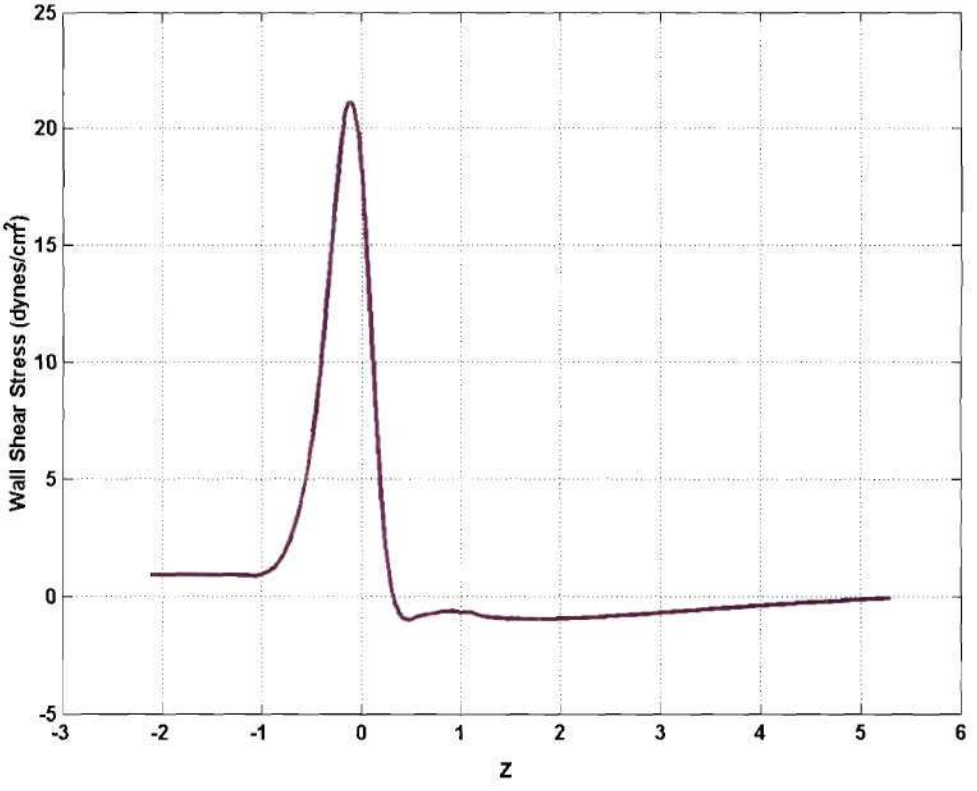

(b) Wall shear stress plot

Figure 3.31: Wall Shear Stress distributions for validation of the FIDAP 8 CFD code.

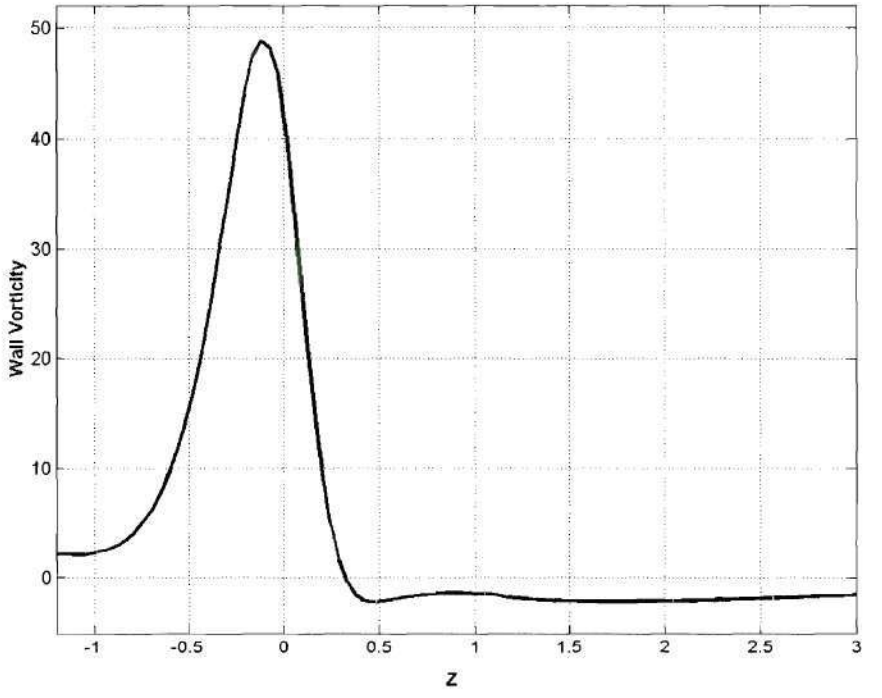

(a) Wall vorticity results derived from FIDAP simulation.(Re = 200)

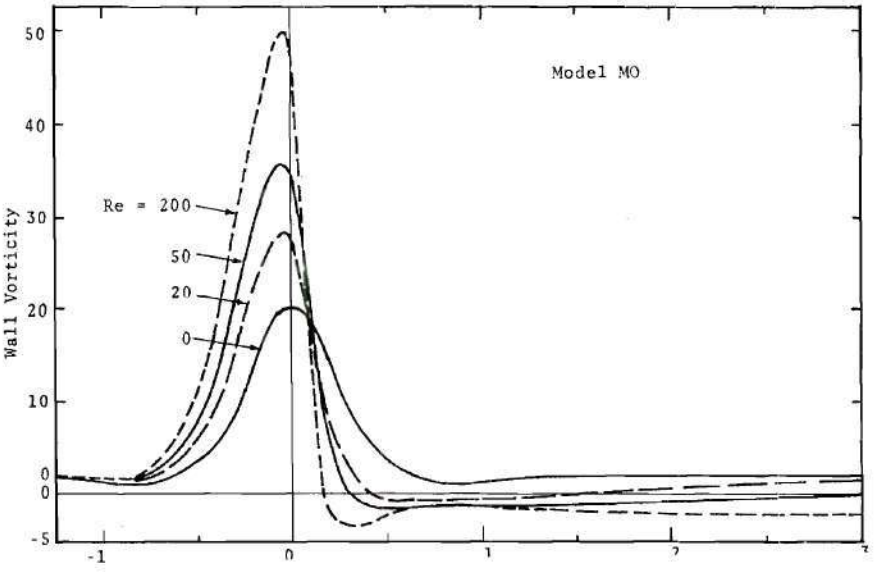

(b) Wall Vorticity results from Deshpande, 1977.

Figure 3.32: CFD validation using wall vorticity in a 75.0% symmetric stenosis model (a) results from FIDAP 8 CFD simulation and (b) results from Deshpande, 1977.

CFD Grid Sensitivity/Independence

The grid sensitivity/independence studies are shown in Figures 3.33 through 3.36. Generally, good agreement was found between all combinations of total number of nodes used in the computational geometry and the distance between the first node and the wall location (Figures 3.33a and 3.35a). Large WSS values were observed at the entrance of the model for all computational grids, caused by errors associated with interpolating the MRI velocity data to the entrance grid. WSS values differed by up to 2.5 dynes/cm^2 at the point of maximum stenosis (Figure 3.33b). This was caused by different node locations along the axial dimension. The last set of data (blue lines) recorded WSS values just proximal to the other computational grids. Therefore, the absolute comparison of WSS values was not possible due to different axial node locations caused by the finite element automatic grid creation software. However, the maximum difference only represented a 1.8% error. This problem was not observed in the other axial data extracted (Figure 3.35 b). The WSS values were observed to be in much better agreement.

Good agreement between the last two data sets (purple and blue) was observed in all of the data sets. An unexpected deviation in WSS values was observed in Figure 3.36b. The second set of computational grids was approximately 0.4 dynes/cm^2 above the other data sets. This might have been caused by larger errors associated with the boundary layer – bulk finite element grid interface.

The computational time required to run the different simulations was significant when the total number of nodes in the computational grid was increased. However, the increase in computational time was minimal when nodes were clustered closer to the wall

while leaving the total number of nodes relatively unchanged. Based on this data, all computational grids were designed to have the first node located approximately 250μm from the wall with the total number of nodes being approximately 330,000.

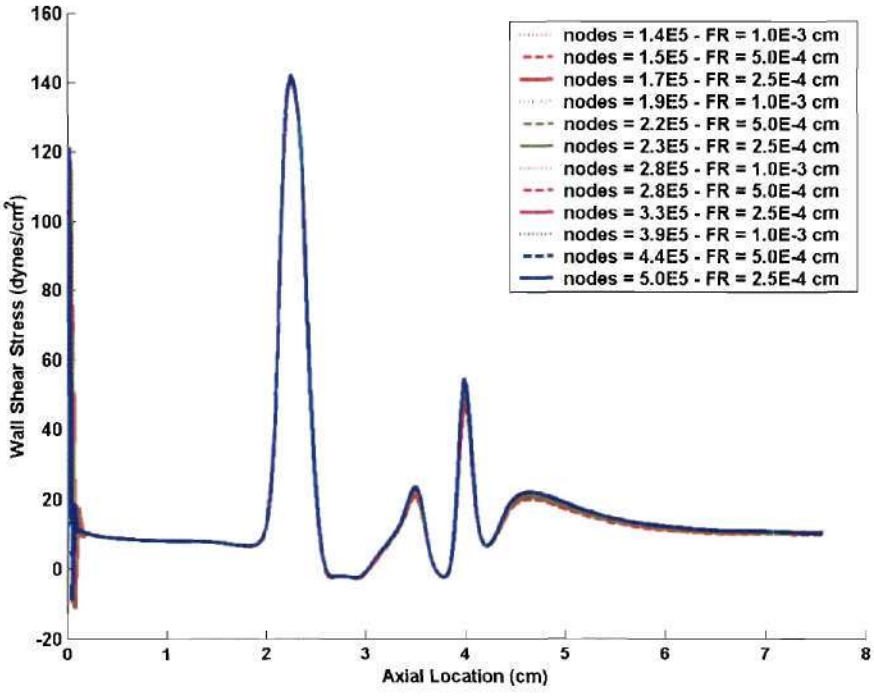

(a) Wall Shear Stress for one angular location along all axial locations.

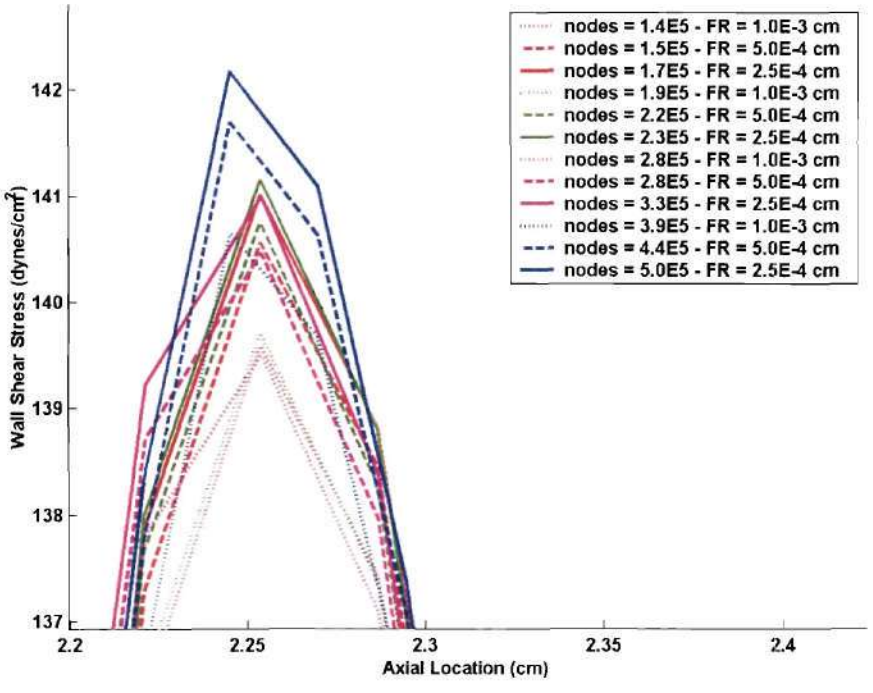

(b) grid sensitivity data at maximum WSS values

Figure 3.33: Grid sensitivity/independence WSS plots. Nodes = total number of nodes used in the computational geometry. FR = distance from wall to the first node in the boundary layer.

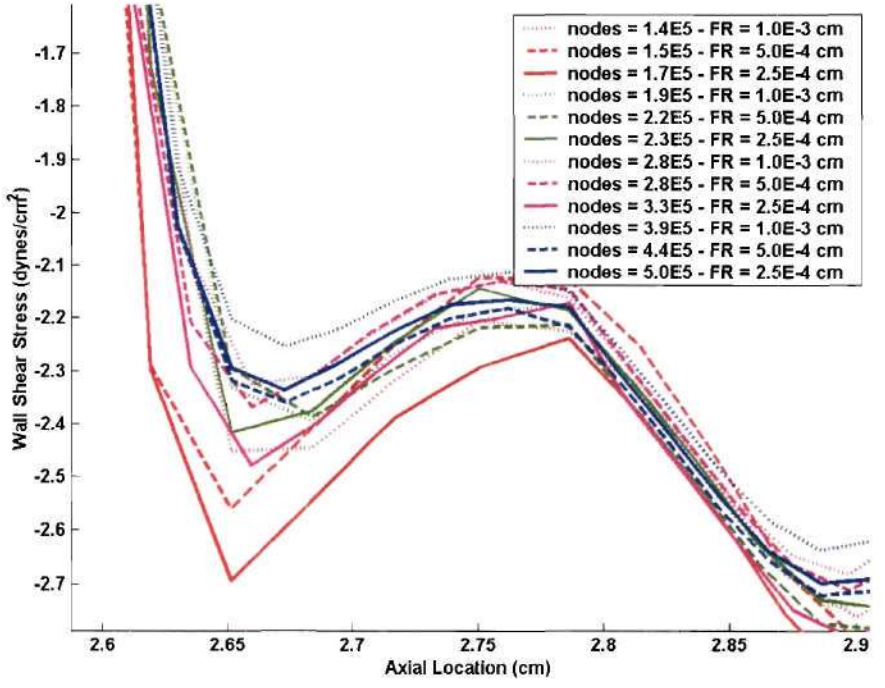

(a) grid sensitivity data at minimum WSS values

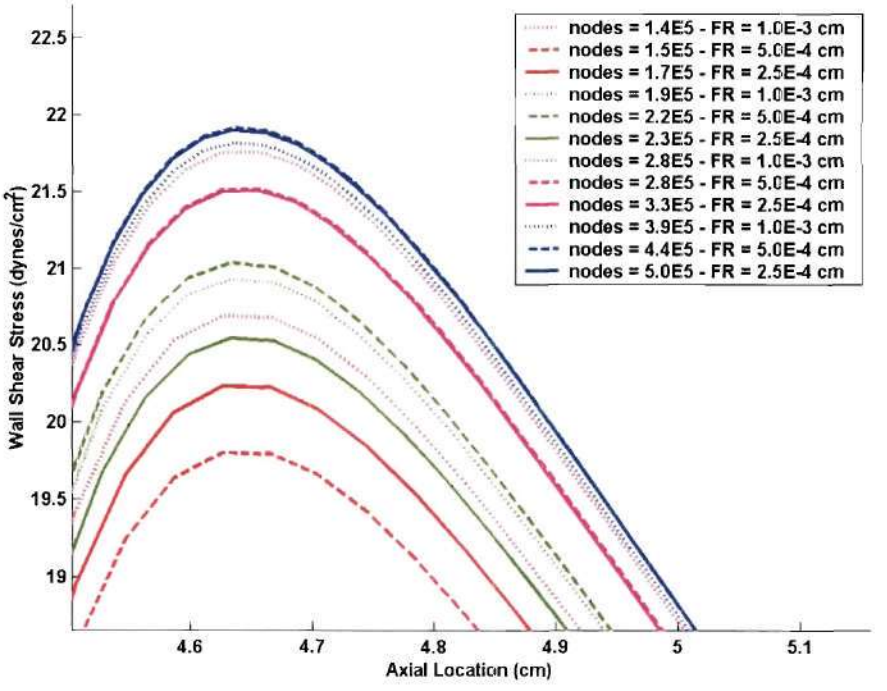

(b) grid sensitivity data at point of maximum WSS deviation.

Figure 3.34: Grid sensitivity/independence WSS plots. Nodes = total number of nodes used in the computational geometry. FR = distance from wall to the first node in the boundary layer.

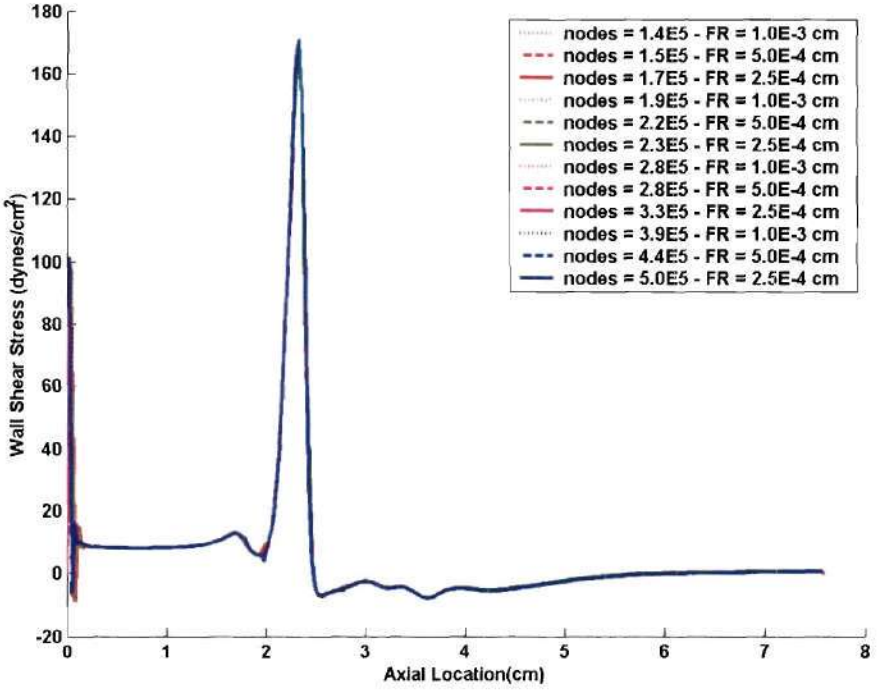

(a) Wall Shear Stress for another angular location along all axial locations.

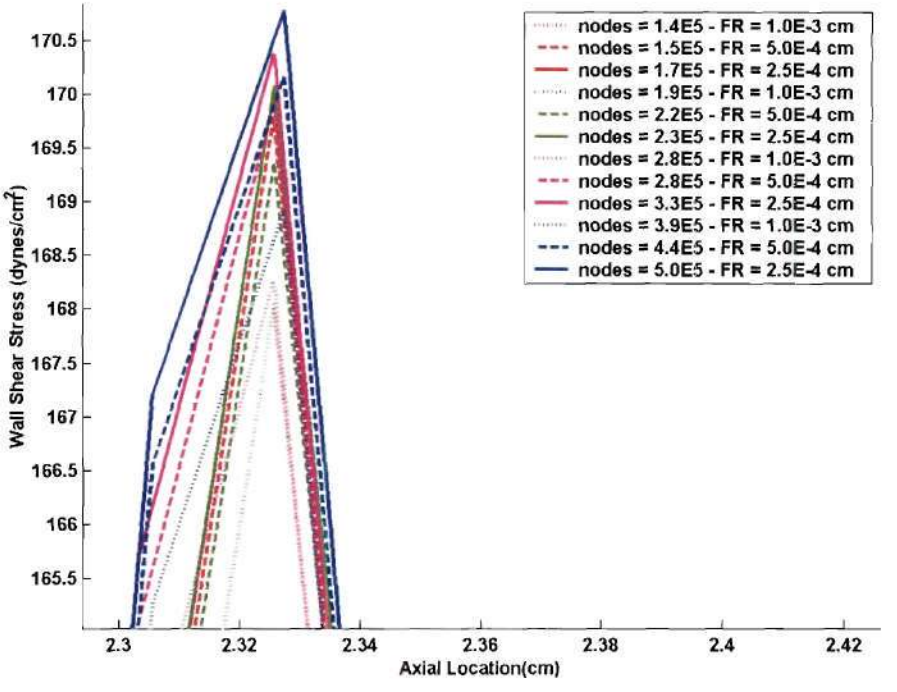

(b) grid sensitivity data at maximum WSS values

Figure 3.35: Grid sensitivity/independence WSS plots. Nodes = total number of nodes used in the computational geometry. FR = distance from wall to the first node in the boundary layer.

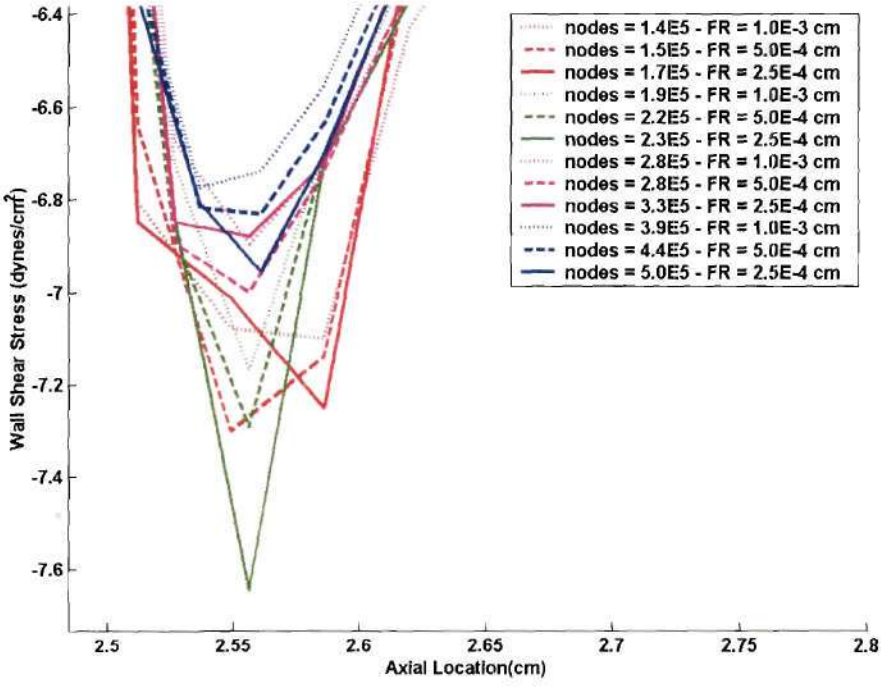

(a) grid sensitivity data at minimum WSS values

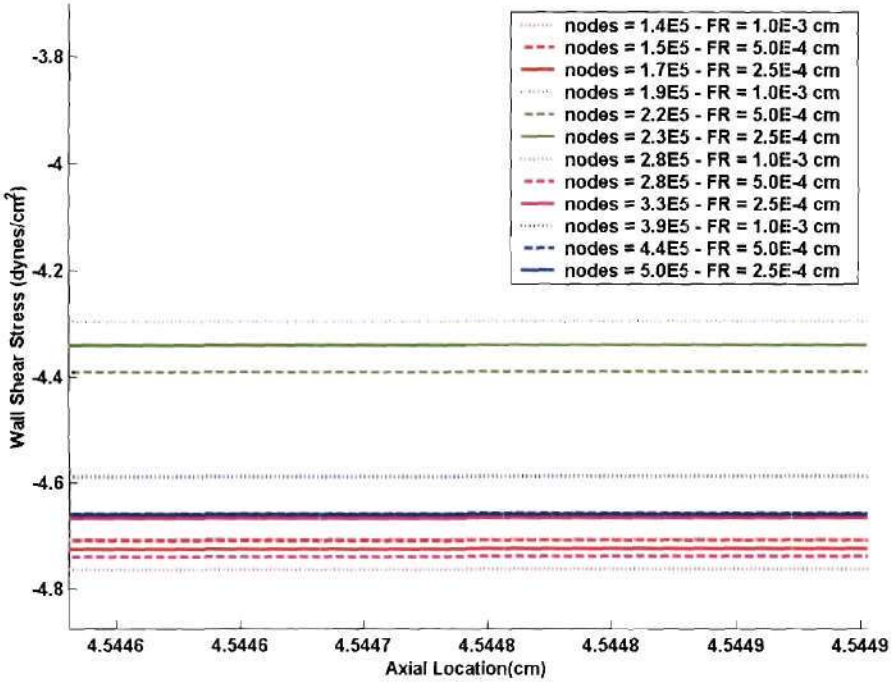

(b) grid sensitivity data at maximum WSS values

Figure 3.36: Grid sensitivity/independence WSS plots. Nodes = total number of nodes used in the computational geometry. FR = distance from wall to the first node in the boundary layer.

Gold Standard WSS Values

0.0% Stenosis Geometry / Average and Peak Flow Rates

Theoretical values of WSS were used as the gold standard values. The solution of the Navier-Stokes equations for the fully developed flow of a Newtonian fluid through a smooth cylindrical geometry yielded the following equations for WSS:

$$WSS = \frac{8V\mu}{D} = \frac{32\mu Q}{\pi D^3}$$

where V = mean velocity

μ = dynamic viscosity (0.04 Poise)

Q = volumetric flow rate (average = 4.5 cm^3/sec, peak = 20.96 cm^3/sec)

D = diameter (0.635 cm)

The solution of these equations yielded WSS values of 7.16 dynes/cm^2 for the average flow rate and 20.96 dynes/cm^2 for the peak flow rate.

52.7% Stenosis Geometry / Average and Peak Flow Rates

The gold standard WSS values for the 52.7% stenosis model are shown in Figures 3.37 through 3.42. WSS contour plots for the average and peak flow rates are shown in Figure 3.37. The maximum WSS values were located just proximal to the location of the maximum stenosis. The maximum WSS values were 62.43 dynes/cm^2 and 280.79 dynes/cm^2 for the average and peak flow rates, respectively. The WSS contours in the post-stenotic recirculation regions are shown in Figure 3.38. The minimum WSS values were -2.80 dynes/cm^2 and -17.87 dynes/cm^2 for the average and peak flow rates, respectively. For the average flow rate, the point of flow separation occurred 0.21cm distal to the point of maximum stenosis. The reattachment point was located 0.88cm

distal to the point of maximum stenosis. Therefore, the calculated recirculation region length was 0.67cm. For the peak flow rate, the point of flow separation occurred 0.14cm distal to the point of maximum stenosis, and the reattachment point was 2.068cm distal to the point of maximum stenosis. The total length of the recirculation region was 1.928cm (See Table 3.1). Therefore, the separation point was located more proximal and the point of reattachment was located more distal for the peak flow rate case yielding a longer recirculation region. Two-dimensional WSS plots are shown in Figure 3.39 for both flow rates. A triphasic curve was observed in the recirculation region for the peak flow rate WSS values. This was thought to be the recirculating fluid encountering the distal end of the stenosis geometry. As the retrograde fluid encountered this geometry, some of the force associated with the fluid was oriented in more of a perpendicular vector with relation to the wall. Therefore, in this region, the fluid forces imparted more of a pressure force than a shearing force compared to the straight geometry located distal to the stenosis geometry. Figures 3.40 and 3.41 represent graphs of the maximum and minimum WSS regions for the average and peak flow rates, respectively. In all of these graphs, eight equally spaced (in the angular (θ) direction) WSS plots for each geometry and flow rate are represented. Differences in the WSS plots were observed for all cases. For the average flow rate, differences of approximately 1.5 dynes/cm^2 and 0.15 dynes/cm^2 were observed for the maximum and minimum WSS, respectively. For the peak flow rate, differences of approximately 6.5 dynes/cm^2 and 3.0 dynes/cm^2 were observed for the maximum and minimum WSS, respectively. These differences were thought to result from errors associated with the computational grids and the numerical solution of the Navier-Stokes equations and represented the inherent error associated with

the numerical method employed. Figure 3.42 shows the 2D WSS plots for the average and peak flow rates superimposed to illustrate the large differences in peak WSS and recirculation regions.

	52.7% Stenosis Average Flow Rate	**52.7% Stenosis Peak Flow Rate**	**75.0% Stenosis Average Flow Rate**
Maximum WSS (dynes/cm^2)	62.43	280.79	196.35
Minimum WSS (dynes/cm^2)	-2.80	-17.87	-9.34
Separation Point (cm distal to stenosis)	0.21	0.14	0.12
Reattachment Point (cm distal to stenosis)	0.88	2.07	3.68
Recirculation Length (cm)	0.67	1.93	3.56

Table 3.1: Gold Standard WSS and recirculation region parameters.

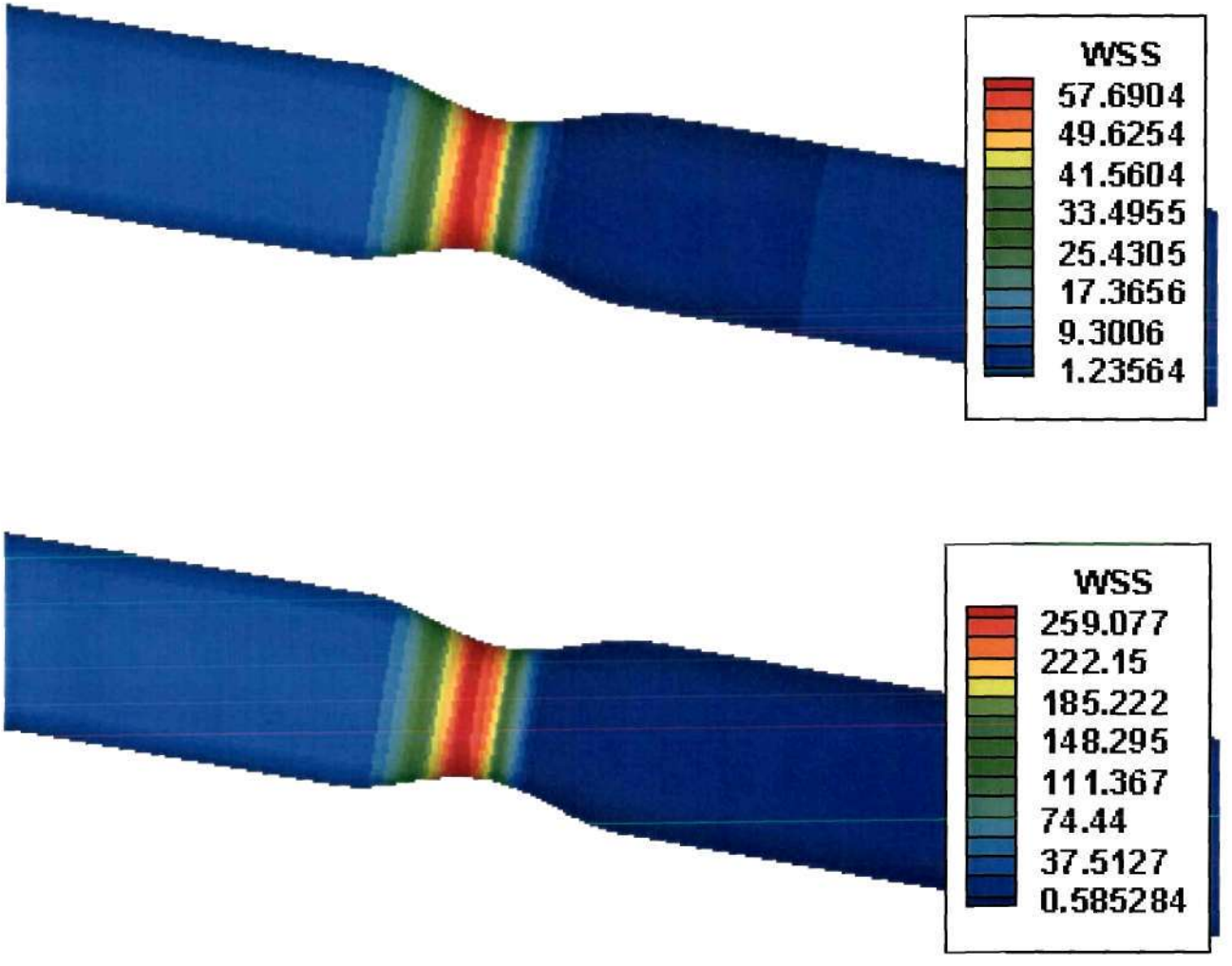

Figure 3.37: 52.7% stenosis gold standard WSS contours.

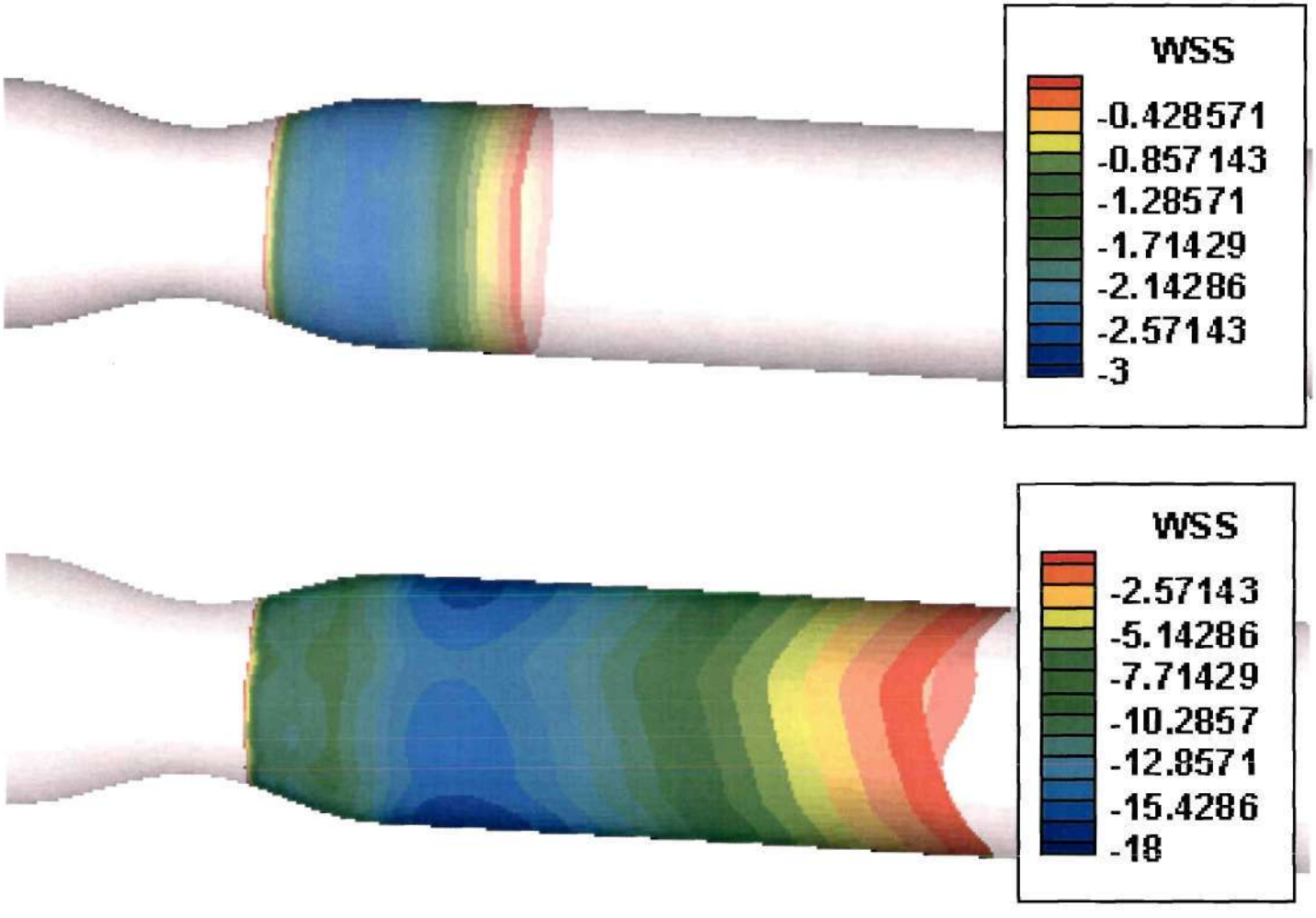

Figure 3.38: 52.7% gold standard recirculation zones.

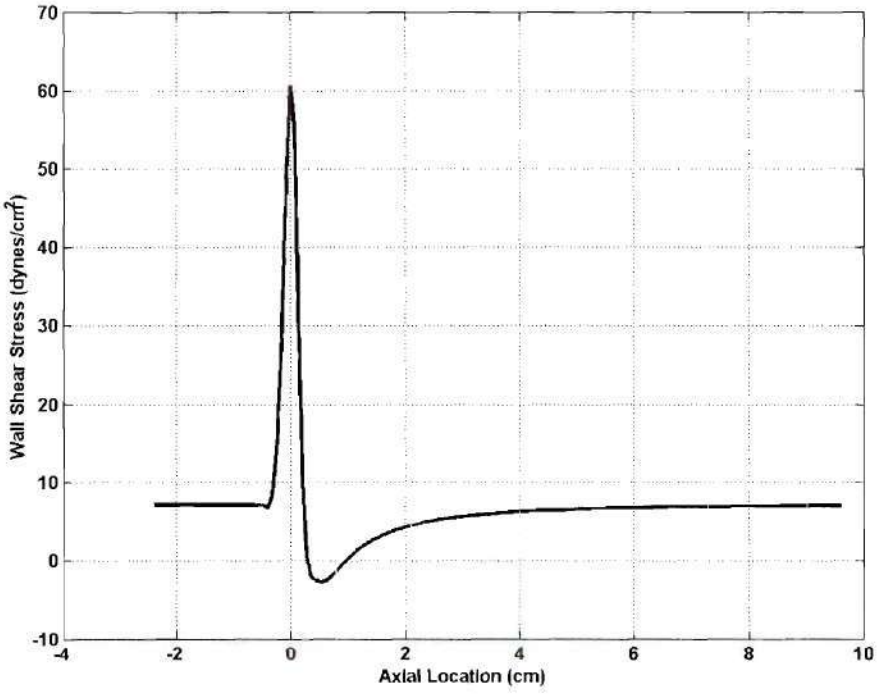

(a) average flow rate

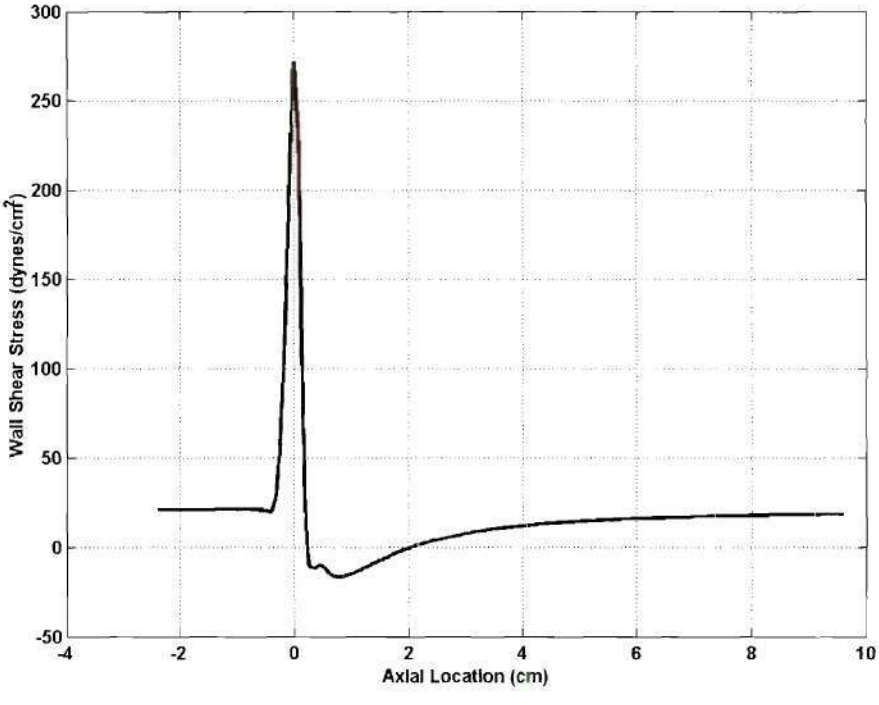

(b) peak flow rate

Figure 3.39: 52.7% gold standard 2D WSS plots for (a) average and (b) peak flow rates.

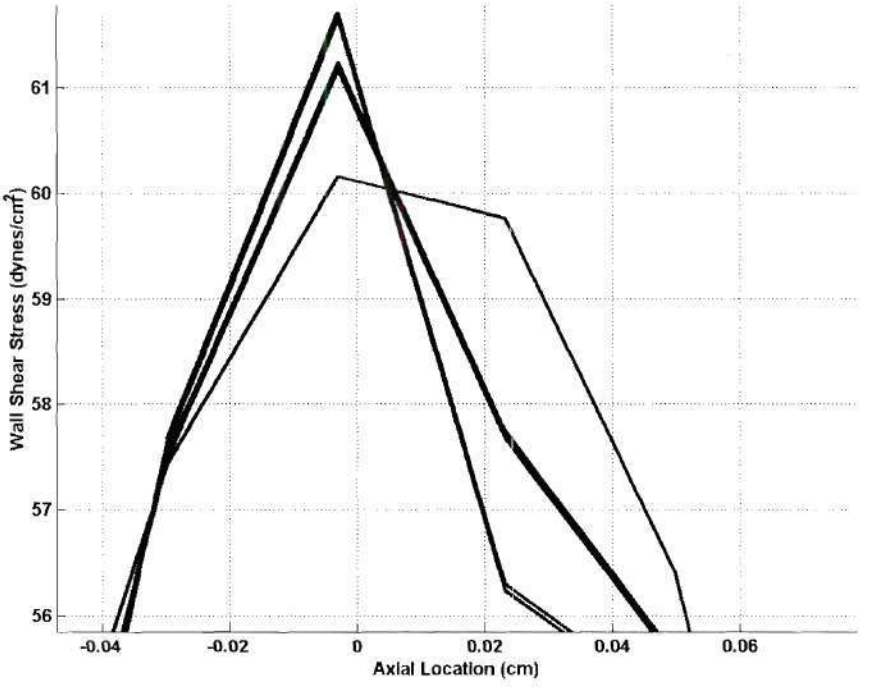

(a) maximum WSS

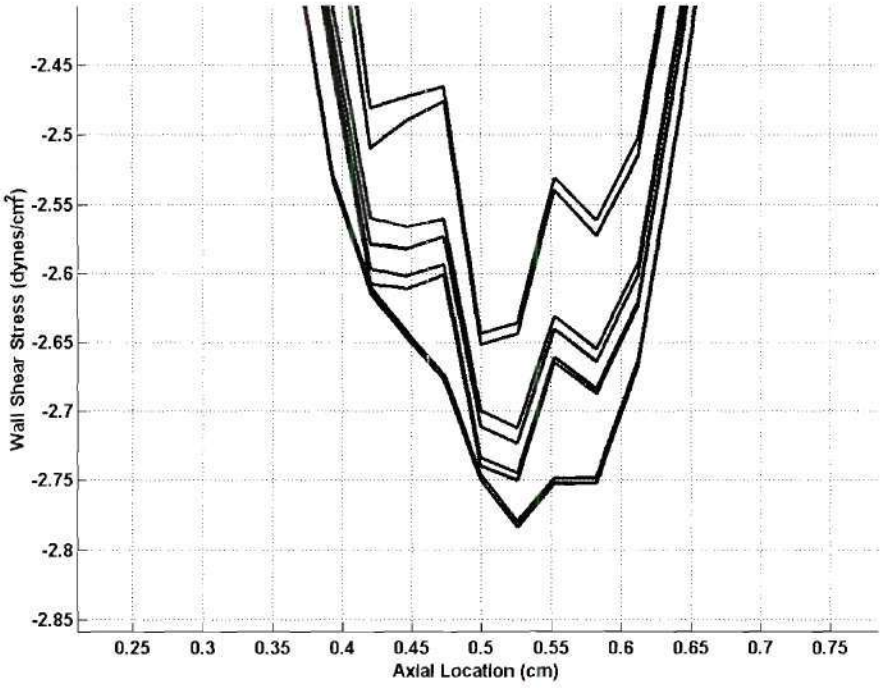

(b) minimum WSS

Figure 3.40: 52.7% stenosis average flow rate gold standard WSS graphs.

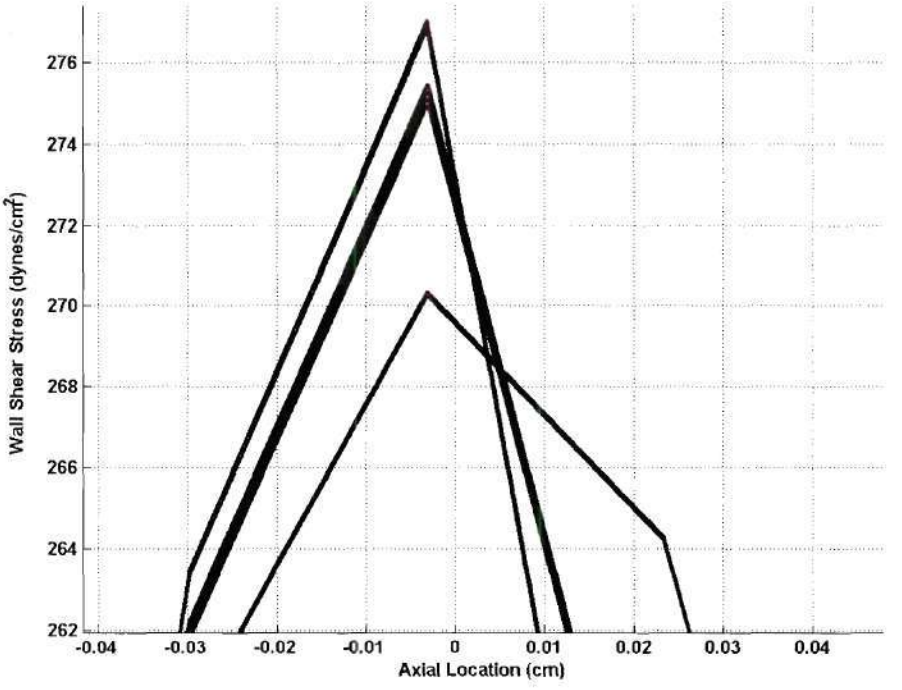

(a) maximum WSS graph.

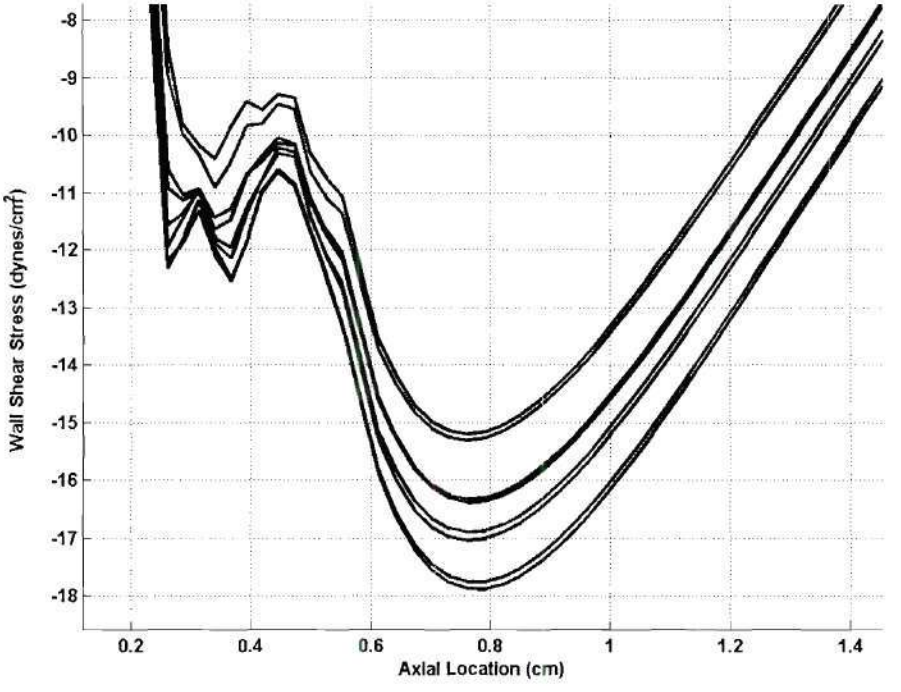

(b) minimum WSS graph.

Figure 3.41: 52.7% stenosis peak flow rate gold standard WSS plots.

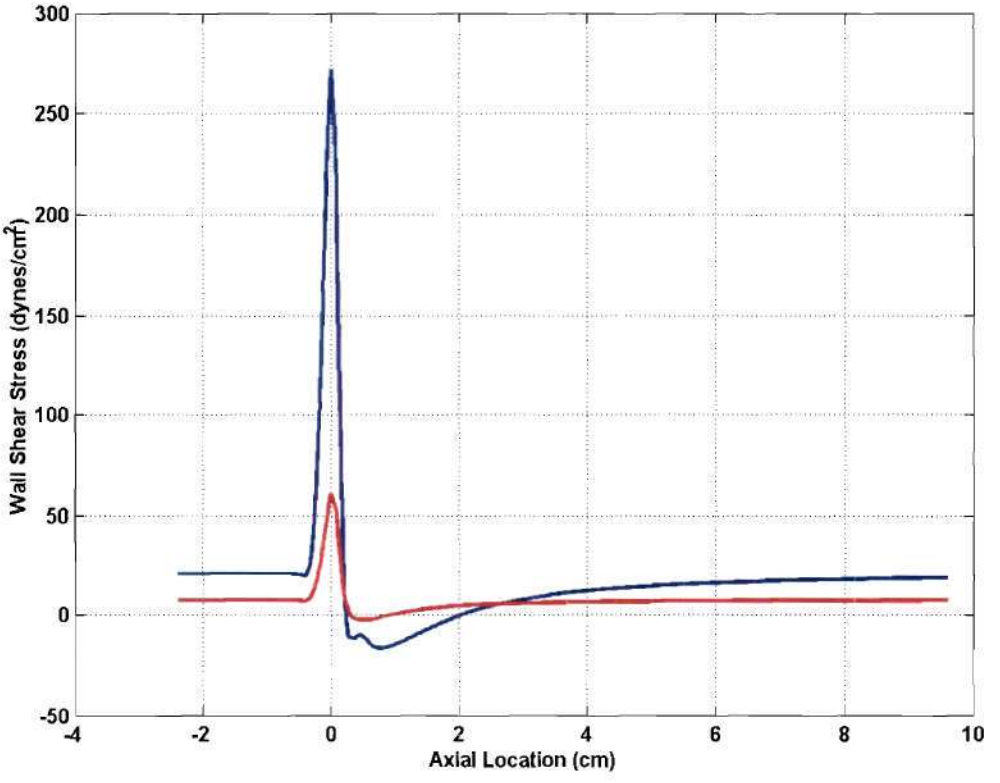

Figure 3.42: 52.7% stenosis average and peak flow rate WSS graphs.

75.0% Stenosis Geometry / Average and Peak Flow Rates

The gold standard WSS values for the 75.0% stenosis model are shown in Figures 3.43 through 3.45. The WSS contour plot for the average flow rate is shown in Figure 3.43a. The maximum WSS values were located just proximal to the location of the maximum stenosis. The maximum WSS value was 196.35 dynes/cm^2. The WSS contours in the post-stenotic recirculation regions are shown in Figure 3.43b. The minimum WSS value was –9.34 dynes/cm^2. The point of flow separation occurred 0.12cm distal to the point of maximum stenosis, and the reattachment point was located 3.68cm distal to the point of maximum stenosis. Therefore, the calculated recirculation region length was 3.56cm. Two-dimensional WSS plots are shown in Figure 3.44. A triphasic curve was observed in the recirculation region for the peak flow rate WSS values. This was thought to be the recirculating fluid encountering the distal end of the stenosis geometry as in the 52.7% stenosis geometry. As the retrograde fluid encountered this geometry, some of the force associated with the fluid was oriented in more of a perpendicular vector with relation to the wall. Therefore, in this region the fluid forces imparted more of a pressure force than a shearing force compared to the straight geometry located distal to the stenosis geometry. This triphasic WSS pattern was even more evident in the 75.0% stenosis geometry due to the more acute geometry causing more of the fluid force to be oriented perpendicular to the wall. Figure 3.44b represents a graph of the maximum WSS regions. In this graph, eight equally spaced (in the angular (θ) direction) WSS plots are represented. Differences in the WSS plots were observed for all cases. Differences of approximately 1.5 dynes/cm^2 and 0.5 dynes/cm^2

were observed for the maximum and minimum WSS, respectively. As for the 52.7% stenosis, these differences were thought to result from errors associated with the computational grids and the numerical solution of the Navier-Stokes equations and represented the inherent error associated with the numerical method employed. An example of the asymmetric computational grid used in these studies is shown in Figure 3.45.

A convergent solution was not obtained for the 75.0% stenosis at peak flow rate model. For the flow visualization studies, this model had turbulent flow patterns (see Figure 3.4), which were not modeled in the FIDAP 8.0 code. If a convergent solution had been obtained using a laminar CFD code, the solution probably would have been erroneous. As observed in flow visualization, the recirculation region at the peak flow rate for the 75.0% stenosis model was shorter compared to the average flow rate. This was due to turbulent interactions between the largely laminar and low velocity recirculation region and the turbulent jet which would not have been modeled using a laminar CFD code.

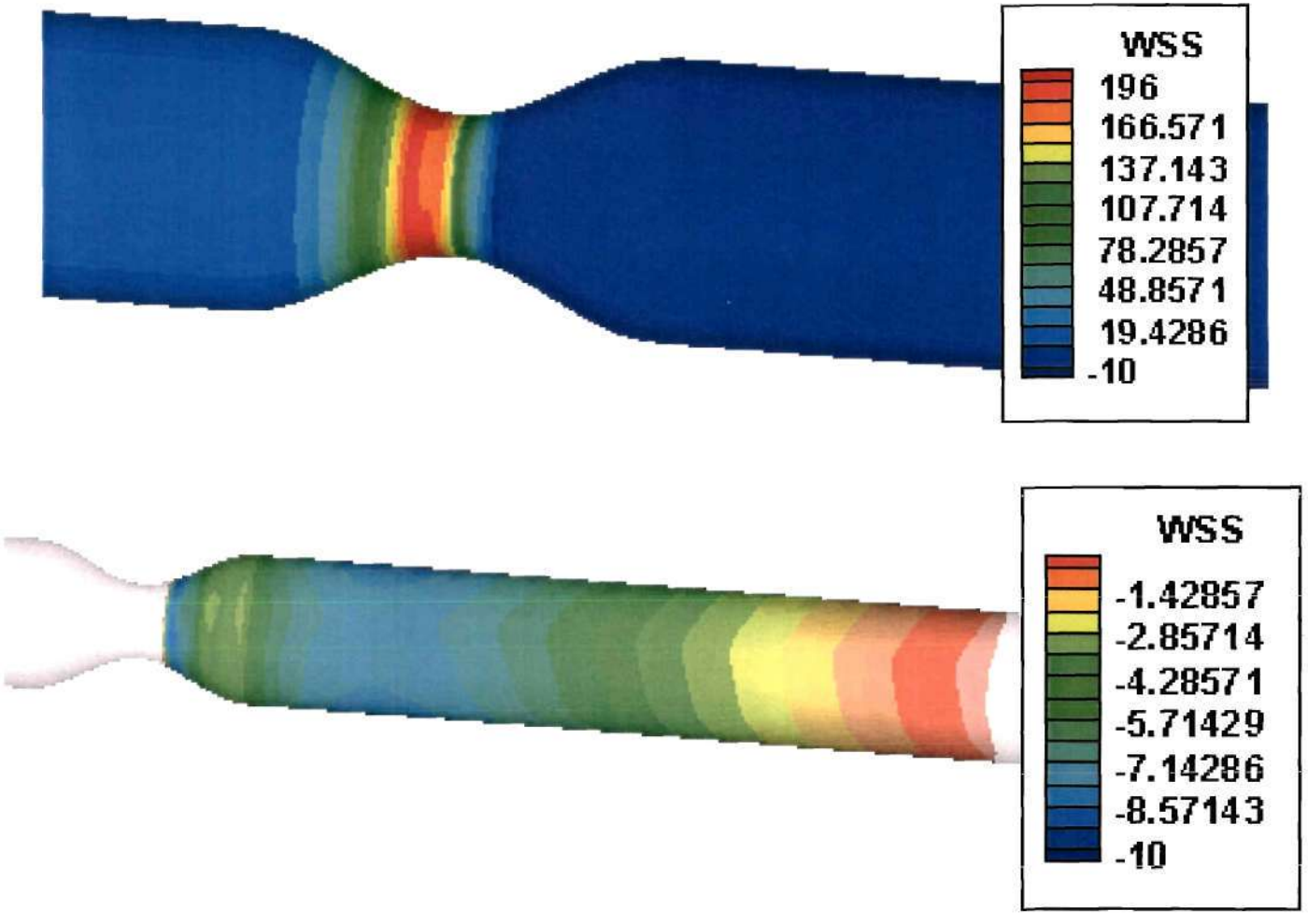

Figure 3.43: 75% stenosis average flow rate WSS contour and recirculation region plots.

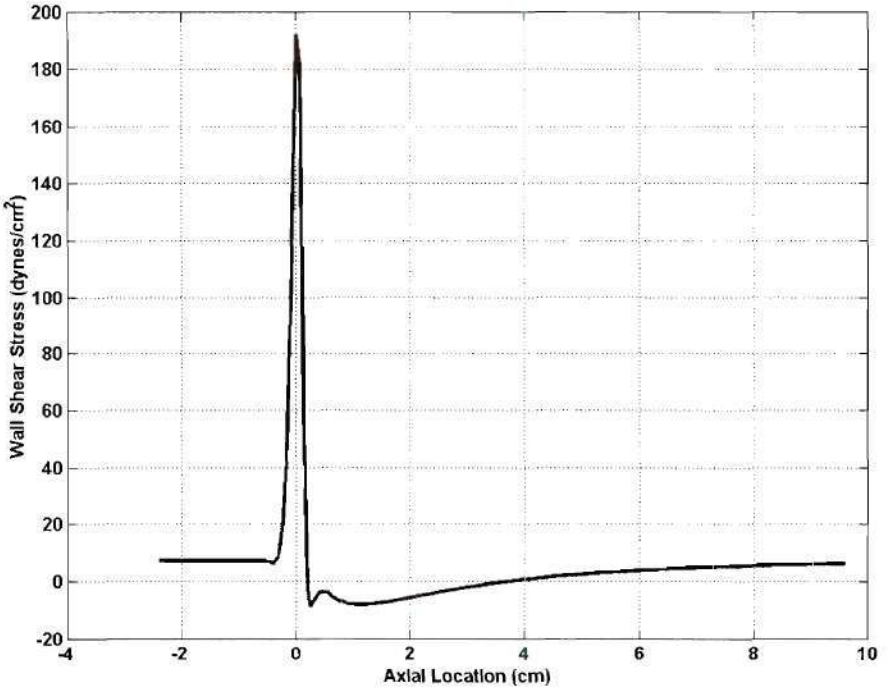

(a) total WSS graph.

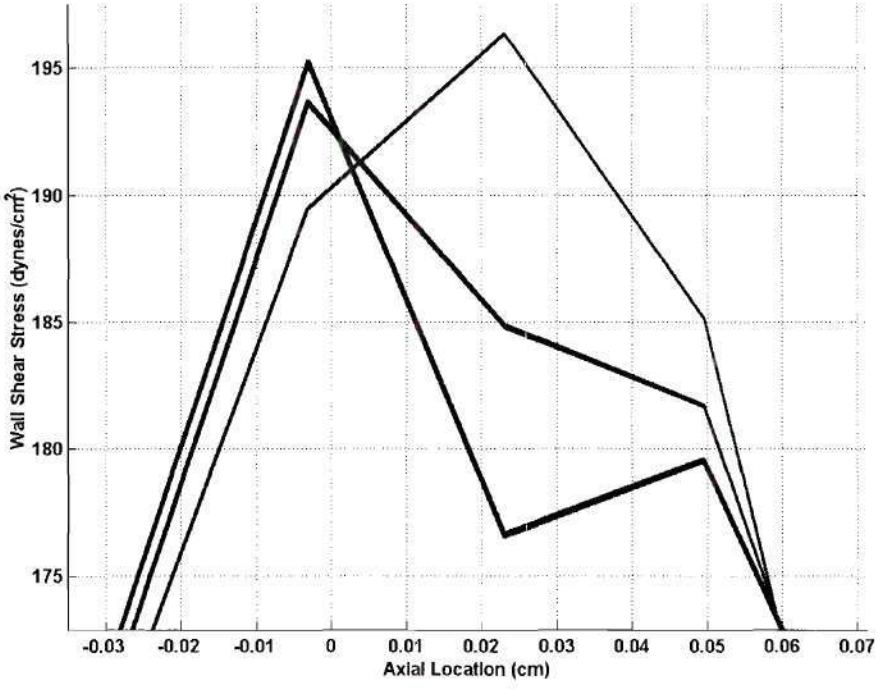

(b) maximum WSS graph.

Figure 3.44: 75% stenosis average flow rate gold standard WSS graph.

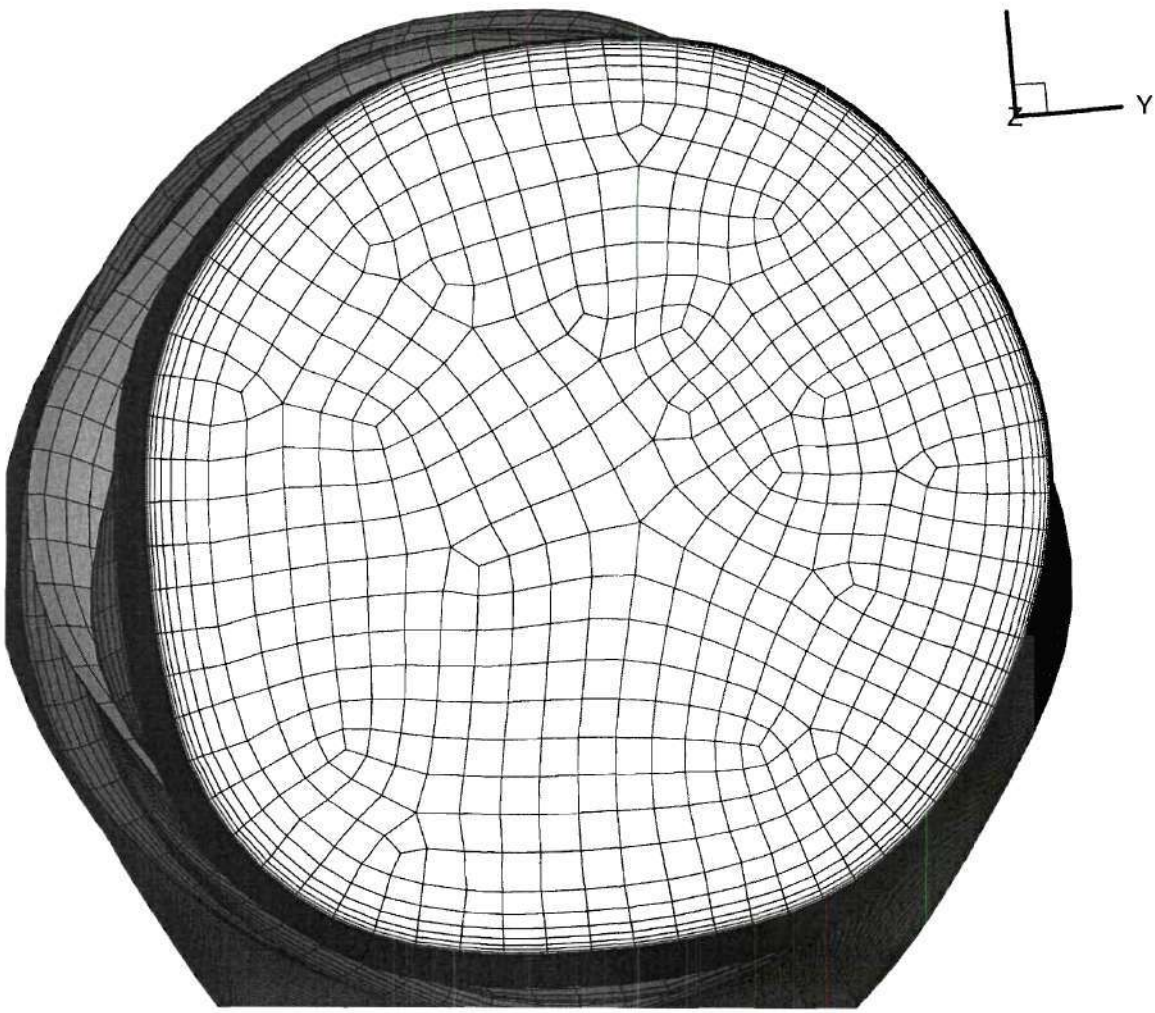

Figure 3.45: Example of finite element computational mesh.

CFD Simulations - Ideal Geometries and PC-MRI Derived Boundary Conditions

In order to determine the effects of the PC-MRI derived inlet velocity profile boundary conditions independent of the MRI derived geometries, CFD simulations were executed using these boundary conditions with the ideal geometries. The results were then compared to the gold standard CFD simulations.

0.0% Stenosis Geometry / Average Flow Rate

The PC-MRI derived inlet velocity profile for the 0.0% stenosis model under average flow conditions is shown in Figure 3.46. The overall shape of the velocity profile illustrated in Figure 3.46a was parabolic which was expected for all of the models due to the long entrance length tubing used in the MRI flow loop. The peak velocity was approximately 30.0 cm/sec, which was close to the theoretical value of 28.4 cm/sec. This velocity profile was applied to the CFD entrance region computational grid. The velocities along the perimeter were then assigned a zero velocity to satisfy the no-slip boundary condition at the wall. Therefore, large near-wall velocity gradients were present since the near-wall velocity values are not uniformly zero. Figure 3.46b illustrates which nodes on the entrance region computational grid were assigned negative velocities. Since negative velocities were not expected in fully developed, steady, laminar flow fields through a straight cylindrical tube, the negative velocity values were caused by errors associated with obtaining the velocity data using PC-MRI.

The 2D WSS graph for the 0.0% stenosis under average flow rates conditions is illustrated in Figure 3.47. Large positive and negative WSS values were seen in the entrance region of the model. These were attributed to the large velocity gradients caused by employing the no-slip boundary condition to non-zero near-wall velocity

values. These large entrance WSS values are also illustrated in the 3D WSS graph shown in Figure 3.50a. These WSS values dissipated further down stream as seen by the converging mean WSS value and the decreasing standard deviation magnitude. The mean WSS value distal to the entrance effects was 7.44 dynes/cm^2. This represented a 3.9% error relative to the theoretical WSS value of 7.16 dynes/cm^2.

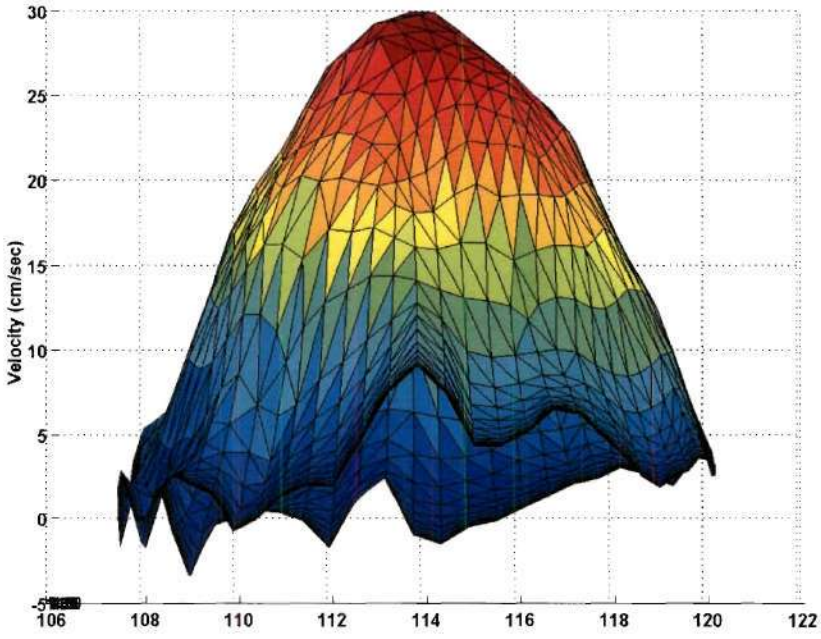

(a) PC-MRI derived entrance velocity profile.

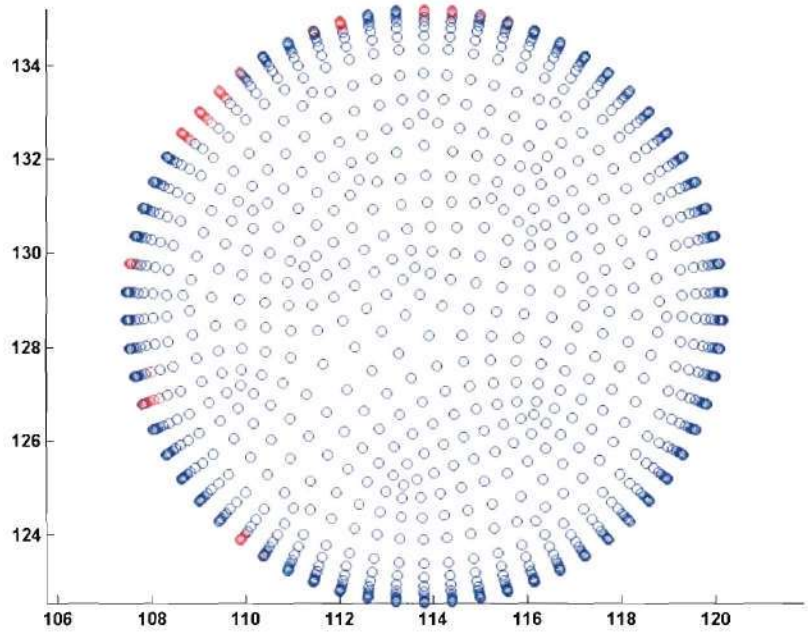

(b) negative velocities assigned to the entrance region computational grid are shown in red.

Figure 3.46: 0.0% stenosis average flow rate entrance boundary condition velocity profiles.

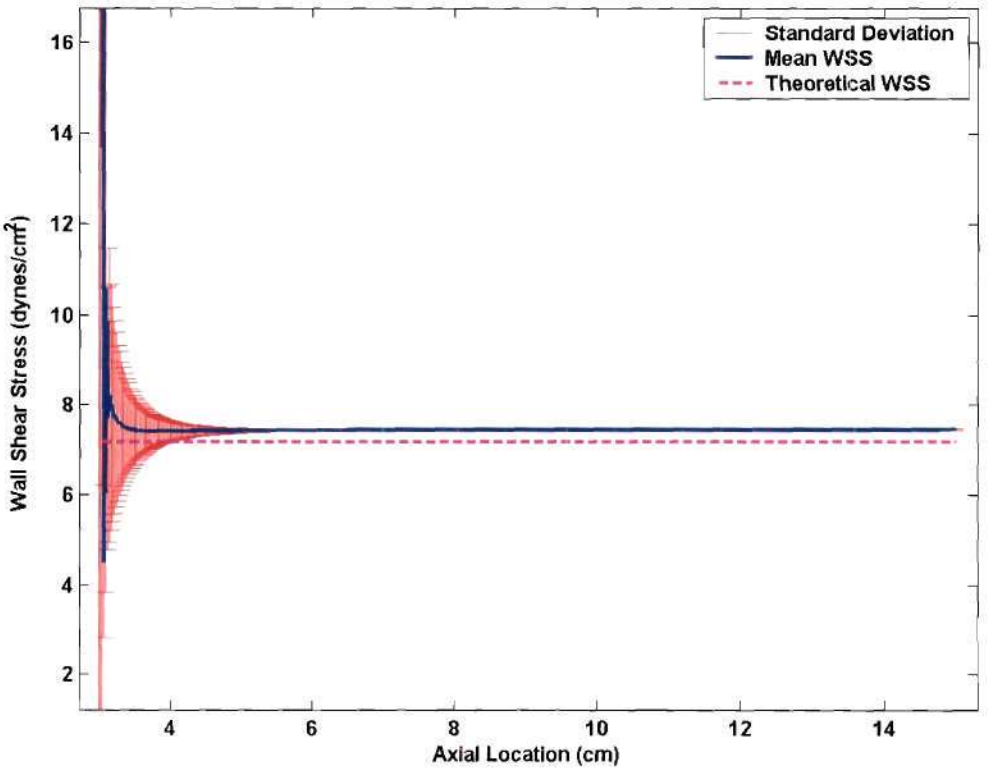

Figure 3.47: 0.0% stenosis average flow rate ideal geometry with PC-MRI derived boundary conditions WSS graph.

0.0% Stenosis Geometry / Peak Flow Rate

The PC-MRI derived inlet velocity profile for the 0.0% stenosis model under peak flow rate conditions is shown in Figure 3.48. The overall shape of the velocity profile illustrated in Figure 3.48a was parabolic which was expected for all of the models due to the long entrance length tubing used in the MRI flow loop. The maximum velocity was approximately 70 cm/sec, which was lower than the theoretical values of 83.2 cm/sec. This velocity profile was applied to the CFD entrance region computational grid. The velocities along the perimeter were then assigned a zero velocity to satisfy the no-slip boundary condition at the wall. Therefore, large near-wall velocity gradients were present since the near-wall velocity values are not uniformly zero. Figure 3.48b illustrates which nodes on the entrance region computational grid were assigned negative velocities based on the interpolation of the PC-MRI measured velocities. As compared to the average flow rate case, a larger number of near-wall velocity values were negative.

The 2D WSS graph for the 0.0% stenosis under average flow rates conditions is illustrated in Figure 3.49. Large negative WSS values were seen in the entrance region of the model. These were attributed to the large velocity gradients caused by employing the no-slip boundary condition to non-zero near-wall velocity values. These large entrance WSS values are also illustrated in the 3D WSS graph shown in Figure 3.50b. These WSS values dissipated further down stream as seen by the converging mean WSS value and the decreasing standard deviation magnitude. However, this process occurred over a longer axial distance compared to the average flow rate case. The mean WSS value distal to the entrance effects was 14.62 dynes/cm^2. This represented a 30.2% error relative to the theoretical WSS value of 20.96 dynes/cm^2. The large near-wall negative velocity

errors were thought to have reduced the overall flow rate recorded from the PC-MRI data effectively reducing the average WSS value. For steady laminar flow of a Newtonian fluid through a smooth straight cylindrical geometry, the relationship between the flow rate and the WSS is direct and linear.

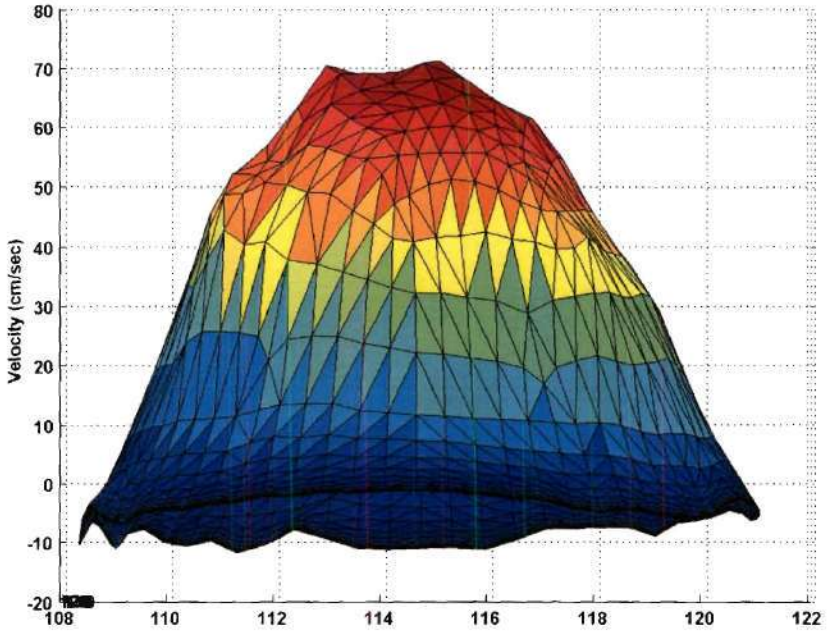

(a) PC-MRI derived entrance velocity profile.

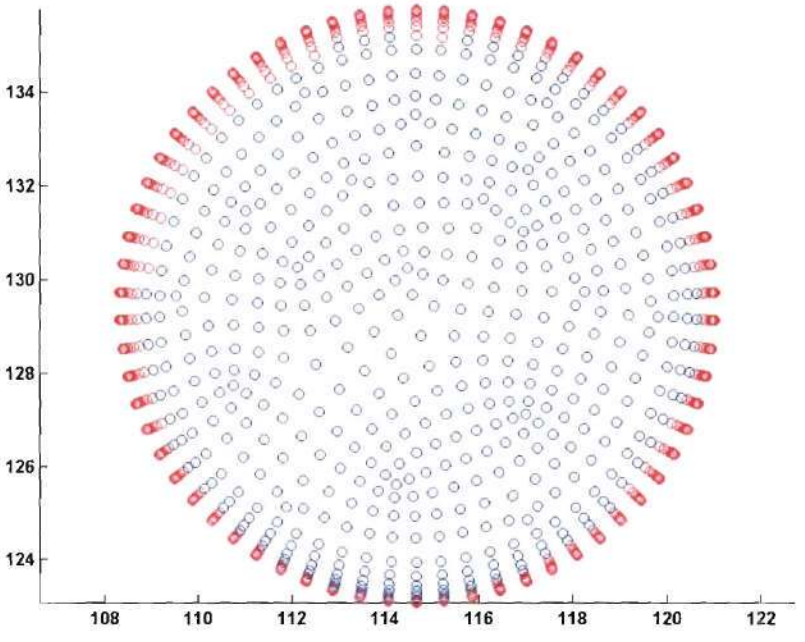

(b) negative velocities assigned to the entrance region computational grid are shown in red.

Figure 3.48: 0.0% stenosis peak flow rate entrance boundary condition velocity profiles.

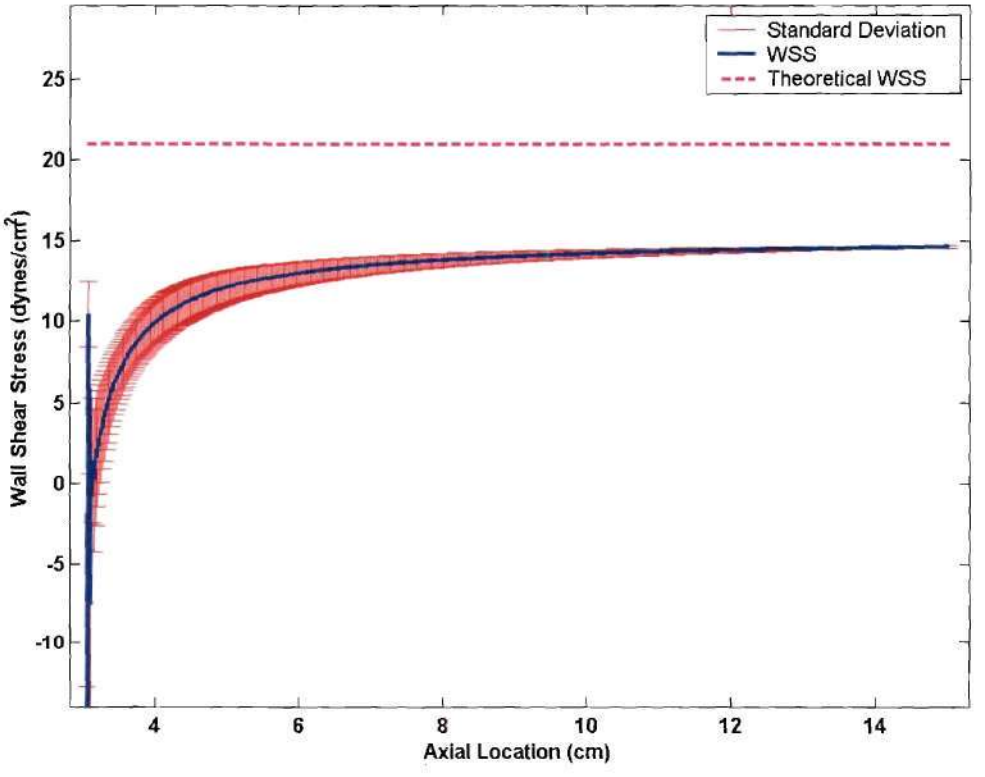

Figure 3.49: 0.0% stenosis peak flow rate ideal geometry with PC-MRI derived boundary conditions WSS graph.

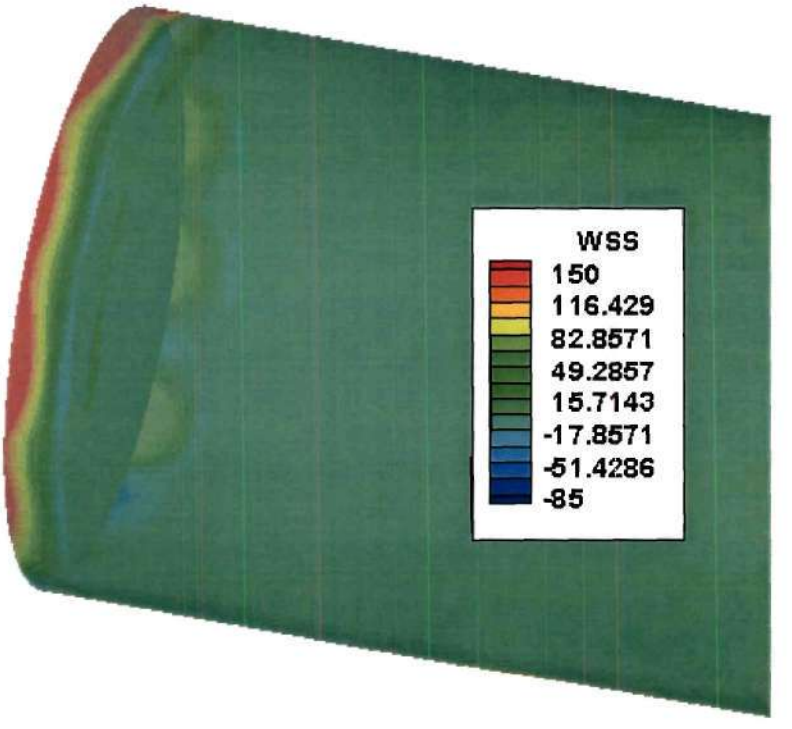

(a) average flow rate

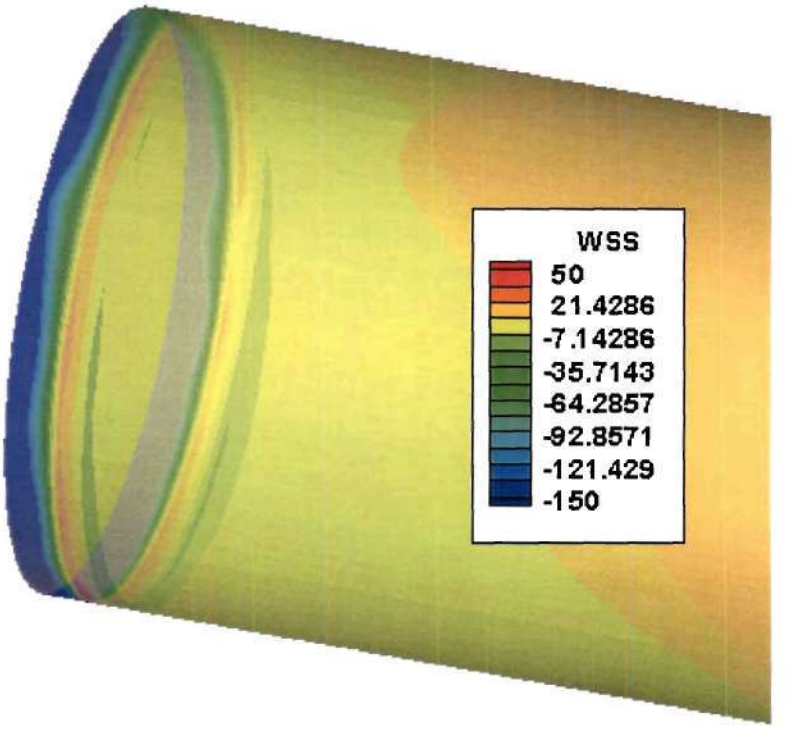

(b) peak flow rate

Figure 3.50: 3D entrance WSS contour plots for 0.0% stenosis models at (a) average and (b) peak flow rate. Ideal geometry and PC-MRI derived entrance boundary conditions.

52.7% Stenosis Geometry / Average Flow Rate

The PC-MRI derived inlet velocity profile for the 52.7% stenosis model under average flow rate conditions is shown in Figure 3.51. The velocity profile had a parabolic shape. The maximum velocity was approximately 27 cm/sec, which was close to the theoretical value of 28.4 cm/sec. Near-wall velocity values were both positive and negative. The 2D WSS graphs are shown in figure 3.52. The axial location of the maximum stenosis agreed with the gold standard WSS values. The average WSS located far from the stenosis proximally and distally was slightly lower than the gold standard values. The maximum WSS was 49.36 dynes/cm^2, which represented a 20.9% underestimation of the gold standard value, 62.43 dynes/cm^2. The minimum WSS value was –2.05 dynes/cm^2, which represented a 36.1% overestimation of the gold standard value of –2.80 dynes/cm^2 (see Table 3.2). Three-dimensional WSS contour graphs are shown in Figure 3.53 with the corresponding recirculation WSS contour graphs shown in Figure 3.54. The WSS patterns were similar to the gold standard data. The separation and reattachment points were located 0.22cm and 0.78cm distal to the maximum stenosis, respectively. The length of the recirculation region was 0.56cm, which was shorter compared to the gold standard recirculation region (see Table 3.2).

	Average Flow Rate Gold Standard	Average Flow Rate PC-MRI Boundary Conditions	Peak Flow Rate Gold Standard	Peak Flow Rate PC-MRI Boundary Conditions
Maximum WSS (dynes/cm^2) [% error]	62.43	49.36 [-20.9%]	280.79	138.07 [-50.8]
Minimum WSS (dynes/cm^2) [% error]	-2.80	-2.05 [36.1%]	-17.87	-6.58 [63.2]
Separation Point (cm distal to stenosis)	0.21	0.22	0.14	0.17
Reattachment Point (cm distal to stenosis)	0.88	0.78	2.07	1.49
Recirculation Length (cm)	0.67	0.56	1.93	1.32

Table 3.2: 52.7% stenosis average and peak flow rate data summary comparing gold standard values to CFD results using ideal geometries and inlet boundary conditions derived from PC-MRI velocity data. Negative percent errors refer to under estimations while positive errors refer to over estimations.

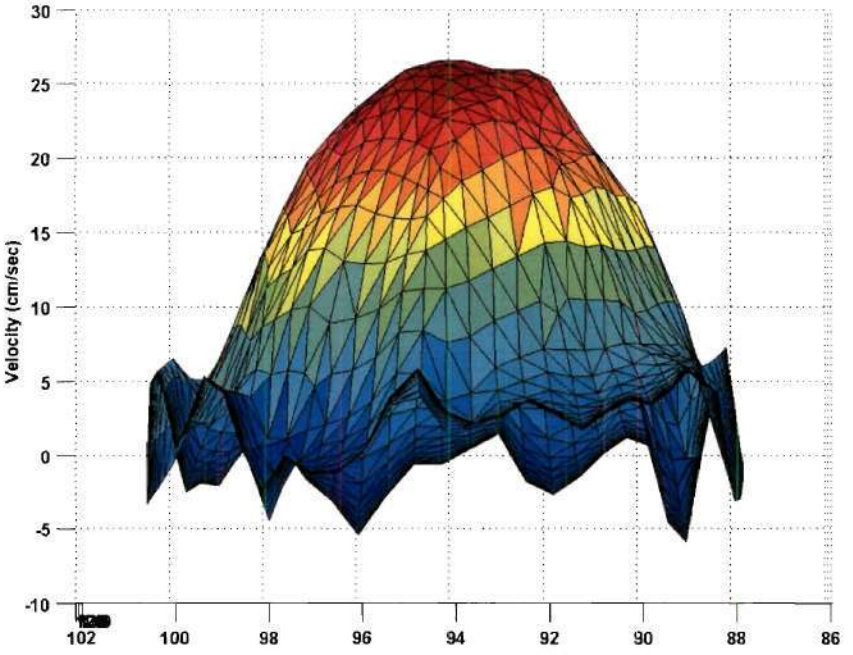

(a) PC-MRI derived entrance velocity profile.

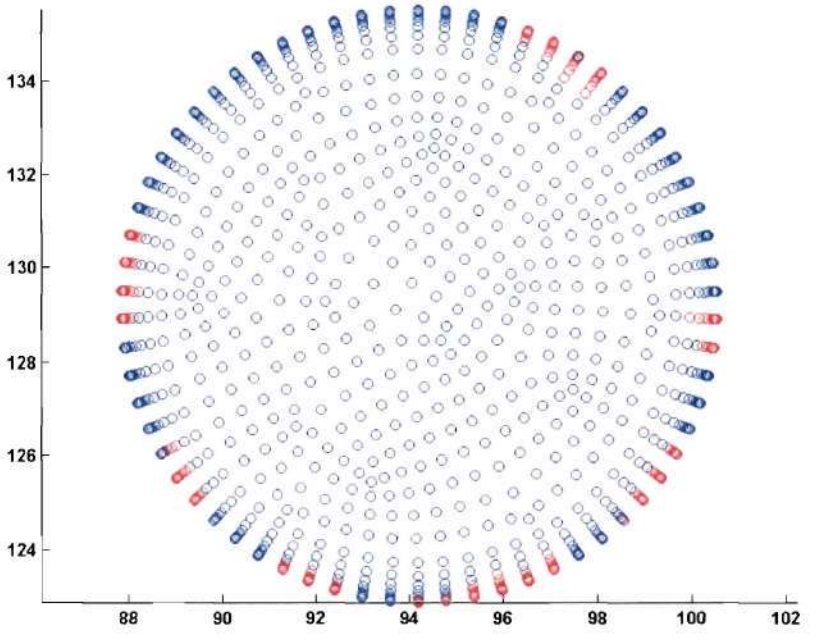

(b) negative velocities assigned to the entrance region computational grid are shown in red.

Figure 3.51: 52.7% stenosis average flow rate entrance boundary condition velocity profiles.

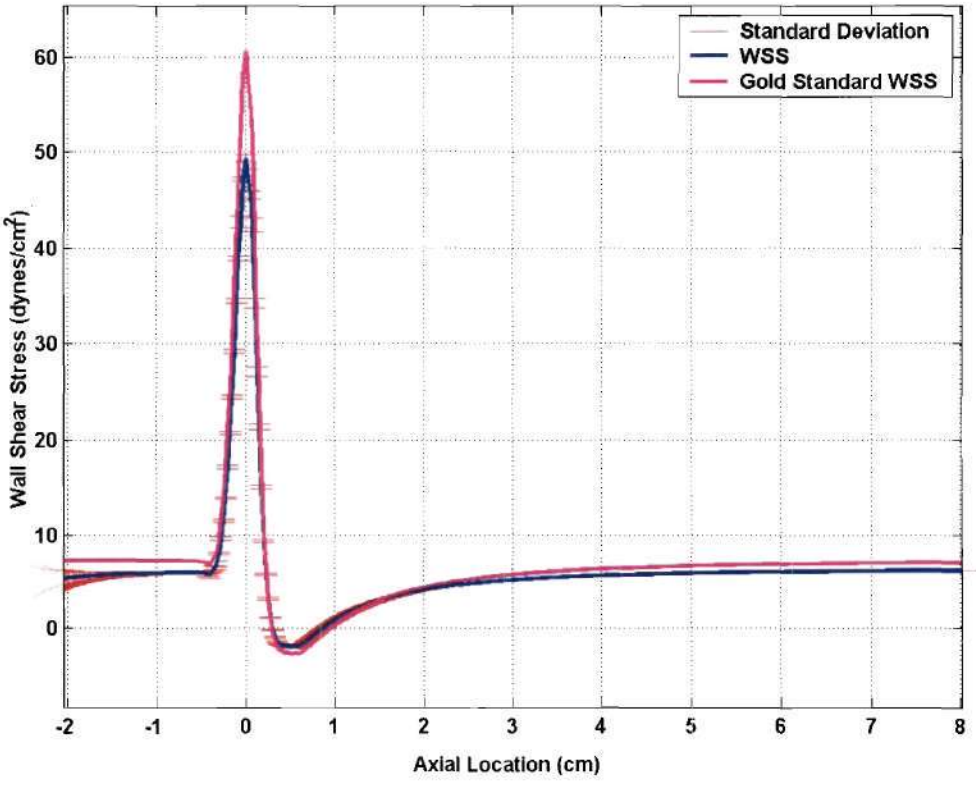

(a) 2D WSS graph

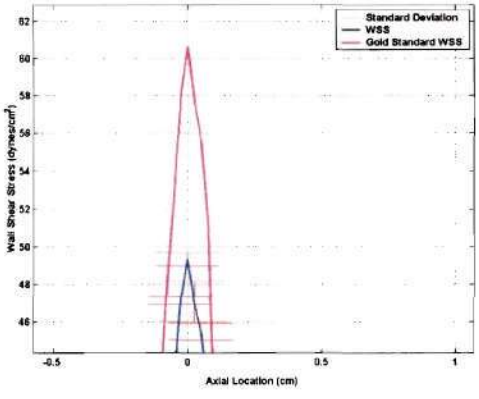

(b) maximum WSS

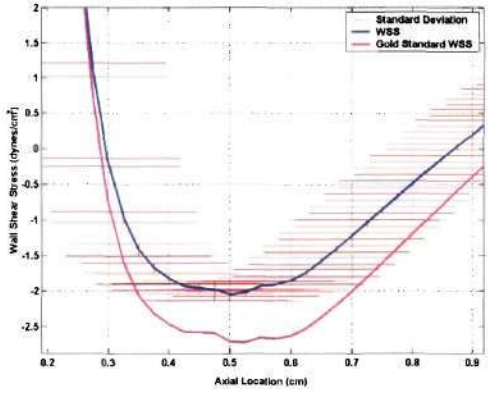

(c) minimum WSS

Figure 3.52: 52.7% stenosis average flow rate ideal geometry with PC-MRI derived boundary conditions WSS graph (a) entire axial WSS graph (b) maximum WSS and (c) minimum WSS.

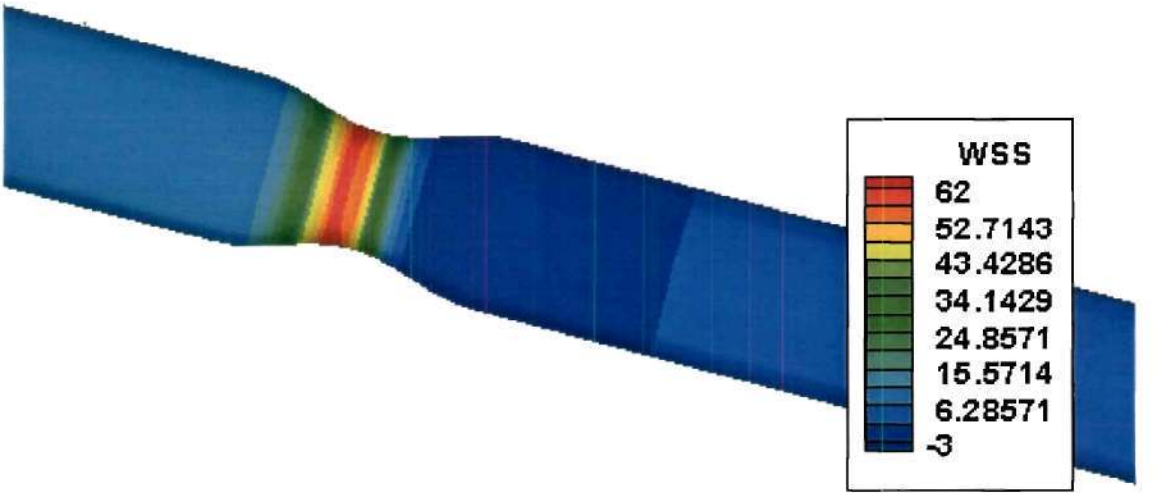

(a) gold standard (ideal geometry and ideal boundary conditions).

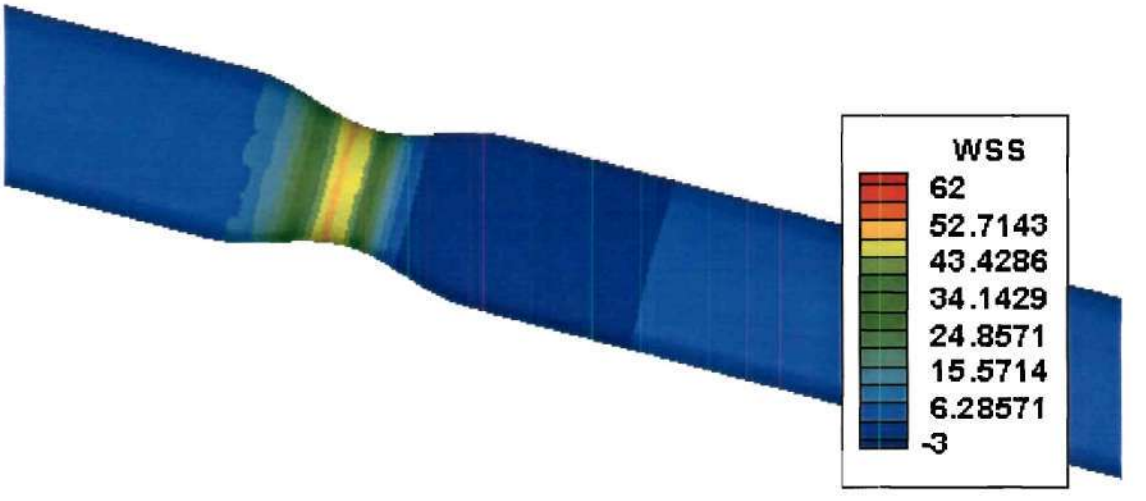

(b) Ideal geometry / PC-MRI derived boundary conditions.

Figure 3.53: 52.7% stenosis average flow rate 3D WSS contour graphs.

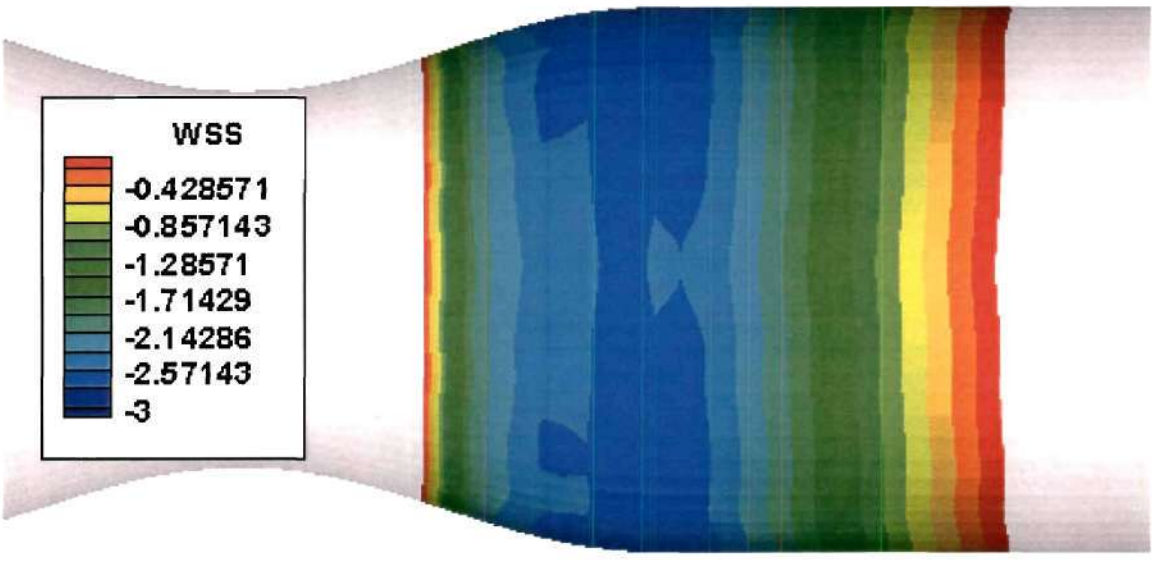

(a) gold standard (ideal geometry and ideal boundary conditions).

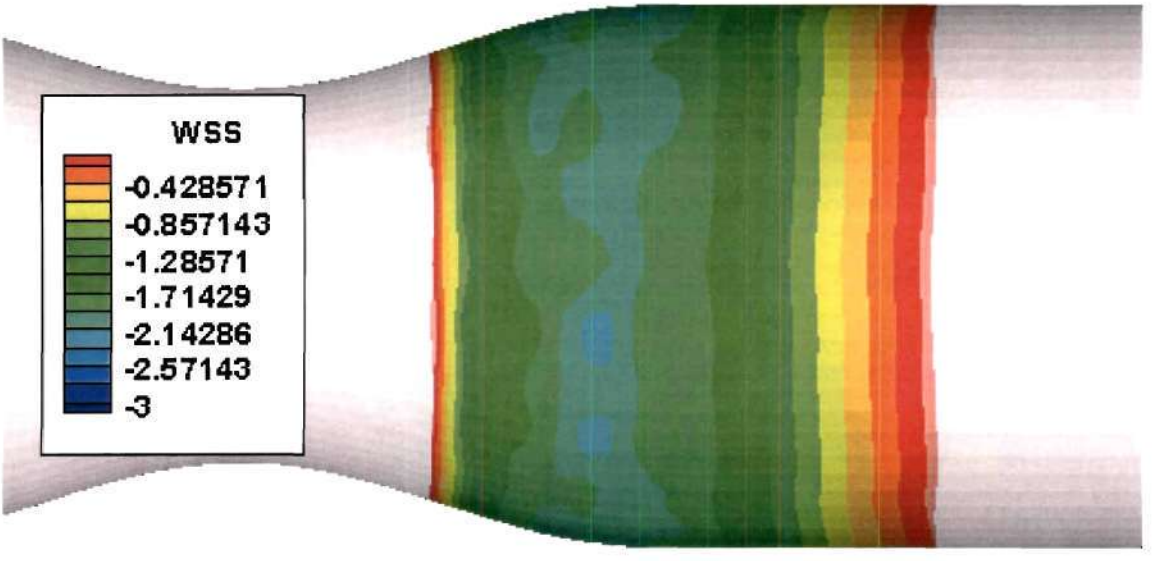

(b) Ideal geometry / PC-MRI derived boundary conditions.

Figure 3.54: 52.7% stenosis average flow rate 3D recirculation WSS contour graphs.

52.7% Stenosis Geometry / Peak Flow Rate

The PC-MRI derived inlet velocity profile for the 52.7% stenosis model under peak flow rate conditions is shown in Figure 3.55. The velocity profile had a parabolic shape. The maximum velocity was approximately 72 cm/sec, which was less than the theoretical value of 83.2 cm/sec. Near-wall velocity values were almost entirely negative. The 2D WSS graphs are shown in figure 3.56. The axial location of the maximum stenosis agreed with the gold standard WSS values. The average WSS located far from the stenosis proximally and distally was lower than the gold standard values. The maximum WSS was 138.07 dynes/cm^2, which represented a 50.8% underestimation of the gold standard value, 280.79 dynes/cm^2. The minimum WSS value was –6.58 dynes/cm^2, which represented a 63.2% overestimation of the gold standard value of –17.87 dynes/cm^2 (see Table 3.2). Three-dimensional WSS contour graphs are shown in Figure 3.57 with the corresponding recirculation WSS contour graphs shown in Figure 3.58. The WSS patterns were similar to the gold standard data. The separation and reattachment points were located 0.17cm and 1.49cm distal to the maximum stenosis, respectively. The length of the recirculation region was 1.32cm, which was much shorter, compared to the gold standard recirculation region (see Table 3.2).

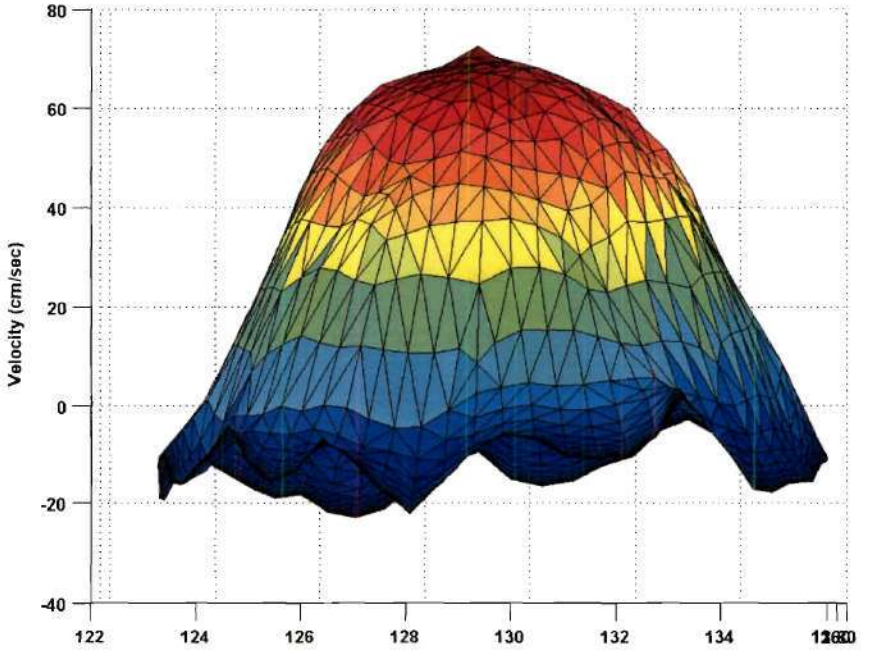

(a) PC-MRI derived entrance velocity profile.

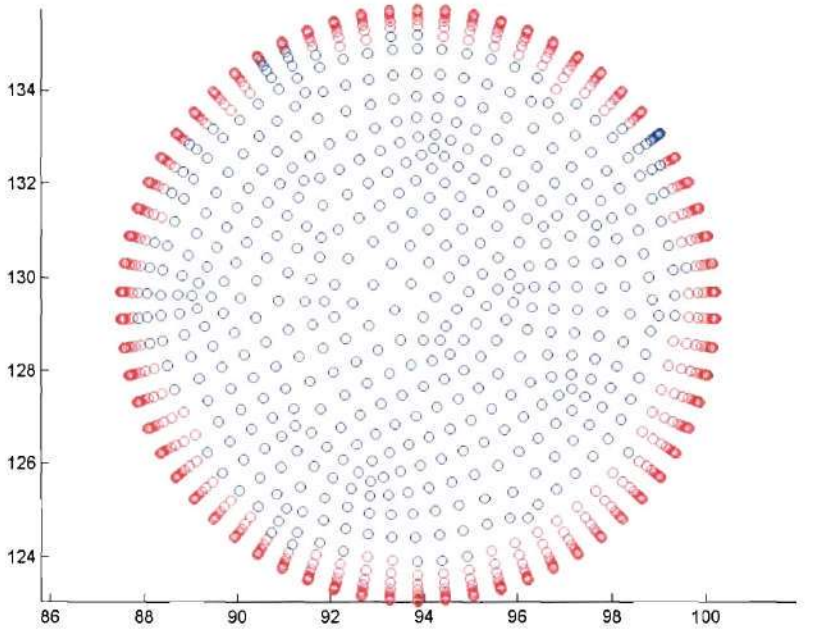

(b) negative velocities assigned to the entrance region computational grid are shown in red.

Figure 3.55: 52.7% stenosis peak flow rate entrance boundary condition velocity profiles.

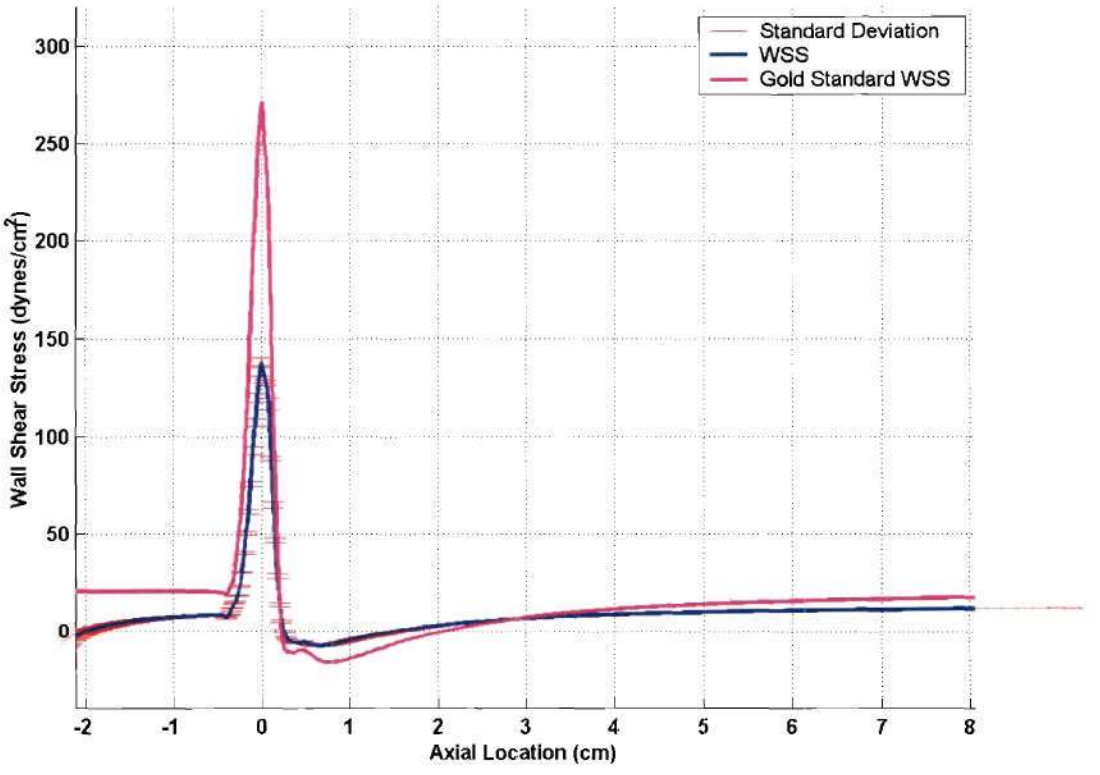

(a) 2D WSS graph

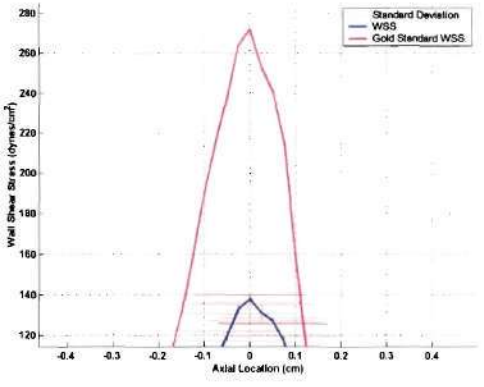

(b) maximum WSS

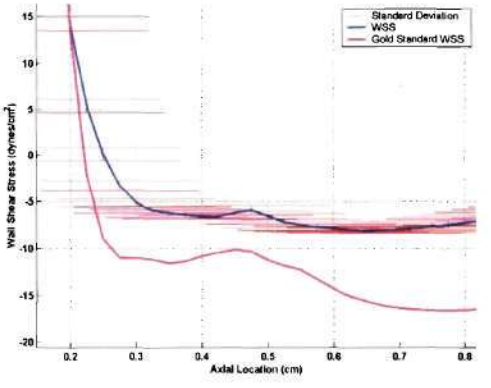

(c) minimum WSS

Figure 3.56: 52.7% stenosis peak flow rate ideal geometry with PC-MRI derived boundary conditions WSS graph (a) entire axial WSS graph (b) maximum WSS and (c) minimum WSS.

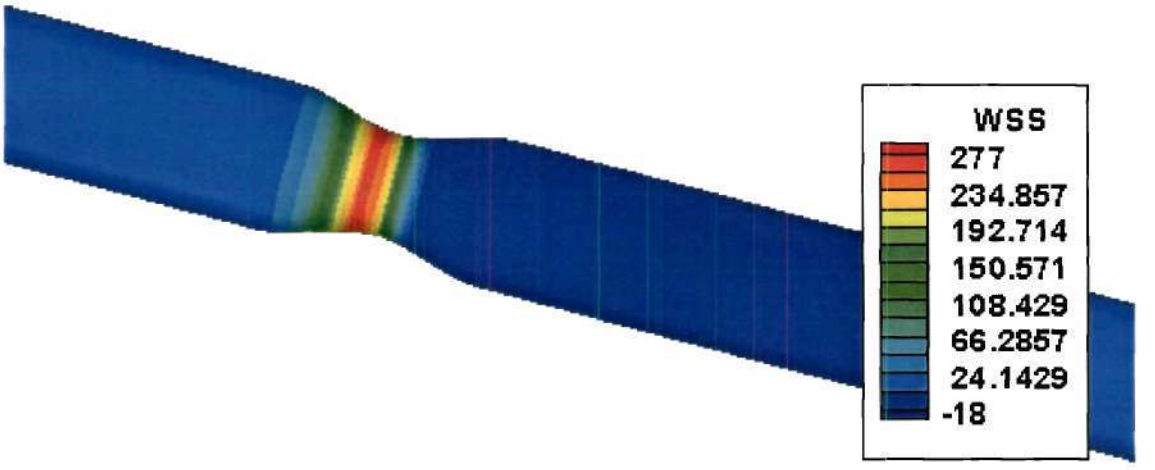

(a) gold standard (ideal geometry and ideal boundary conditions).

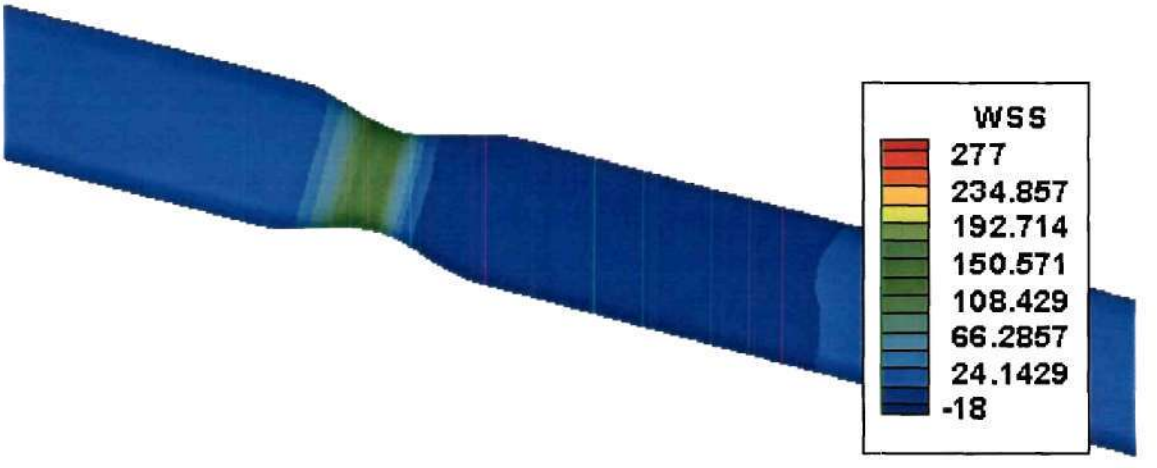

(b) Ideal geometry / PC-MRI derived boundary conditions.

Figure 3.57: 52.7% stenosis peak flow rate 3D WSS contour graphs.

(a) gold standard (ideal geometry and ideal boundary conditions).

(b) Ideal geometry / PC-MRI derived boundary conditions.

Figure 3.58: 52.7% stenosis peak flow rate 3D recirculation WSS contour graphs.

75.0% Stenosis Geometry / Average Flow Rate

The PC-MRI derived inlet velocity profile for the 75.0% stenosis model under average flow rate conditions is shown in Figure 3.59. The velocity profile had a parabolic shape. The maximum velocity was approximately 27 cm/sec, which was close to the theoretical value of 28.4 cm/sec. Near-wall velocity values are mostly positive. The 2D WSS graphs are shown in Figure 3.60. The axial location of the maximum stenosis agreed with the gold standard WSS values. The average WSS located far from the stenosis proximally and distally was slightly lower than the gold standard values. The maximum WSS was 175.27 dynes/cm^2, which represented a 10.7% underestimation of the gold standard value, 196.35 dynes/cm^2. The minimum WSS value was –7.32 dynes/cm^2, which represented a 21.6% overestimation of the gold standard value of –9.34 dynes/cm^2 (see Table 3.3). Three-dimensional WSS contour graphs are shown in Figure 3.61 with the corresponding recirculation WSS contour graphs shown in Figure 3.62. The WSS patterns were similar to the gold standard data. The separation and reattachment points were located 0.12cm and 3.55cm distal to the maximum stenosis, respectively. The length of the recirculation region was 3.43cm, which was slightly shorter, compared to the gold standard recirculation region (see Table 3.3).

	Average Flow Rate Gold Standard	Average Flow Rate PC-MRI Boundary Conditions
Maximum WSS (dynes/cm^2) [% error]	196.35	175.27 [-10.7%]
Minimum WSS (dynes/cm^2) [% error]	-9.34	-7.32 [21.6%]
Separation Point (cm distal to stenosis)	0.12	0.12
Reattachment Point (cm distal to stenosis)	3.68	3.55
Recirculation Length (cm)	3.50	3.43

Table 3.3: 75.0% stenosis average flow rate data summary comparing gold standard values to CFD results using ideal geometries and inlet boundary conditions derived from PC-MRI velocity data. Negative percent errors refer to under estimations while positive errors refer to over estimations.

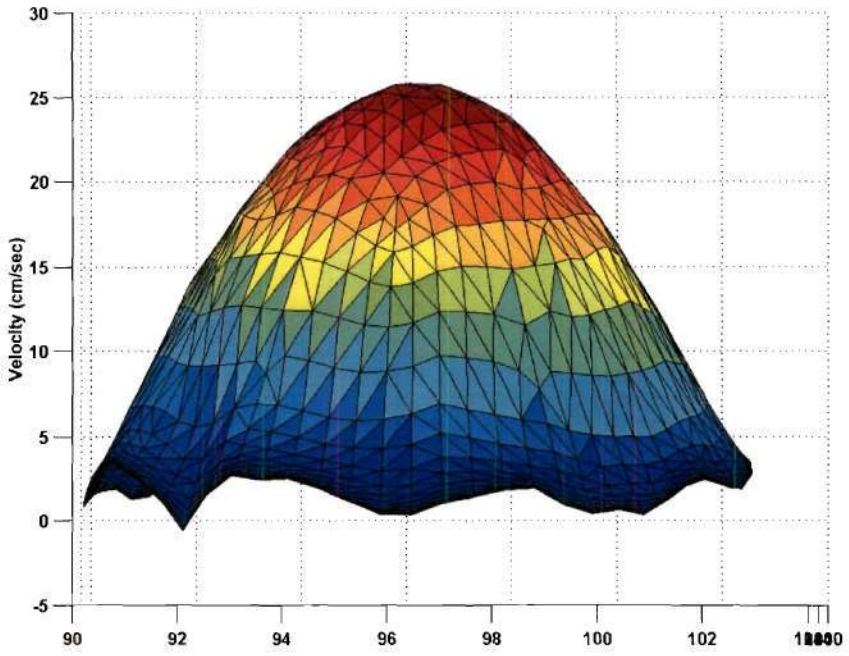

(a) PC-MRI derived entrance velocity profile.

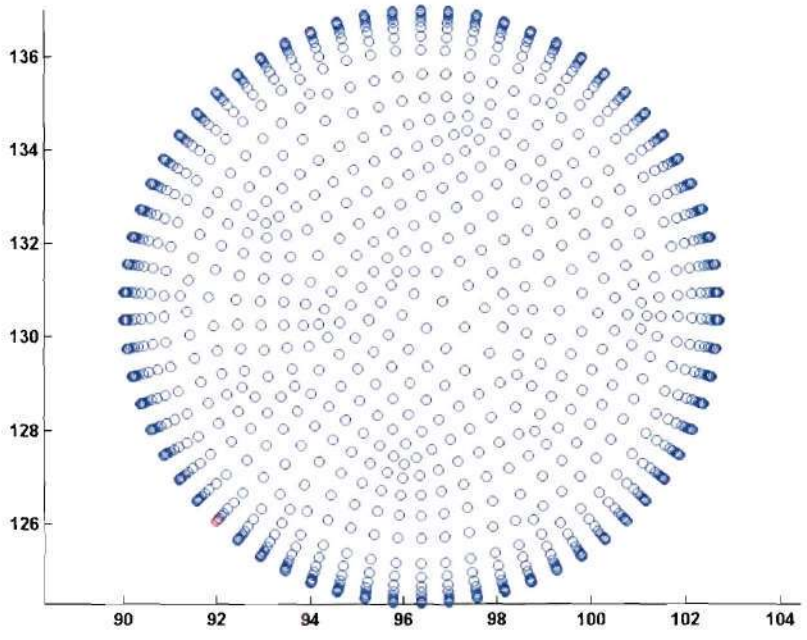

(b) negative velocities assigned to the entrance region computational grid are shown in red.

Figure 3.59: 52.7% stenosis average flow rate entrance boundary condition velocity profiles.

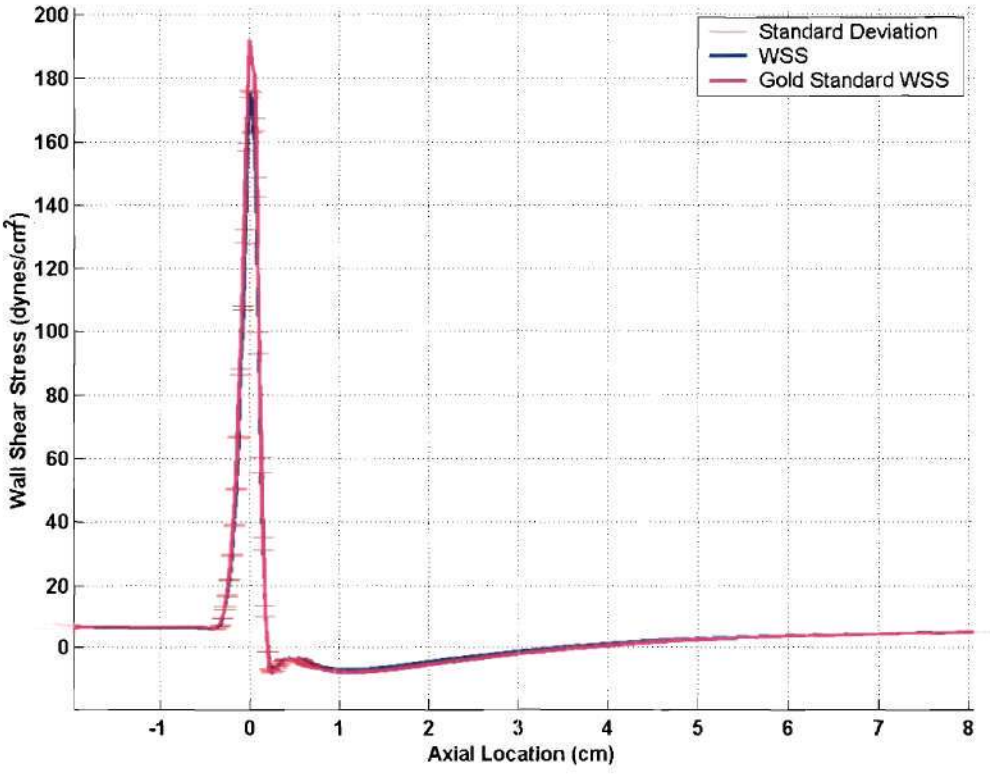

(a) 2D WSS graph.

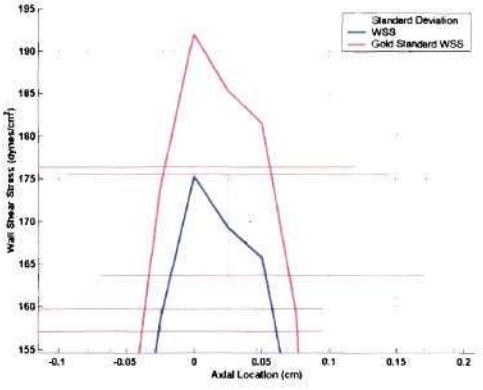

(b) maximum WSS

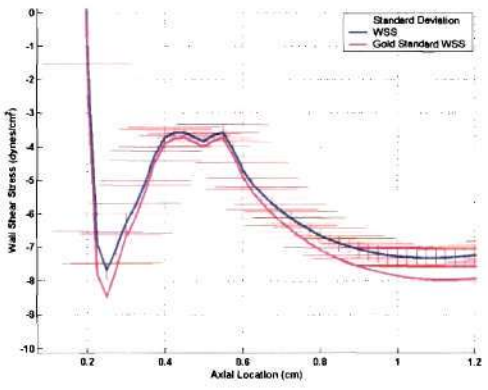

(c) minimum WSS

Figure 3.60: 75.0% stenosis average flow rate ideal geometry with PC-MRI derived boundary conditions WSS graph (a) entire axial WSS graph (b) maximum WSS and (c) minimum WSS.

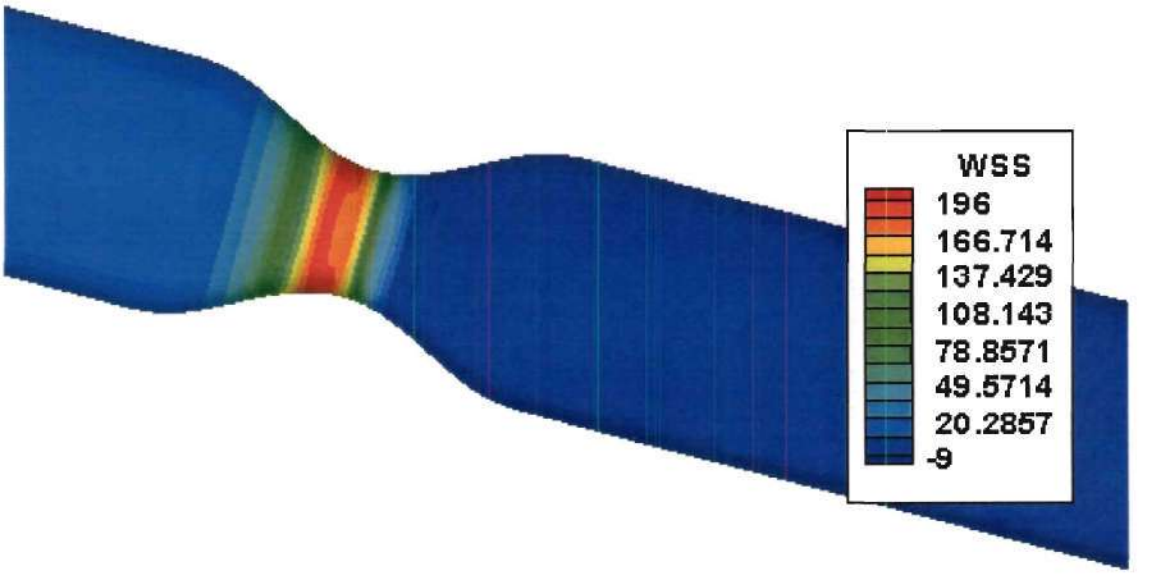

(a) gold standard (ideal geometry and ideal boundary conditions).

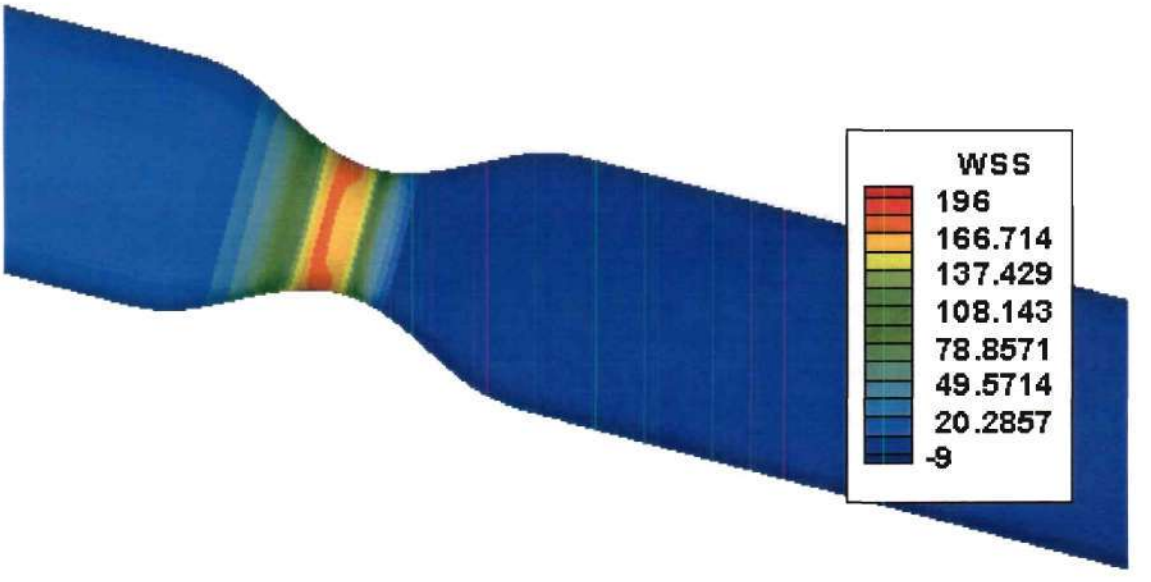

(b) Ideal geometry / PC-MRI derived boundary conditions.

Figure 3.61: 75.0% stenosis average flow rate 3D WSS contour graphs.

(a) gold standard (ideal geometry and ideal boundary conditions).

(b)Ideal geometry / PC-MRI derived boundary conditions.

Figure 3.62: 75.0% stenosis average flow rate 3D recirculation WSS contour graphs.

CFD Simulations - MRI Derived Geometries

0.0% Stenosis Geometry – Average Flow Rate

The PC-MRI derived inlet velocity profile is illustrated in Figure 3.63. Although the same PC-MRI data were used to reconstruct the inlet velocity profile shown in Figure 3.46, a different inlet velocity profile was created due to the different computational grid and inlet geometry created from the MRI geometry data. The resulting WSS profiles are shown in Figure 3.64. All eight axial WSS profiles illustrated the variability associated with the WSS data. Since the geometry was symmetrical and the inlet flow conditions were fully developed, due to the sufficiently long entrance tubing, all eight axial WSS profiles should have been equal. However, wide variations in WSS between the eight profiles were observed including variations of over 14 dynes/cm^2 (Figure 3.64b). The eight axial WSS profiles were averaged to obtain mean WSS values and standard deviations. The large standard deviations observed in Figure 3.65a also illustrate the large variation in WSS data. The mean WSS values were neither entirely above nor below the theoretical value of 7.16 dynes/cm^2. When the idealized boundary conditions were used on the same MRI derived geometry, the same variations and high standard deviations in WSS were observed (Figures 3.65b and 3.66). These variations were therefore contributed to the irregularities associated with geometry reconstructed from the MRI images. The same similarities in WSS distribution were observed in the 3D WSS contour graphs (Figure 3.67).

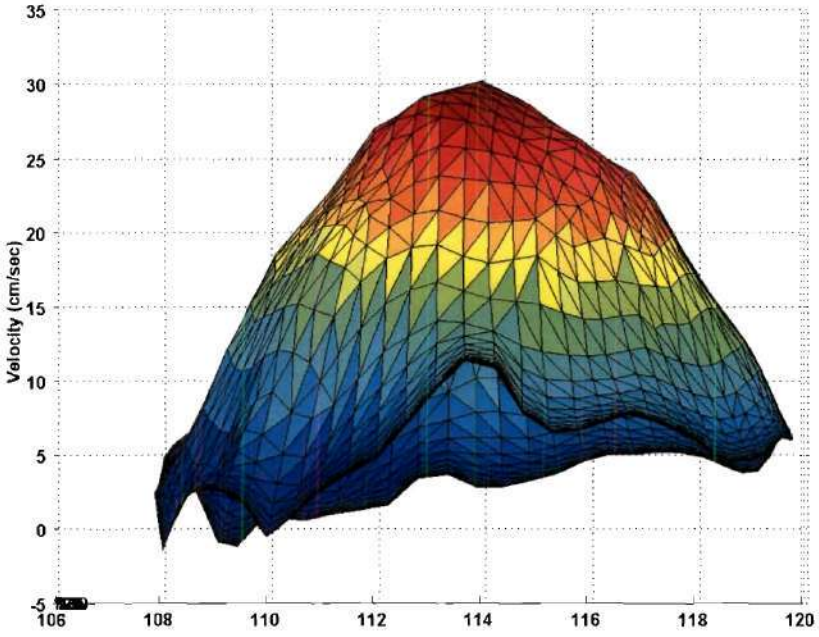

(a) PC-MRI derived inlet velocity profile

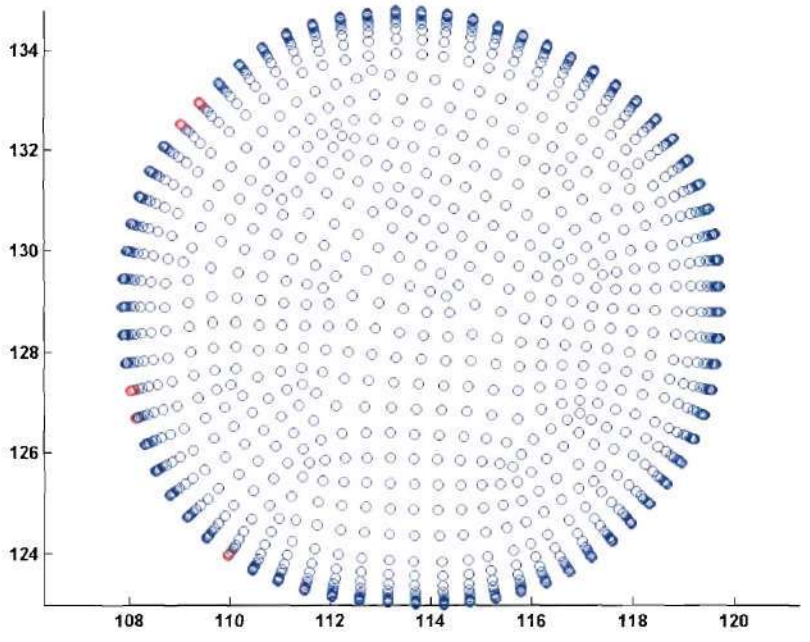

(b) negative velocities assigned to the entrance region computational grid are shown in red.

Figure 3.63: 0.0% stenosis average flow rate entrance boundary condition velocity profile applied to the MRI derived geometry.

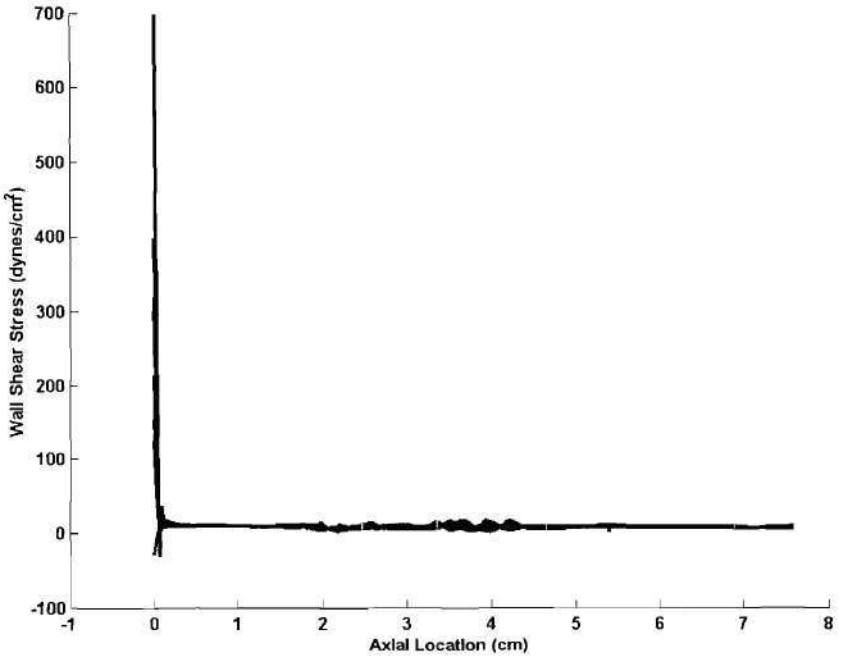

(a) total WSS graph.

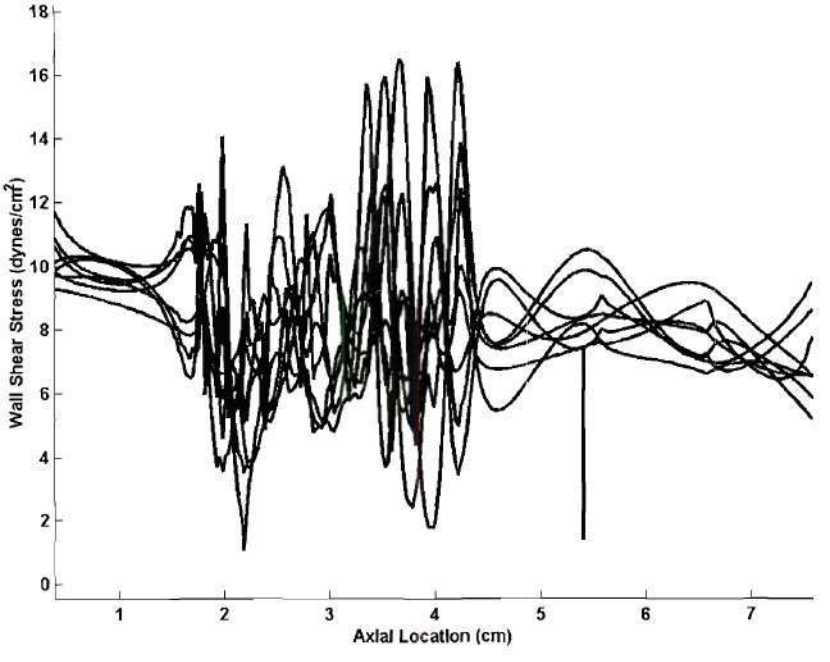

(b) close-up WSS graph.

Figure 3.64: 0.0% stenosis average flow rate MRI geometry and boundary conditions. WSS graphs along eight equally spaced (in the angular direction) axial lines.

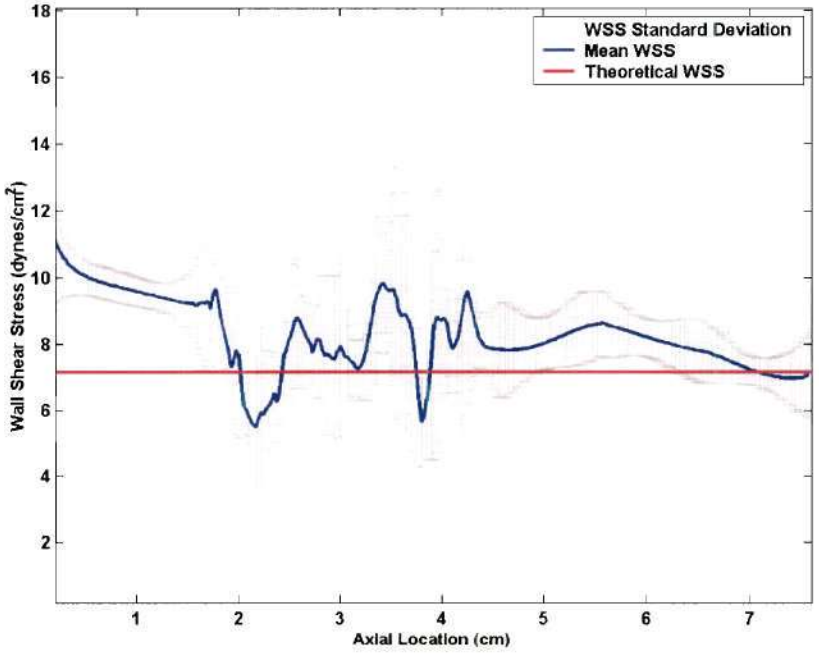

(a) MRI derived geometry and PC-MRI derived boundary conditions

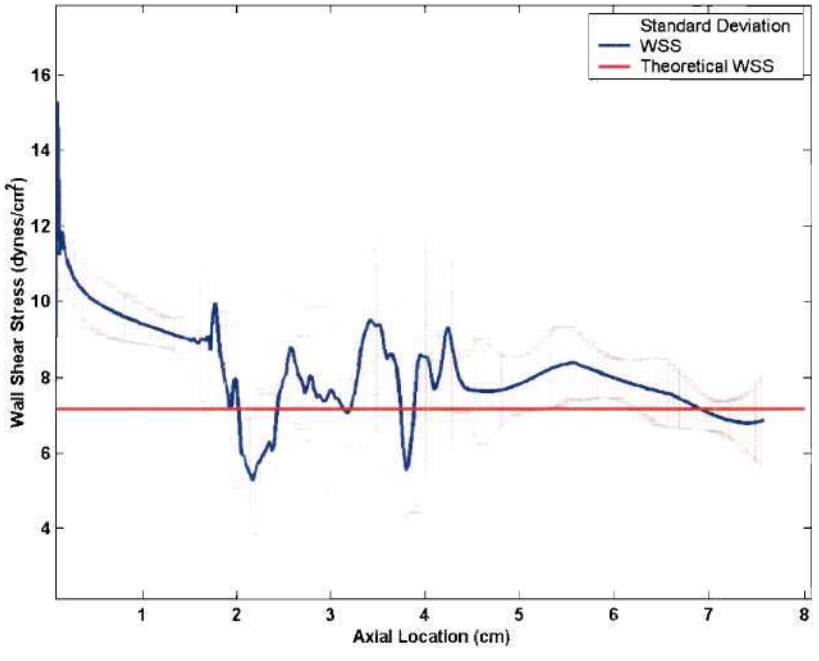

(b) MRI derived geometry and idealized boundary conditions.

Figure 3.65: 0.0% stenosis average flow rate mean WSS graphs using MRI derived geometries with (a) PC-MRI derived inlet boundary conditions and (b) idealized inlet boundary conditions.

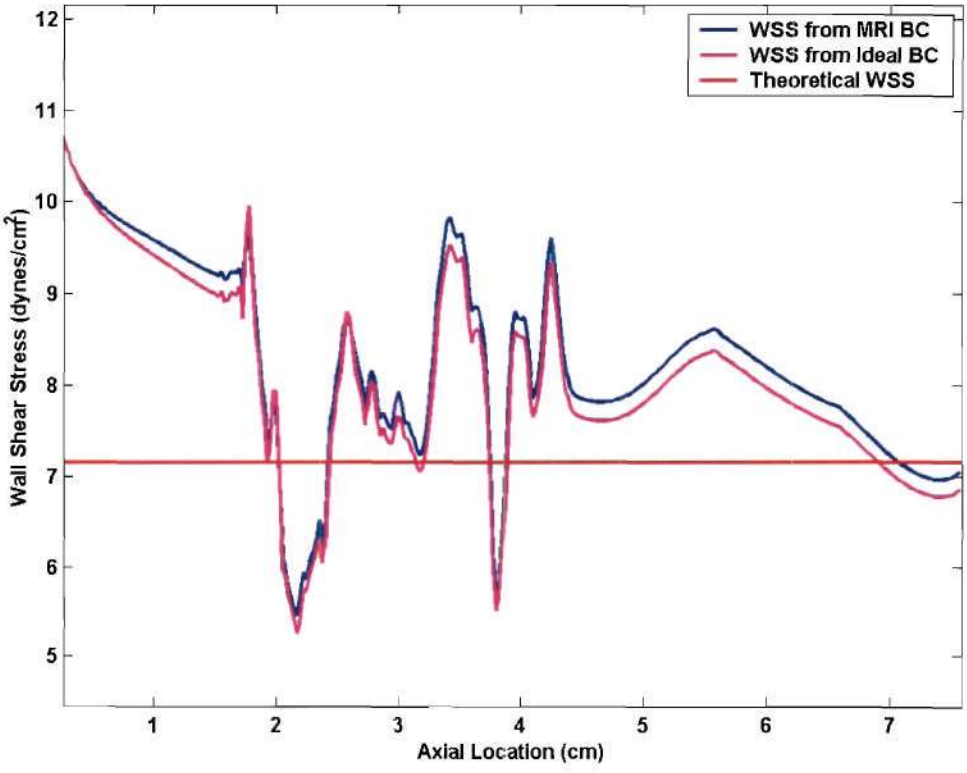

Figure 3.66: 0.0% stenosis average flow rate WSS graph comparing the PC-MRI and idealized inlet boundary conditions.

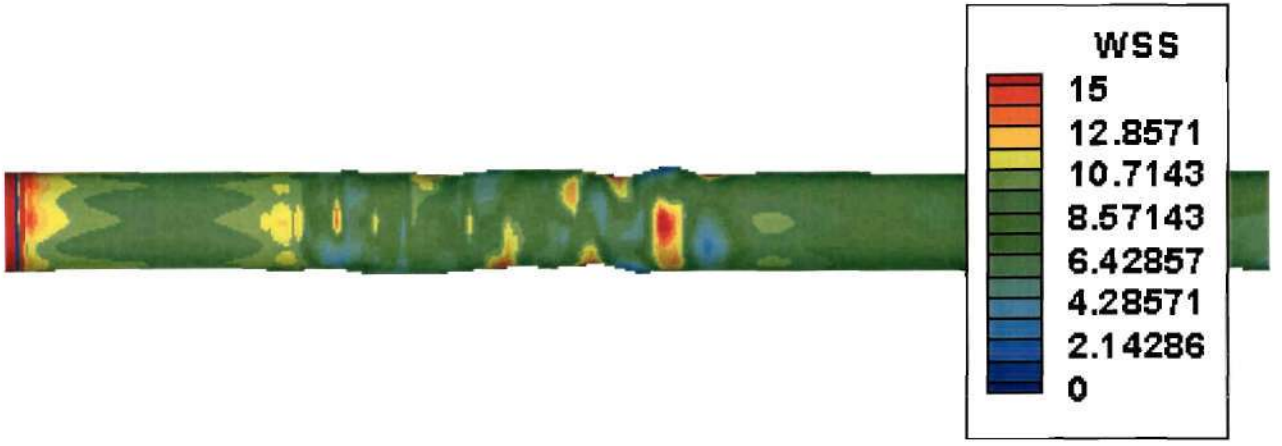

(a) PC-MRI derived inlet boundary conditions.

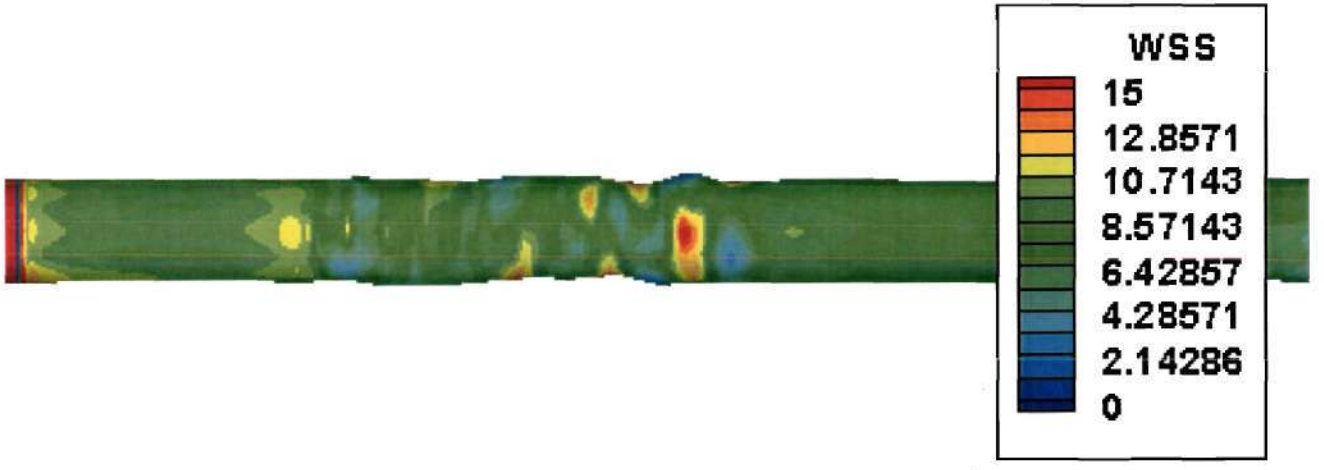

(b) idealized inlet boundary conditions.

Figure 3.67: 3D WSS contour graphs of the 0.0% stenosis model under average flow rate conditions. Geometries reconstructed from MRI images with (a) PC-MRI derived and (b) idealized inlet boundary conditions.

0.0% Stenosis Geometry – Peak Flow Rate

The PC-MRI derived inlet velocity profile is illustrated in Figure 3.68. Although the same PC-MRI data were used to reconstruct the inlet velocity profile shown in Figure 3.68, a different inlet velocity profile was created due to the different computational grid and inlet geometry created from the MRI geometry data. However, the same near-wall negative velocities were observed. The resulting WSS profiles are shown in Figure 3.69. All eight axial WSS profiles illustrated the variability associated with the WSS data. Since the geometry was symmetrical and the inlet flow conditions were fully developed, due to the sufficiently long entrance tubing, all eight axial WSS profiles should have been equal. However, wide variations in WSS between the eight profiles were observed including variations of over 30 dynes/cm^2 (Figure 3.69b).

The eight axial WSS profiles were averaged to obtain mean WSS values and standard deviations. The large standard deviations observed in Figure 3.70a also illustrate the large variation in WSS data. The mean WSS values were all less than the theoretical value of 20.96 dynes/cm^2. This was caused by the overall reduction in volumetric flow rate caused by the near-wall negative velocities observed in the inlet velocity profile. When the idealized boundary conditions were used on the same MRI derived geometry, the same variations and high standard deviations in WSS were observed (Figures 3.70b and 3.71). These variations were therefore contributed to the irregularities associated with geometry reconstructed from the MRI images. However, the mean WSS values better approximated the theoretical WSS value. The same similarities in WSS distribution were observed in the 3D WSS contour graphs (Figure 3.72). The overall

WSS values were higher for the idealized inlet velocity profile compared to the PC-MRI derived inlet velocity profile.

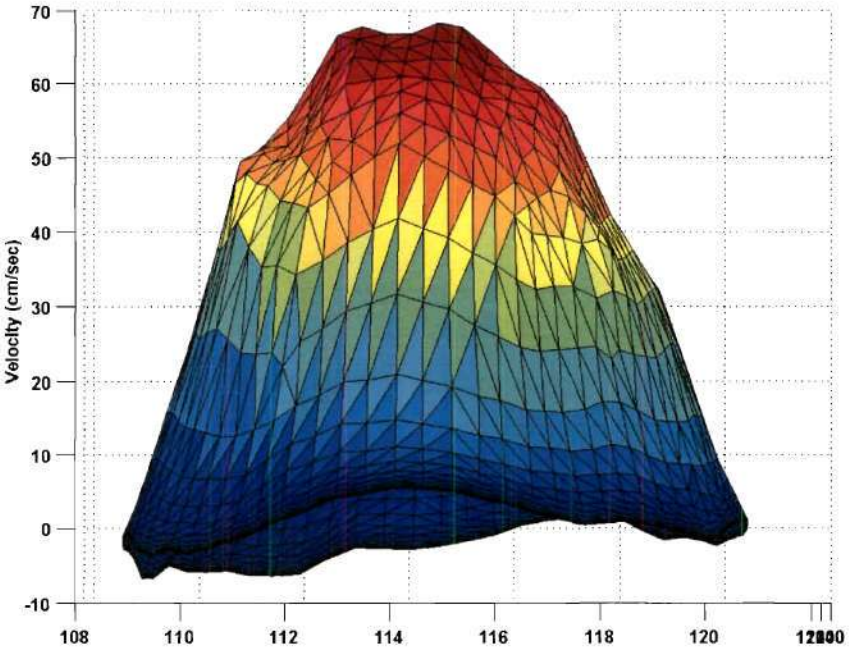

(a) PC-MRI derived inlet velocity profile

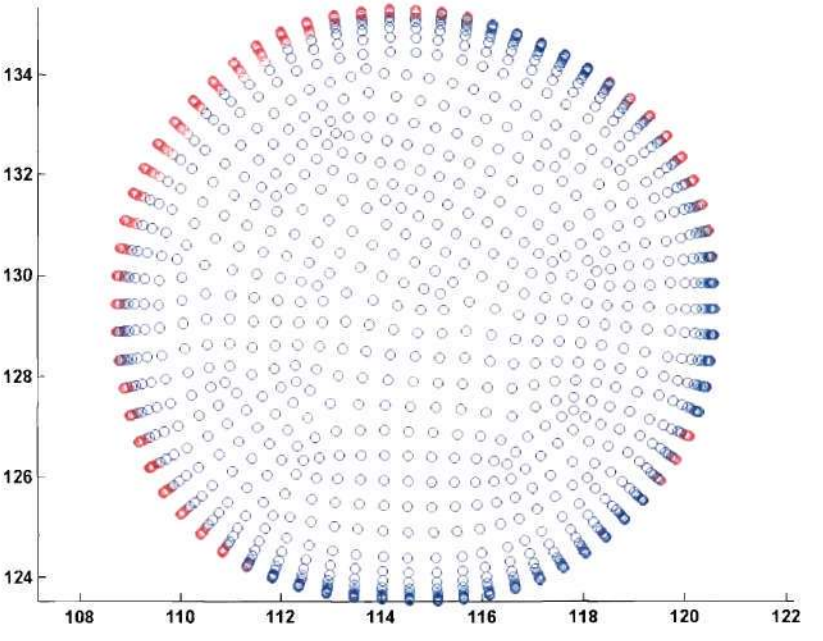

(b) negative velocities assigned to the entrance region computational grid are shown in red.

Figure 3.68: 0.0% stenosis peak flow rate entrance boundary condition velocity profile applied to the MRI derived geometry.

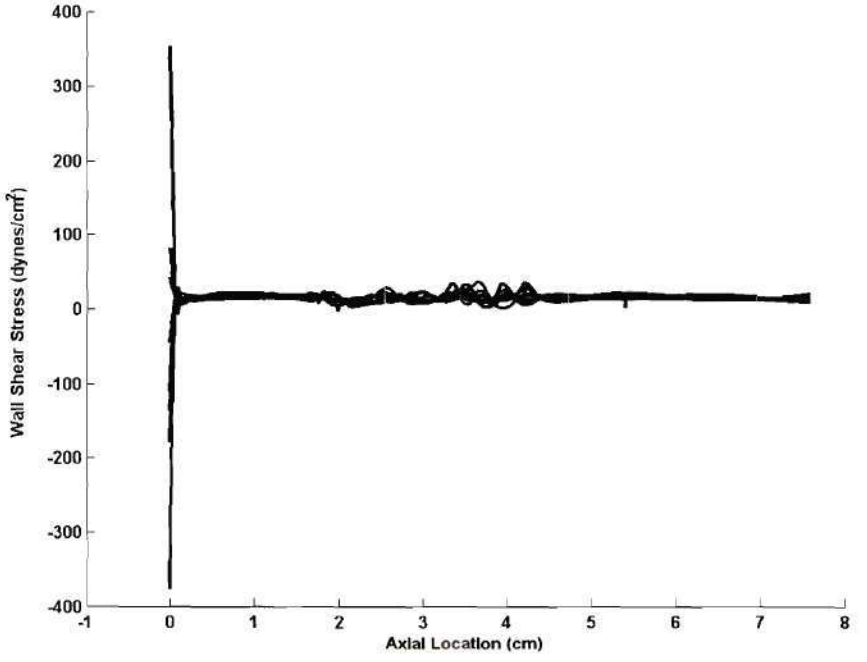

(a) total WSS graph.

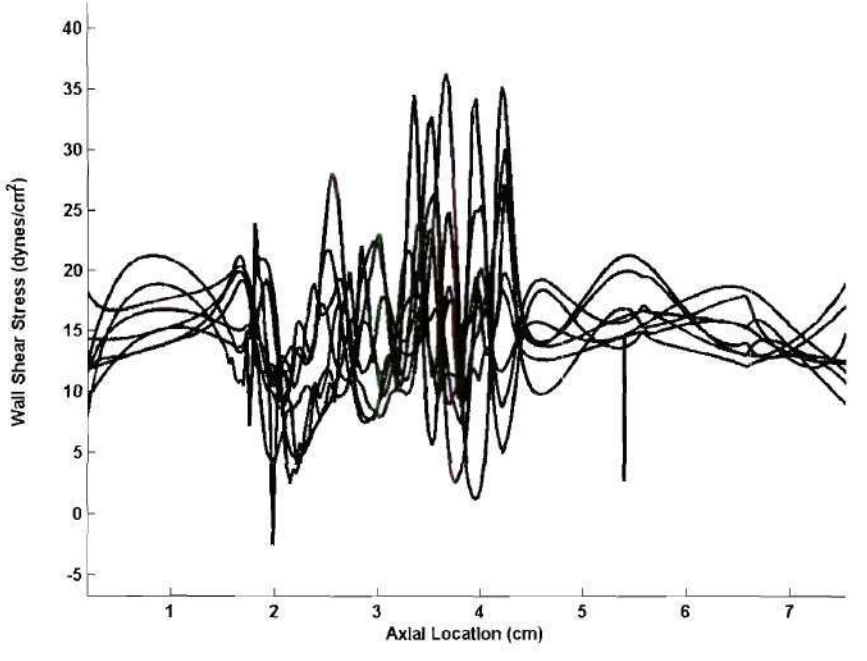

(b) close-up WSS graph.

Figure 3.69: 0.0% stenosis peak flow rate MRI geometry and boundary conditions. WSS graphs along eight equally spaced (in the angular direction) axial lines.

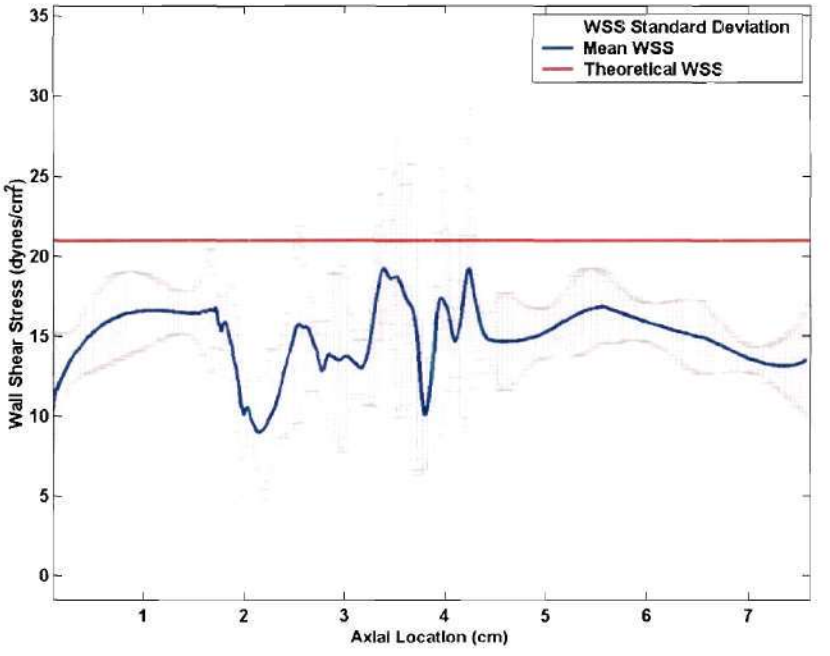

(a) MRI derived geometry and PC-MRI derived boundary conditions

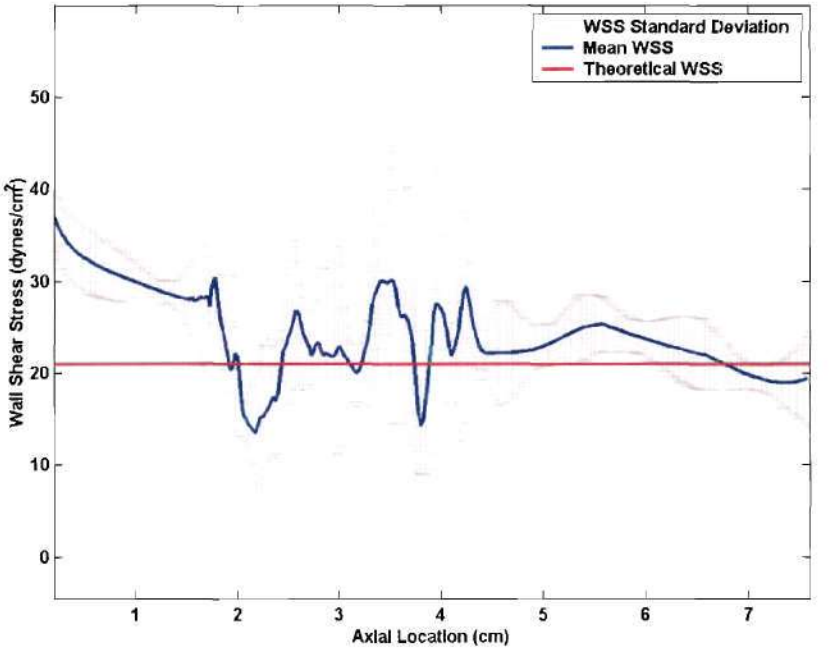

(c) MRI derived geometry and idealized boundary conditions.

Figure 3.70: 0.0% stenosis peak flow rate mean WSS graphs using MRI derived geometries with (a) PC-MRI derived inlet boundary conditions and (b) idealized inlet boundary conditions.

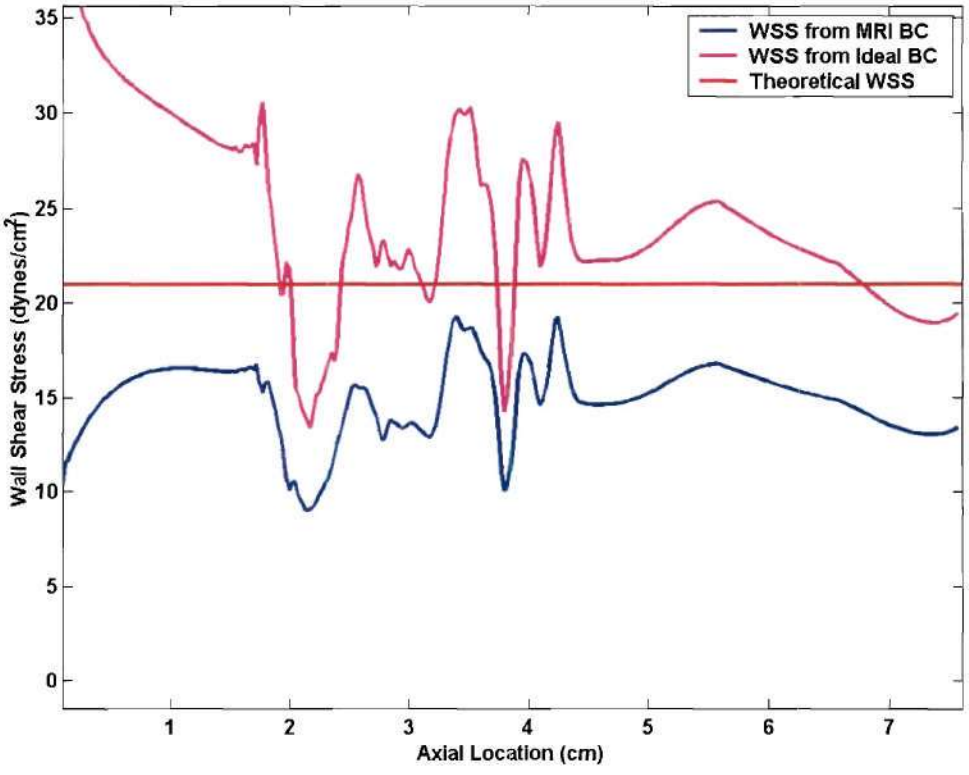

Figure 3.71: 0.0% stenosis peak flow rate WSS graph comparing the PC-MRI and idealized inlet boundary conditions.

(a) PC-MRI derived inlet boundary conditions.

(b) idealized inlet boundary conditions.

Figure 3.72: 3D WSS contour graphs of the 0.0% stenosis model under peak flow rate conditions. Geometries reconstructed from MRI images with (a) PC-MRI derived and (b) idealized inlet boundary conditions.

52.7% Stenosis Geometry – Average Flow Rate

The PC-MRI velocity profile applied to the MRI derived geometry is illustrated in Figure 3.73. The eight axial WSS profiles were averaged to obtain mean WSS values and standard deviations. The large standard deviations observed in Figure 3.74a illustrate the large variation in WSS data. In order to isolate the effects of the reconstructed MRI geometry on the WSS distributions, a CFD simulation was also run using the MRI derived geometry and an idealized inlet boundary condition (Figure 3.74b). Large WSS standard deviations were also observed in this data set. The maximum and minimum WSS values, as well as the corresponding percent errors relative to gold standard values, are presented in Table 3.4. The idealized boundary condition simulation approximated the gold standard WSS values better compared to the PC-MRI boundary condition simulation (Figure 3.75). The 3D WSS contours followed the same pattern for both cases (Figure 3.76). The 3D WSS contour graph for the MRI derived geometry and PC-MRI derived inlet boundary condition is compared to the gold standard values in Figure 3.77. The recirculation areas for the two models are compared to the gold standard values in Figure 3.77. The recirculation regions for the MRI derived geometry were asymmetrical. This pattern was independent of the boundary condition employed. Areas of recirculation were also observed proximal to the stenosis for the MRI geometries. These areas were considered errors caused by the coarse geometry derived from the MRI data.

	Maximum WSS (dynes/cm^2) [% error]	Minimum WSS (dynes/cm^2) [%error]
52.7% Stenosis Average Flow Rate		
Ideal Geometry Ideal BC	62.43 [gold standard]	-2.80 [gold standard]
Ideal Geometry MRI BC	49.36 [-20.9%]	-2.05 [36.1%]
MRI Geometry Ideal BC	43.75 [-29.9%]	-1.06 [62.1%]
MRI Geometry MRI BC	35.43 [-43.2%]	-0.66 [76.4%]
52.7% Stenosis Peak Flow Rate		
Ideal Geometry Ideal BC	280.79 [gold standard]	-17.87 [gold standard]
Ideal Geometry MRI BC	138.07 [-50.8%]	-6.58 [63.2%]
MRI Geometry Ideal BC	193.80 [-31.0%]	-7.15 [60.0%]
MRI Geometry MRI BC	107.10 [-61.9%]	-4.57 [74.4%]
75.0% Stenosis Average Flow Rate		
Ideal Geometry Ideal BC	196.35 [gold standard]	-9.34 [gold standard]
Ideal Geometry MRI BC	175.27 [-10.7%]	-7.32 [21.6%]
MRI Geometry Ideal BC	165.92 [-15.5%]	-5.87 [37.2%]
MRI Geometry MRI BC	148.01 [-24.6%]	-5.41 [42.1%]

Table 3.4: Comparison of the maximum and minimum WSS values derived from the four CFD simulation sets for the 52.7% stenosis and 75.0% stenosis geometries. Negative percent errors refer to under estimations while positive errors refer to over estimations.

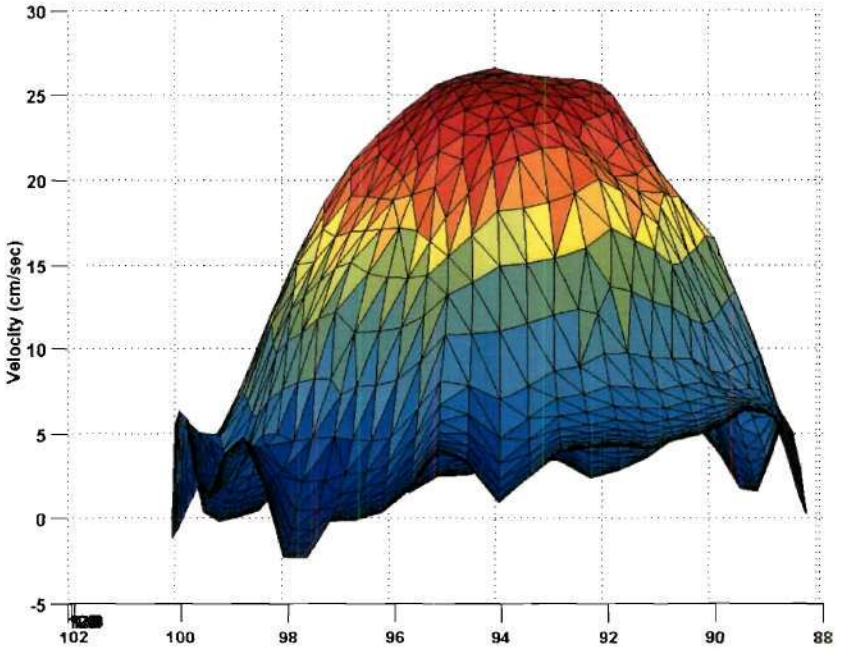

(a) PC-MRI derived inlet velocity profile

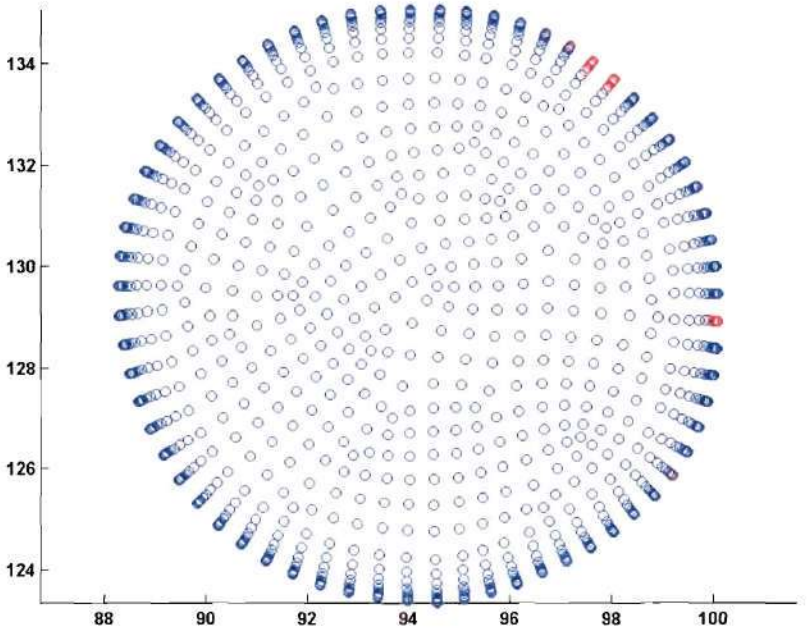

(b) negative velocities assigned to the entrance region computational grid are shown in red.

Figure 3.73: 52.7% stenosis average flow rate entrance boundary condition velocity profile applied to the MRI derived geometry.

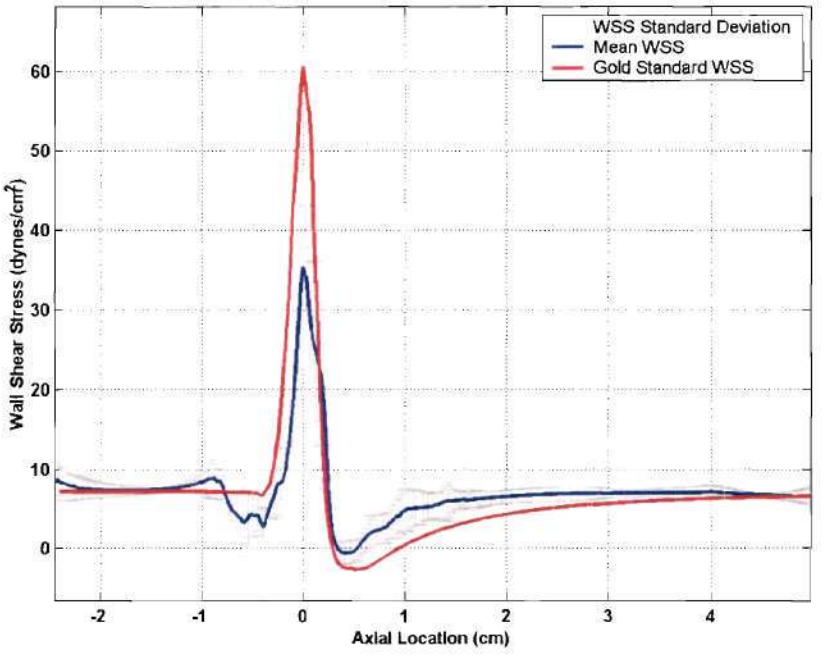

(a) MRI derived geometry and PC-MRI derived boundary conditions

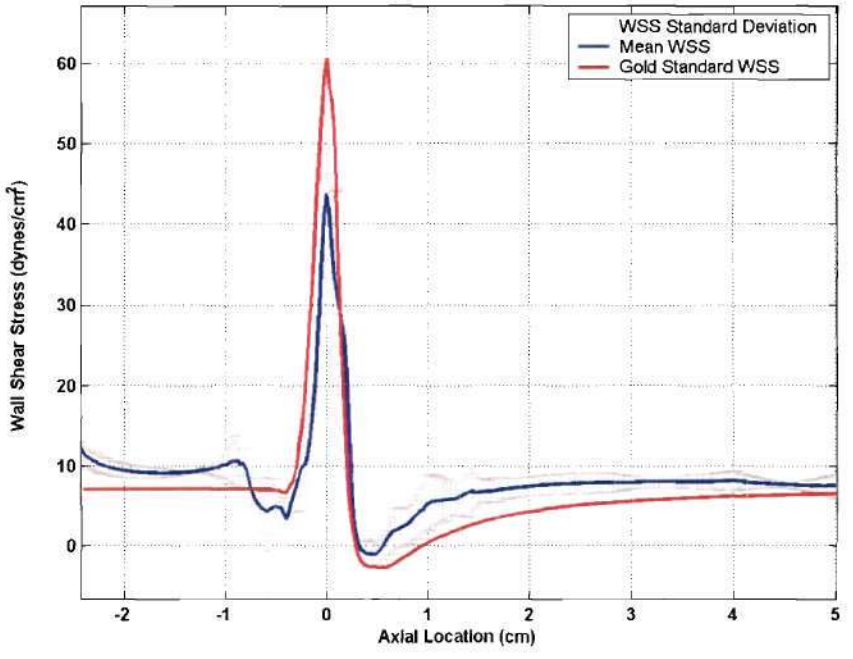

(d) MRI derived geometry and idealized boundary conditions.

Figure 3.74: 52.7% stenosis average flow rate mean WSS graphs using MRI derived geometries with (a) PC-MRI derived inlet boundary conditions and (b) idealized inlet boundary conditions.

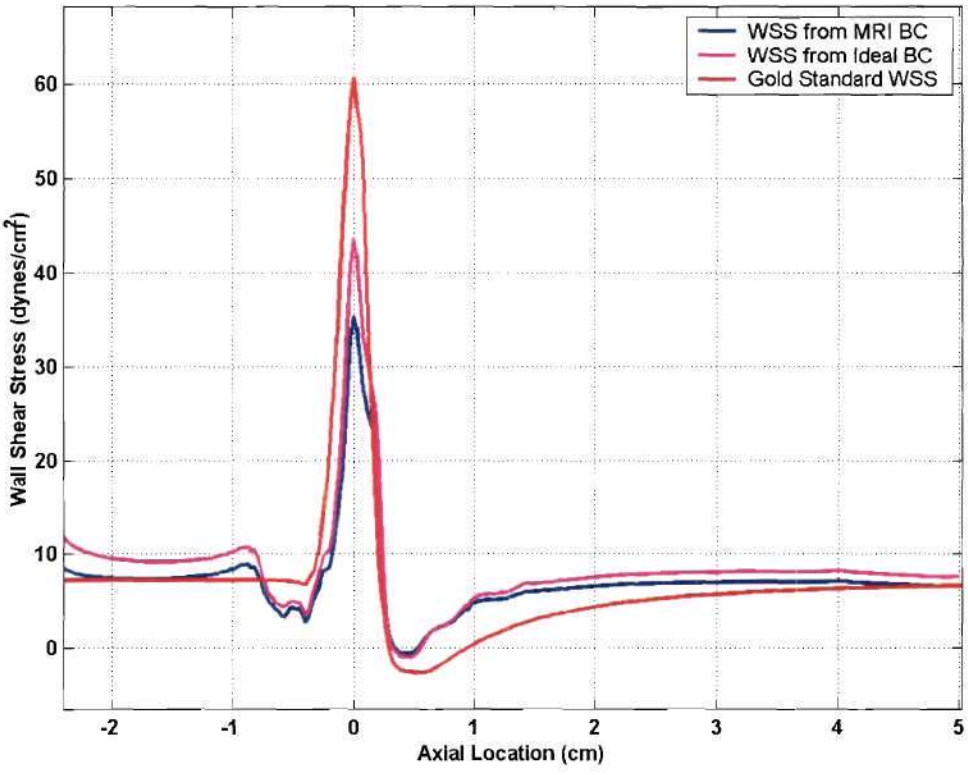

Figure 3.75: 52.7% stenosis average flow rate WSS graph comparing the PC-MRI and idealized inlet boundary conditions.

(a) PC-MRI derived inlet boundary conditions.

(b) idealized inlet boundary conditions.

Figure 3.76: 3D WSS contour graphs of the 52.7% stenosis model under average flow rate conditions. Geometries reconstructed from MRI images with (a) PC-MRI derived and (b) idealized inlet boundary conditions.

(a) MRI derived geometry and PC-MRI inlet boundary conditions.

(b) idealized geometry and idealized inlet boundary conditions : Gold Standard

Figure 3.77: 3D WSS contour graphs of the 52.7% stenosis model under average flow rate conditions. Comparing WSS values derived entirely from MRI data to the gold standard.

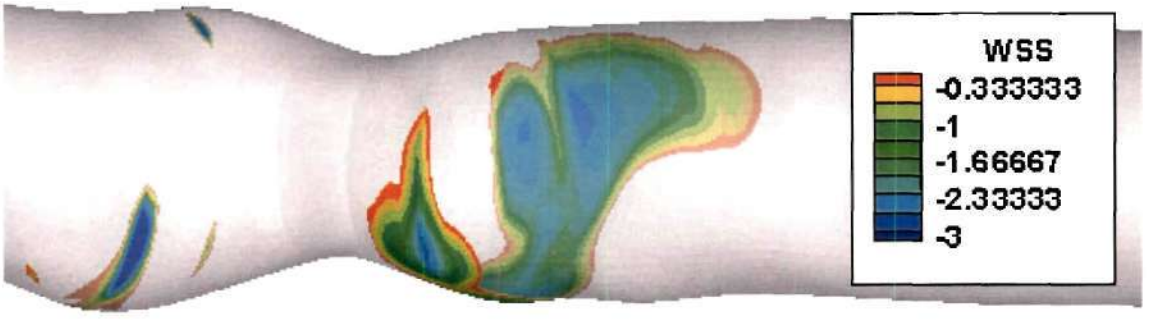

(a) MRI derived geometry and PC-MRI derived inlet boundary conditions.

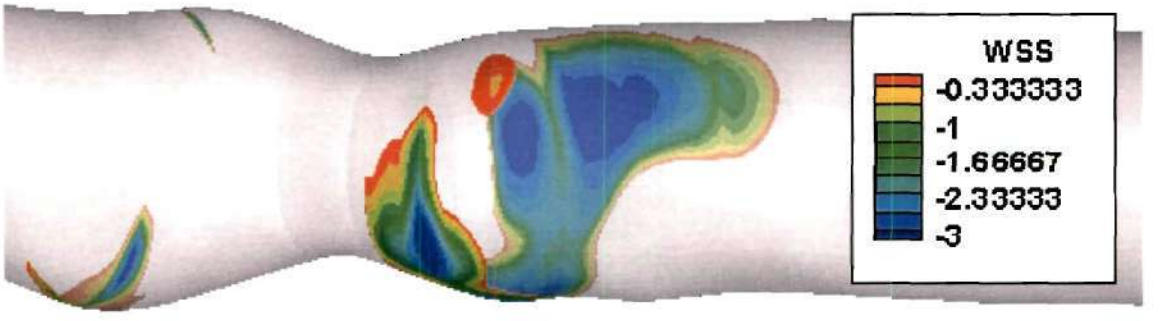

(b) MRI derived geometry and idealized inlet boundary conditions.

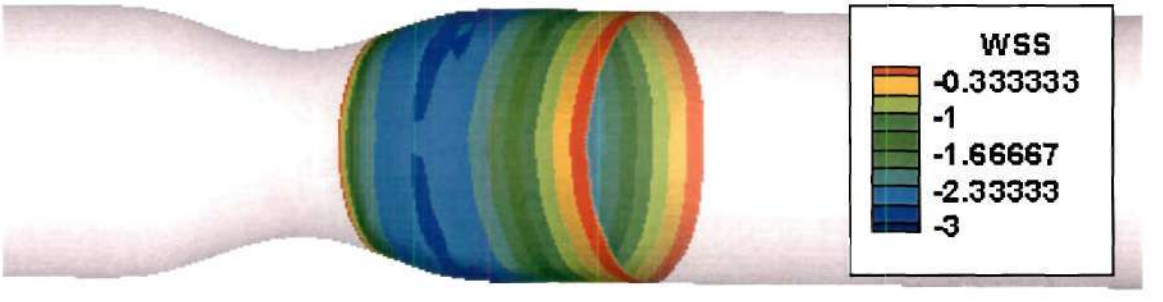

(c) Idealized geometry and idealized inlet boundary conditions.

Figure 3.78: 3D recirculation region WSS contour graphs of the 52.7% stenosis model under average flow rate conditions (a) MRI geometry/PC-MRI inlet boundary conditions (b) MRI geometry/idealized inlet boundary conditions and (c) idealized geometry and idealized inlet boundary conditions.

52.7% Stenosis Geometry – Peak Flow Rate

The PC-MRI velocity profile applied to the MRI derived geometry is illustrated in Figure 3.79. The eight axial WSS profiles were averaged to obtain mean WSS values and standard deviations. The large standard deviations observed in Figure 3.80a illustrate the large variation in WSS data. In order to isolate the effects of the reconstructed MRI geometry on the WSS distributions, a CFD simulation was also run using the MRI derived geometry and an idealized inlet boundary condition (Figure 3.80b). Large WSS standard deviations were also observed in this data set. The maximum and minimum WSS values, as well as the corresponding percent errors relative to gold standard values, are presented in Table 3.4. The idealized boundary condition simulation approximated the gold standard WSS values better compared to the PC-MRI boundary condition simulation (Figure 3.81). The 3D WSS contours followed the same pattern for both cases (Figure 3.82). Lower WSS magnitudes are evident in the PC-MRI derived inlet boundary condition model in both Figures 3.81 and 3.82. The 3D WSS contour graph for the MRI derived geometry and PC-MRI derived inlet boundary condition is compared to the gold standard values in Figure 3.83. The recirculation areas for the two models are compared to the gold standard values in Figure 3.84. The recirculation regions for the MRI derived geometry were asymmetrical. This pattern was independent of the boundary condition employed. Areas of recirculation were also observed proximal to the stenosis for the MRI geometries. These areas were considered errors caused by the coarse geometry derived from the MRI data.

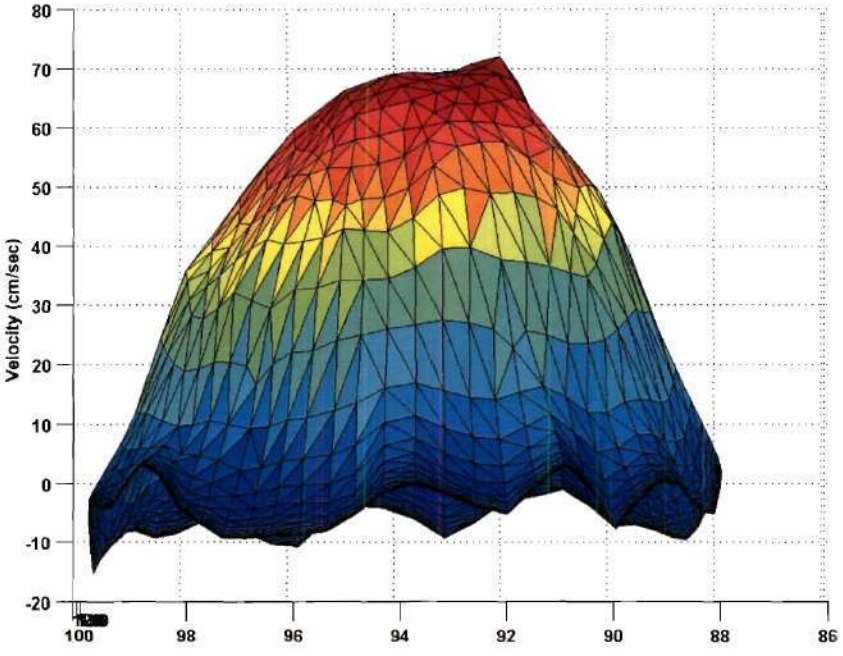

(a) PC-MRI derived inlet velocity profile

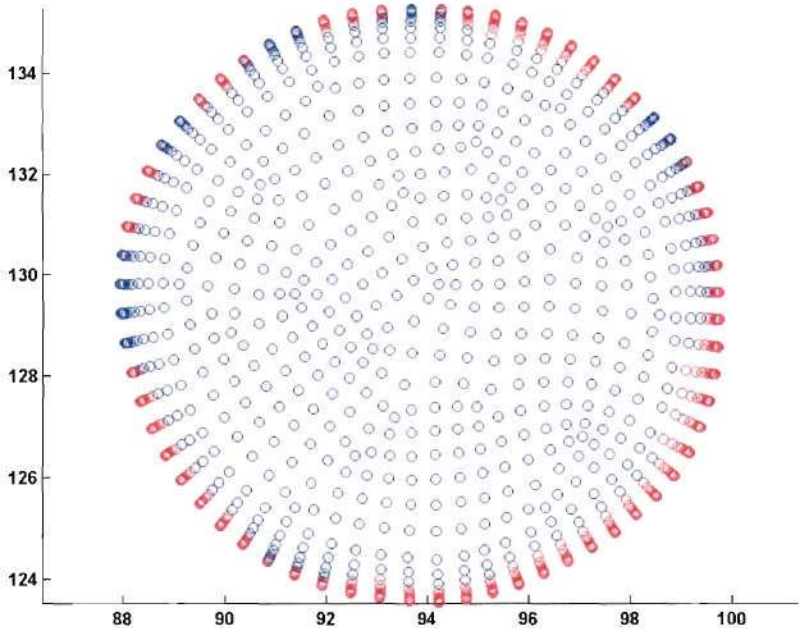

(b) negative velocities assigned to the entrance region computational grid are shown in red.

Figure 3.79: 52.7% stenosis peak flow rate entrance boundary condition velocity profile applied to the MRI derived geometry.

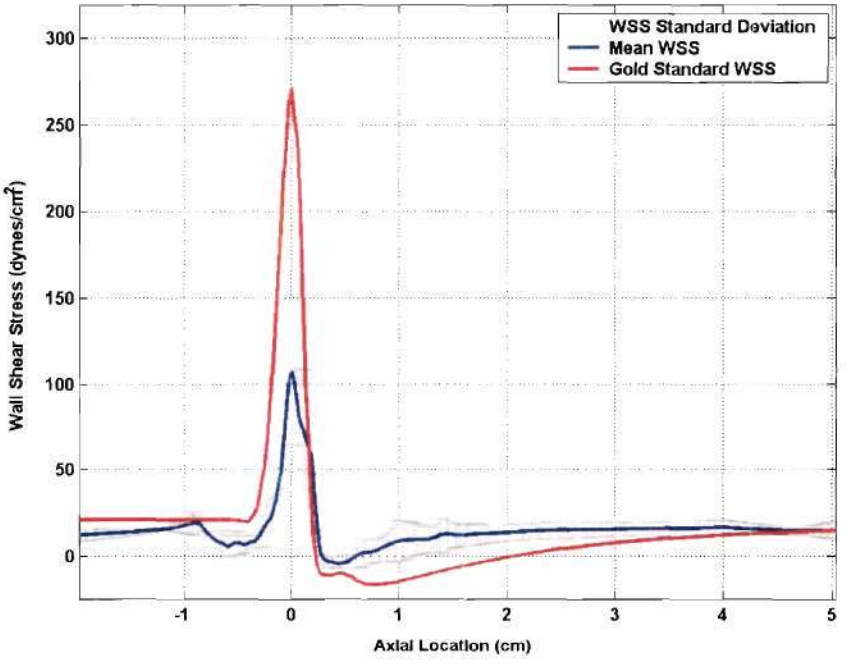

(a) MRI derived geometry and PC-MRI derived boundary conditions

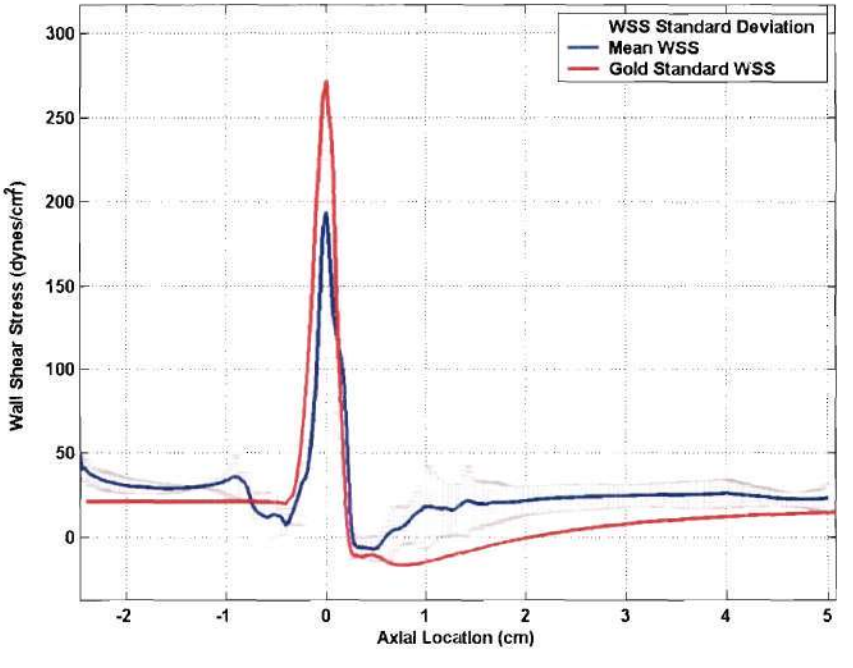

(b) MRI derived geometry and idealized boundary conditions.

Figure 3.80: 52.7% stenosis peak flow rate mean WSS graphs using MRI derived geometries with (a) PC-MRI derived inlet boundary conditions and (b) idealized inlet boundary conditions.

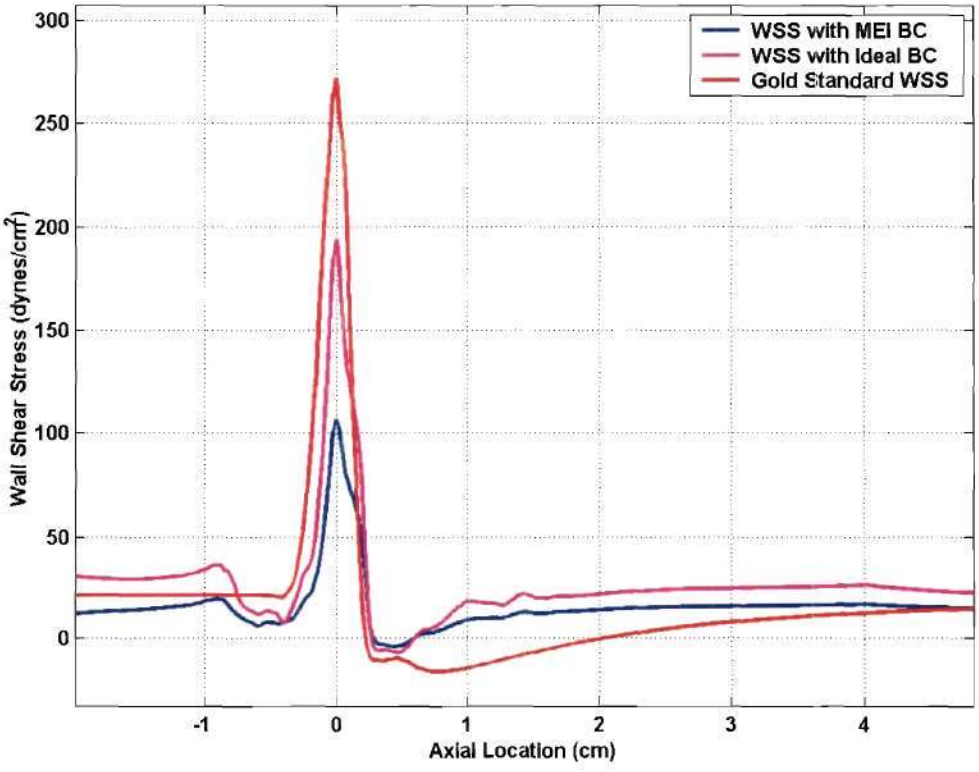

Figure 3.81: 52.7% stenosis peak flow rate WSS graph comparing the PC-MRI and idealized inlet boundary conditions.

(a) MRI derived geometry and PC-MRI inlet boundary conditions.

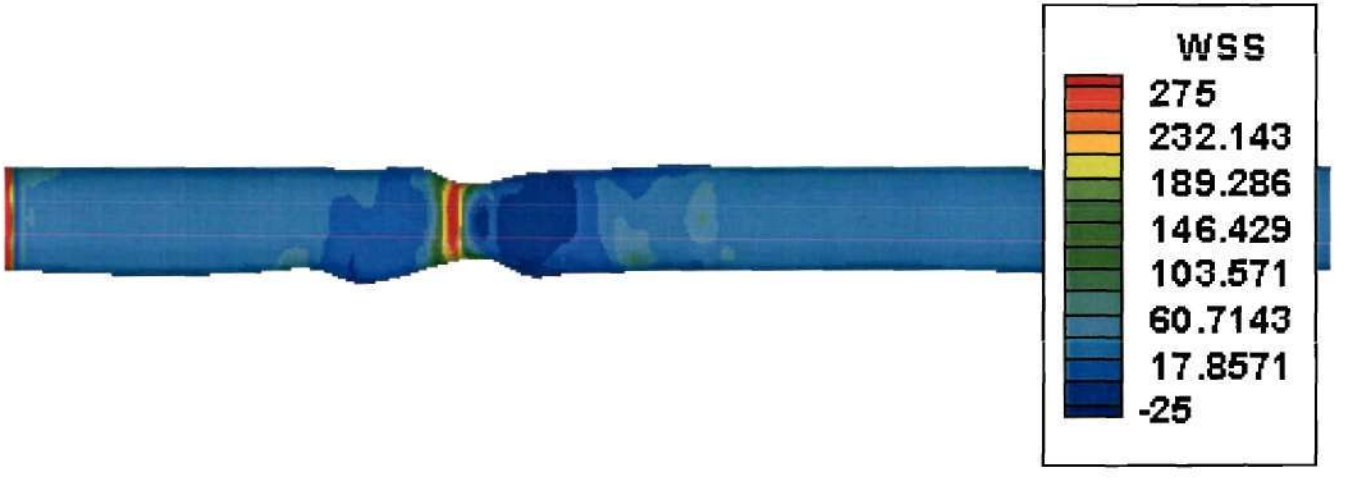

(b) idealized inlet boundary conditions.

Figure 3.82: 3D WSS contour graphs of the 52.7% stenosis model under peak flow rate conditions. Geometries reconstructed from MRI images with (a) PC-MRI derived and (b) idealized inlet boundary conditions.

(a) MRI derived geometry and PC-MRI inlet boundary conditions.

(b) idealized geometry and idealized inlet boundary conditions : Gold Standard

Figure 3.83: 3D WSS contour graphs of the 52.7% stenosis model under peak flow rate conditions. Comparing WSS values derived entirely from MRI data to the gold standard.

(a) MRI derived geometry and PC-MRI derived inlet boundary conditions.

(b) MRI derived geometry and idealized inlet boundary conditions.

(c) Idealized geometry and idealized inlet boundary conditions.

Figure 3.84: 3D recirculation region WSS contour graphs of the 52.7% stenosis model under peak flow rate conditions (a) MRI geometry/PC-MRI inlet boundary conditions (b) MRI geometry/idealized inlet boundary conditions and (c) idealized geometry and idealized inlet boundary conditions.

75.0% Stenosis Geometry – Average Flow Rate

The PC-MRI velocity profile applied to the MRI derived geometry is illustrated in Figure 3.85. The eight axial WSS profiles were averaged to obtain mean WSS values and standard deviations. The large standard deviations observed in Figure 3.86a illustrate the large variation in WSS data. In order to isolate the effects of the reconstructed MRI geometry on the WSS distributions, a CFD simulation was also run using the MRI derived geometry and an idealized inlet boundary condition (Figure 3.86b). Large WSS standard deviations were also observed in this data set. The maximum and minimum WSS values as well as the corresponding percent errors relative to gold standard values are presented in Table 3.4. The idealized boundary condition simulation approximated the gold standard WSS values better compared to the PC-MRI boundary condition simulation (Figure 3.87). Both simulations were unable to accurately predict the recirculation region length. The 3D WSS contours followed the same pattern for both cases (Figure 3.88). The 3D WSS contour graph for the MRI derived geometry and PC-MRI derived inlet boundary condition is compared to the gold standard values in Figure 3.89. The recirculation areas for the two models are compared to the gold standard values in Figure 3.90. The recirculation regions for the MRI derived geometry were asymmetrical. This pattern was independent of the boundary condition employed. The velocity contours for the MRI geometry and PC-MRI defined inlet boundary conditions are illustrated in Figure 3.91. Asymmetric velocity contours were observed distal to the stenosis. These patterns were not observed in the gold standard velocity contour graph (Figure 3.92). Figures 3.93 through 3.96 represent streamlines through the MRI defined and PC-MRI boundary condition model. The streamlines were observed to bend toward

one side of the geometry and create a region of recirculation on the contralateral side. Figures 3.95 and 3.96 show a single streamline trace beginning at the inlet area and passing through the recirculation area. The complex flow path illustrated the complex three dimensional flow patterns simulated in the model. The gold standard streamline graph is illustrated in Figure 3.97. The recirculation areas were observed to be symmetric and well formed. The streamline patterns suggested that the flow patterns were two-dimensional with no angular velocity components present.

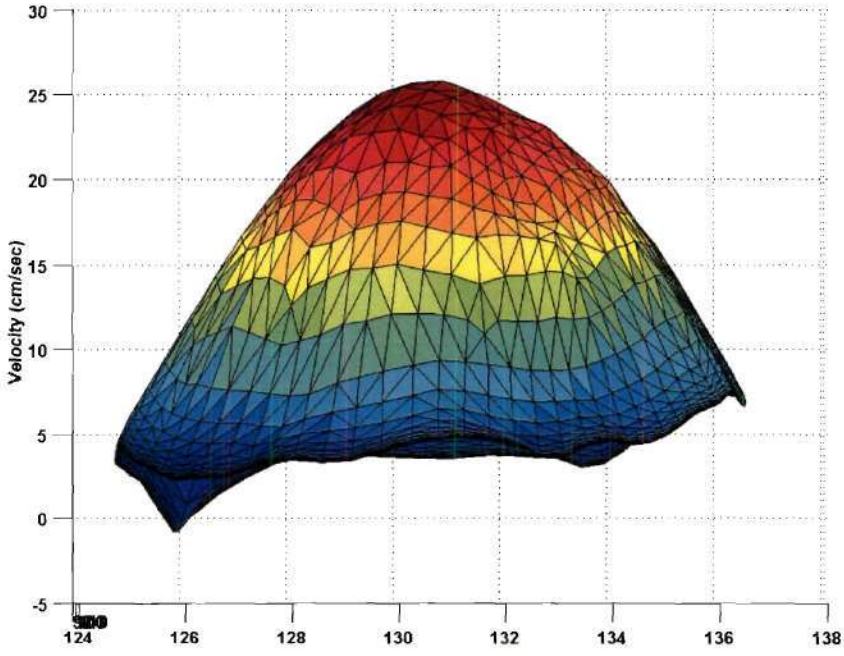

(a) PC-MRI derived inlet velocity profile

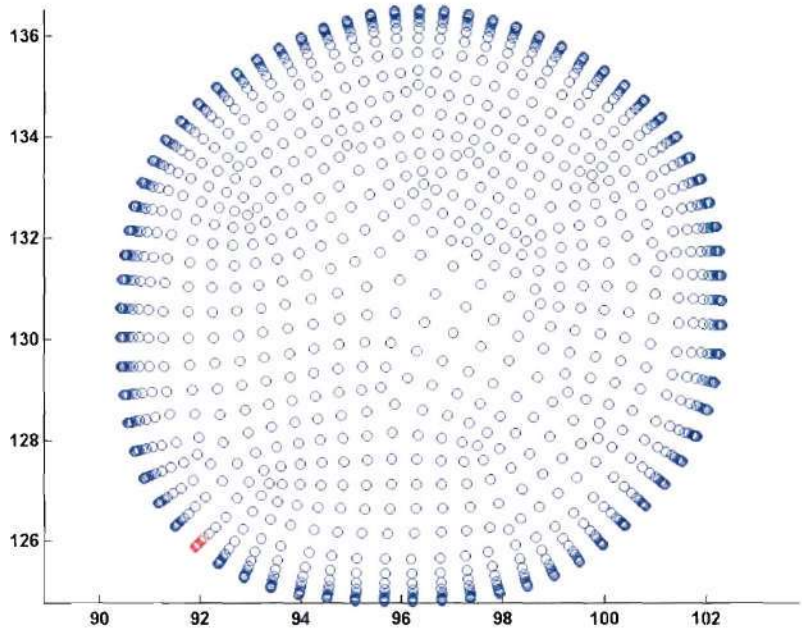

(b) negative velocities assigned to the entrance region computational grid are shown in red.

Figure 3.85: 75.0% stenosis average flow rate entrance boundary condition velocity profile applied to the MRI derived geometry.

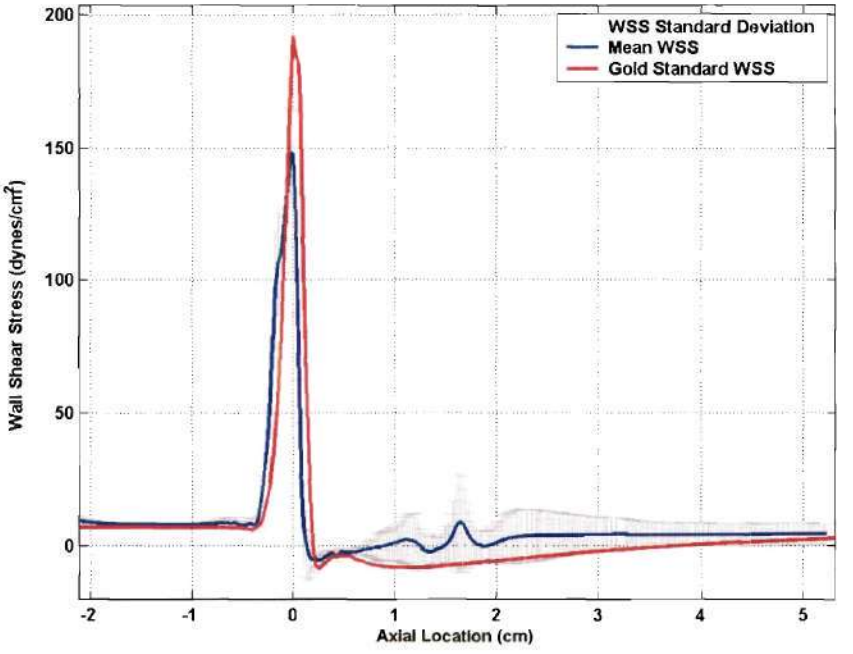

(a) MRI derived geometry and PC-MRI derived boundary conditions

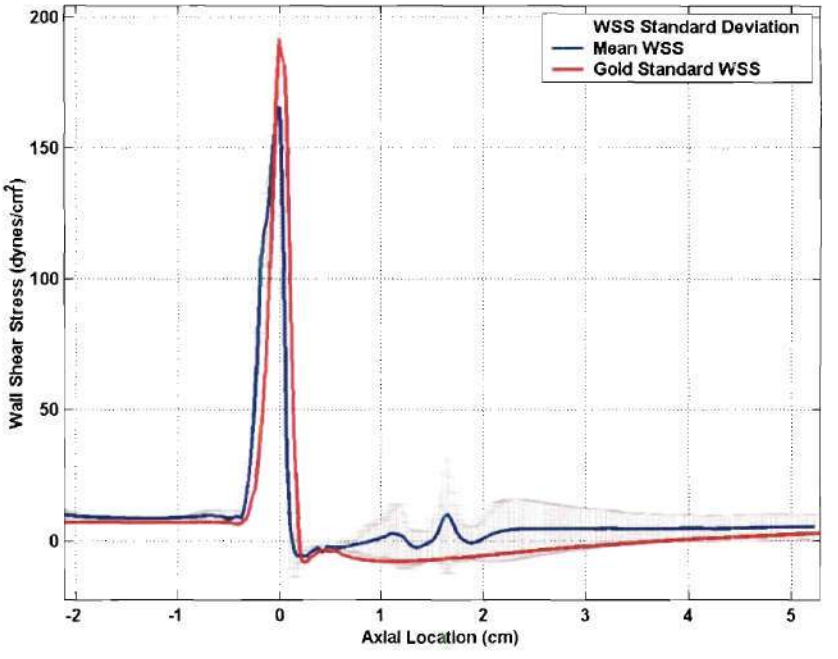

(b) MRI derived geometry and idealized boundary conditions.

Figure 3.86: 75.0% stenosis average flow rate mean WSS graphs using MRI derived geometries with (a) PC-MRI derived inlet boundary conditions and (b) idealized inlet boundary conditions.

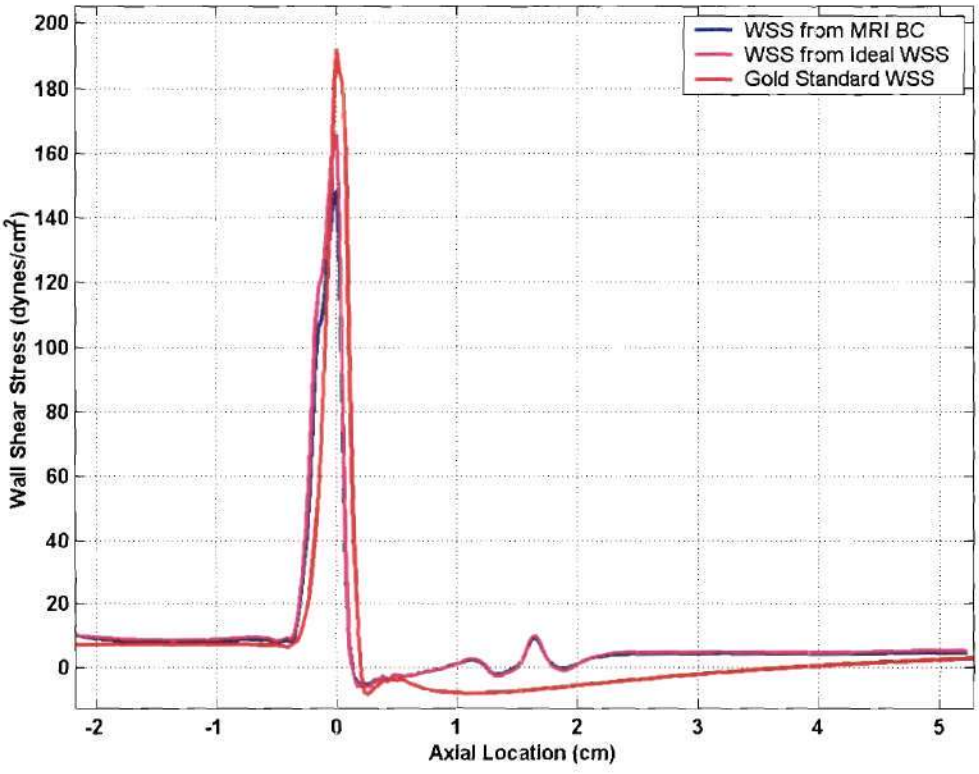

Figure 3.87: 75.0% stenosis average flow rate WSS graph comparing the PC-MRI and idealized inlet boundary conditions.

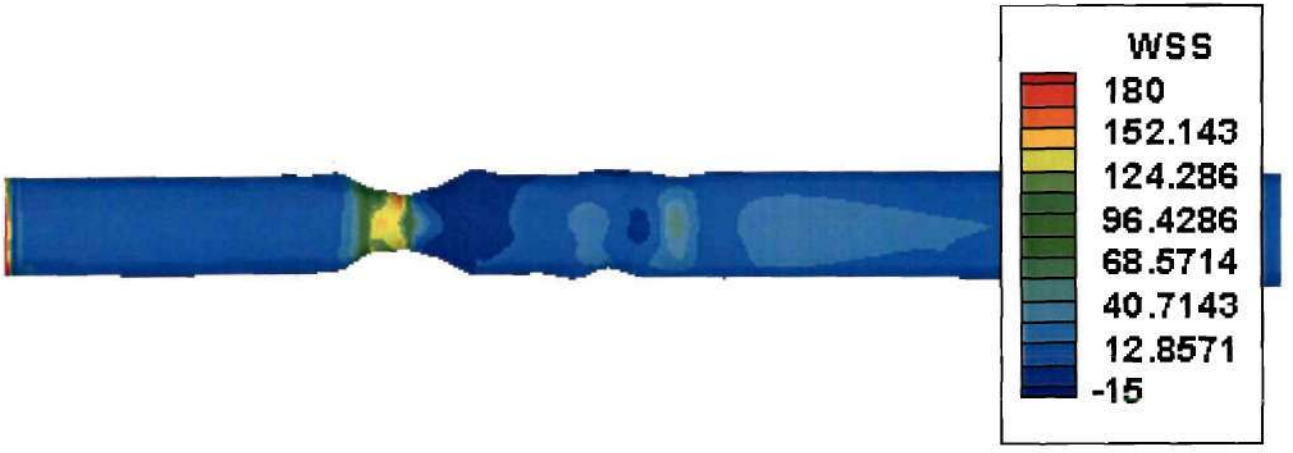

(a) MRI derived geometry and PC-MRI inlet boundary conditions.

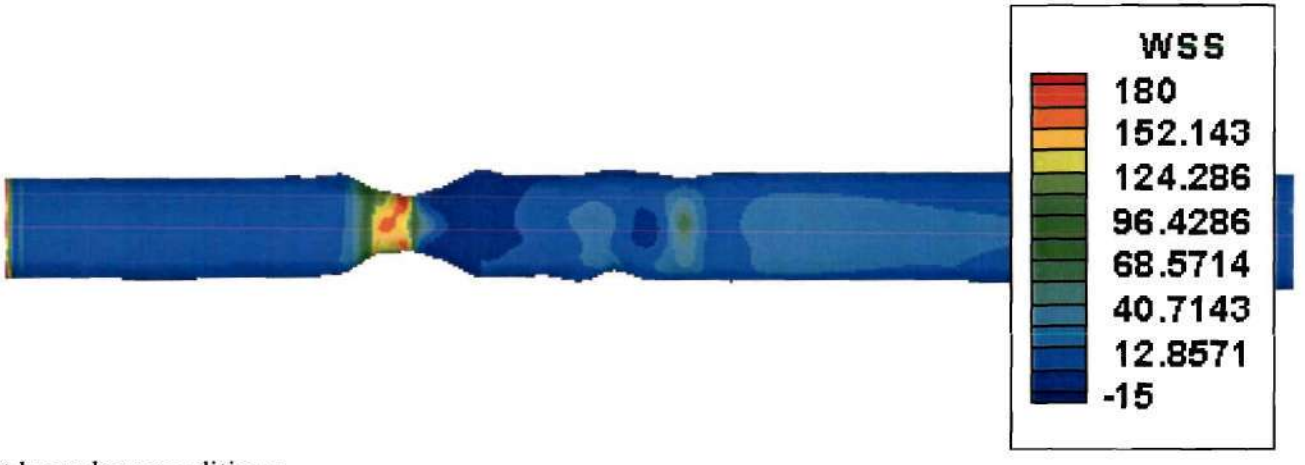

(b) idealized inlet boundary conditions.

Figure 3.88: 3D WSS contour graphs of the 75.0% stenosis model under average flow rate conditions. Geometries reconstructed from MRI images with (a) PC-MRI derived and (b) idealized inlet boundary conditions.

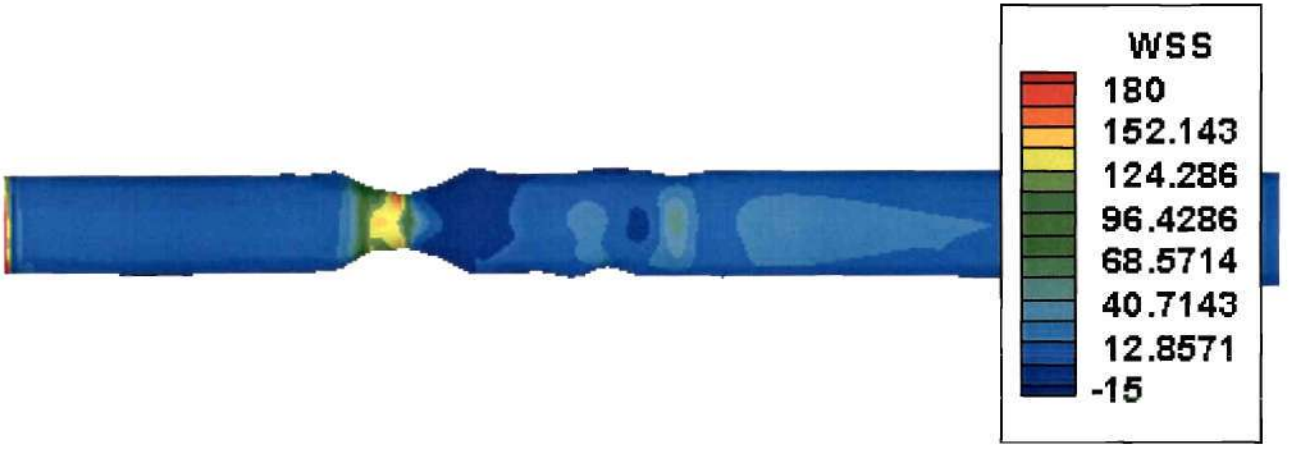

(a) MRI derived geometry and PC-MRI inlet boundary conditions.

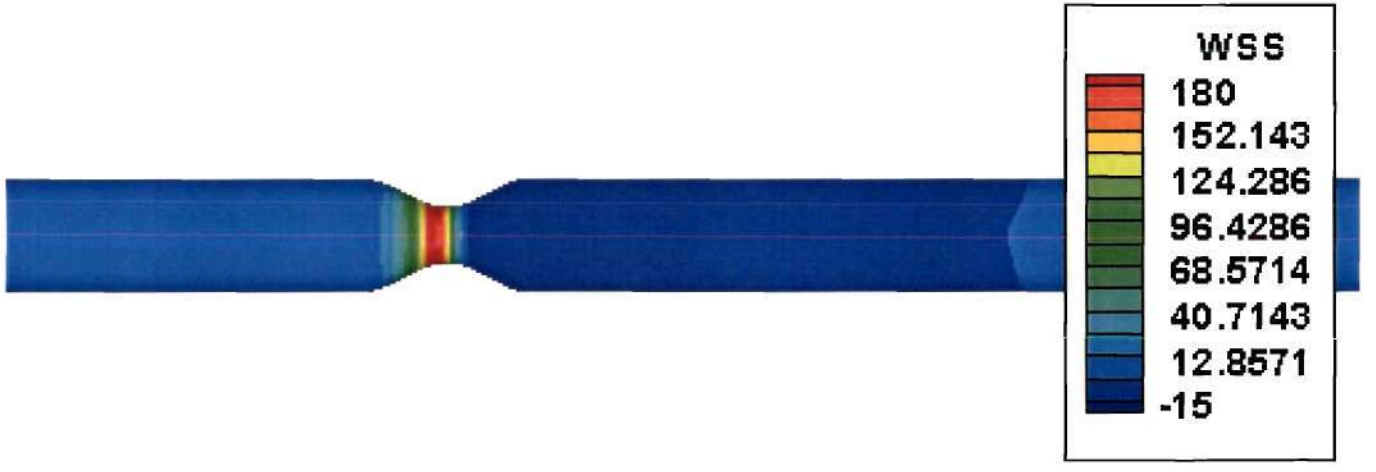

(b) idealized geometry and idealized inlet boundary conditions : Gold Standard

Figure 3.89: 3D WSS contour graphs of the 75.0% stenosis model under average flow rate conditions. Comparing WSS values derived entirely from MRI data to the gold standard.

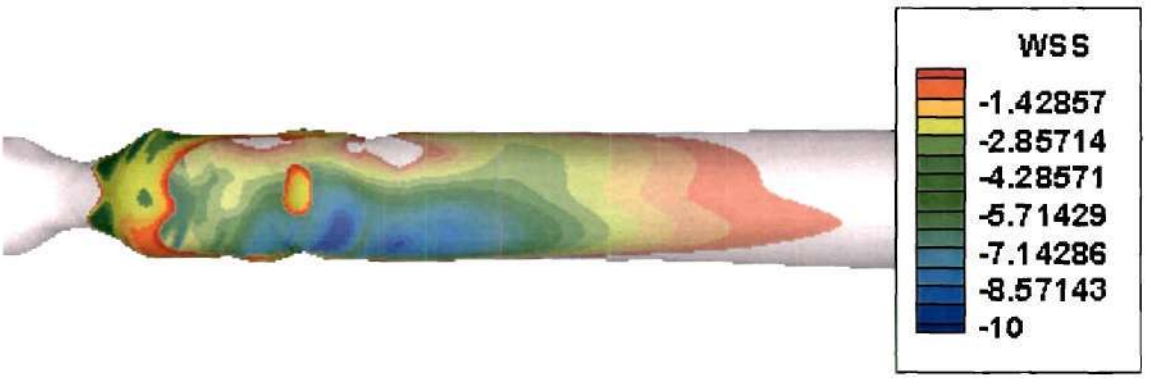

(a) MRI derived geometry and PC-MRI derived inlet boundary conditions.

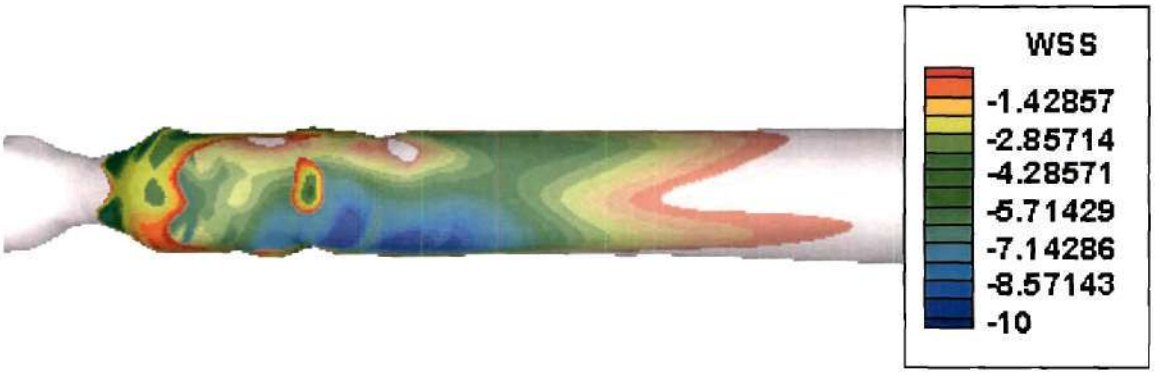

(b) MRI derived geometry and idealized inlet boundary conditions.

(c) Idealized geometry and idealized inlet boundary conditions.

Figure 3.90: 3D recirculation region WSS contour graphs of the 75.0% stenosis model under average flow rate conditions (a) MRI geometry/PC-MRI inlet boundary conditions (b) MRI geometry/idealized inlet boundary conditions and (c) idealized geometry and idealized inlet boundary conditions.

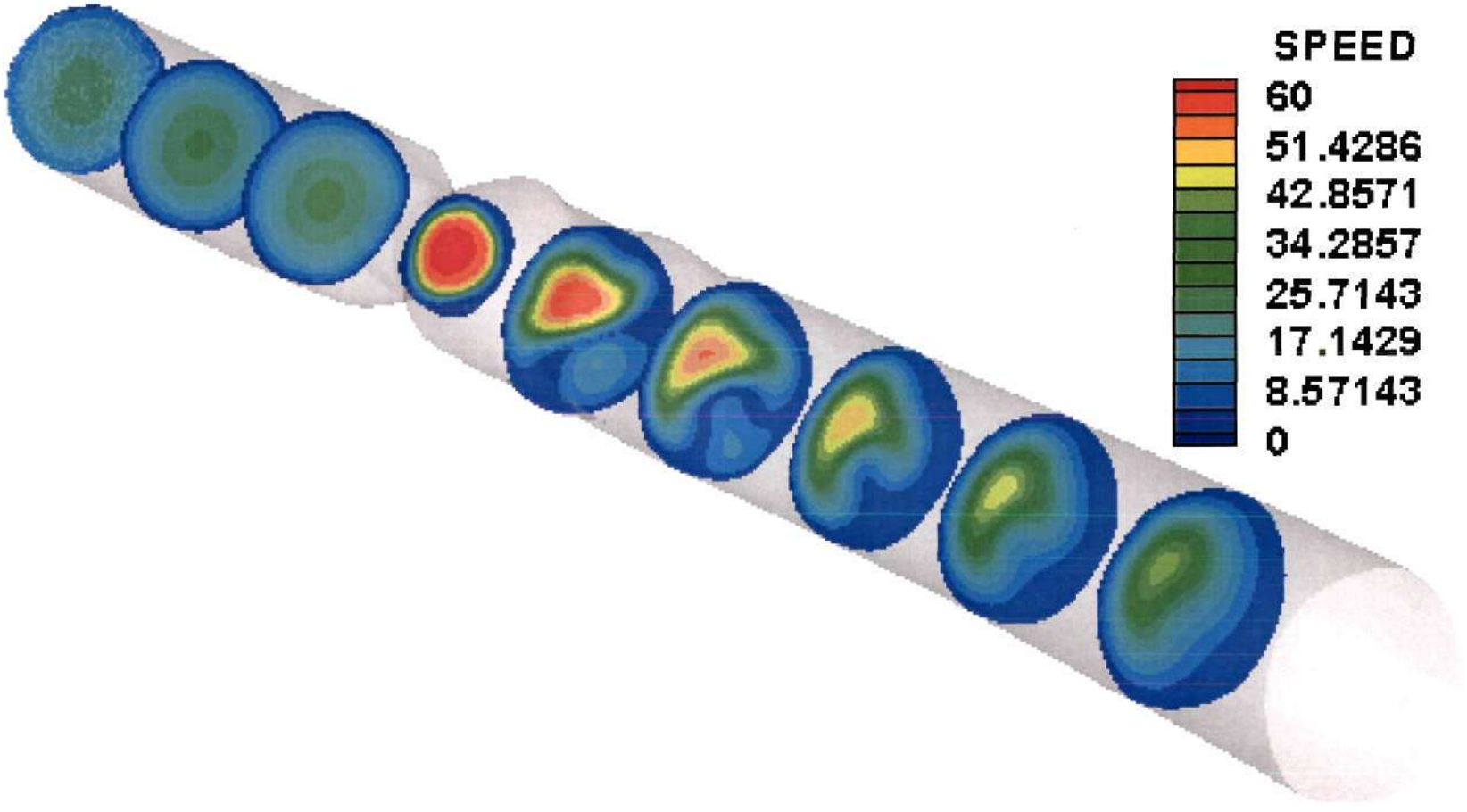

Figure 3.91: Velocity contours through the 75.0% stenosis model under average flow rate conditions. MRI derived geometry and PC-MRI derived inlet boundary conditions.

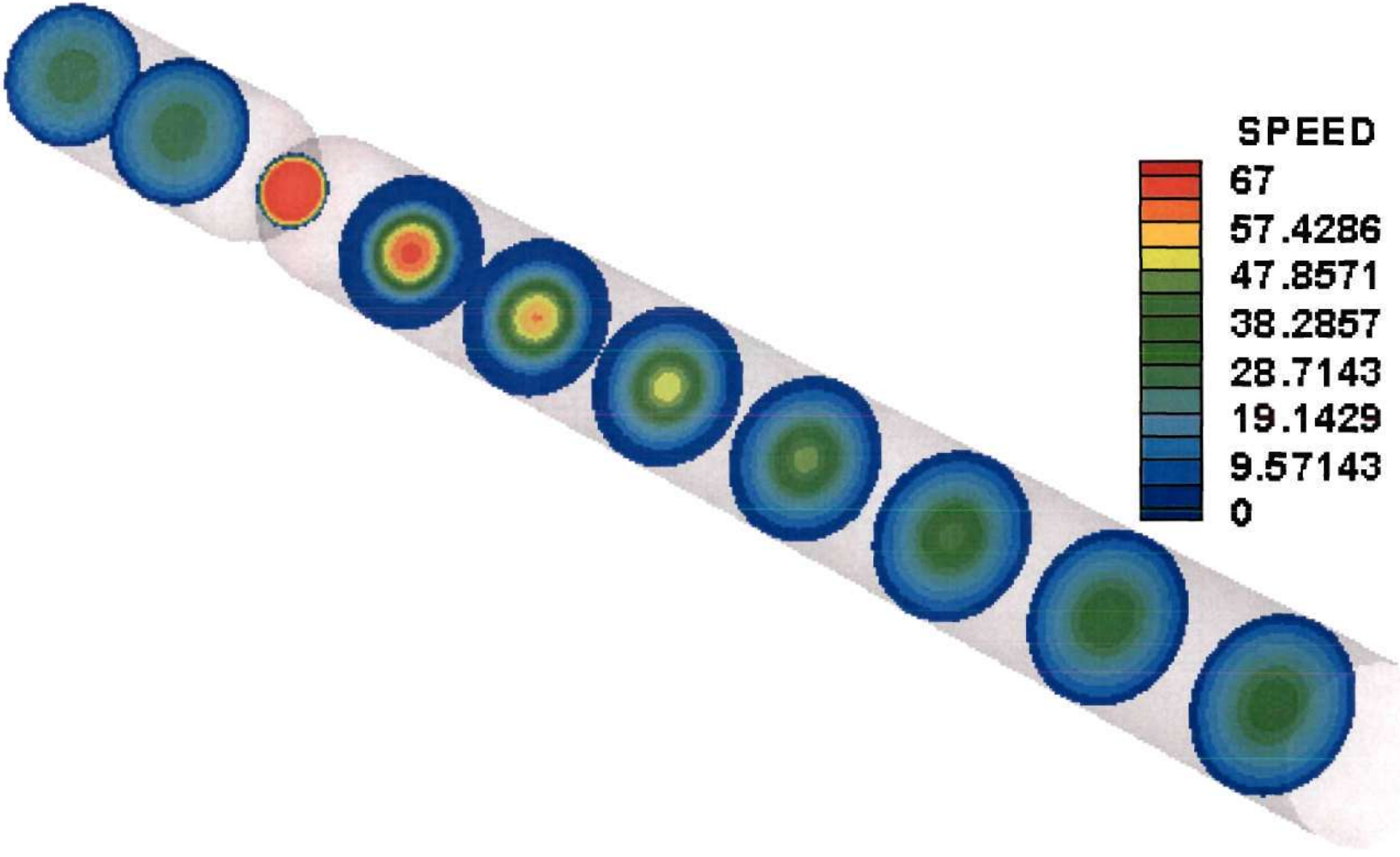

Figure 3.92: Gold standard velocity contours through the 75.0% stenosis model under average flow rate conditions. Idealized geometry and idealized inlet boundary conditions.

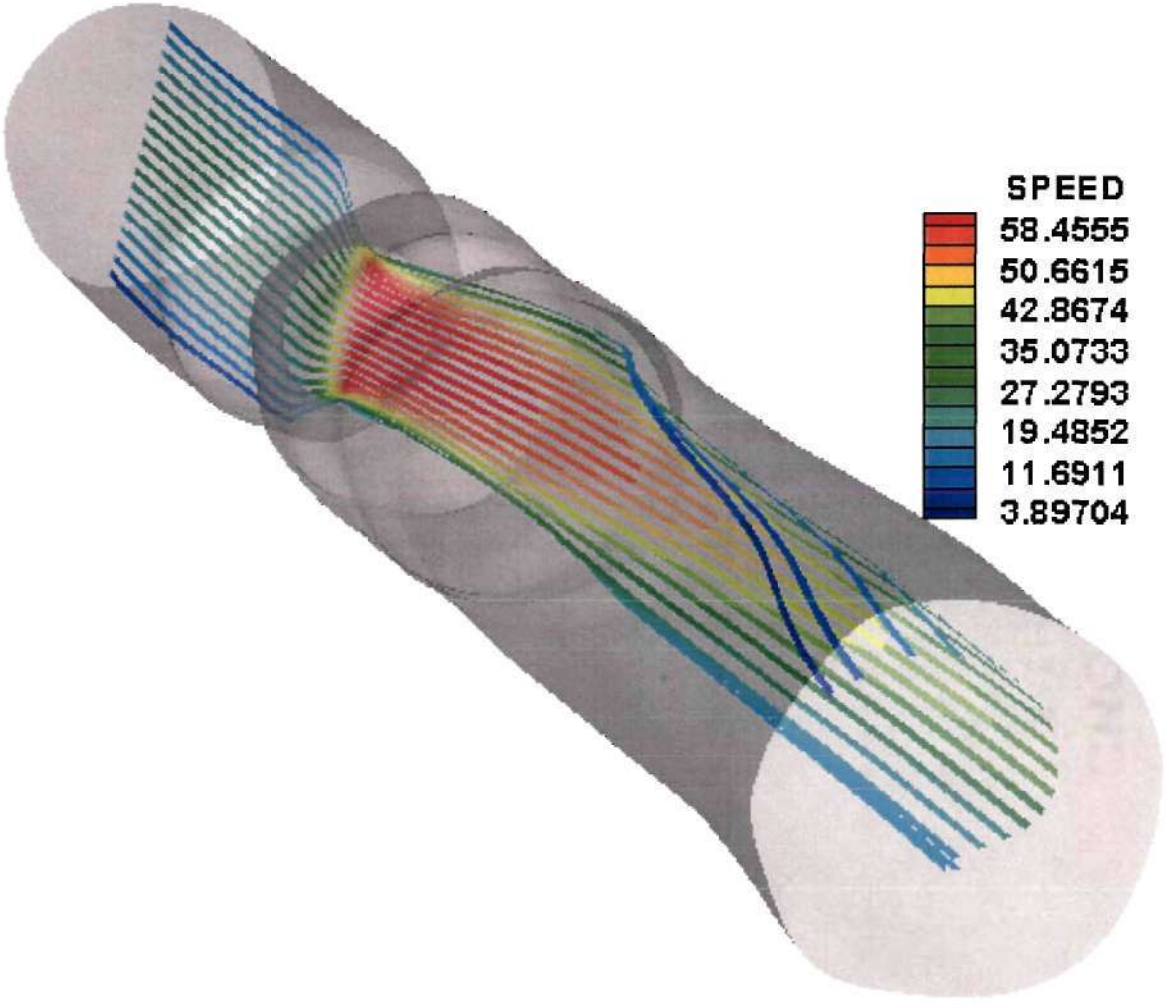

Figure 3.93: Streamlines from the 75.0% stenosis model under average flow rate conditions. MRI derived geometry and PC-MRI derived inlet boundary conditions. Streamlines in the recirculation region are not illustrated.

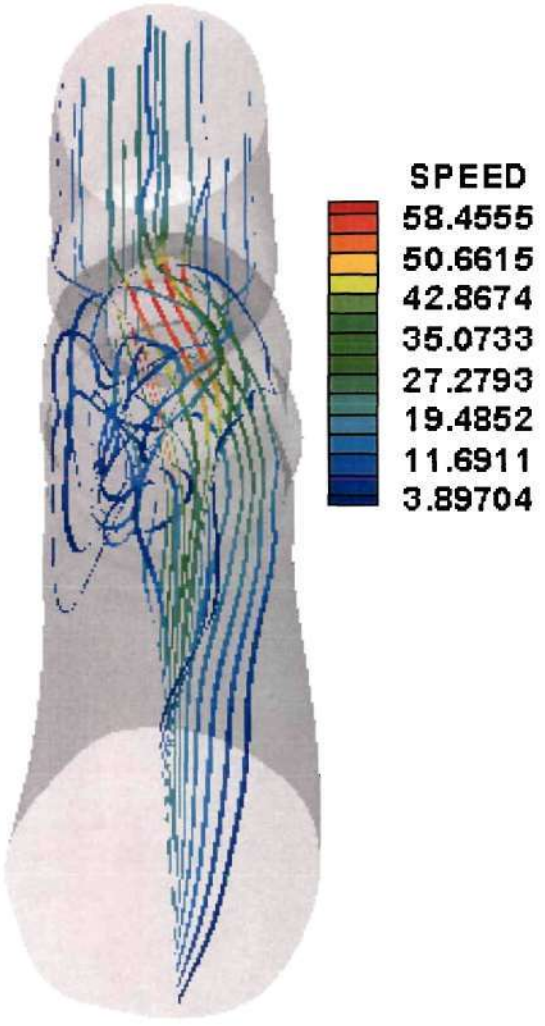

Figure 3.94: Streamlines from the 75.0% stenosis model under average flow rate conditions. MRI derived geometry and PC-MRI derived inlet boundary conditions. Recirculation region on the right side of the model distal to the stenosis.

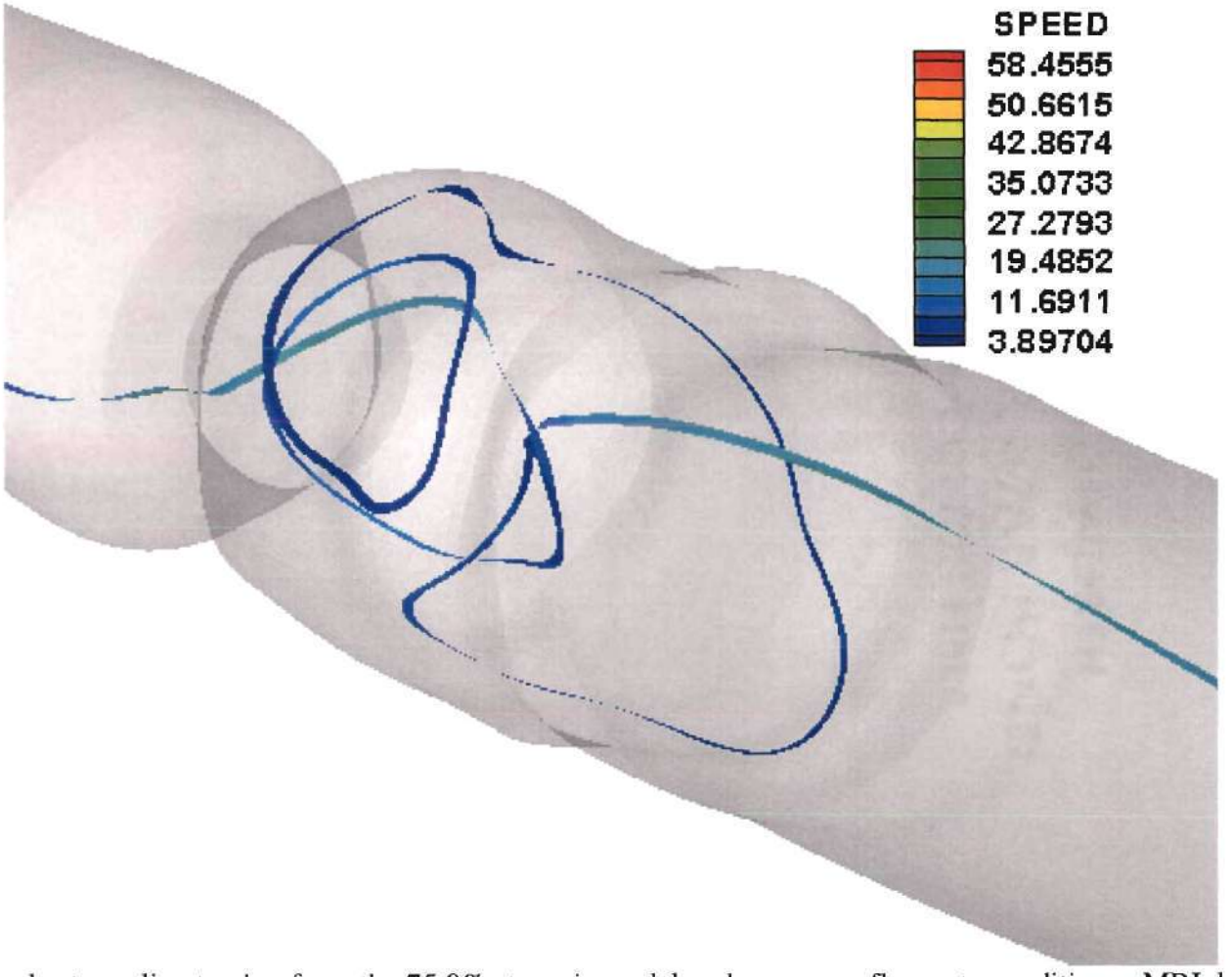

Figure 3.95: A single streamline tracing from the 75.0% stenosis model under average flow rate conditions. MRI derived geometry and PC-MRI derived inlet boundary conditions. Side view.

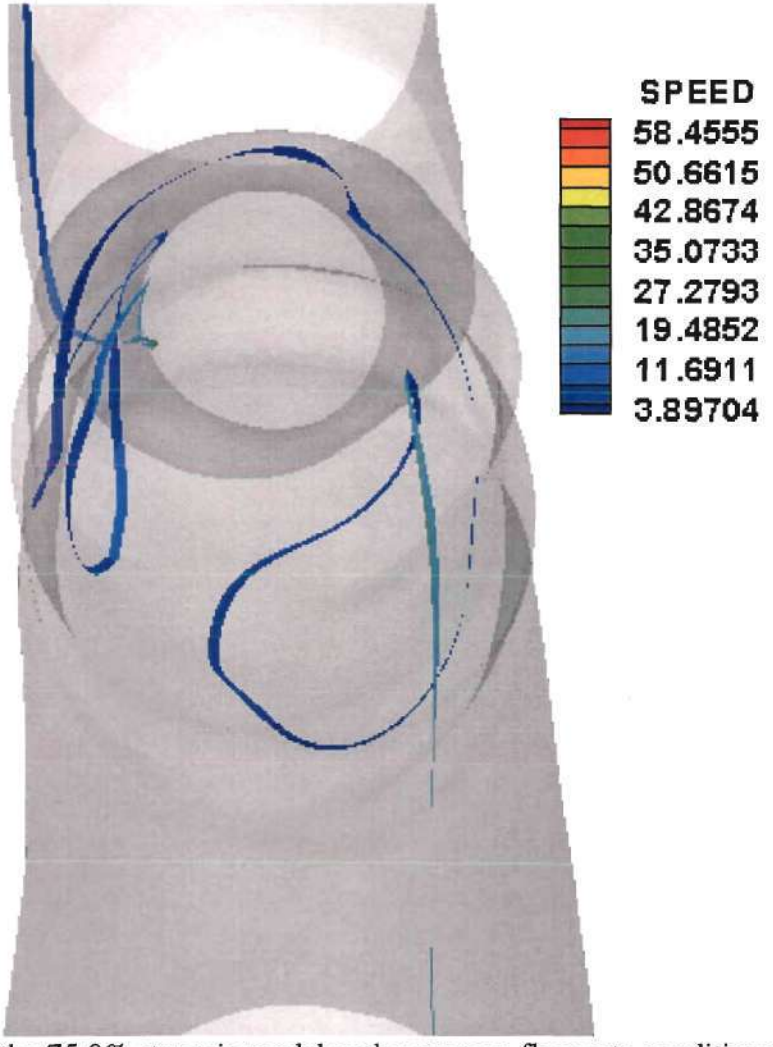

Figure 3.96: A single streamline tracing from the 75.0% stenosis model under average flow rate conditions. MRI derived geometry and PC-MRI derived inlet boundary conditions. Luminal view.

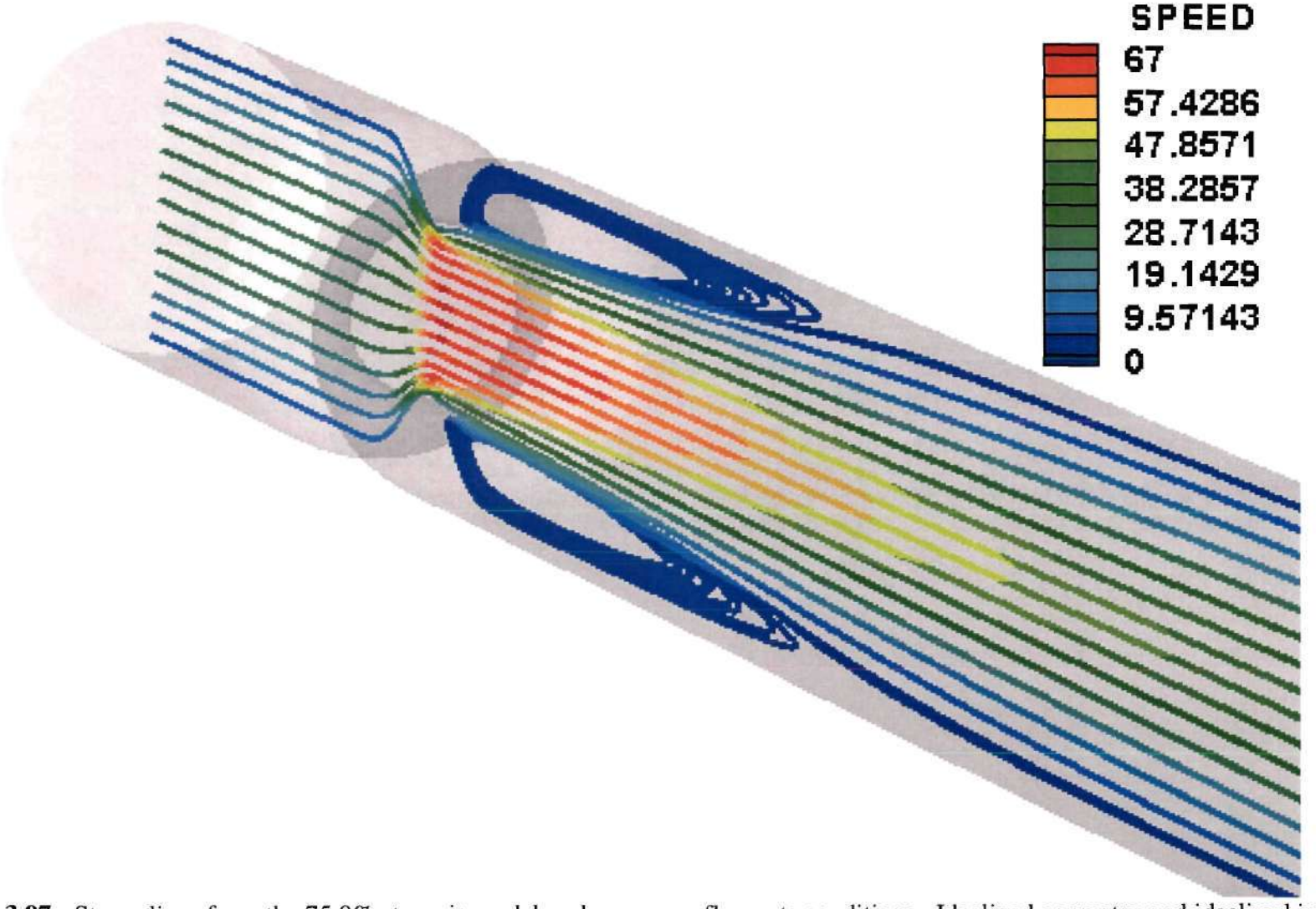

Figure 3.97: Streamlines from the 75.0% stenosis model under average flow rate conditions. Idealized geometry and idealized inlet boundary conditions.

Inlet Boundary Condition Flow Rates

To determine the independent effects of the inlet boundary conditions and the MRI derived geometry on the WSS values calculated, the CFD inlet volumetric flow rates for all CFD simulations were tabulated in Table 3.5.

	Volumetric Flow Rate (cm^3/sec)	**% Error**
0.0% Stenosis Average Flow Rate		
Measured from MRI Flow Loop	4.50	Gold Standard
Ideal Geometry / MRI BC	4.66	3.6%
MRI Geometry / Ideal BC	4.42	1.6%
MRI Geometry / MRI BC	4.55	1.2%
0.0% Stenosis Peak Flow Rate		
Measured from MRI Flow Loop	13.16	Gold Standard
Ideal Geometry / MRI BC	9.31	29.3%
MRI Geometry / Ideal BC	12.97	1.5%
MRI Geometry / MRI BC	9.07	31.1%
52.7% Stenosis Average Flow Rate		
Measured from MRI Flow Loop	4.50	Gold Standard
Ideal Geometry / Ideal BC	4.48	0.5%
Ideal Geometry / MRI BC	3.87	14.0%
MRI Geometry / Ideal BC	4.40	2.2%
MRI Geometry / MRI BC	3.80	15.5%
52.7% Stenosis Peak Flow Rate		
Measured from MRI Flow Loop	13.17	Gold Standard
Ideal Geometry / Ideal BC	13.12	0.3%
Ideal Geometry / MRI BC	8.55	35.1%
MRI Geometry / Ideal BC	12.90	2.0%
MRI Geometry / MRI BC	8.91	32.3%
75.0% Stenosis Average Flow Rate		
Measured from MRI Flow Loop	4.50	Gold Standard
Ideal Geometry / Ideal BC	4.48	0.4%
Ideal Geometry / MRI BC	4.19	6.8%
MRI Geometry / Ideal BC	4.42	1.7%
MRI Geometry / MRI BC	4.08	9.4%

Table 3.5: Inlet volumetric flow rates for all CFD simulations.

WSS Calculations Directly from PC-MRI Velocity Data

0.0% Stenosis Geometry - Average Flow Rate

The WSS values derived directly from the PC-MRI data for the 0.0% stenosis geometry under average flow rate conditions are illustrated in Figure 3.98. All six curve-fitting methods are shown in comparison to the theoretical WSS value in Figure 3.98a. All of the methods that enforced the no-slip boundary condition by forcing the velocities at the wall to zero more accurately predicted the WSS values in the model. However, greater variations in WSS values between adjacent PC-MRI slices were observed for these cases compared to the calculations that did not change the wall velocity values. Overall, the quadratic curve fitting technique with enforcement of the no-slip boundary condition most closely represented the theoretical WSS value. The eight individual axial WSS plots that were used to create the quadratic curve fitting with no-slip boundary condition mean WSS graph are represented in Figure 3.98b. Variations within each axial location were as great as 15 dynes/cm^2 with the maximum standard deviation reaching ± 12 dynes/cm^2. In some cases, both positive and negative WSS values were reported for different angular wall locations located at the same axial location.

0.0% Stenosis Geometry - Peak Flow Rate

The WSS values derived directly from the PC-MRI data for the 0.0% stenosis geometry under peak flow rate conditions are illustrated in Figure 3.99. All six curve-fitting methods are shown in comparison to the theoretical WSS value in Figure 3.99a. All of the methods that enforced the no-slip boundary condition by forcing the velocities

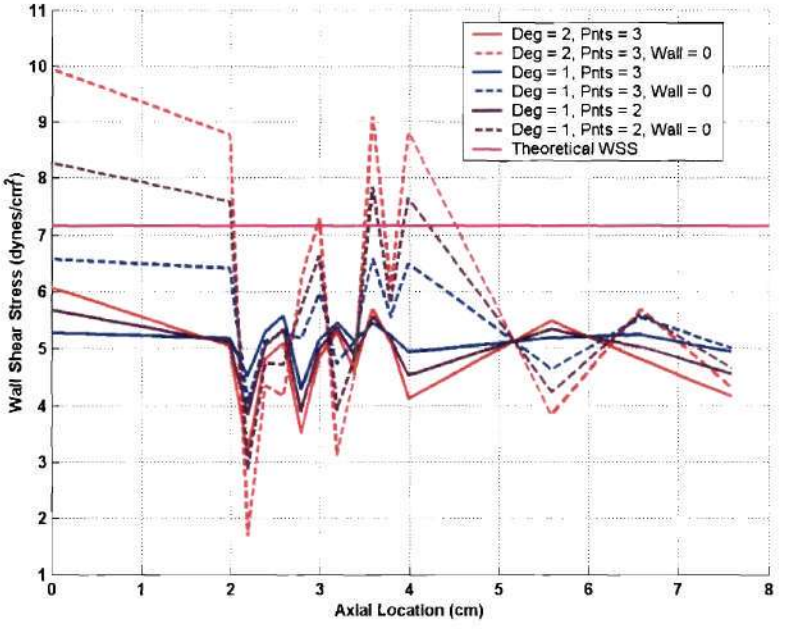

(a) six different methods of calculating WSS. Deg = degree of polynomial fit to near-wall data, Pnts = number of near-wall data points used, Wall = 0 forces the velocity at the wall to zero.

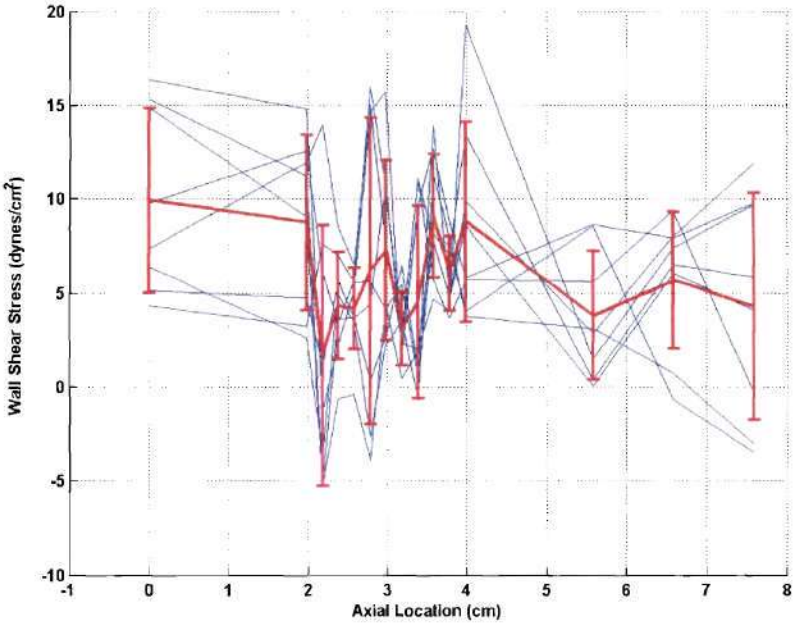

(b) quadratic curve fit with wall velocities forced to zero. All eight axial data sets (blue) and the mean WSS values with standard deviations.

Figure 3.98: 0.0% stenosis average flow rate. WSS values derived directly from PC-MRI data

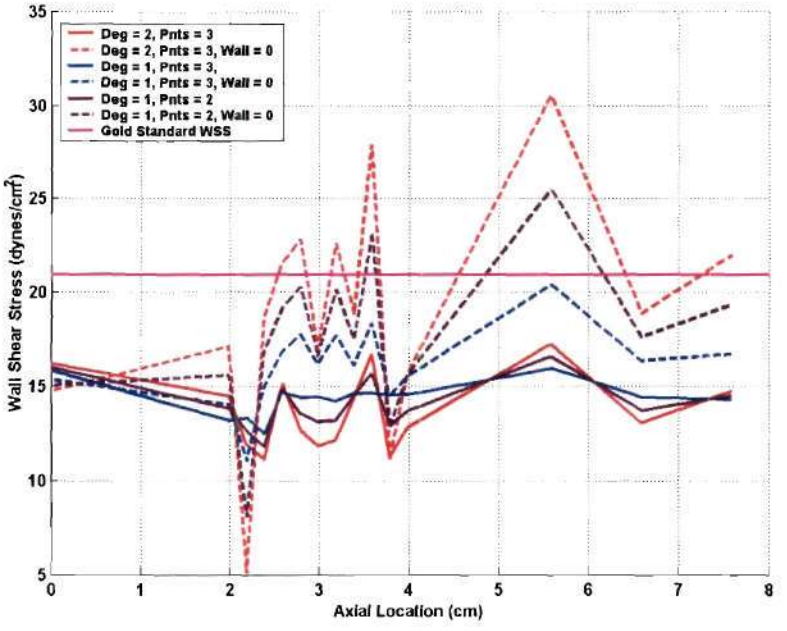

(a) six different methods of calculating WSS. Deg = degree of polynomial fit to near-wall data, Pnts = number of near-wall data points used, Wall = 0 forces the velocity at the wall to zero.

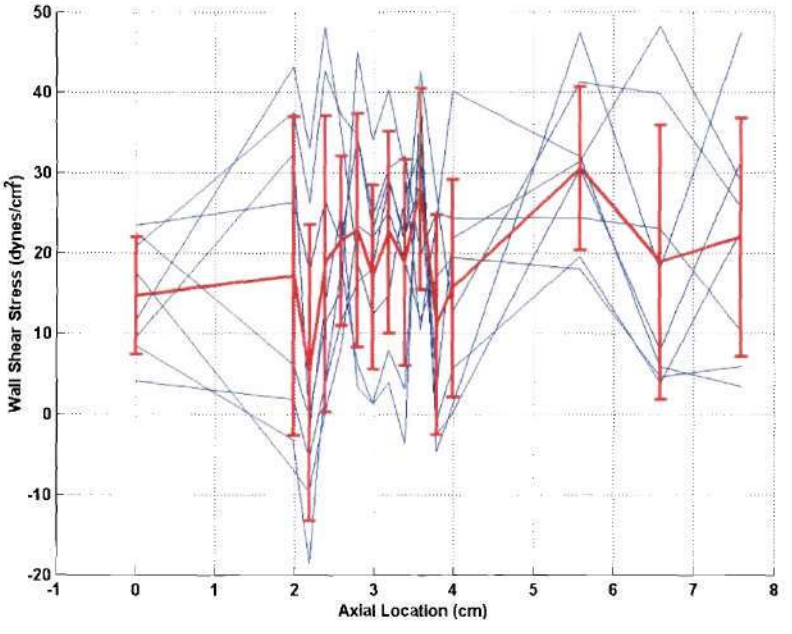

(b) quadratic curve fit with wall velocities forced to zero. All eight axial data sets (blue) and the mean WSS values with standard deviations.

Figure 3.99: 0.0% stenosis peak flow rate. WSS values derived directly from PC-MRI data.

at the wall to zero more accurately predicted the WSS values in the model. However, greater variations in WSS values between adjacent PC-MRI slices were observed for these cases compared to the calculations that did not change the wall velocity values. Overall, the quadratic curve fitting technique with enforcement of the no-slip boundary condition most closely represented the theoretical WSS value. The eight individual axial WSS plots that were used to create the quadratic curve fitting with no-slip boundary condition mean WSS graph are represented in Figure 3.99b. Variations within each axial location were as great as 60 dynes/cm^2 with the maximum standard deviation reaching ± 20 dynes/cm^2. In some cases, both positive and negative WSS values were reported for different angular wall locations located at the same axial location.

52.7% Stenosis Geometry - Average Flow Rate

The WSS values derived directly from the PC-MRI data for the 52.7% stenosis geometry under average flow rate conditions are illustrated in Figures 3.100 and 3.101. All six curve-fitting methods are shown in comparison to the theoretical WSS value in Figure 3.100. The same pattern seen in the 0.0% stenosis models of the quadratic curve-fitting method with the no-slip boundary condition having wide slice-to-slice variations while best approximating the gold standard WSS curve was observed. The maximum and minimum WSS values for the quadratic curve fitting with the no-slip boundary condition method are reported in Table 3.6. The maximum WSS value was almost three times less than the gold standard value. Furthermore, the WSS derived from the PC-MRI data failed to show any true recirculation zone with only one axial location having a negative mean WSS value. The eight different axial WSS plots used to create the mean

WSS plot using the quadratic curve fitting with no-slip boundary condition technique are shown in figure 3.101. As with the 0.0% stenosis models, wide variations in WSS were observed at each slice location. For each axial WSS plot, the maximum WSS value occurred at the actual point of maximum stenosis. In the recirculation region, some axial WSS plots showed WSS values below the gold standard values while others entirely failed to detect any recirculation.

	Maximum WSS (dynes/cm^2) [% error]	**Minimum WSS (dynes/cm^2) [%error]**
52.7% Stenosis Average Flow Rate		
Gold Standard from CFD	62.43	-2.80
Quadratic Curve Fit with V_{wall}=0	21.59 [-65.4%]	-2.05 [26.8%]
52.7% Stenosis Peak Flow Rate		
Gold Standard from CFD	280.79	-17.87
Quadratic Curve Fit with V_{wall}=0	83.13 [-70.4%]	0.18 [101.0%]
75.0% Stenosis Average Flow Rate		
Gold Standard from CFD	196.35	-9.34
Quadratic Curve Fit with V_{wall}=0	51.59 [-73.7%]	-14.59 [-56.2%]

Table 3.6: Maximum and minimum WSS values derived from fitting quadratic curves to near-wall velocity data (V_{wall} forced to zero) derived directly from PC-MRI.

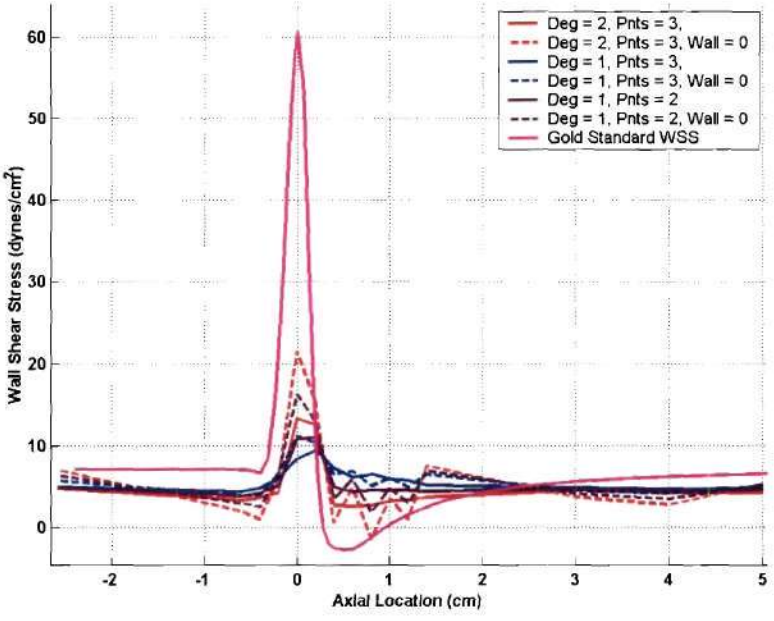

(a) six different methods of calculating WSS.

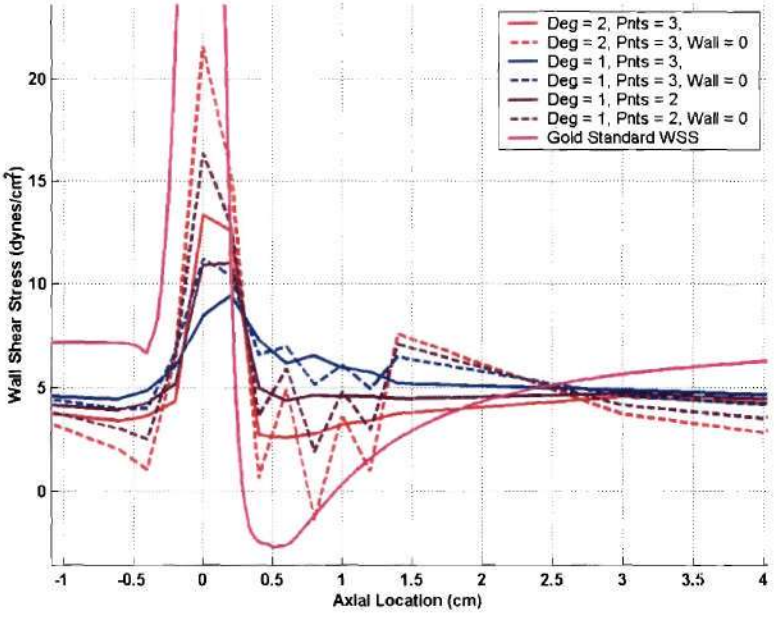

(b) detailed view of graph (a)

Figure 3.100: 52.7% stenosis average flow rate. WSS values derived directly from PC-MRI data. Deg = degree of polynomial fit to near-wall data, Pnts = number of near-wall data points used, and Wall = 0 forces the velocity at the wall to zero.

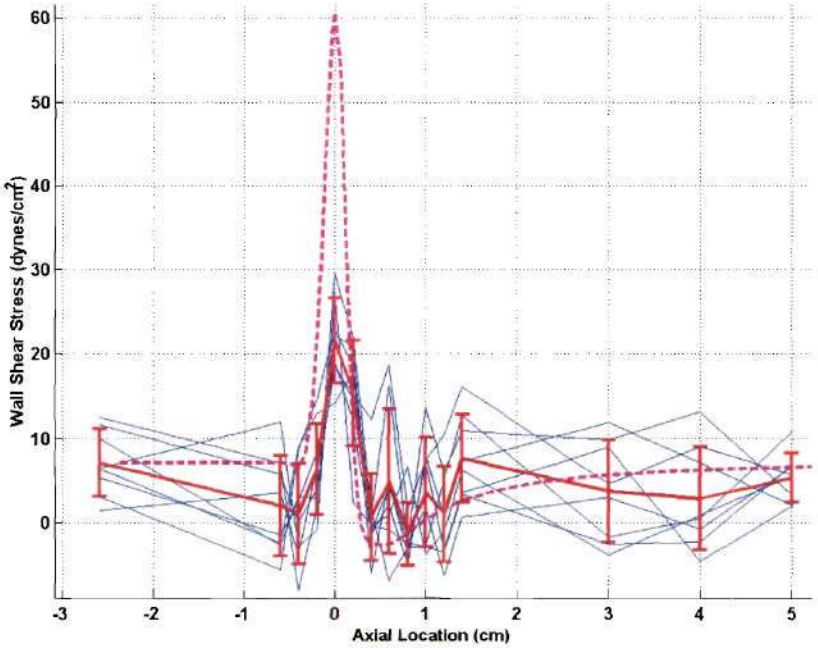

(a) graph of entire axial length.

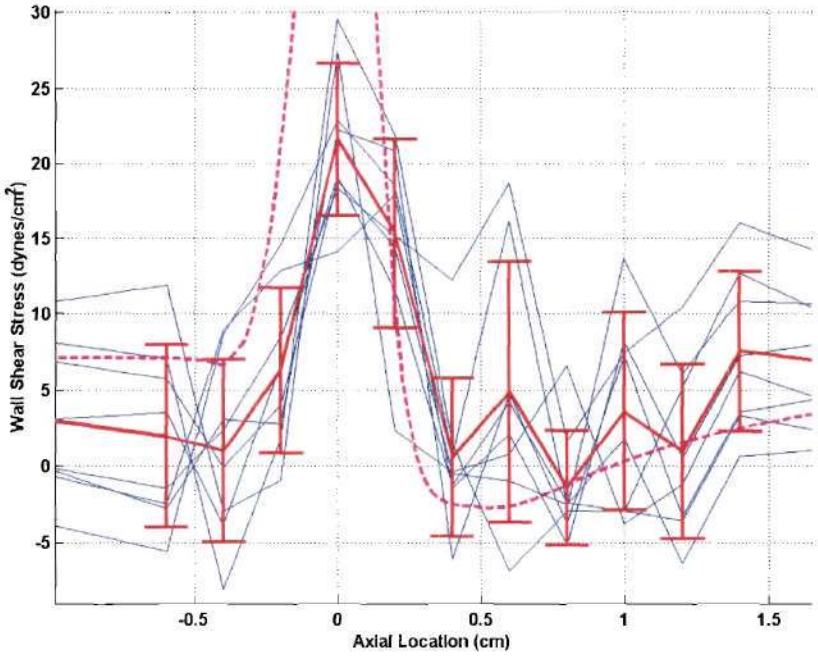

(b) detailed view of graph (a).

Figure 3.101: 52.7% stenosis average flow rate. Quadratic curve fit with wall velocities forced to zero. All eight axial data sets (blue) and the mean WSS values with standard deviations. Gold standard is represented as dashed line.

52.7% Stenosis Geometry - Peak Flow Rate

The WSS values derived directly from the PC-MRI data for the 52.7% stenosis geometry under peak flow rate conditions are illustrated in Figures 3.102 and 3.103. All six curve-fitting methods are shown in comparison to the theoretical WSS value in Figure 3.102. The same pattern seen in the 0.0% stenosis models (the quadratic curve-fitting method with the no-slip boundary condition having wide slice-to-slice variations while best approximating the gold standard WSS curve) was observed. The maximum and minimum WSS values for the quadratic curve fitting with the no-slip boundary condition method are reported in Table 3.6. The maximum WSS value was over three times less than the gold standard value. Furthermore, the WSS derived from the PC-MRI data failed to show any true recirculation zone with no negative mean WSS values reported at any axial location. The eight different axial WSS plots used to create the mean WSS plot using the quadratic curve fitting with no-slip boundary condition technique are shown in figure 3.103. As with the 0.0% stenosis models and the 52.7% stenosis model at average flow rate, wide variations in WSS were observed at each slice location. For each axial WSS plot, the maximum WSS value occurred at the actual point of maximum stenosis. In the recirculation region, some axial WSS plots showed WSS values below the gold standard values while others entirely failed to detect any recirculation.

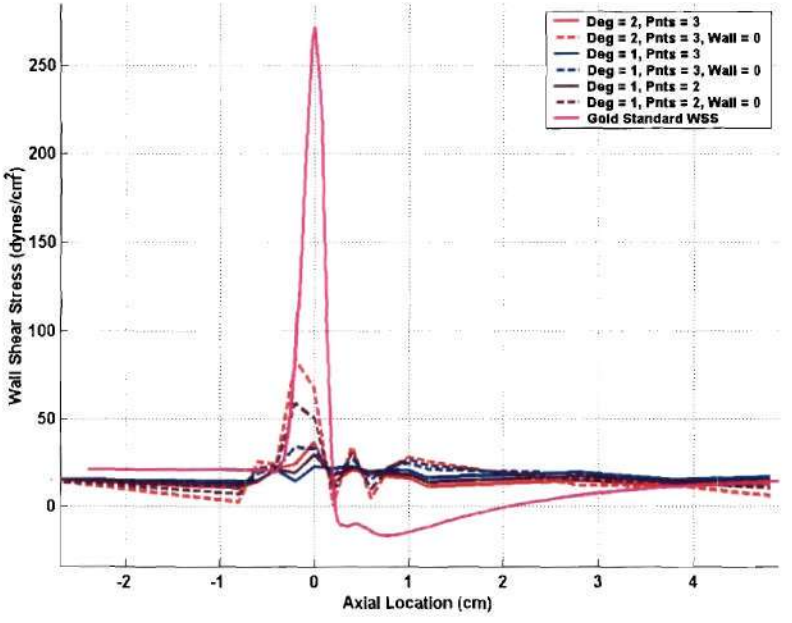

(a) six different methods of calculating WSS.

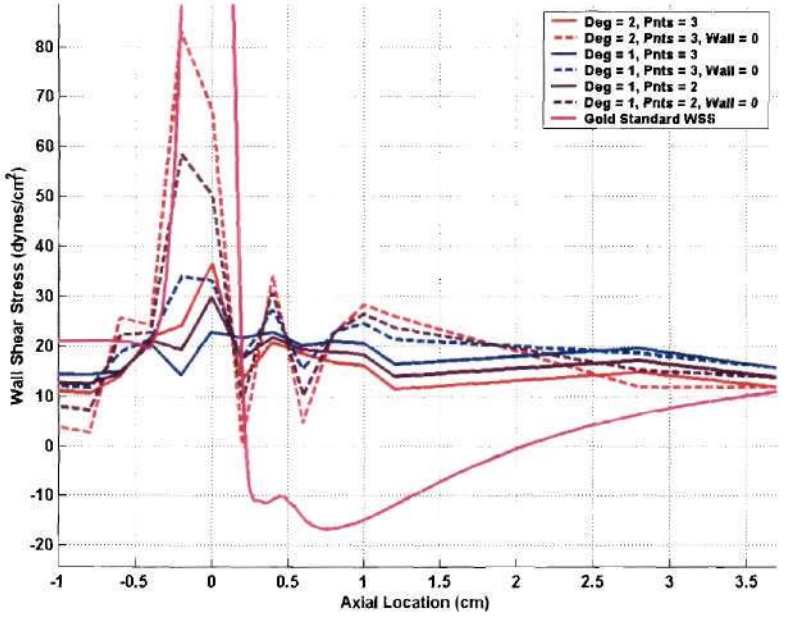

(b) detailed view of graph (a)

Figure 3.102: 52.7% stenosis peak flow rate. WSS values derived directly from PC-MRI data. Deg = degree of polynomial fit to near-wall data, Pnts = number of near-wall data points used, and Wall = 0 forces the velocity at the wall to zero.

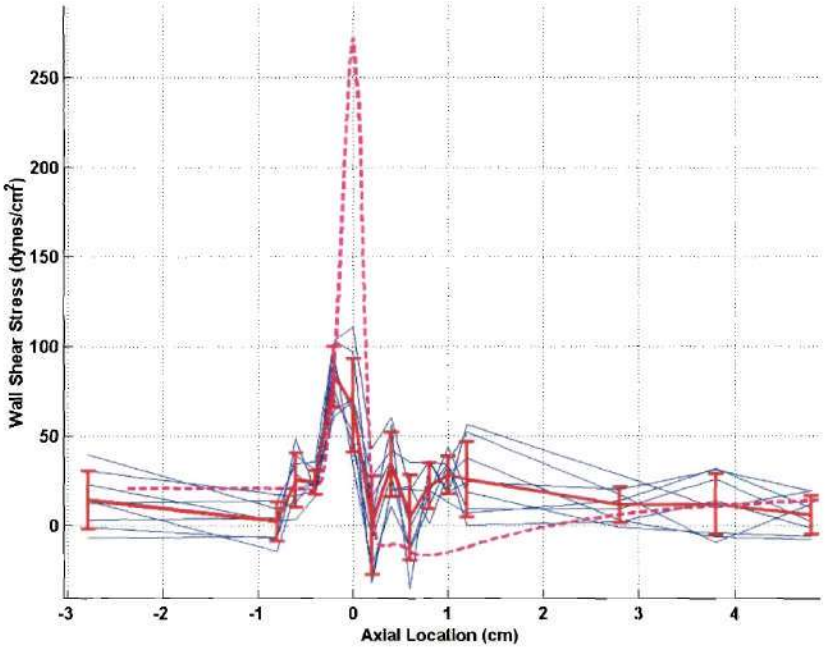

(a) graph of entire axial length.

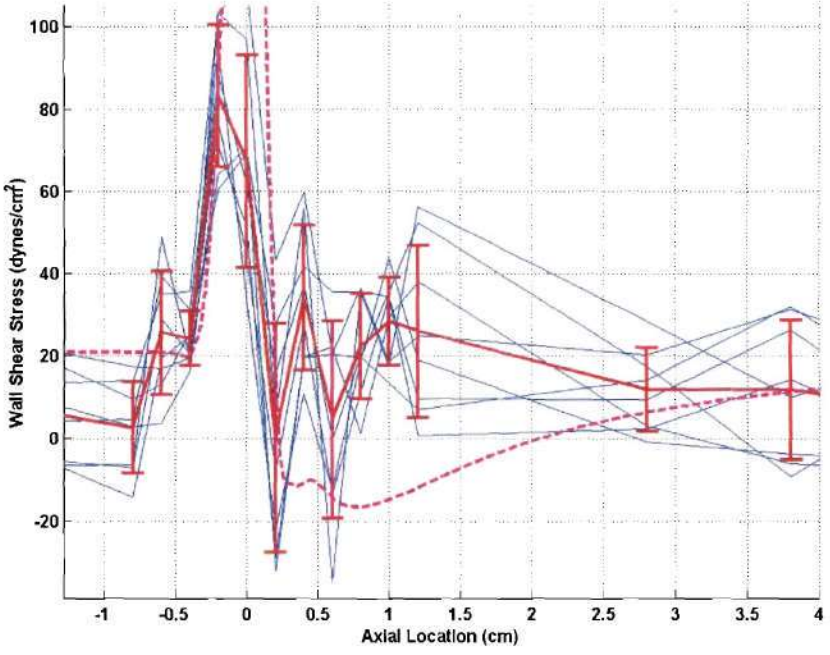

(b) detailed view of graph (a).

Figure 3.103: 52.7% stenosis peak flow rate. Quadratic curve fit with wall velocities forced to zero. All eight axial data sets (blue) and the mean WSS values with standard deviations. Gold standard is represented as dashed line.

75.0% Stenosis Geometry - Average Flow Rate

The same patterns seen in the previous models were observed for the 75.0% stenosis model under average flow conditions and are illustrated in Figure 3.104 and 3.105. The maximum WSS calculated using the quadratic curve fitting with no-slip boundary condition method was approximately four times less than the gold standard values. Unlike the 52.7% models, a recirculation area was predicted which agreed well with the gold standard data. Wide standard deviations in the data sets were observed as in the other models studied.

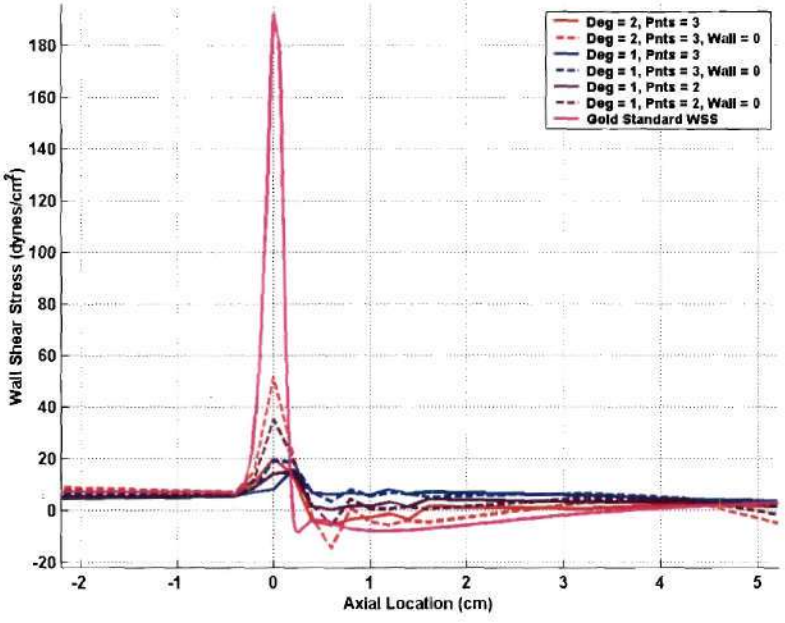

(a) six different methods of calculating WSS.

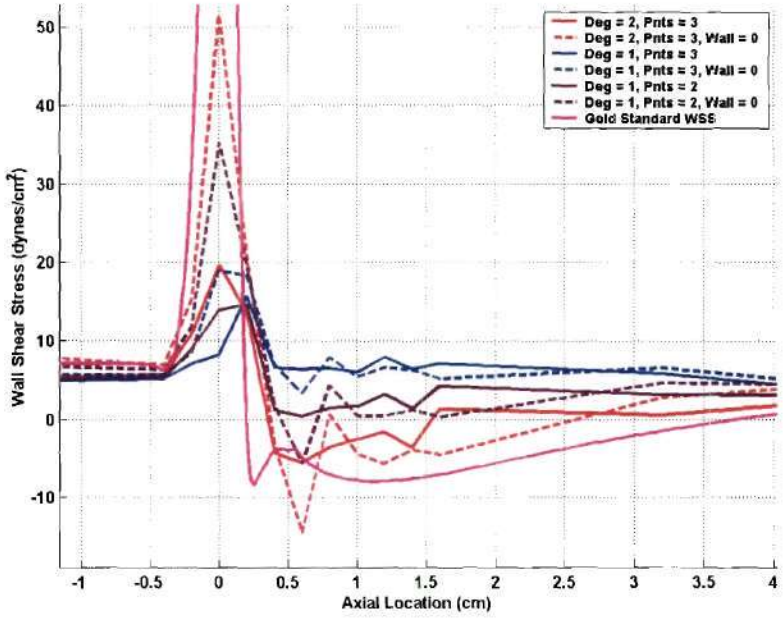

(b) detailed view of graph (a)

Figure 3.104: 75.0% stenosis average flow rate. WSS values derived directly from PC-MRI data. Deg = degree of polynomial fit to near-wall data, Pnts = number of near-wall data points used, and Wall = 0 forces the velocity at the wall to zero.

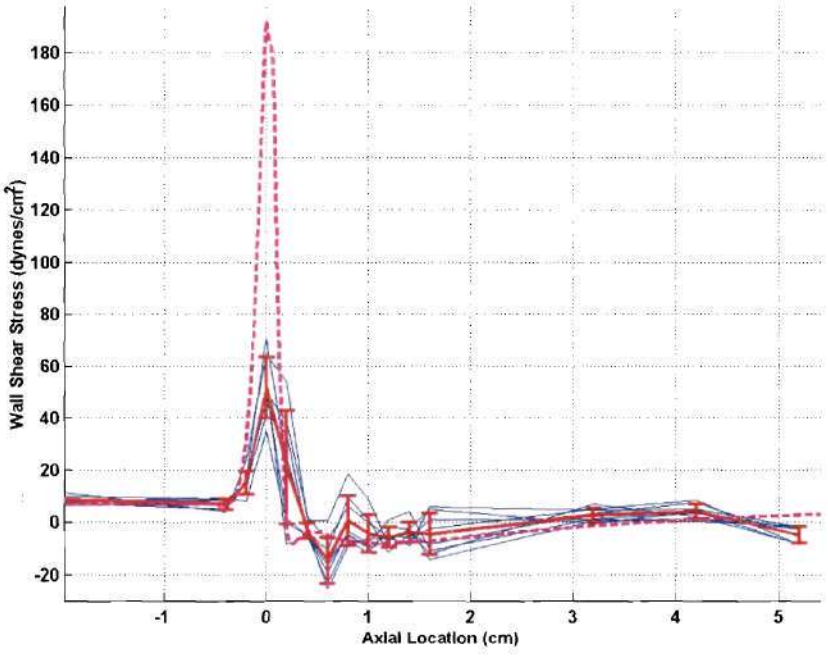

(a) graph of entire axial length.

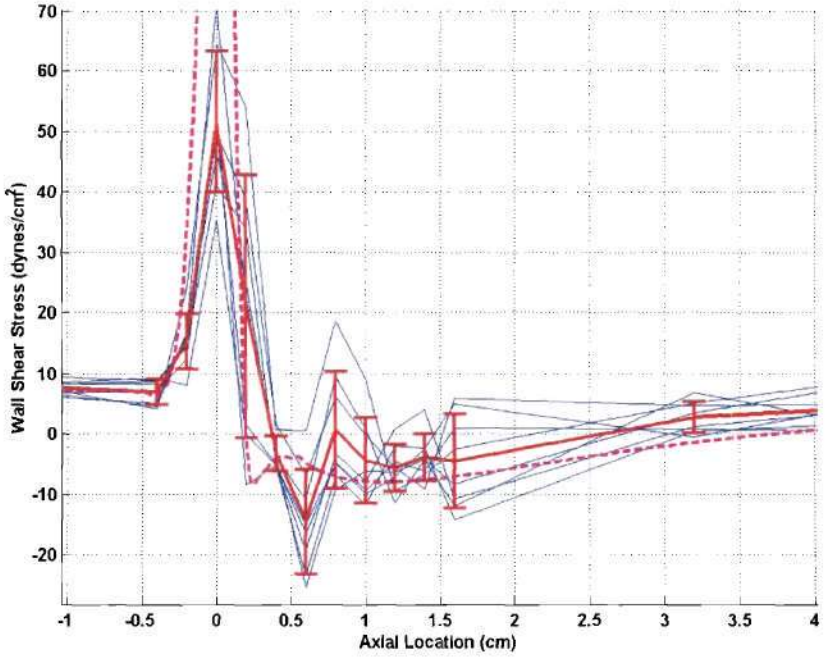

(b) detailed view of graph (a).

Figure 3.105: 75.0% stenosis average flow rate. Quadratic curve fit with wall velocities forced to zero. All eight axial data sets (blue) and the mean WSS values with standard deviations. Gold standard is represented as dashed line.

Summary

Graphs comparing the WSS values derived from CFD and quadratic curve fitting directly to the PC-MRI data with no-slip boundary conditions are compared to each other and to gold standard WSS values in Figures 3.106 – 3.110. For the 0.0% stenosis geometries, larger standard deviations were observed for the WSS values derived directly from the PC-MRI data compared to the CFD simulations. The CFD WSS values were closer to the theoretical WSS values for the average flow rate case (Figure 3.106). The WSS values derived directly from the PC-MRI data better approximated the theoretical WSS values for the peak flow rate. The CFD derived WSS values for the peak flow rate were lower than the theoretical WSS values at all axial locations (Figure 3.107).

For the stenosis geometries, the maximum and minimum WSS values for both methods are summarized in Table 3.7. The CFD derived maximum WSS values were closer to the gold standard values for all cases. The minimum WSS derived from quadratic curve fitting to the PC-MRI data were closer to the gold standard than the CFD simulation. However, the axial location of the minimum WSS was located distal to the gold standard minimum WSS value (see Figure 3.108). The CFD derived minimum WSS for the 52.7% stenosis geometry at the peak flow rate was closer to the gold standard value compared to the direct calculation from the PC-MRI data. The CFD simulation also detected a region of recirculation, which was not detected using the direct calculation method (Figure 3.109).

For the 75.0% stenosis geometry, the CFD simulation did a much better job predicting the maximum WSS value. However, the direct calculation of WSS from the PC-MRI data better represented the recirculation region (Figure 3.110).

	Maximum WSS (dynes/cm^2) [% error]	Minimum WSS (dynes/cm^2) [%error]
52.7% Stenosis Average Flow Rate		
Gold Standard	62.43	-2.80
CFD Using MRI Geometry and BC	35.43 [-43.2%]	-0.66 [76.4%]
Quadratic Curve Fit with V_{wall}=0	21.59 [-65.4%]	-2.05 [26.8%]
52.7% Stenosis Peak Flow Rate		
Gold Standard	280.79	-17.87
CFD Using MRI Geometry and BC	107.10 [-61.9%]	-4.57 [74.4%]
Quadratic Curve Fit with V_{wall}=0	83.13 [-70.4%]	0.18 [101.0%]
75.0% Stenosis Average Flow Rate		
Gold Standard	196.35	-9.34
CFD Using MRI Geometry and BC	148.01 [-24.6]	-5.41 [42.1]
Quadratic Curve Fit with V_{wall}=0	51.59 [-73.7%]	-14.59 [-56.2%]

Table 3.7: Summary table comparing maximum and minimum WSS values derived from (1) CFD simulations based on MRI derived geometry and PC-MRI derived inlet boundary conditions and (2) quadratic curve fitting directly to the PC-MRI velocity data with no-slip boundary condition enforcement.

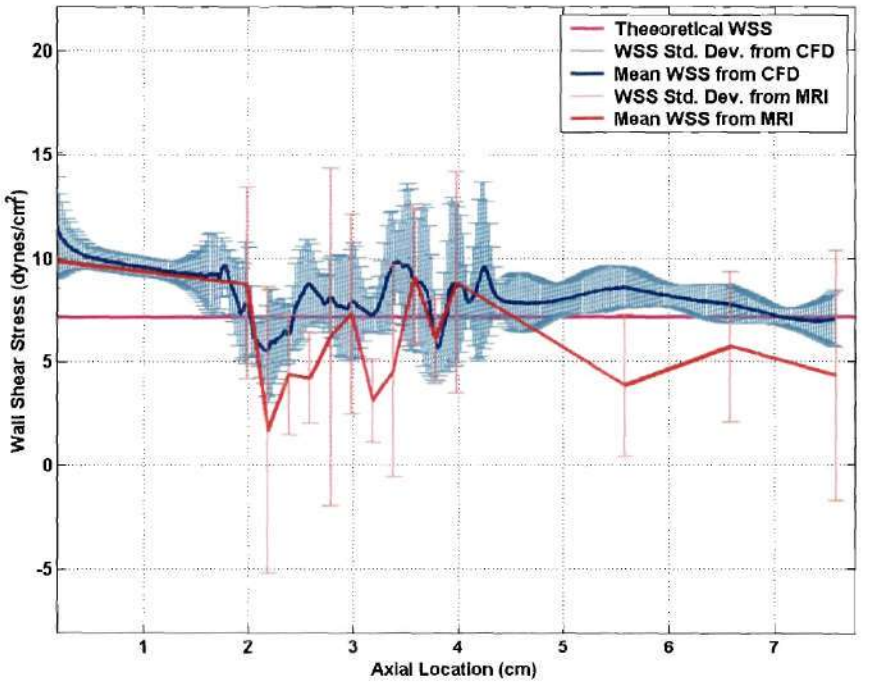

(a) mean WSS with standard deviations.

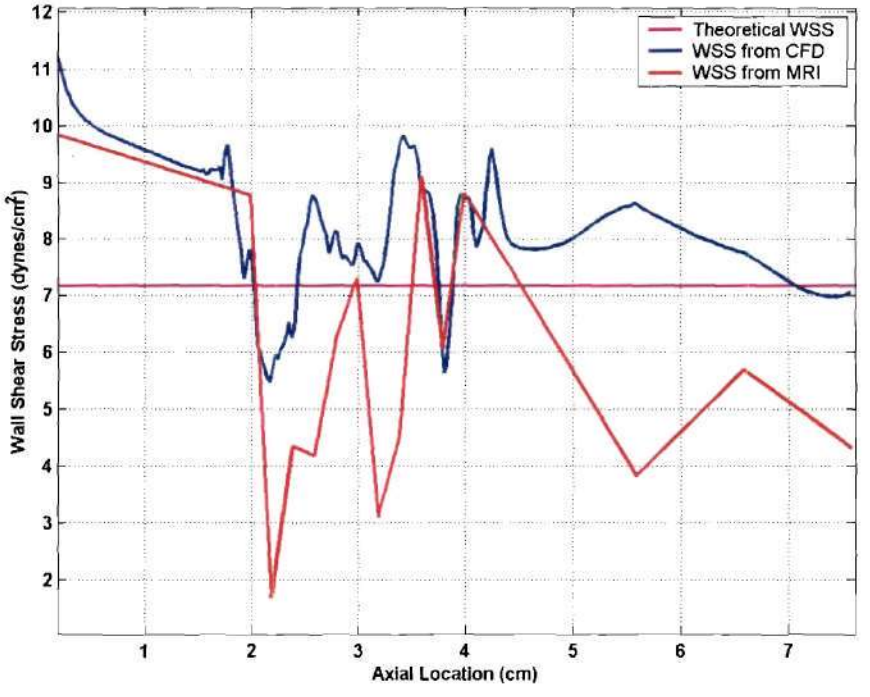

(b) mean WSS.

Figure 3.106: Summary slide for 0.0% stenosis at average flow rate.

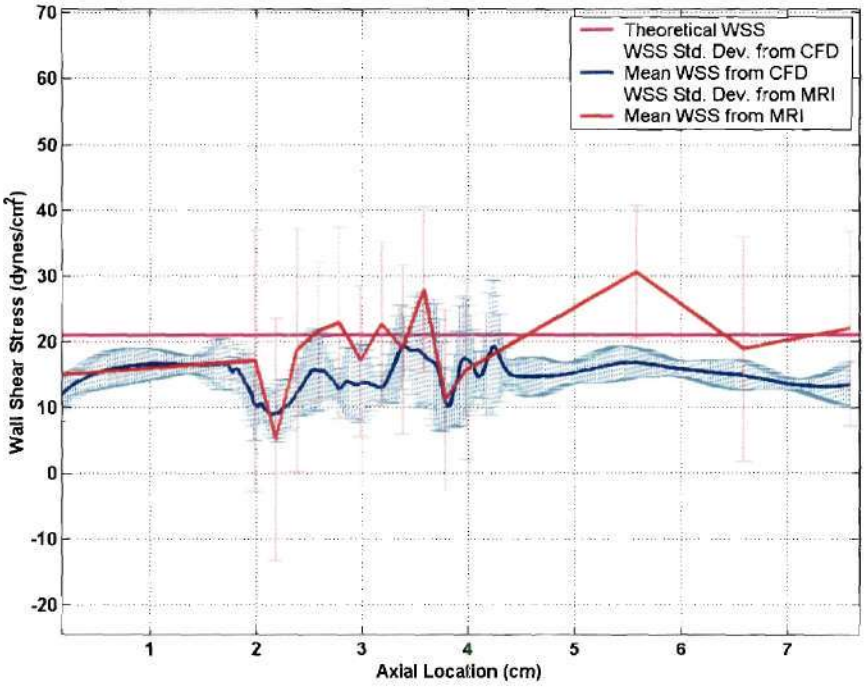

(a) mean WSS with standard deviations.

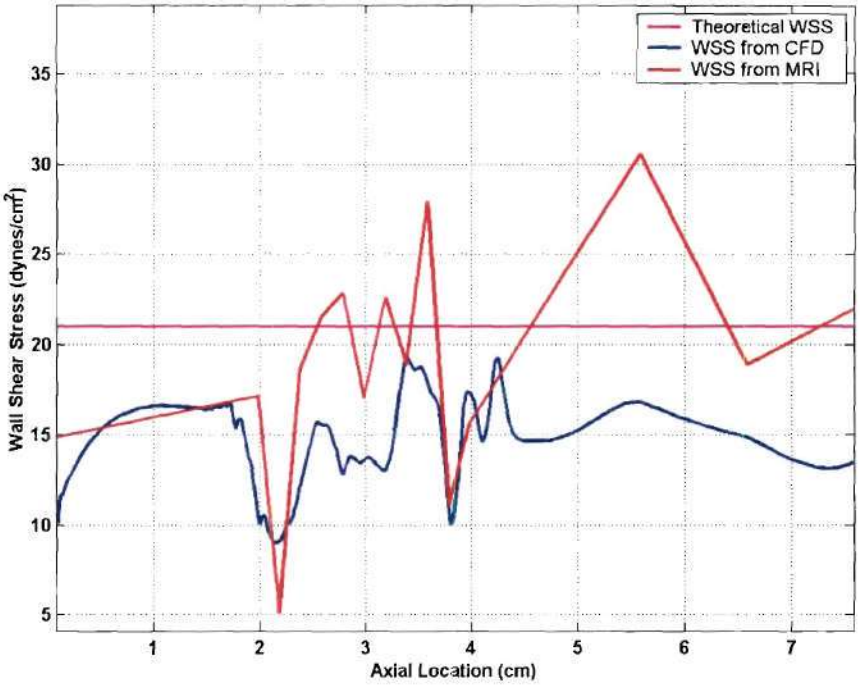

(b) mean WSS.

Figure 3.107: Summary slide for 0.0% stenosis at peak flow rate.

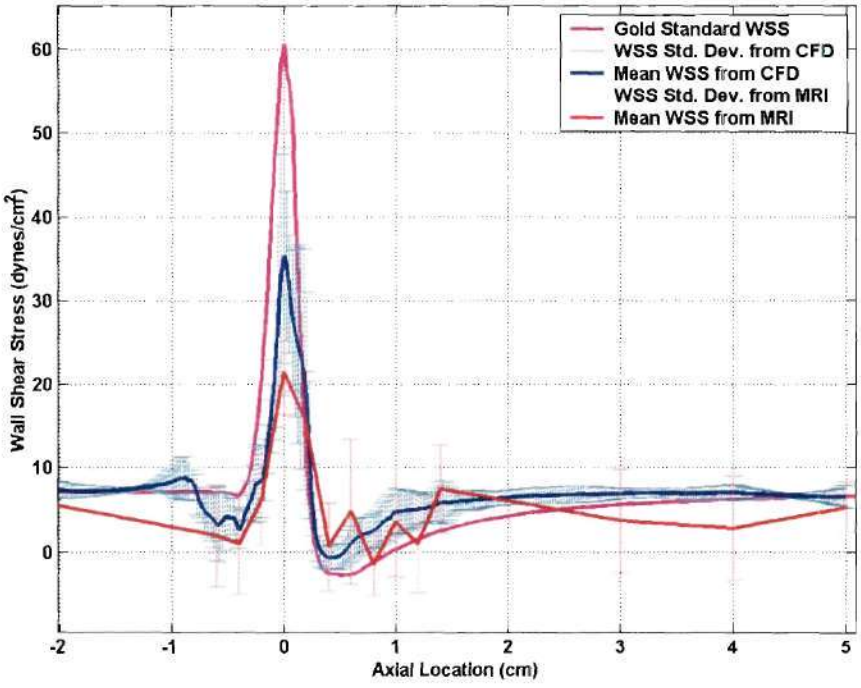

(a) mean WSS with standard deviations.

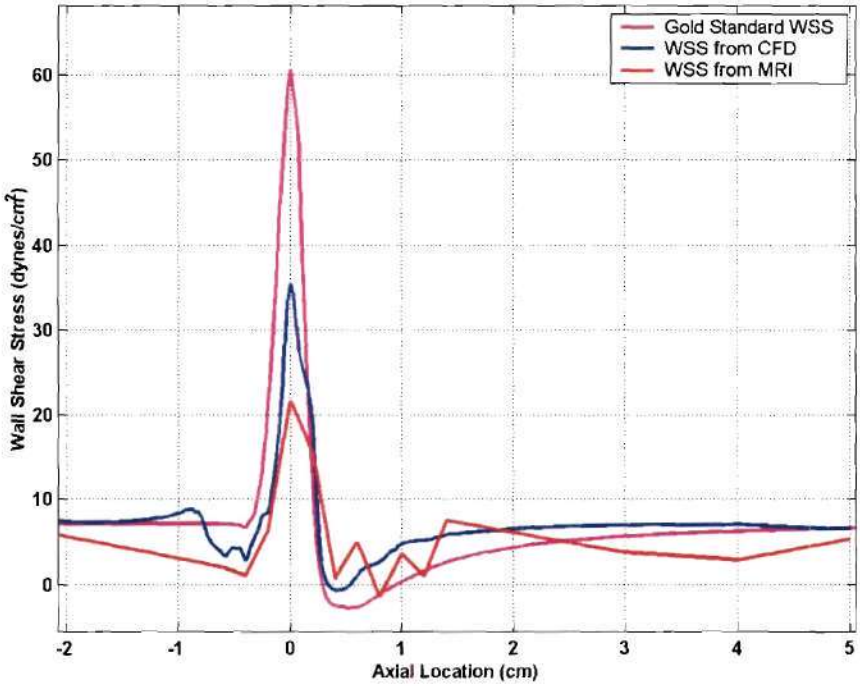

(b) mean WSS.

Figure 3.108: Summary slide for 52.7% stenosis at average flow rate.

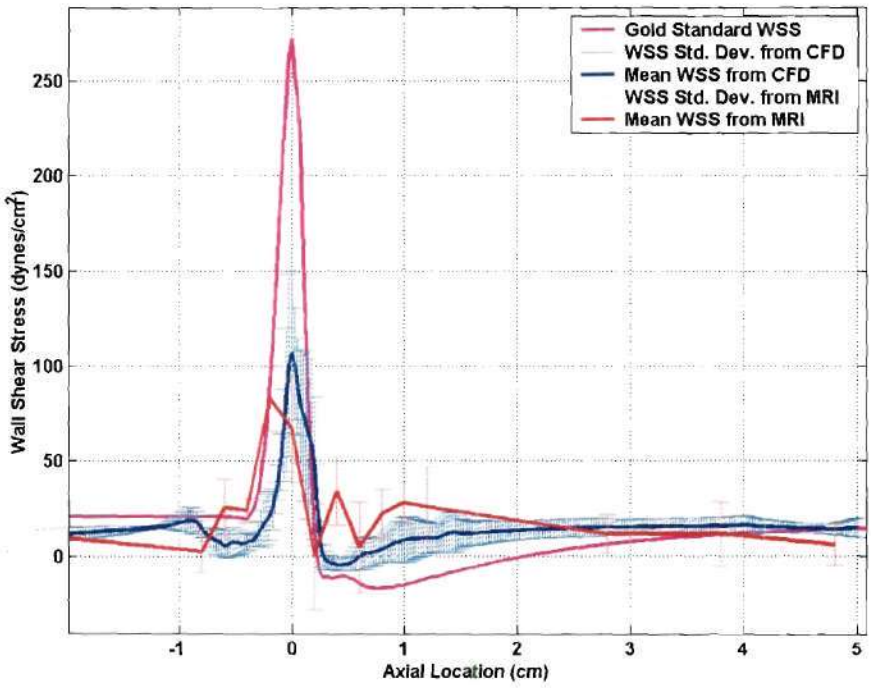

(a) mean WSS with standard deviations.

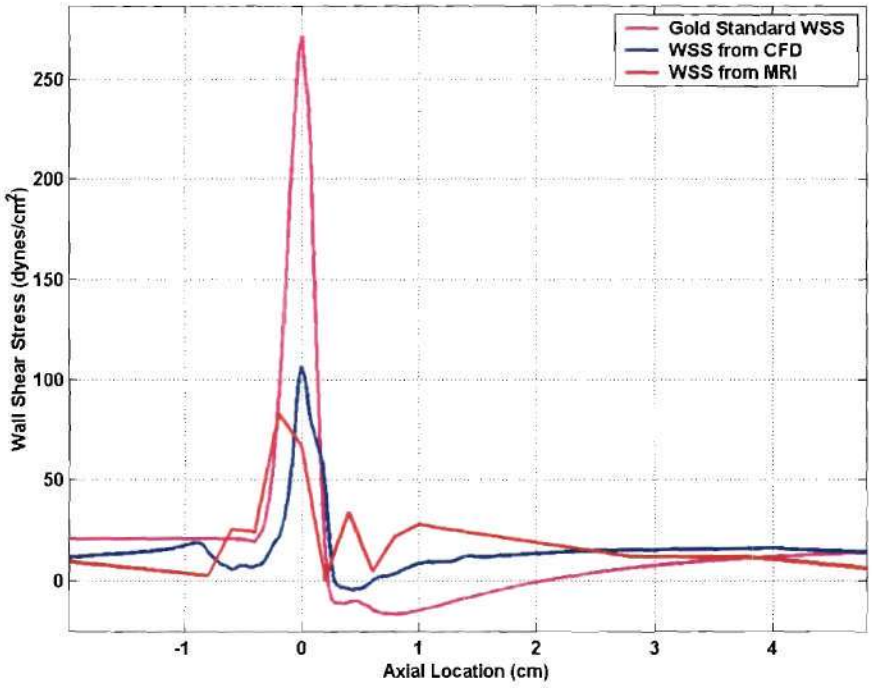

(b) mean WSS.

Figure 3.109: Summary slide for 52.7% stenosis at peak flow rate.

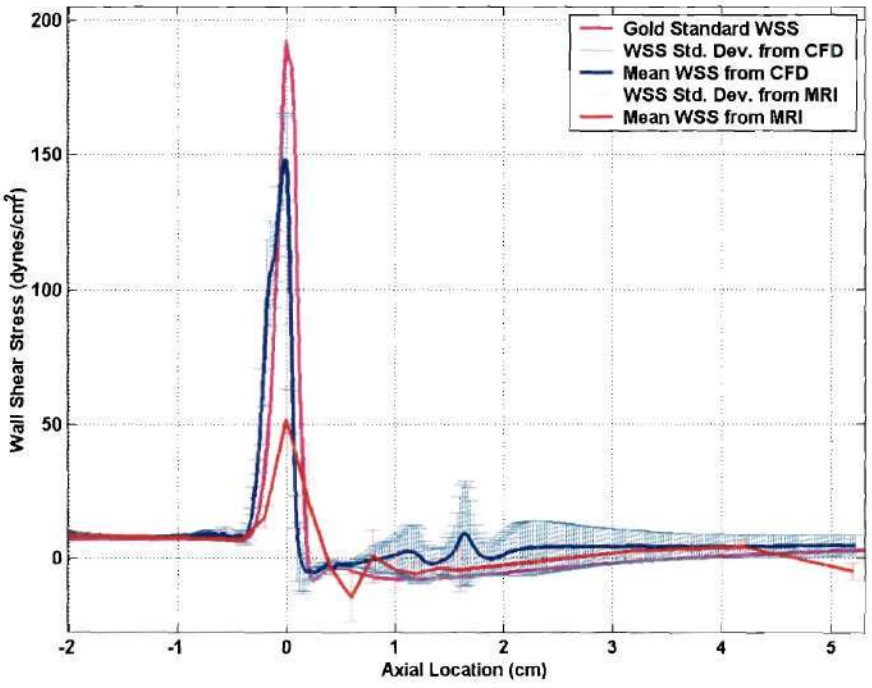

(a) mean WSS with standard deviations.

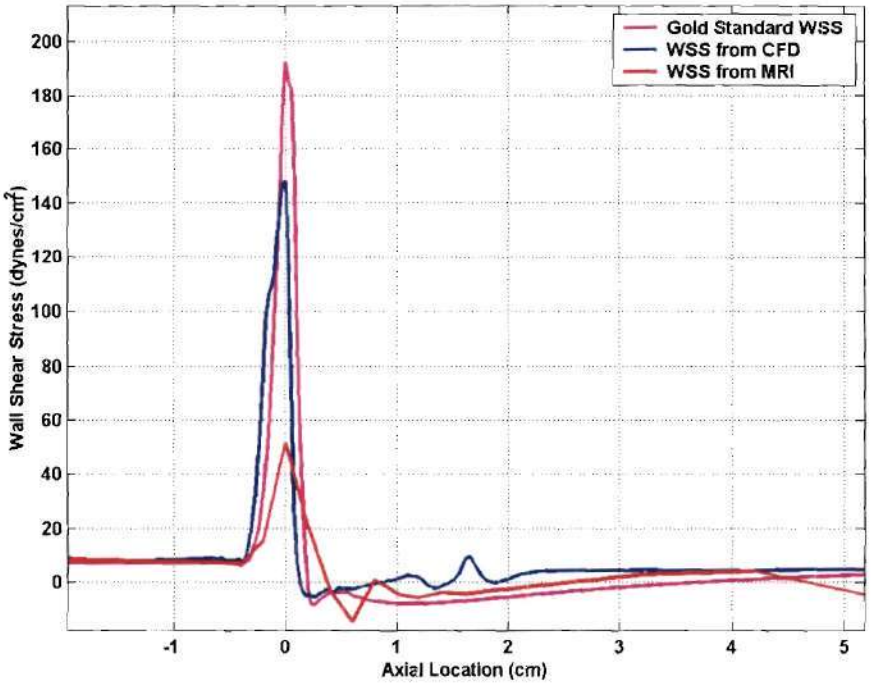

(b) mean WSS.

Figure 3.110: Summary slide for 75.0% stenosis at average flow rate.

CHAPTER IV

DISCUSSION

Experimental Approach

Clinically Relevant Approach

The experimental approaches used in these experiments sought to recreate clinically realistic arterial models and MRI imaging parameters. The scaling of any parameter during PC-MRI data acquisition will lead to non-reproducible results clinically. For example, scaling the arterial phantom geometry while retaining the highest MRI scan matrix will artificially increase the resolution of the resulting images. Increasing the size of the arterial phantom geometry as well as the scan matrix to create the same resolution as expected *in vivo* artificially increases the signal-to-noise ratio by increasing the number of protons per voxel. Selecting a wide slice thickness can also artificially increase the signal-to-noise ratio. In order to capture detailed arterial geometries such as bifurcations and stenoses, the slice thickness must be set sufficiently thin in order to prevent acute geometric entities from being averaged out due to proton signal averaging occurring over large voxel dimensions.

The use of phantom models with liquids having viscosities different from blood also creates artificial increases in data quality. If the geometric scale of the phantoms are equal to the *in vivo* cases in order to match the Reynolds number while using a liquid with a lower viscosity than blood (such as water), the average fluid velocity in the model would be required to be decreased. In doing so, the distance that the protons travel during a set echo time is decreased compared to the clinical case. With protons traveling

smaller distances between excitation and read-out times, the errors associated with proton acceleration and phase mixing would be smaller.

The use of phantoms without cylindrical geometries is also important. The idealized fully developed parabolic velocity profile created by steady flow through such geometries does not occur at any location in the large-to-medium sized arteries where vascular disease is most predominate. The blood vessel bifurcations and curvatures as well as the pulsatility of the pressure and flow waveforms continuously affect the velocity profiles. The errors associated with experimental approaches developed in straight tube models and subsequently applied to clinical images do not represent potential errors in an actual clinical situation.

In addition to not scaling any fluid dynamic parameters during phase contrast studies, it is important to use phantom materials that mimic blood vessel tissue when scanned. Using phantoms made of glass or plastic create artificially precise edge locations that would normally be ambiguous in clinical images. However, the errors in velocity data which occur at the phantom material-working fluid interface create more errors than occur clinically. In all, the PVA phantoms, clinically relevant flow conditions, and MRI scanning parameters used in these studies represent the most realistic PC-MRI phantom studies yet performed.

Flow Visualization and Magnetic Resonance Image Correlation

The flow visualization experiments illustrated the presence of recirculation zones in both stenosis geometries under average and peak flow conditions. Post-stenotic jets were present in all models. Laminar jets were observed to expand until reaching the wall

down stream from the 52.7% stenosis model under average and peak flow rates as well as the 75.0% stenosis model at the average flow rate (Figures 4.1, 4.2, and 4.3). These observations were consistent with the PC-MRI derived velocity profiles that showed narrow parabolic profiles with higher maximum velocities distal to the stenoses (Figures 4.12, 4.13, 4.17, 4.18, 4.22, and 4.23). Turbulent flow patterns were observed in the post-stenotic region of the 75.0% stenosis model under the peak flow condition. Turbulent streaklines were observed in the post-stenotic jet as well as in the recirculation region. These observations correlated well with the PC-MRI images in which complete loss of signal was observed distal to the stenosis (Figures 4.26d, 4.28b, and 4.30b). The PVA modeling material created noise in the PC-MRI data sets. The noise made the blood vessel wall interface more ambiguous compared to glass and plastic phantoms. However, the PVA was also observed to register velocity values that were not random but rather biased in negative velocity values. For example, the PVA material in Figures 4.10a, 4.19a, 4.20b, and 4.25a were all observed to register negative values. This occurred in the first slice, which was slightly larger (5mm) to obtain better CFD inlet boundary condition data, as well as slices further downstream. Further analysis of the complete MRI data sets showed that the negative velocities were not carried throughout the entire model but were rather only observed at certain slice locations. These locations were not consistent from model to model or when the same phantoms were used with different flow rates. This may also be connected to the observation that the WSS values calculated directly from the MRI data followed a saw-tooth pattern where one lower WSS value was often followed by a higher WSS value which was often followed by a lower WSS value (see Figure 4.98a for example). These observations taken together suggest that the MRI

data collected at one slice may have been affected by the excitation or relaxation of protons within an adjacent slice. Furthermore, the data collected under higher velocities had a higher incidence of the PVA material registering a negative velocity. This suggested that the velocity of the fluid of the model might also have influenced the noise produced by the PVA material.

Grid Sensitivity / Independence

The WSS plots used to evaluate the grid independence of the computational models did exhibit patterns toward a grid independent solution as the number of nodes used was increased (see Figures 4.33-4.36). However, in all of the idealized CFD simulation, 3D WSS contours exhibited inhomogeneities not expected in symmetrical models. Prakash and Ethier (2001) also noted that the computational grid resolution required to produce grid independent WSS solutions was very large (>190,000). It was suggested from their observations that an adaptive mesh refinement methodology would be a logical way to approach a grid independent solution without increasing the computational time significantly. Without using the adaptive gridding techniques, a grid independent solution could not be obtained for their studies. The data presented in Figures 4.33-4.36 also suggest that the distance between the model wall and the adjacent node also affected the WSS contours and grid independence. However, as nodes were placed closer to the wall without adding additional angular node locations, the aspect ratio of the near-wall elements became increasingly unfavorable. This added to the computational errors associated with the discretized and truncated Taylor series expansions representing the derivatives of the Navier-Stokes equations. Furthermore, the

growth rate from one element to an adjacent element should not exceed a ratio of 0.5 to prevent further computational errors. Therefore, the decision to place more nodes closer to the wall to better resolve near-wall velocity vectors and WSS values must be weighed against the additional computational errors created. Overall observations of the grid independence studies showed that small variations in the WSS contour graphs occurred when different computational grids were employed. However, the overall distribution and magnitude of the WSS values were not drastically affected by grids using 100,000 nodes compared to grids using 500,000 nodes. The errors associated with grid dependent solutions were small when compared to errors associated with edge detection, computational geometry reconstruction and smoothing, and inlet boundary condition definition encountered in the present studies. Therefore, given the limitations in computational speed and storage capacity as well as the need for fast data acquisition and presentation for clinical decision-making, CFD hemodynamic simulations may not require grid independent solutions to yield optimum clinical outcomes.

WSS Values Calculated from CFD Solutions

For each geometry and flow rate, four different CFD simulations were carried out to determine the independent and additive effects of the reconstructed computational geometries and PC-MRI derived boundary conditions on the predicted WSS values. The results of these experiments are summarized in Table 4.4.

To determine the effects of the PC-MRI derived inlet boundary conditions independent of the MRI derived geometries, these inlet velocity profiles were applied to the corresponding idealized stenosis geometries. In all cases, the WSS distributions observed at the inlet region of the models were greatly affected by the PC-MRI prescribed inlet velocity profile. However, these effects were quickly dissipated. The WSS patterns for the idealized geometries just proximal to the stenoses were observed to be smooth and asymptotically approaching steady state levels. The major effects of the inlet boundary conditions were the average flow rates predicted by the PC-MRI data rather than the actual velocity profile. Given these volumetric flow rates, the theoretical WSS values for the steady flow of a Newtonian fluid through a smooth, straight, cylindrical pipe were calculated. The WSS values derived from the average flow rate CFD results were very close to the theoretical WSS values just proximal to the stenosis. Furthermore, the WSS values approached the same values distal to the stenosis and related recirculation zone. The peak flow rate CFD simulations underestimated the theoretical WSS value proximal to the stenosis as well as at the point of flow field recover distal to the recirculation zone. This was caused by an underestimation in the inlet volumetric flow rate magnitude and was not affected by the inlet velocity profile shape.

The volumetric flow rates of all studies were computed and summarized in Table 4.5. For the average flow rate cases, the volumetric flow rate errors were 3.6%, 14.0%, and 6.8% for the 0.0%, 52.7%, and 75.0% stenosis models, respectively. However, the errors for the peak flow rate models were 29.3% and 35.1% for the 0.0% and the 52.7% stenosis models, respectively. Further analysis of the entrance velocity profiles for the peak flow rate simulations (Figures 4.48 and 4.55) showed a significant number of PC-MRI derived negative velocity values assigned to the near-wall nodes in the inlet computational grid. These errors were attributed to the same problems discussed earlier regarding the PVA material and the excitation and relaxation of protons in adjacent slices.

The effects caused by the geometry reconstruction independent of the PC-MRI derived inlet boundary conditions were determined by applying idealized inlet velocity profiles to the MRI derived computational geometries. The errors associated with the geometries were also observed in the models using the PC-MRI derived boundary conditions and the MRI derived computational geometries. The same WSS patterns were observed for both simulations. The magnitudes of the WSS values were lower for the PC-MRI defined boundary condition simulations due to the errors associated with the corresponding underestimation of the volumetric flow rates.

In addition to the errors in maximum and minimum WSS caused by the geometry reconstruction, the MRI derived geometries also caused errors between WSS values examined at the same axial locations but different angular locations. This is illustrated in Figures 4.64 and 4.69 where the eight WSS versus axial location plots, which were used to create the mean WSS and standard deviation values, are displayed in the same figure.

The eight WSS plots appeared to oscillate independently of each other. Furthermore, the oscillations appeared to be greater at the center of the model compared to the entrance and exit regions. These oscillations were caused by small bumps created in the geometry. These geometric errors occurred at the stage of smoothing the individual edges detected from each MRI slice as well as the construction of the 3D geometry by using spline lines to connect the individual edges. The oscillations increased at the center of the model since more slices were taken at that location which corresponded to the stenosis position. The spline algorithm used to connect those slices was forced to match the first and second derivative of adjacent edge points that were separated by only 2mm. The entrance and exit locations appeared to have lower errors due to less geometry fluctuations. In these regions, the spline algorithm used to connect the adjacent slices had a greater distance to create a curve matching the first and second derivatives. Therefore, the curves connecting these slices allowed the curvature to change more gradually. Consequently, the desire to obtain more information about local geometry curvature by using a greater number of slices with smaller thicknesses, must be balanced against the decreased signal-to-noise ratio and the greater errors created by meshing the two-dimensional edges with less intervening space into a three-dimensional computational geometry.

The asymmetric velocity profiles were also observed to affect the WSS contours. The WSS contour plots for the stenosis geometries are shown in Figures 4.78, 4.84, and 4.90. For all cases, the plots showed asymmetric WSS contours with a region where no recirculation was present. This also occurred for the CFD simulations using the MRI derived geometries and the ideal inlet boundary conditions suggesting this was a

geometric error. The WSS values in the stenosis geometries appeared to be influenced by the post-stenotic laminar jets. Due to geometry asymmetry proximal to the stenosis and through the stenosis, the post-stenotic laminar jets appeared to be skewed toward one side of the phantom wall. This was illustrated in the velocity contour plot for the 75.0% stenosis model under average flow rate conditions shown in Figure 4.91. The resulting asymmetric recirculation zone is shown in Figure 4.94. The geometric errors occurring proximal to the stenosis influenced the velocity vectors and WSS values at that location as well as areas distal to the stenosis. Therefore, errors generated by computational geometry reconstruction from MRI images can propagate downstream through the model.

Therefore, the reconstruction of the geometry was the predominate source of error for the average flow rate cases for all three geometries. For the peak flow experiments, the PC-MRI derived boundary condition was the predominate source of error for the 0.0% and 52.7% stenosis geometries (see Table 4.4).

Given these results, the application of this geometry reconstruction technique to clinical cases is limited. Each simulation that represented the results expected clinically (geometry and inlet boundary conditions derived from MRI data) was able to predict post-stenotic recirculation zones. The extent of these zones at their maximum length approached the gold standard values. The simulations were also able to predict the point of maximum stenosis which correlated with the maximum WSS values. However, in order to reduce the geometric errors, the computational geometries would need to be smoother. By further smoothing the geometries, the effects of acute changes in the vessel wall contour that are actually present in the blood vessels could be lost. The results of this study confirm that the presence of these acute changes can cause large fluctuations in

WSS values locally as well as at downstream locations. The errors associated with using this technique on asymmetric stenosis geometries has not been tested. However, the possibility of pre-stenosis geometry errors skewing the post-stenotic jet toward the wall expected to have a recirculation zone could cause the false-negative errors (no recirculation error predicted when one is present).

WSS Values Calculated Directly from PC-MRI Velocity Data

0.0% Stenosis Models

The WSS values derived from the 0.0% stenosis model can be compared to the results from other investigators that have used the same simple model. For this study, the quadratic curve fitting applied to the two velocity points adjacent to the wall and the wall velocity, which was forced to zero, yielded the best results (Figures 4.98a and 4.99b). The eight angular locations where the WSS was measured for each slice were averaged to determine the mean WSS values and corresponding standard deviations. The errors associated with mean WSS values calculated for the 0.0% stenosis models were 18.14% and 9.5% for the average and peak flow rates, respectively. Both WSS values were underestimations of the theoretical values.

Masaryk et al. (1999) reported an error of 17% when linear curves were fitted to the near-wall velocity data and the edge location was predicted to sub-pixel resolution. These results were better than the linear curve fitting without special edge detection techniques as well as the quadratic curve fitting which yielded 59% and 22% errors, respectively. In these studies, agar phantoms were used to replicate the fluid-vessel wall

interface just as PVA was used in the current study. However, a 10mm slice thickness and a 0.7mm in-plane resolution were used for each MRI image acquired.

Frayne et al. (1995) reported WSS errors of 15% when using a special Fourier encoded scan sequence. However, this sequence required 136 minutes to acquire the data. This large scan time would not be practical in the clinical setting due to the limited MRI resources available. A slice thickness of 20mm was used for this study with an in-plane resolution of 0.78mm.

Oyre et al. (1998b, 1998c) estimated WSS errors of 2.3% and 6.3% for two different flow rates examined. The diameter of the model was 8mm. The slice thickness used was 7mm and the in-plane resolution was 0.5mm. It was stated in the results that "For each flow rate, we made 10 measurements where the acquisition matrix relative to the vessel wall was moved randomly (from 0.1 – 3.5 mm) to different in-plane positions...." This methodology created ten-times as many points available for the near-wall 3D parabolic curve fitting technique used. Although not reported, the MRI scan time required to obtain this data was probably increased ten fold as well. The other inconsistency associated with this study was the WSS values that were measured were approximately 0.87 dynes/cm^2 and 1.26 dynes/cm^2. Even though the dynamic viscosity of the fluid used in this study was approximately three times less viscous compared to blood, the strain rates measured in the system were lower than those expected clinically. Therefore, errors associated with fitting curves to rapidly changing near-wall velocity values would be less evident in this study.

The WSS values obtained from this study for the 0.0% stenosis models agreed well with the results from previous studies that utilized similar techniques. However, the

2mm slice thickness utilized in this study was narrower compared to the other studies (7mm – 20mm). A narrow slice thickness decreased the signal-to-noise ratio, however it was required to detect acute changes in normal and/or pathological arterial geometries. As in the CFD studies, the large variation in WSS values calculated at different angular location within the same axial MRI slice resulted in large WSS standard deviations.

52.7% and 75.0% Stenosis Geometries

For the stenosis geometries, the quadratic curve fitting to the two velocity points adjacent to the wall and the wall velocity, which was forced to zero, yielded the best results as in the 0.0% stenosis geometries (Figures 4.100, 4.102, and 4.103). For all of the models, this curve fitting technique yielded the highest maximum WSS value at the stenosis as well as the lowest minimum WSS values in the recirculation zone. By forcing the wall values to zero, any PC-MRI velocity errors associated with the PVA-phantom wall interface were eliminated. However, by prescribing the wall velocity independent of the other adjacent velocity data recorded, large slice-to-slice variations were observed which resulted in larger standard deviations.

Large WSS standard deviations were also observed for the WSS data calculated from the stenosis geometries. In all cases, the WSS values did increase at the point of maximum stenosis; however, the maximum WSS values calculated severely underestimated the gold standard values (Table 4.6). The distance over which the WSS values peak at the point of maximum stenosis was approximately 1mm. However, due to signal-to-noise ratio considerations, the smallest slice thickness acquired was 2mm. Therefore, either steady state pre-stenosis velocities or lower post-stenosis velocities

were voxel averaged into the data used to calculate the near-wall strain rate. Furthermore, signal-to-noise ratio concerns also limited the in-plane resolution to 0.5mm, which restricted the velocity information available to predict the derivative of the near-wall velocity profile. Partial volume effects associated with determining the near-wall velocity data, as well as the wall location, also contributed to the large errors associated with the maximum WSS values.

The results of this study suggested that limited WSS data could be obtained from the direct calculation of WSS from PC-MRI velocity data. Large errors in wall shear stress were observed for geometries other than straight cylinders. Furthermore, large WSS standard deviations resulted from large variations in WSS data calculated at different wall locations within the same MRI slice. This suggested that the ability to detect any pattern of WSS values in asymmetric geometries where averaging of WSS values is not possible could be severely limited.

Conclusions

The results comparing the direct calculation method and the CFD method used to calculate WSS in this study are shown in Figures 4.106 through 4.110 and Table 4.7. For all cases, the WSS standard deviations were lower for the CFD simulations compared to the direct calculation of WSS from PC-MRI velocity data. In the 52.7% and 75.0% stenosis geometries, the CFD simulations also predicted the maximum WSS values better than the direct calculation method. The extents of the post-stenotic recirculation zones were underestimated by both methods. The CFD derived recirculation zone better approximated the gold standard values for the 52.7% stenosis geometry under peak flow

rate conditions. The recirculation zones estimated from the direct calculation method more closely matched the gold standard values for the 52.7% and 75.0% stenosis geometries under average flow rate conditions. However, the recirculation zone WSS data from this method were less consistent between adjacent MRI data slices.

The errors associated with the direct calculation of WSS from PC-MRI velocity data were associated with the low resolution of near-wall velocity data as well as the inability to accurately determine the wall location from the MRI geometry images. The errors associated with the CFD studies were dependent on the flow rates. At the average flow rates, the computational geometries reconstructed from the MRI geometry data were asymmetrical and irregular. This caused large variations in the WSS values along the axis of the models as well as large standard deviations in WSS measurements at each individual axial location. These errors were dependent upon the distance between adjacent MRI data slices due to large variations in the curvature of the surfaces used to connect the adjacent edge representations. At high flow rates, the PC-MRI derived inlet volumetric flow rates were lower than the actual values measured from the MRI flow loop. This caused an overall decrease in the WSS values derived for the 0.0% and 52.7% stenosis geometries. The irregular computational geometries contributed to the errors for the high flow rate simulations; however, the underestimation of the volumetric flow rate was a larger source of error.

This study showed the feasibility of using the combination of PC-MRI and CFD to non-invasively determine arterial WSS values. The errors associated with this method can be reduced by obtaining higher resolution MRI geometry data and by investigating the under estimations of volumetric flow rates reported in the PC-MRI data at higher flow

rates. The combination of PC-MRI and CFD offers a non-invasive method of determining volumetric flow rates, blood velocity fields, and WSS values which can be used to guide clinical therapy.

Future Work

A large source of error in the CFD studies was the irregularities in the computational geometries reconstructed from the MRI geometry images. A central problem that has not been addressed is what degree of geometry smoothing minimizes errors associated with geometry reconstruction without significantly masking arterial geometry variations that actually exist in patients. Since atherosclerotic plaques are focal in both axial and angular locations in the vasculature, even small areas of low or highly oscillatory WSS values may induce changes in endothelial and vascular smooth muscle cells that promote plaque formation.

The WSS results were associated with large standard deviations for both the CFD simulations and the direct calculation from the PC-MRI velocity data. These represented large variations in WSS values calculated at different angular locations within the same MRI or CFD axial location. Given that symmetrical geometries and fully developed entrance flow conditions were used in the phantom flow loop, these values should have been equal. Since several physiological arterial geometries and pathological atherosclerotic plaques are not symmetrical, the ability of these methodologies to provide meaningful WSS data without averaging values at each axial location is questionable. Therefore, studies including asymmetric phantom geometries should be performed to determine the feasibility of these studies under more physiological conditions.

In the same manner, experiments incorporating pulsatile flow conditions would also create more physiological conditions to test the models. An MRI compatible pulsatile pump or pulsatile value would be required for these studies. The distance required between the metallic pulsatile pump and the models available for this study caused pulsatile waveform dissipation as well as superimposing wave reflections that resulted in non-uniform and non-physiological flow waveforms within the phantom models.

Since MRI image resolution was a large factor in determining the accuracy of WSS values derived from both methods tested, performing similar tests in 3T MRI scanners should be explored. The higher magnetic gradients could allow for greater in-plane and slice thickness resolution that would decrease CFD geometry irregularities as well as provide greater near-wall velocity data.

APPENDIX A

WSS CALCULATION APPROXIMATION

The definition of wall shear stress is the dynamic viscosity of the fluid multiplied by the gradient of the three-dimensional velocity vector parallel to the arterial wall, evaluated at the wall. For a Newtonian fluid, this can be written as

$$\tau_{wall} = \mu \left(\frac{\partial \vec{V}_{\tan gent}}{\partial \hat{N}} \right)_{wall}$$

In order to obtain all three components of the velocity vector using phase contrast MRI, the total scan time is increased by three times compared to the time required to obtain one component. Efforts should be investigated to reduce MRI scan time since it is a limited clinical resource. Furthermore, given the errors associated with reconstructing arterial geometries from MRI images, the computation to determine the vector normal to the wall at every wall location examined may add more error to the final WSS value.

Two-dimensional CFD studies were used to determine the error associated with calculating WSS values with only the axial component of the velocity vector and without regard to its orientation to the normal vector to the wall. A computational geometry representing the 75.0% symmetric stenosis was created as shown in Figure A.1. Two-dimensional simulations were used to take advantage of the symmetry of the geometry in order to minimize computational errors associated with grid aspect ratios and to gain greater resolution of the near-wall velocity profile by using a high grid density throughout the model. The convergent axial and radial velocity contours are shown in

Figures A.2a and A.2b, respectively. The pressure gradient is shown in Figure A.2c. The convergent three-dimensional velocity vectors were used to calculate the WSS in three different ways. The true WSS was calculated by first decomposing the velocity vector field into components perpendicular and tangent to the wall. The near-wall velocity profiles were then determined by isolating the tangent velocity vectors located along the normal vector to the wall at each wall location examined. The derivative of this velocity profile was taken at the location of the wall and multiplied by the dynamic viscosity used in the CFD simulation.

The first approximation method used only the axial velocity components (not decomposed) located along the normal vector to the wall to determine the near-wall velocity profile. The derivative of the velocity profile was taken at the wall and multiplied by the dynamic viscosity. This case represents a three times faster MRI scan time compared to the first method, and it still takes into consideration the orientation of the velocity values to the local arterial geometry.

The second approximation used only the decomposed axial velocity components as in the first approximation method. However, the local geometry was not considered when the near-wall velocity vectors were determined. Instead, the velocity profiles were constructed from velocity values taken from lines drawn in the radial direction from the wall without regard to the orientation of the radial lines to the local curvature of the arterial geometry. This methodology also represents a three times faster MRI scan time compared to the first method. However, the arterial geometry reconstructed from the MRI images does not affect the WSS solutions except for the determination of the wall location (no local curvature effects).

The results from these three methods are shown in Figures A.3 and A.4. Figure A.3 shows no gross differences between the methods along the entire length of the computational geometry. Figure A.4 shows that the maximum deviation of the WSS approximations occured at the point of maximum stenosis. The methodology that does not make any assumptions predicted a maximum WSS value of approximately 200 dynes/cm^2. The first approximation methodology that used only axial velocity components aligned normal to the local wall curvature predicted a maximum WSS value of 180 dynes/cm^2 (a 10% error). The second assumption methodology that used only axial velocity components without regard to their orientation to the local wall curvature predicted a maximum WSS value of approximately 170 dynes/cm (a 15% error). Moreover, all three methods were able to adequately detect the post-stenotic recirculation region.

Given the errors associated with the MRI resolution and arterial geometry reconstruction, the orders of these errors are below those observed for the 3D CFD simulations and the direct calculation of WSS from the PC-MRI data. Therefore, a three-times reduction in MRI scan time can be realized without significantly adding to the errors associated with calculating WSS values. Furthermore, given the problems associated with reconstructing arterial geometries from MRI images, the WSS calculation method that relies upon the MRI geometry data to only determine the wall location and not the local wall curvature may actually reduce the errors associated with determining WSS values compared to more complex and time consuming methodologies.

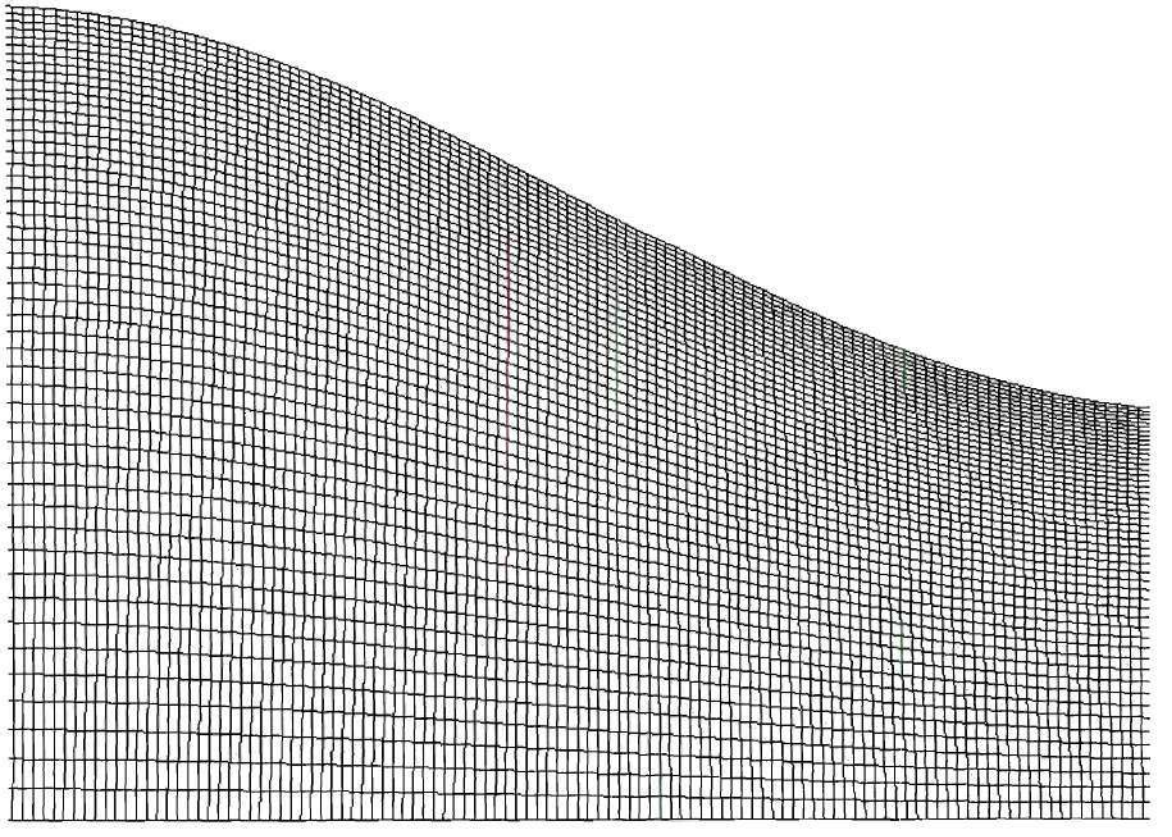

Figure A.1: A representative area of the two dimensional computational grid.

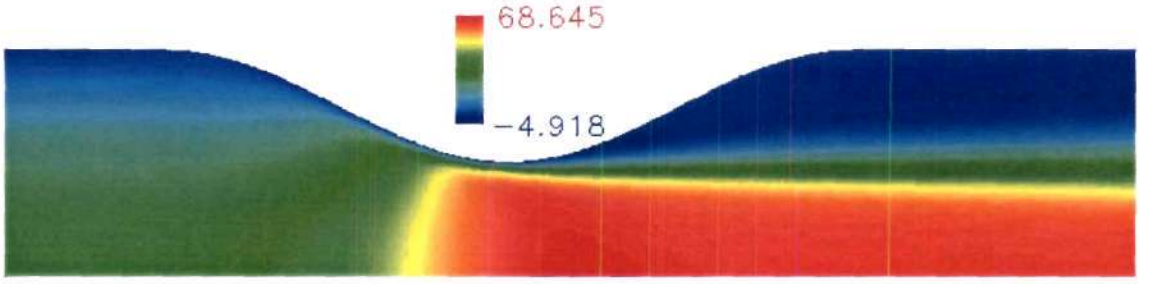

(a) Axial velocity contour plot (cm/sec).

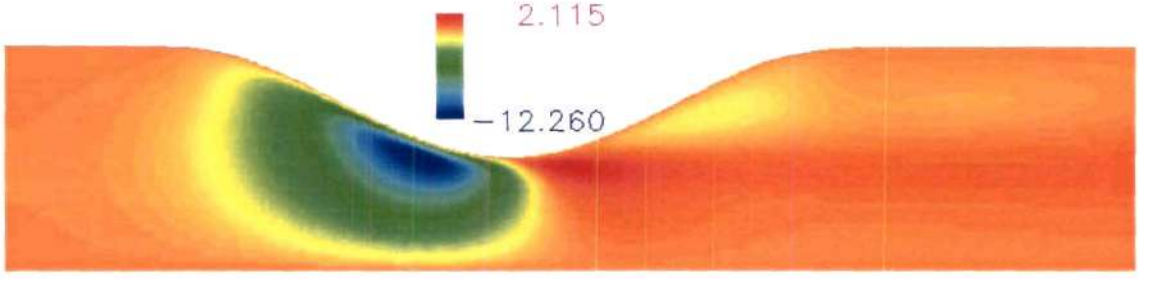

(b) Radial velocity contour plot (cm/sec).

(c) Pressure contour plot (dynes/cm^2)

Figure A.2: Contour plots of the convergent CFD solution using two-dimensional ideal 75.0% symmetrical stenosis geometry and ideal inlet boundary conditions. (a) axial velocity (b) radial velocity and (c) pressure.

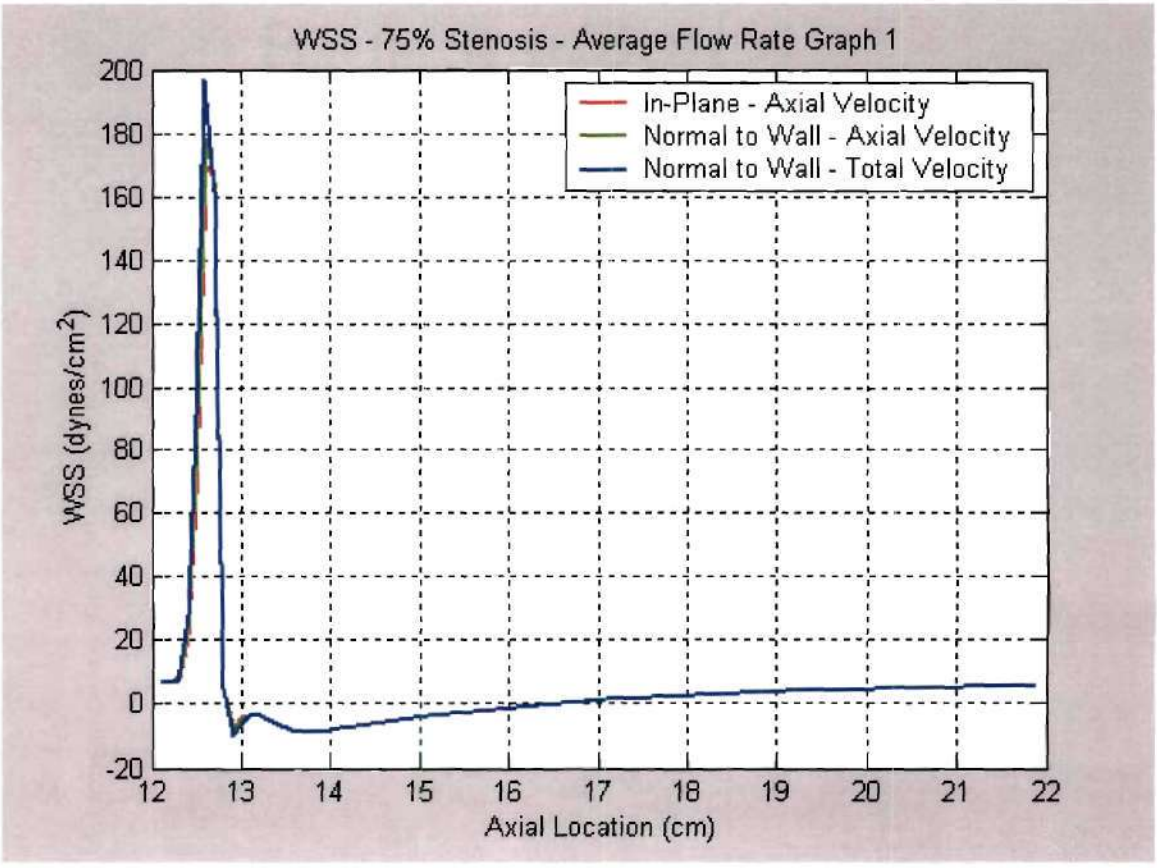

Figure A.3: Plot of the three methods used to compute the WSS values.

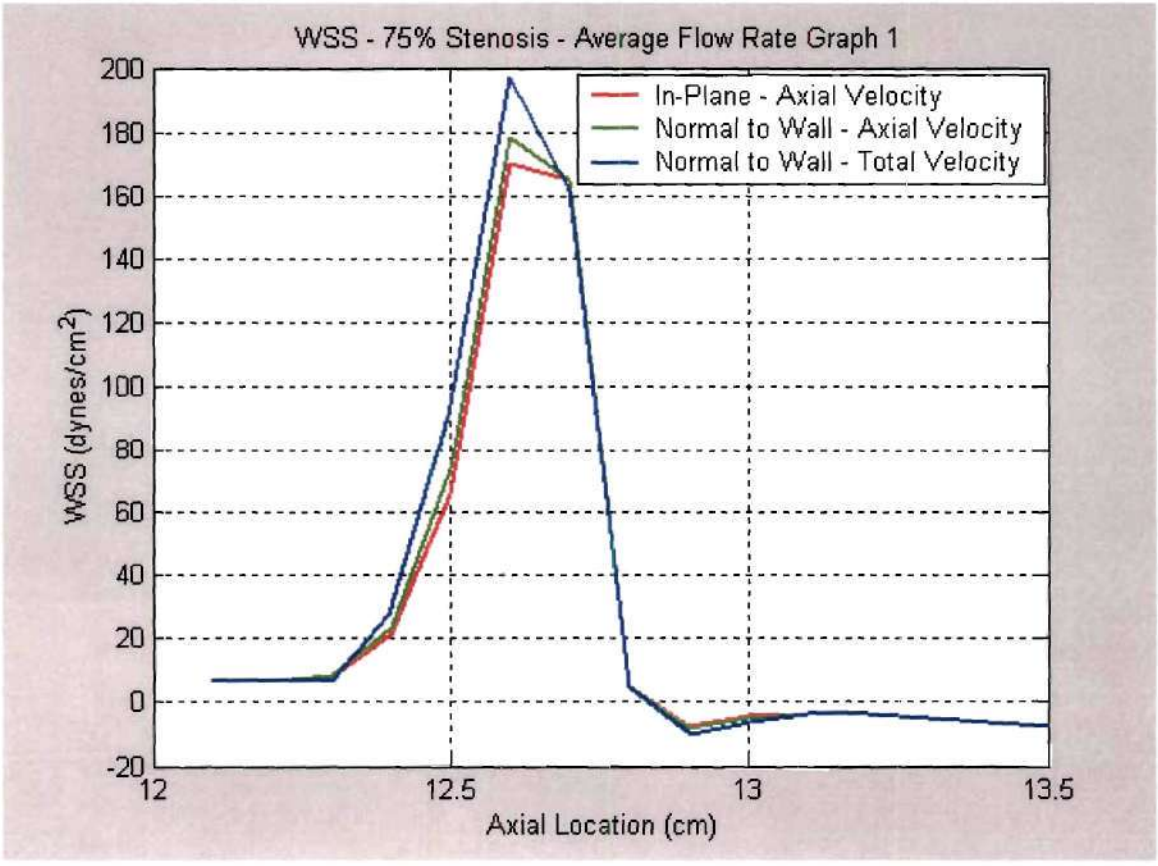

Figure A.4: Plot of the three methods used to compute the WSS values at the location of the stenosis.

APPENDIX B

MATLAB PROGRAMS

```
% PROGRAM MRIWSSMAIN
% Written by Daniel Roberts Karolyi
% This program calculates wall shear stress values
%   directly from phase contrast MRI velocity
%   data.
% The MRI file to be used for edge detection is read
%   in using the IMAGEIN function.
% The Phase Contrast - MRI is read in using the PHASEIn
%   function. The images must be in 256X256 16-bit or
%   8-bit unsigned integer files. The maximum encoded
%   velocity must be specified in the maxvel variable.
% The edge is detected from the MRI image data using the
%   EDGEDETECT function.
% The edge data is then smoothed using a nearest-neighbor
%   filter scheme in the function SMOOTHFIL
% The points on the edge where WSS will be determined
%   are then calculated in the function WSSBOUNDARYPNTS.
% The velocity profiles between these points are then
%   determined in the function VELPROFILE.
% This data is then converted from units of PIXELS to units
%   of centimeters in the function PIXTOCM. The location
%   of the velocity data is then converted from absolute
%   (x,y) coordinates to "distance to the edge" in the
%   function XYTODIST.
% The WSS is then determined in the function WSSCALC and
%   written to the file 'wss.txt' in the function WRITEWSS.
%============================================================
%IMPORTANT IMPORTANT IMPORTANT IMPORTANT IMPORTANT
% There is a known bug in the IMPROFILE function in the
% Image Processing Toolbox 2.2.2 (R12) that has been fixed
% in MATLAB 6.1 (R12.1). As a work-around for users of
% MATLAB 6.0 (R12), please change line 137 of IMPROFILE.M
% from
%
%       profi = interp1(s,prof,(0:n-1)*max(s)/(n-1));
%
% to
%
%       profi = interp1(s,prof,0:(max(s)/(n-1)):max(s));
%
% The file should be located at:
%       $MATLAB\toolbox\images\images\improfile.m
% where $MATLAB is the MATLAB root directory.
%============================================================

clear all;
```

```
close all;

delete wssmean.txt
delete centervel.txt

imprefix1 = 'geom500';        % prefix of image files #1-9
imprefix2 = 'geom50';         % prefix of image files 10 or greater
phprefix1 = 'avvel500';       % prefix of phase files #1-9
phprefix2 = 'avvel50';        % prefix of phase files 10 or greater
imsufix = '.dat';             % suffix of image files
phsufix = '.dat';             % suffix of phase files

z = [0,1.986:0.2:3.986,5.586:1:9.586];% axial locations of MRI slices

filternum = 5; % number of passes through smoothing filter

maxvel = 100; % maximum encoded velocity in the phase contrast MRI files.

% 'curvefit' determines the interpolation algorithm to be
% used to determine the velocity values from the PC-MRI data
% Possible inputs are: 'nearest' 'bilinear' 'bicubic'
curvefit = 'bicubic';


pointnum = 2;% number of near wall points to be used in WSS calculation
degree = 1; % degree of polynomial to be fit to near wall velocity data
wallzero = 1; % determines if the wall velocities should
        %           1 = set to zero
        %           0 = do not alter PC value
mu = 0.04; % the dynamic viscosity of the fluid (poise)
wss = 0; % initialization

for i = [1:15]  % file numbers to be used
  numb = int2str(i);
  if i < 10
    image1 = [imprefix1, numb, imsufix];
    image2 = [phprefix1, numb, phsufix];
  else
    image1 = [imprefix2, numb, imsufix];
    image2 = [phprefix2, numb, imsufix];
  end

  A2 = IMAGEIN(image1);
  B2 = PHASEIN(image2,maxvel,i);
  [x,y,cx,cy] = EDGEDETECT(A2);
```

```
    for j = 1:filternum
        [x,y] = SMOOTHFIL(x,y);
    end

    [x,y,cx,cy] = POSITIONXY(x,y,cx,cy,B2);
    CENTERVEL(B2,cx,cy,z,i);
    [velline] = WSSBOUNDARYPNTS(x,y);
    velline2(:,:,:,i) = velline;
    [veldata,kmax] = VELPROFILE(velline,B2,curvefit);
    [veldata(:,1),veldata(:,2)] = PIXTOCM(veldata(:,1),...
        veldata(:,2),0.05);
    [veldata] = XYTODIST(veldata,kmax);
    [velcurvfit,delcurv,wss] = WSSCALC(veldata,kmax,i,pointnum,...
        degree,mu,wallzero,wss);
end

figure;
hold on;
for i = 1:8
    plot(z(1:15),wss(:,i));
end

for i = 1:15
    wssmean(i) = mean(wss(i,:));
    wssstd(i) = std(wss(i,:));
end
errorbar(z(1:15), wssmean, wssstd);
```

```
function A2 = IMAGEIN(image);
% Written by Daniel Roberts Karolyi
% Function IMAGEIN reads in a 256X256 16-bit image
% image is the file name to be opened
% A2 is the data array representing the MRI image.

% fopen and fread store the data in the variable A
% the 'r' option makes the file read only within the function
% the 'b' option refers to the data being IEEE floating point
%      with big-endian byte ordering. The 'l' option can be
%      substituted if IEEE floating point with little-endian
%      byte ordering is desired (BYTE SWAPPING).
[fid,message] = fopen(image,'r','b');

[A,count] = fread(fid,[256,256],'uint16');

% Converts the data from integers to floating point data
%    with a maximum value of 1 and a minimum value of 0
% The pixel order is swapped (i,j -> j,i) for correct
%    displaying of the image with the imshow function.
A1=double(A);

c=max(A1);

d=max(c);
[maxi maxj] = size(A1);

for i = 1:maxi
  for j = 1:maxj
    A2(j,i)=A1(i,j)./d;
  end
end
```

```
function B2 = PHASEIN(image,maxvel,z);
% Written by Daniel Roberts Karolyi
% This function reads in the phase contrast MRI data file.
% This file should be in 256X256 format with 16-bit
%  unsigned integer values.

% fopen and fread store the data in the variable A
% the 'r' option makes the file read only within the function
% the 'b' option refers to the data being IEEE floating point
%     with big-endian byte ordering. The 'l' option can be
%     substituted if IEEE floating point with little-endian
%     byte ordering is desired (BYTE SWAPPING).
[fid,message] = fopen(image,'r','b');
[B,count] = fread(fid,[256,256],'uint16');

% Although the file format must be 16-bit, the actual data
% may be stored as 16-bit or 8-bit. This loop determines
% if it is 16 or 8 bit data by looking at the maximum
% integer in the file. If the maximum integer is greater
% than 255(that is 256 starting counting at zero), the data
% is treated as 16-bit. Otherwise, the data is treated as
% 8-bit.
if max(max(B)) >255
   maxraw = 4095;
else
   maxraw = 255;
end

% Phase contrast MRI data is encoded from -maxvel to maxvel
% over the entire range of integers available. For the case
% of 16-bit data that is 0 to 4095 and for 8-bit data that
% is 0 to 255. The integer representing a velocity of zero
% is calculated as one-half of the maximum possible integer
% rounded down to the nearest integer. This value is stored
% as the variable 'zerolevel'.
zerolevel = maxraw/2 - 0.5;

[imax jmax] = size(B);

% This loop converts the phase contrast MRI elocity data
% from vlaues represented as encoded integers to units of
% cm/sec.
for i = 1:imax
  for j = 1:jmax
     if (z == 1) | (z > 12)
        B2(j,i) = ((B(i,j) - zerolevel)*(maxvel/zerolevel));
```

```
    else
      B2(j,i) = ((B(i,j) - zerolevel)*(75/zerolevel));
    end
  end
end
```

```
function [x,y,cx,cy] = EDGEDETECT(A2);
% Written by Daniel Roberts Karolyi
% This program detects the edge of MRI image data.
% A2 is the array representation of the MRI image
% x,y represent arrays of (x,y) points located along
%   the edge.

% The image is threshold and converted to a black and
%   white image. The second input variable can be
%   changed to allow more strict or more relaxed
%   threshold ng criteria. The black and white image
%   is stored as the array 'bwmri'.
bwmri = im2bw(A2,0.4);

[imax jmax] = size(bwmri);

% This function performs two morphological operations on the
%   black and white image. A dilation followed by an erosion.
% The result of these morphological operations is to assure as
%    smooth a edge contour as possible by normalizing edge
%    pixel values.
bwmri = bwmorph(bwmri,'close');

% This function displays the black and white image overlaid
% with possible edge detection contour lines. The number
% of lines can be adjusted with the second input variable to
% the imcontour function.
figure;
imcontour(bwmri,1);

% At this point, the user must specify which contour line
% should be selected as the edge. This is done by selecting
% the pointer from the image toolbox and clicking on the
% correct line with the mouse. Enter must be pressed
% after clicking on the correct line.
pause;
line = gco;

% These functions get the x and y locations of points
% located along the edge.
x = get(line,'xdata');
y = get(line,'ydata');

% The get commands write a NaN variable as the last
% value in both the 'x' and 'y' arrays. These NaN
% values are deleted from the data set.
```

```
[imax trash] = size(x);
x(imax) = [];
y(imax) = [];


figure(101);
imshow(A2,[]);
pause;
[cx cy trash] = impixel;
```

```
function [x,y] = SMOOTHFIL(x,y);
% Written by Daniel Roberts Karolyi
% This function smooths the edges using a
%   nearest-neighbor filter scheme.
% x and y represent arrays of (x,y) coordinates
%   of points located on the edge.

[imax trash] = size(x);
[jmax trash] = size(y);

% The plot commands here and at the end of the
%   function can be un-commented to plot the
%   results of each successive pass through the filter

% These commands calculate the updated value of the
%   x and y values located in the FIRST position of
%   the arrays. This step is required because
%   this calculation requires data at the beginning
%   and end of the arrays.
x2(1) = (x(imax-1) + x(1) + x(2))/3;
y2(1) = (y(imax-1) + y(1) + y(2))/3;

% These commands calculate the updated value of the
%   x and y values not at the end of the arrays.
for i = 2:imax-1
   x2(i) = (x(i-1) + x(i) + x(i+1))/3;
   y2(i) = (y(i-1) + y(i) + y(i+1))/3;
end

% These commands calculate the updated value of the
%   x and y values located in the LAST position of
%   the arrays. This step is required because
%   this calculation requires data at the beginning
%   and end of the arrays.
x2(imax) = (x(imax-1) + x(imax) + x(2))/3;
y2(imax) = (y(imax-1) + y(imax) + y(2))/3;

% These commands update the 'x' and 'y' arrays
%   with the filter edge points locations. The
%   newly update 'x' and 'y' arrays are passed
%   back to the main program.
x = x2';
y = y2';
```

```
function [x,y,cx,cy] = POSITIONXY(x,y,cx,cy,B2);
% Written by Daniel Roberts Karolyi

figure(100);
imshow(B2,[]);
pause;
[nx ny trash] = impixel;

if nx > cx
   x = x + (nx-cx);
   cx = nx;
else
  x = x - (cx - nx);
  cx = nx;
end

if ny > cy
   y = y + (ny-cy);
   cy = ny;
else
  y = y - (cy - ny);
  cy = ny;
end
```

```
function CENTERVEL(B2,cx,cy,z,filenum)
% Written by Daniel Roberts Karolyi

cenvel = interp2(B2,cx,cy);

fid = fopen('centervel.txt','a');

geomout = [z(filenum), cx, cy, cenvel];
fprintf(fid,'%10.6f %10.6f %10.6f %10.f\n',geomout);

fclose(fid);
```

```
function [velline] = WSSBOUNDARYPNTS(x,y);
% Written by Daniel Roberts Karolyi
% This function determines the points along the
% edge where wall shear stress values will be
% calculated. These data are stored as the
% array 'velline'. Essentially 4 lines are selected
% which span the entire diameter of the edge figure.
% The lines are selected to roughly cut the image into
% eight equal parts.

xmin = min(x);
ymin = min(y);
xmax = max(x);
ymax = max(y);

% This loop determined the location within the arrays
% 'x' and 'y' where the minimum and maximum values of
% x and y occur. These points will be used to make a
% horizontal line across the edge image and a vertical
% line up and down the edge image.
[imax trash] = size(x);
for i = 1 : imax
   if x(i) == xmin
      xminnum = i;
   end
   if x(i) == xmax
      xmaxnum = i;
   end
   if y(i) == ymin
      yminnum = i;
   end
   if y(i) == ymax
      ymaxnum = i;
   end
end

% These commands determined which data from the
% 'x' and 'y' arrays should be used to find the
% diagonal lines. These points will be roughly half
% way along the circumference between the points used
% for the horizontal and vertical lines. The points are
% stores in the variables 'quad1', 'quad2', 'quad3', 'quad4'
% which represent the four quadrants of the image.
if xminnum < yminnum
   quad3 = ceil((xminnum+yminnum)/2);
else
```

```
   quad3 = ceil((xminnum + (yminnum + imax))/2);
   if quad3 > imax
      quad3 = quad3 - imax;
   end
end

if yminnum < xmaxnum
   quad4 = ceil((yminnum+xmaxnum)/2);
else
   quad4 = ceil((yminnum + (xmaxnum + imax))/2);
   if quad4 > imax
      quad4 = quad4 - imax;
   end
end

if xmaxnum < ymaxnum
   quad1 = ceil((xmaxnum+ymaxnum)/2);
else
   quad1 = ceil((xmaxnum + (ymaxnum + imax))/2);
   if quad1 > imax
      quad1 = quad1 - imax;
   end
end

if ymaxnum < xminnum
   quad2 = ceil((ymaxnum+xminnum)/2);
else
   quad2 = ceil((ymaxnum + (xminnum + imax))/2);
   if quad2 > imax
      quad2 = quad2 - imax;
   end
end

% The edge points where wss is to be calculated are stored in the
% variable 'velline'.
velline(1,1,1) = x(xminnum);
velline(1,2,1) = y(xminnum);
velline(2,1,1) = x(xmaxnum);
velline(2,2,1) = y(xmaxnum);
velline(1,1,2) = x(quad3);
velline(1,2,2) = y(quad3);
velline(2,1,2) = x(quad1);
velline(2,2,2) = y(quad1);
velline(1,1,3) = x(yminnum);
velline(1,2,3) = y(yminnum);
velline(2,1,3) = x(ymaxnum);
```

```
velline(2,2,3) = y(ymaxnum);
velline(1,1,4) = x(quad4);
velline(1,2,4) = y(quad4);
velline(2,1,4) = x(quad2);
velline(2,2,4) = y(quad2);
```

```
function [veldata,kmax] = VELPROFILE(velline,B2,curvefit);
% Written by Daniel Roberts Karolyi
%============================================================
%IMPORTANT IMPORTANT IMPORTANT IMPORTANT IMPORTANT
% There is a known bug in the improfile function in the
% Image Processing Toolbox 2.2.2 (R12) that has been fixed
% in MATLAB 6.1 (R12.1). As a work-around for users of
% MATLAB 6.0 (R12), please change line 137 of IMPROFILE.M
% from
%
%     profi = interp1(s,prof,(0:n-1)*max(s)/(n-1));
%
% to
%
%     profi = interp1(s,prof,0:(max(s)/(n-1)):max(s));
%
% The file should be located at:
%   $MATLAB\toolbox\images\images\improfile.m
% where $MATLAB is the MATLAB root directory.
%============================================================

[imax jmax kmax] = size(velline);
n = 1;
for k = 1:kmax
  [xc, yc, c] = improfile(B2, (velline(:,1,k)'),...
    (velline(:,2,k)'),curvefit);
   [imax trash] = size(xc);
   for i = 1: imax
     veldata(n,1) = xc(i);
     veldata(n,2) = yc(i);
     veldata(n,3) = c(i);
     veldata(n,4) = k;
     n = n + 1;
   end
end
```

```
function [x,y] = PIXTOCM(x,y,ratio);
% Written by Daniel Roberts Karolyi
% This function converts MRI image data from units of
%   pixels to cm.
% Ratio represents the number of square centimeters
%   each pixel represents
% NOTE: This program assumes that the MRI image matrix
%   is uniform(i.e. the pixels are square).
% The original MRI data ranges from 1 to 256 for a
%   256X256 matrix. This program converts the data
%   to centimeters starting with zero centimeters.

x = (x * ratio) - ratio;
y = (y * ratio) - ratio;
```

```
function veldata = XYTODIST(veldata,kmax);
% Written by Daniel Roberts Karolyi

[imax trash] = size(veldata);
test = 0;
for k = 1:kmax
  clear test;
  n = 0;
  startn = 1;
  for i = 1:imax
    if veldata(i,4) == k
      n = n + 1;
      test(n,1) = veldata(i,1);
      test(n,2) = veldata(i,2);
    else
      if veldata(i,4) < k
        startn = startn + 1;
      end
    end
  end
  xref = test(1,1);
  yref = test(1,2);
  for j = startn:startn + n - 1
    veldata(j,1) = veldata(j,1) - xref;
    veldata(j,2) = veldata(j,2) - yref;
  end
end

for i = 1:imax
  veldata(i,5) = sqrt(veldata(i,1)^2 + veldata(i,2)^2);
end
```

```
function [velcurvfit,delcurv,wss] = WSSCALC(veldata,kmax,znum,pointnum, ...
degree, nu, wallzero,wss)
% Written by Daniel Roberts Karolyi

[imax,trash] = size(veldata);
m = 1;
for k = 1:kmax
   n = 0;
   test =[];
   for i = 1:imax
     if veldata(i,4) == k   % veldata(i,4) = line number
        n = n + 1;
        test(n,1) = veldata(i,5); %veldata(i,5) = distance value
        test(n,2) = veldata(i,3); %celdata(i,3) = velocity value
     end
   end
   if wallzero == 1
      test(1,2) = 0; % switch to set edge velocity equal to zero
      test(n,2) = 0; % switch to set edge velocity equal to zero
   end
   velcurvfit(m,:) = polyfit(test(1:pointnum,1),test(1:pointnum,2),degree); % curve fitting
   delcurv(m,:) = polyder(velcurvfit(m,:)); % take derivative of curve
   wss(znum,m) = nu * polyval(delcurv(m,:),test(1,1)); % evaluate derivative at edge
   m = m + 1;
   velcurvfit(m,:) = polyfit(test(n-pointnum+1:n,1),test(n-pointnum+1:n,2),degree);
                     % curve fitting
   delcurv(m,:) = polyder(velcurvfit(m,:)); % take derivative of curve
   wss(znum, m) = -(nu * polyval(delcurv(m,:),test(n,1))); % evaluate derivative at edge
   m = m + 1;
end;
```

```
% PROGRAM MRICONTMAIN
% Written by Daniel Roberts Karolyi
% This program determines the edge location of MRI images.
% MRI file data is read in and stored as the array 'A2'
% The edge is determined.  Points along the edge are saved
%   as the arrays 'x' and 'y'. The centroid of the shape
%   determined by edge detection is stored as the
%   variables 'cx' and 'cy'
% The data is converted from units of pixel to centimeters
% The shapes determined from edge detection are all aligned
%   with the first MRI slice by comparing centroid values.
% The edges are smoothed using a nearest-neighbor filter scheme.
% The edge point data is written to the file 'cfdgeom.txt'.
% The format of this file is
%     <x-location> <y-location> <z-location>

clear all;
close all;

delete cfdgeom.txt

% Files are of the form prefix-number-suffix
% Prefix1 is used for images numbered 1 through 9
% Prefix2 is used for images numbered 10 or greater
prefix1 = 'geom500'; %
prefix2 = 'geom50';
sufix = '.dat';

% z represents the axial locations of the MRI slices
z = [0,1.986:0.2:3.986,5.586:1:9.586];

% filternum is the number of times the smoothing filter
%     is run on the raw edge data.
filternum = 5;


for i = 1:15
   numb = int2str(i);
   if i < 10 % sets up file name for files numbered 1- 9
     image = [prefix1, numb, sufix];
   else  % sets up file name for files numbered 10 or greater
     image = [prefix2, numb, sufix];
   end

   A2 = IMAGEIN(image); % reads in the image file
   [x,y,cx,cy] = EDGEDETECT(A2); % determines the edge location
```

```
   [x,y] = PIXTOCM(x,y,0.05); % converts from pixels to cm
   [cx,cy] = PIXTOCM(cx,cy,0.05); % converts from pixels to cm

   % This loop aligns all of the edges with the first edge
   % by matching centroid location.
   if i == 1
      cxone = cx;
      cyone = cy;
   else
      [x,y,cx,cy] = CENTERALL(x,y,cx,cy,cxone,cyone);
   end

   % This loop smooths the edges using a nearest-neighbor
   %      filter scheme.
   for j = 1:filternum
      [x,y] = SMOOTHFIL(x,y);
   end

   WRITECFDGEOM(x,y,z,i); % Writes the CFD geometry data
                          %    to the file cfdgeom.txt

end
```

```
function WRITEWCFDGEOM(x,y,z,filenum);
% Written by Daniel Roberts Karolyi
% This function writes the edge point data
%   to a file for input into GAMBIT (a CFD
%   grid generator).
% 'x', 'y', and 'z' represent arrays of data
%   points.
% filenum represent the specific number of
%   slice whose data is represented in 'x' and 'y'.
% The data is stored in the file cfdgeom.txt. The
%   data is appended to the file each time this
%   function is called. Therefore, it is important
%   that this file be deleted before a new set of
%   data is run through this function.

% The 'a' option means that the file will be appended.
numb = int2str(filenum);
if filenum < 10
   fname = ['geom500',numb,'.txt'];
else
   fname = ['geom50',numb,'.txt'];
end

fid = fopen(fname,'a');

[imax trash] = size(x);
fprintf(fid,'%3.0f %1.0f\n', [imax, 1]);
for i = 1:imax
   geomout = [x(i),y(i),z(filenum)];
   fprintf(fid,'%10.6f %10.6f %10.6f\n',geomout);
end

fclose(fid);
```

```
% PROGRAM MRIBC.m
% Written by Daniel Roberts Karolyi
% This program creates inlet boundary condition statements for FIDAP
% Nodes comprising elements that are located on the inlet face of the
%    geometry are read in from the file elementnode.txt. This data
%    was obtained by CUTTING and PASTING the INLET boundary element
%    information from the *.FDNEUT file.
%    File format is <ELEMENT NUMBER> <NODE #1> <NODE #2>
%       <NODE #3> <NODE #4>
% The spatial location of these nodes are determined by maching node
%    number to the x-y-z spatial location of the node found in the
%    file nodeloc.txt. This data was obtained by CUTTING and
%    PASTING the element node composition data from the
%    *.FDNEUT file.
%    File format is <NODE NUMBER> <X-Coordinate> < Y-Coordinate>
%       <Z-Coordinate>
% The inlet velocity boundary condition is determined by interpolating
%    the velocity data from the phase constast MRI file designated
%    by the variable "phase" in this program. This is a 256X256
%    16bit OR 8-bit unsigned integer file. The maximum encoaded
%    velocity must also be specified as the variable 'maxvel' in
%    this program.
% Once all of the nodes have been assigned a velocity value from
%    interpolation, the proper syntax is written for each node to
%    the file inletbc.txt
% The information from this file sould be CUT and PASTED into the
%    approriate location of the *.FIPREP file.

clear all;
%close all;

% phase is the file name of the phase contrast MRI file to be used
%    for inlet boundary condition information.
% maxvel = the maximum encoaded velocity selected at the time of
%    MRI imaging.
phase = '22.000.00.02.00.00';
maxvel = 100;

% Variable that determines the interpolation method to be used.
% Possible values are 'linear', 'nearest', 'spline', and 'cubic'.
intermeth = 'linear';

load elementnode.txt

inel = elementnode;
clear elementnode;
```

```
[imax jmax] = size(inel);

% This loop extractes the nodes that are located on the inlet face
%    and saves them as the array "elemnum".
n = 0;
for i = 1:imax
   for j = 2:jmax
      n = n + 1;
      elemnum(n) = inel(i,j);
   end
end

clear inel;

% The node numbers are sorted to be in increasing order.
elemnum = sort(elemnum');

[imax trash] = size(elemnum);

% Since the elements on the inlet create a closed surface, each node
%      must be a point on more than one element. This loop finds
%      duplicate node numbers and deleted them from the array
%      'elemnum'.
i = 2;
while(i <= imax)
   if elemnum(i) == elemnum(i-1)
      elemnum(i) = [];
      imax = imax - 1;
   else
      i = i + 1;
   end
end

load nodeloc.txt

[imax trash] = size(elemnum);
[jmax trash] = size(nodeloc);

% This loop matches node numbers in the array 'elemnum' with
%     node numbers(and their cooresponding x-y-z locations) from
%     the file nodeloc. The x-y-z locations are then written to
%     the 2nd, 3rd, and 4th columns of the array 'elemnum'.
% The file format for the array 'elemnum' is now
%      <node number> <x-location> <y-location> <z-location>
for i = 1:imax
```

```
   next = 0;
   for j = 1:jmax
      if elemnum(i) == nodeloc(j,1)
         elemnum(i,2) = nodeloc(j,2);
         elemnum(i,3) = nodeloc(j,3);
         elemnum(i,4) = nodeloc(j,4);
         next = 1;
      end
      if next == 1, break, end
   end
end

clear nodeloc;

%  These statements turn the x-y-z coordinates from units of
%      centimeters to units of pixels.  This is necessary in order
%      to interpolate the phase contrast MRI data which is stored
%      as pixels.
elemnum(:,2) = elemnum(:,2) + 4.67607606865;
elemnum(:,3) = elemnum(:,3) + 6.42834877295;
elemnum(:,2) = elemnum(:,2) - 0.016755;
elemnum(:,3) = elemnum(:,3) - 0.017975;


elemnum(:,2) = (elemnum(:,2) + 0.05)/0.05;
elemnum(:,3) = (elemnum(:,3) + 0.05)/0.05;
elemnum(:,4) = (elemnum(:,4) + 0.05)/0.05;


%  This function reads in the phase contrast MRI file and scales the
%      values from pixel intensity to cm/sec.  More information is
%      available in the PHASEIN.m function file.
B2 = PHASEIN(phase,maxvel);

x = 1:256;
y = 1:256;
[imax trash] = size(elemnum);

%  This loop assignes a velocity value to each node number by
%      interpolating the phase contrast MRI array 'B2' in
%      two dimensions.  This value is stored in the 5th column
%      of the elemnum array.
%  The file format for the array 'elemnum' is now
%      <node number> <x-location> <y-location> <z-location> <velocity>
for i = 1:imax
   elemnum(i,5) = interp2(x,y,B2,elemnum(i,2), elemnum(i,3),intermeth);
```

```
end

figure;
hold on;
for i = 1:imax
   if elemnum(i,5) > 0
      plot3(elemnum(i,2), elemnum(i,3), elemnum(i,5),'ob');
   else
      plot3(elemnum(i,2), elemnum(i,3), elemnum(i,5),'or');
   end
end

axis equal;
figure;
t = delaunay(elemnum(:,2), elemnum(:,3));
trimesh(t,elemnum(:,2), elemnum(:,3), elemnum(:,5));
figure;
trisurf(t,elemnum(:,2), elemnum(:,3), elemnum(:,5));



% These commands open the file 'inletbc.txt. and write the text data
%      to be CUT and PASTED into the *.FDNEUT file.
% Line example : BCNODE(ADD,UZ,NODES=234,CONSTANT=28)
% If the inlet velocities are to be aligned alond the x or y axes,
%      the UZ should be replaced with UX or UY respectively.
fid = fopen('inletbc.txt','a');
for i = 1:imax
   nodenum = int2str(elemnum(i,1));
   velval = num2str(elemnum(i,5));
   outstr = (['BCNO(UZ,NODES=',nodenum,',CONSTANT =',velval,')']);
   fprintf(fid,'%s\n',outstr);
   outstr = (['BCNO(UX,NODES=',nodenum,',CONSTANT = 0)']);
   fprintf(fid,'%s\n',outstr);
   outstr = (['BCNO(UY,NODES=',nodenum,',CONSTANT = 0)']);
   fprintf(fid,'%s\n',outstr);
end

fclose(fid);
```

```
% PROGRAM INELEMENT.m
% Written by Daniel Roberts Karolyi
% This program creates inlet boundary condition statements for FIDAP
% Nodes comprising elements that are located on the inlet face of the
%    geometry are read in from the file elementnode.txt. This data
%    was obtained by CUTTING and PASTING the INLET boundary element
%    information from the *.FDNEUT file.
%    File format is <ELEMENT NUMBER> <NODE #1> <NODE #2>
%       <NODE #3> <NODE #4>
% The spatial location of these nodes are determined by maching node
%    number to the x-y-z spatial location of the node found in the
%    file nodeloc.txt. This data was obtained by CUTTING and
%    PASTING the element node composition data from the
%    *.FDNEUT file.
%    File format is <NODE NUMBER> <X-Coordinate> < Y-Coordinate>
%       <Z-Coordinate>
% The inlet velocity boundary condition is determined by interpolating
%    the velocity data from the phase constast MRI file designated
%    by the variable "phase" in this program. This is a 256X256
%    16bit OR 8-bit unsigned integer file. The maximum encoaded
%    velocity must also be specified as the variable 'maxvel' in
%    this program.
% Once all of the nodes have been assigned a velocity value from
%    interpolation, the proper syntax is written for each node to
%    the file inletbc.txt
% The information from this file sould be CUT and PASTED into the
%    approriate location of the *.FIPREP file.

clear all;
%close all;

% phase is the file name of the phase contrast MRI file to be used
%    for inlet boundary condition information.
% maxvel = the maximum encoaded velocity selected at the time of
%    MRI imaging.
phase = '22.000.00.02.00.00';
maxvel = 100;

% Variable that determines the interpolation method to be used.
% Possible values are 'linear', 'nearest', 'spline', and 'cubic'.
intermeth = 'linear';

load elementnode.txt

inel = elementnode;
clear elementnode;
```

```
[imax jmax] = size(inel);

% This loop extractes the nodes that are located on the inlet face
%    and saves them as the array "elemnum".
n = 0;
for i = 1:imax
   for j = 2:jmax
      n = n + 1;
      elemnum(n) = inel(i,j);
   end
end

clear inel;

% The node numbers are sorted to be in increasing order.
elemnum = sort(elemnum');

[imax trash] = size(elemnum);

% Since the elements on the inlet create a closed surface, each node
%      must be a point on more than one element.  This loop finds
%      duplicate node numbers and deleted them from the array
%      'elemnum'.
i = 2;
while(i <= imax)
   if elemnum(i) == elemnum(i-1)
      elemnum(i) = [];
      imax = imax - 1;
   else
      i = i + 1;
   end
end

load nodeloc.txt

[imax trash] = size(elemnum);
[jmax trash] = size(nodeloc);

% This loop matches node numbers in the array 'elemnum' with
%    node numbers(and their cooresponding x-y-z locations) from
%    the file nodeloc.  The x-y-z locations are then written to
%    the 2nd, 3rd, and 4th columns of the array 'elemnum'.
% The file format for the array 'elemnum' is now
%      <node number> <x-location> <y-location> <z-location>
for i = 1:imax
```

```
   next = 0;
   for j = 1:jmax
      if elemnum(i) == nodeloc(j,1)
         elemnum(i,2) = nodeloc(j,2);
         elemnum(i,3) = nodeloc(j,3);
         elemnum(i,4) = nodeloc(j,4);
         next = 1;
      end
      if next == 1, break, end
   end
end

clear nodeloc;

%  These statements turn the x-y-z coordinates from units of
%     centimeters to units of pixels.  This is necessary in order
%     to interpolate the phase contrast MRI data which is stored
%     as pixels.
elemnum(:,2) = elemnum(:,2) - 0.016755;
elemnum(:,3) = elemnum(:,3) - 0.017975;


elemnum(:,2) = (elemnum(:,2) + 0.05)/0.05;
elemnum(:,3) = (elemnum(:,3) + 0.05)/0.05;
elemnum(:,4) = (elemnum(:,4) + 0.05)/0.05;


%  This function reads in the phase contrast MRI file and scales the
%     values from pixel intensity to cm/sec.  More information is
%     available in the PHASEIN.m function file.
B2 = PHASEIN(phase,maxvel);

x = 1:256;
y = 1:256;
[imax trash] = size(elemnum);

%  This loop assignes a velocity value to each node number by
%     interpolating the phase contrast MRI array 'B2' in
%     two dimensions.  This value is stored in the 5th column
%     of the elemnum array.
%  The file format for the array 'elemnum' is now
%     <node number> <x-location> <y-location> <z-location> <velocity>
for i = 1:imax
   elemnum(i,5) = interp2(x,y,B2,elemnum(i,2), elemnum(i,3),intermeth);
end
```

```
figure;
hold on;
for i = 1:imax
   if elemnum(i,5) > 0
      plot3(elemnum(i,2), elemnum(i,3), elemnum(i,5),'ob');
   else
      plot3(elemnum(i,2), elemnum(i,3), elemnum(i,5),'or');
   end
end

axis equal;
figure;
t = delaunay(elemnum(:,2), elemnum(:,3));
trimesh(t,elemnum(:,2), elemnum(:,3), elemnum(:,5));
figure;
trisurf(t,elemnum(:,2), elemnum(:,3), elemnum(:,5));

% These commands open the file 'inletbc.txt. and write the text data
%      to be CUT and PASTED into the *.FDNEUT file.
% Line example : BCNODE(ADD,UZ,NODES=234,CONSTANT=28)
% If the inlet velocities are to be aligned alond the x or y axes,
%      the UZ should be replaced with UX or UY respectively.
fid = fopen('inletbc.txt','a');
for i = 1:imax
   nodenum = int2str(elemnum(i,1));
   velval = num2str(elemnum(i,5));
   outstr = (['BCNO(UZ,NODES=',nodenum,',CONSTANT =',velval,')']);
   fprintf(fid,'%s\n',outstr);
   outstr = (['BCNO(UX,NODES=',nodenum,',CONSTANT = 0)']);
   fprintf(fid,'%s\n',outstr);
   outstr = (['BCNO(UY,NODES=',nodenum,',CONSTANT = 0)']);
   fprintf(fid,'%s\n',outstr);
end

fclose(fid);
```

```
% PROGRAM IDEALBC.m
% Written by Daniel Roberts Karolyi
% This program creates inlet boundary condition statements for FIDAP
% Nodes comprising elements that are located on the inlet face of the
%    geometry are read in from the file elementnode.txt. This data
%    was obtained by CUTTING and PASTING the INLET boundary element
%    information from the *.FDNEUT file.
%    File format is <ELEMENT NUMBER> <NODE #1> <NODE #2>
%       <NODE #3> <NODE #4>
% The spatial location of these nodes are determined by maching node
%    number to the x-y-z spatial location of the node found in the
%    file nodeloc.txt. This data was obtained by CUTTING and
%    PASTING the element node composition data from the
%    *.FDNEUT file.
%    File format is <NODE NUMBER> <X-Coordinate> < Y-Coordinate>
%       <Z-Coordinate>
% The inlet velocity boundary condition is determined by interpolating
%    the velocity data from the phase constast MRI file designated
%    by the variable "phase" in this program. This is a 256X256
%    16bit OR 8-bit unsigned integer file. The maximum encoaded
%    velocity must also be specified as the variable 'maxvel' in
%    this program.
% Once all of the nodes have been assigned a velocity value from
%    interpolation, the proper syntax is written for each node to
%    the file inletbc.txt
% The information from this file sould be CUT and PASTED into the
%    approriate location of the *.FIPREP file.

clear all;
%close all;

load elementnode.txt

inel = elementnode;
clear elementnode;

[imax jmax] = size(inel);

% This loop extractes the nodes that are located on the inlet face
%   and saves them as the array "elemnum".
n = 0;
for i = 1:imax
  for j = 2:jmax
    n = n + 1;
    elemnum(n) = inel(i,j);
  end
```

```
end

clear inel;

% The node numbers are sorted to be in increasing order.
elemnum = sort(elemnum');

[imax trash] = size(elemnum);

% Since the elements on the inlet create a closed surface, each node
%     must be a point on more than one element. This loop finds
%     duplicate node numbers and deleted them from the array
%     'elemnum'.
i = 2;
while(i <= imax)
   if elemnum(i) == elemnum(i-1)
      elemnum(i) = [];
      imax = imax - 1;
   else
      i = i + 1;
   end
end

load nodeloc.txt

[imax trash] = size(elemnum);
[jmax trash] = size(nodeloc);

% This loop matches node numbers in the array 'elemnum' with
%     node numbers(and their cooresponding x-y-z locations) from
%     the file nodeloc. The x-y-z locations are then written to
%     the 2nd, 3rd, and 4th columns of the array 'elemnum'.
% The file format for the array 'elemnum' is now
%     <node number> <x-location> <y-location> <z-location>
for i = 1:imax
   next = 0;
   for j = 1:jmax
      if elemnum(i) == nodeloc(j,1)
         elemnum(i,2) = nodeloc(j,2);
         elemnum(i,3) = nodeloc(j,3);
         elemnum(i,4) = nodeloc(j,4);
         next = 1;
      end
      if next == 1, break, end
   end
end
```

```
clear nodeloc;

minloc = min(elemnum);
maxloc = max(elemnum);

format long;
centerx = (maxloc(1,2) + minloc(1,2))/2
centery = (maxloc(1,3) + minloc(1,3))/2


% Determine velocity distribution
[imax jmax] = size(elemnum);
for i = 1:imax
   radius = sqrt((abs((elemnum(i,2)-centerx)^2))+...
      (abs((elemnum(i,3)-centery)^2)));
   elemnum(i,5) = -(28.4/0.3175^2)*radius^2 + 28.4;
end

figure;
hold on;
for i = 1:imax
   if elemnum(i,5) > 0
      plot3(elemnum(i,2), elemnum(i,3), elemnum(i,5),'ob');
   else
      plot3(elemnum(i,2), elemnum(i,3), elemnum(i,5),'or');
   end
end

axis equal;
figure;
t = delaunay(elemnum(:,2), elemnum(:,3));
trimesh(t,elemnum(:,2), elemnum(:,3), elemnum(:,5));
figure;
trisurf(t,elemnum(:,2), elemnum(:,3), elemnum(:,5));
```

```
% PROGRAM FDP2TP_2
% Written by Daniel Roberts Karolyi
% This program prepares raw data output from FIDAP
%   for data analysis and display in TECPLOT.
% A TECPLOT loader for FIDAP 8.x Data
% Written by Daniel R. Karolyi
% Last Update : 12/8/2001
% Converts FIDAP data to format readable by TECPLOT
% Needs input files from following FIPOST commands
% NEUTRAL(FIPOST,SPEED,FILE="velocity.txt",FVECTOR)
% NEUTRAL(FIPOST,VORTICITY,FILE="vorticity.txt")
% NEUTRAL(FIPOST,REYNOLDS, FILE="reynolds.txt")
% NEUTRAL(FIPOST,PRESSURE, FILE="pressure.txt")
% NEUTRAL(FIPOST,SHEAR,FILE="shear.txt")
% STRSPRINT(VISCOUS,PLOT, TANGENTIAL,TRACTION,ENTITY="wall",
% NOPRINT)
% NEUTRAL(FIPOST,STRSPRINT,FILE="wsstrac.txt",FVECTOR)
% STRSPRINT(VISCOUS, PLOT, TANGENTIAL, FORCE, ENTITY="wall",
% NOPRINT)
% NEUTRAL(FIPOST, STRSPRINT, FILE="wssforce.txt", FVECTOR)
% STRSPRINT(PRESSURE, PLOT, NORMAL, TRACTION, ENTITY="wall",
% NOPRINT)
% NEUTRAL(FIPOST, STRSPRINT, FILE="presstrac.txt", FVECTOR)
% STRSPRINT(PRESSURE, PLOT, NORMAL, FORCE, ENTITY="wall", NOPRINT)
% NEUTRAL(FIPOST, STRSPRINT, FILE="pressforce.txt", FVECTOR)
% STRSPRINT(TOTAL, PLOT, NORMAL, TRACTION, ENTITY="wall",NOPRINT)
% NEUTRAL(FIPOST, STRSPRINT, FILE="totaltrac.txt", FVECTOR)
% STRSPRINT(TOTAL, PLOT, NORMAL, FORCE, ENTITY="wall", NOPRINT)
% NEUTRAL(FIPOST, STRSPRINT, FILE="totalforce.txt", FVECTOR)
%   REMOVE ALL HEADERS FROM THESE FILES
% Also need connectivity information from FDNEUT file.
% Cut this information from the FDNEUT file and save as
%    "connect.txt".
clear all;
close all;
delete tpinall.txt;

% Node location, velocity, and node-number data.
load velocity.txt;
fileout(:,1) = velocity(:,5); % x-position
fileout(:,2) = velocity(:,6); % y-position
fileout(:,3) = velocity(:,7); % z-position
fileout(:,4) = velocity(:,2); % x-velocity
fileout(:,5) = velocity(:,3); % y-velocity
fileout(:,6) = velocity(:,4); % z-velocity
fileout(:,7) = sqrt(velocity(:,2).^2 + velocity(:,3).^2 ...
```

```
   + velocity(:,4).^2); % speed
fileout(:,36) = velocity(:,1); %node number
clear velocity;

% Pressure data
load pressure.txt;
fileout = ADD1D(fileout,pressure,8);
clear pressure;

% Vorticity
load vorticity.txt;
fileout = ADD1D(fileout,vorticity,9);
clear vorticity;

% Reynolds Number
load reynolds.txt;
fileout = ADD1D(fileout, reynolds,10);
clear reynolds;

% Shear
load shear.txt;
fileout = ADD1D(fileout, shear,11);
clear shear;

% Wall Shear Stress (Traction)
load wsstrac.txt;
fileout = ADD3D(fileout, wsstrac, 12);
clear wsstrac;

% Wall Shear Stress (Force)
load wssforce.txt;
fileout = ADD3D(fileout, wssforce, 16);
clear wssforce;

% Pressure (Traction)
load presstrac.txt;
fileout = ADD3D(fileout, presstrac, 20);
clear presstrac;

% Pressure (Force)
load pressforce.txt;
fileout = ADD3D(fileout, pressforce, 24);
clear pressforce;

% Total (Traction)
load totaltrac.txt;
```

```
fileout = ADD3D(fileout, totaltrac, 28);
clear totaltrac;

% Total (Force)
load totalforce.txt;
fileout = ADD3D(fileout, totalforce, 32);
clear totalforce;

load connect.txt;
fid = fopen('tpinall.txt','w');
fprintf(fid,'%s\n','TITLE="CFD-RESULTS"');
fprintf(fid,'%s\n','VARIABLES = "X" "Y" "Z" "UX" "UY" "UZ" "SPEED" ...
"PRESSURE" "VORTICITY" "REYNOLDS" "SHEAR" "WSSX" "WSSY" "WSSZ" ...
"WSSMAG" "WSFX" "WSFY" "WSFZ" "WSFMAG" "PRSX" "PRSY" "PRSZ" ...
"PRSMAG" "PRFX" "PRFY" "PRFZ" "PRFMAG" "TOSX" "TOSY" "TOSZ" ...
"TOSMAG" "TOFX" "TOFY" "TOFZ" "TOFMAG" "NODE-ORDER"');
nodenum = int2str(max(fileout(:,36)));
[elemnum trash] = size(connect);
elemnum = int2str(elemnum);
outstr = (['ZONE N=',nodenum,',E =',elemnum,',F=FEPOINT, ET=BRICK, NV=36']);
fprintf(fid,'%s\n',outstr);
fprintf(fid,'%s\n','DT = (DOUBLE DOUBLE DOUBLE DOUBLE DOUBLE ...
DOUBLE DOUBLE DOUBLE DOUBLE DOUBLE DOUBLE DOUBLE ...
DOUBLE DOUBLE DOUBLE DOUBLE DOUBLE DOUBLE DOUBLE ...
DOUBLE DOUBLE DOUBLE DOUBLE DOUBLE DOUBLE DOUBLE ...
DOUBLE DOUBLE DOUBLE DOUBLE DOUBLE DOUBLE DOUBLE ...
DOUBLE DOUBLE DOUBLE)');
[imax jmax] = size(fileout);

for i = 1:imax
  fileout2 = fileout(i,:);
  fprintf(fid,'%10.6f %10.6f %10.6f %10.6f %10.6f %10.6f %10.6f %10.6f %...
10.6f %10.6f %10.6f %10.6f\n %10.6f %10.6f %10.6f %10.6f %10.6f %10.6f %...
10.6f %10.6f %10.6f %10.6f %10.6f %10.6f\n %10.6f %10.6f %10.6f %10.6f %...
10.6f %10.6f %10.6f %10.6f %10.6f %10.6f %10.6f %10.6f\n',...
    fileout2);
end

clear fileout;
[imax jmax] = size(connect);
for i = 1:imax
    fprintf(fid,'%8.0f %8.0f %8.0f %8.0f %8.0f %8.0f %8.0f %8.0f\n',...
    connect(i,2),connect(i,3), connect(i,7), connect(i,6),...
       connect(i,4), connect(i,5), connect(i,9), connect(i,8));
end
fclose(fid);
```

```
function fileout = ADD1D(fileout,data,nloc)
% Written by Daniel Roberts Karolyi

[imax jmax] = size (data);
for i = 1 :imax
   if data(i,1) == fileout(i,36)
      fileout(i,nloc) = data(i,2);
   else
      err0r('something went wrong')
   end
end
```

```
function fileout = ADD3D(fileout,data,nloc)
% Written by Daniel Roberts Karolyi

[imax jmax] = size (data);
for i = 1 :imax
   if data(i,1) == fileout(i,36)
      fileout(i,nloc) = data(i,2);
      fileout(i,nloc+1) = data(i,3);
      fileout(i,nloc+2) = data(i,4);
      fileout(i,nloc+3) = sqrt(data(i,2)^2 + data(i,3)^2 ...
         + data(i,4)^2);
   else
      err0r('something went wrong')
   end
end
```

```
% PROGRAM WSSMAIN
%  Written by Daniel Roberts Karolyi
% This program takes the eight WSS data sets extracted using Tecplot
% and calculates mean WSS values and standard deviations.
% The extracted data should be labeled:
% for the x-plane extraction 'xplanewss.txt'
% for the y-plane extraction 'yplanewss.txt'
% for the 1st diagonal plane extraction 'diagplanewss.txt'
% for the 2nd diagonal plane extraction 'diagplane2wss.txt'
% the format of the files should be : x-coordinate, y-coordinate, z-coordinate, WSS
% all headers should be removed
%close all;
%clear all;

one = load ('xplanewss.txt');
two = load ('yplanewss.txt');
three = load ('diagplanewss.txt');
four = load ('diagplane2wss.txt');

one = DELZEROWSS(one);
two = DELZEROWSS(two);
three = DELZEROWSS(three);
four = DELZEROWSS(four);

[one1,one2] = SEPARATEY(one,6.46); % number = y-coordinate at center of model
[two1,two2] = SEPARATEX(two,4.66); % number = x-coordinate at center of model
[three1,three2] = SEPARATEX(three,4.66); % number = x-coordinate at center of model
[four1,four2] = SEPARATEX(four,4.66); % number = x-coordinate at center of model

one1 = sortrows(one1,3)
one2 = sortrows(one2,3)
two1 = sortrows(two1,3)
two2 = sortrows(two2,3)
three1 = sortrows(three1,3)
three2 = sortrows(three2,3)
four1 = sortrows(four1,3)
four2 = sortrows(four2,3)

znew = [0:0.025:7.586]'
none1 = interp1(one1(:,3), one1(:,4),znew,'linear');
none2 = interp1(one2(:,3), one2(:,4),znew,'linear');
ntwo1 = interp1(two1(:,3), two1(:,4),znew,'linear');
ntwo2 = interp1(two2(:,3), two2(:,4),znew,'linear');
nthree1 = interp1(three1(:,3), three1(:,4),znew,'linear');
nthree2 = interp1(three2(:,3), three2(:,4),znew,'linear');
nfour1 = interp1(four1(:,3), four1(:,4),znew,'linear');
```

```
nfour2 = interp1(four2(:,3), four2(:,4),znew,'linear');

[imax jmax] = size(znew);
for i = 1:imax
   total(i) = mean([none1(i), none2(i), ntwo1(i), ntwo2(i), nthree1(i),...
      nthree2(i), nfour1(i), nfour2(i)]);
   stdev(i) = std([none1(i), none2(i), ntwo1(i), ntwo2(i), nthree1(i),...
      nthree2(i), nfour1(i), nfour2(i)]);
end

figure;
hold on;
plot(one1(:,3), -one1(:,4));
plot(one2(:,3), -one2(:,4));
plot(two1(:,3), -two1(:,4));
plot(two2(:,3), -two2(:,4));
plot(three1(:,3), -three1(:,4));
plot(three2(:,3), -three2(:,4));
plot(four1(:,3), -four1(:,4));
plot(four2(:,3), -four2(:,4));
errorbar(znew, -total, stdev);
```

```
function filein = DELZEROWSS(filein);
%  Written by Daniel Roberts Karolyi

[imax jmax] = size(filein);
i = 1;
while i <= imax
   if filein(i,4) == 0
      filein(i,:) = [];
      imax = imax - 1;
   else
      i = i + 1;
   end
end
```

```
function [fileout1,fileout2] = SEPARATEX(filein,thresh);
% Written by Daniel Roberts Karolyi

[imax jmax] = size(filein);
m = 0;
n = 0;

for i = 1:imax
   if filein(i,1) > thresh
      m = m +1;
      fileout1(m,:) = filein(i,:);
   else
      n = n + 1;
      fileout2(n,:) = filein(i,:);
   end
end
```

```
function [fileout1,fileout2] = SEPARATEY(filein,thresh);
% Written by Daniel Roberts Karolyi

[imax jmax] = size(filein);
m = 0;
n = 0;

for i = 1:imax
   if filein(i,2) > thresh
      m = m +1;
      fileout1(m,:) = filein(i,:);
   else
      n = n + 1;
      fileout2(n,:) = filein(i,:);
   end
end
```

BIBLIOGRAPHY

Ahmed SA. An experimental investigation of steady and pulsatile flow through a constricted tube. Doctorate Thesis. Georgia Institute of Technology. 1981.

Aiello GA, Trefil JS. The generalized entry flow problem and the establishment of Poiseuille flow in locally constricted tubes. *Journal of Biomechanics.* 1976;9(1):49-54.

American Heart Association. 2001 heart and stroke statistical update. Dallas (TX): American Heart Association; 2000.

Bradley WG Jr, Waluch V, Lai KS, Fernandez EJ, Spalter C. The appearance of rapidly flowing blood on magnetic resonance images. *AJR. American Journal of Roentgenology.* 1984;143(6):1167-74.

Centers for Disease Control and Prevention. Achievements in public health, 1900-1999: Decline in deaths from heart disease and stroke – United States, 1900 – 1999. Hyattsville (MD): United States Department of Health and Human Services, Center for Disease Control and Prevention. 1999;649-656.

Centers for Disease Control and Prevention. Chronic Disease Notes and Reports. 1997;10:2-15.

Chappell DC, Alexander RW, Medford RM, Nerem RM. The regulation of adhesion molecule expression by fluid shear stress in human vascular endothelial cells. In: 1995 Advances in Bioengineering. New York: American Society of Mechanical Engineering. 1995;261-2.

Chu KC, Rutt BK. Polyvinyl alcohol cryogel: an ideal phantom material for MR studies of arterial flow and elasticity. *Magnetic Resonance in Medicine.* 1997;37(2):314-9.

Deshpande MD. Steady laminar and turbulent flow through vascular stenosis models. Doctorate Thesis. Georgia Institute of Technology. 1977.

Diamond SL, Eskin SG, McIntire LV. Fluid flow stimulates tissue plasminogen activator secretion by cultured human endothelial cells. *Science.* 1989;243(4897):1483-5.

Frangos JA, Eskin SG, McIntire LV, Ives CL. Flow effects on prostacyclin production by cultured human endothelial cells. *Science.* 1985;227(4693):1477-9.

Frayne R, Rutt BK. Measurement of fluid-shear rate by Fourier-encoded velocity imaging. *Magnetic Resonance in Medicine.* 1995;34(3):378-87.

Frayne R, Steinman DA, Ethier CR, Rutt BK. Accuracy of MR phase contrast velocity measurements for unsteady flow. *Journal of Magnetic Resonance Imaging.* 1995;5(4):428-31.

Giddens DP, Zarins CK, Glagov S. Response of arteries to near-wall fluid dynamic behavior. *Applied Mechanics Review.* 1990;43:S98-S102.

Giddens DP, Zarins CK, Ku DN, Glagov S. Shear stress effects on arterial diameter. *Proceedings of the 40th Annual Conference on Engineering in Medicine and Biology.* Niagra Falls, NY. 1987.

Glagov S, Weisenberg E, Zarins CK, Stankunavicius R, Kolettis GJ. Compensatory enlargement of human atherosclerotic coronary arteries. *New England Journal of Medicine.* 1987;316(22):1371-5.

Hsieh HJ, Li NQ, Frangos JA. Shear-induced platelet-derived growth factor gene expression in human endothelial cells is mediated by protein kinase C. *Journal of Cellular Physiology.* 1992;150(3):552-8.

Inoue N, Ramasamy S, Fukai T, Nerem RM, Harrison DG. Shear stress modulates expression of Cu/Zn superoxide dismutase in human aortic endothelial cells. *Circulation Research.* 1996;79(1):32-7.

Kamiya A, Togawa T. Adaptive regulation of wall shear stress to flow change in the canine carotid artery. *American Journal of Physiology.* 1980;239(1):H14-21.

Kohler U, Marshall I, Robertson MB, Long Q, Xu XY, Hoskins PR. MRI measurement of wall shear stress vectors in bifurcation models and comparison with CFD predictions. *Journal of Magnetic Resonance Imaging.* 2001;14(5):563-73.

Kozerke S, Botnar R, Oyre S, Scheidegger MB, Pedersen EM, Boesiger P. Automatic vessel segmentation using active contours in cine phase contrast flow measurements. *Journal of Magnetic Resonance Imaging.* 1999;10(1):41-51.

Ku DN, Biancheri CL, Pettigrew RI, Peifer JW, Markou CP, Engels H. Evaluation of magnetic resonance velocimetry for steady flow. *Journal of Biomechanical Engineering.* 1990;112(4):464-72.

Ku DN, Giddens DP, Zarins CK, Glagov S. Pulsatile flow and atherosclerosis in the human carotid bifurcation. Positive correlation between plaque location and low oscillating shear stress. *Arteriosclerosis.* 1985;5(3):293-302.

Langille BL, O'Donnell F. Reductions in arterial diameter produced by chronic decreases in blood flow are endothelium-dependent. *Science.* 1986;231(4736):405-7.

Levesque MJ, Nerem RM, Sprague EA. Vascular endothelial cell proliferation in culture and the influence of flow. *Biomaterials.* 1990;11(9):702-7.

Lieber BB. Ordered and random structures in pulsatile flow through constricted tubes. Doctorate Thesis. Georgia Institute of Technology. 1985.

Long Q, Xu XY, Ariff B, Thom SA, Hughes AD, Stanton AV. Reconstruction of blood flow patterns in a human carotid bifurcation: a combined CFD and MRI study. *Journal of Magnetic Resonance Imaging.* 2000a;11(3):299-311.

Long Q, Xu XY, Bourne M, Griffith TM. Numerical study of blood flow in an anatomically realistic aorto-iliac bifurcation generated from MRI data. *Magnetic Resonance in Medicine.* 2000b;43(4):565-76.

Long Q, Xu XY, Collins MW, Griffith TM, Bourne M. The combination of magnetic resonance angiography and computational fluid dynamics: a critical review. *Critical Reviews in Biomedical Engineering.* 1998;26(4):227-74.

Malek AM, Greene AL, Izumo S. Regulation of endothelin 1 gene by fluid shear stress is transcriptionally mediated and independent of protein kinase C and cAMP. *Proceedings of the National Academy of Sciences of the United States of America.* 1993;90(13):5999-6003.

Malek AM, Jackman R, Rosenberg RD, Izumo S. Endothelial expression of thrombomodulin is reversibly regulated by fluid shear stress. *Circulation Research.* 1994;74(5):852-60.

Mano I, Goshima H, Nambu M, Iio M. New polyvinyl alcohol gel material for MRI phantoms. *Magnetic Resonance in Medicine.* 1986;3(6):921-6.

Masaryk AM, Frayne R, Unal O, Krupinski E, Strother CM. In vitro and in vivo comparison of three MR measurement methods for calculating vascular shear stress in the internal carotid artery. *Ajnr: American Journal of Neuroradiology.* 1999;20(2):237-45.

Milner JS, Moore JA, Rutt BK, Steinman DA. Hemodynamics of human carotid artery bifurcations: computational studies with models reconstructed from magnetic resonance imaging of normal subjects. *Journal of Vascular Surgery.* 1998;28(1):143-56.

Moore JA, Rutt BK, Karlik SJ, Yin K, Ethier CR. Computational blood flow modeling based on in vivo measurements. *Annals of Biomedical Engineering.* 1999a;27(5):627-40.

Moore JA, Steinman DA, Ethier CR. Computational blood flow modelling: errors associated with reconstructing finite element models from magnetic resonance images. *Journal of Biomechanics*. 1998;31(2):179-84.

Moore JA, Steinman DA, Holdsworth DW, Ethier CR. Accuracy of computational hemodynamics in complex arterial geometries reconstructed from magnetic resonance imaging. *Annals of Biomedical Engineering*. 1999b; 27(1):32-41.

Moore JE Jr, Maier SE, Ku DN, Boesiger P. Hemodynamics in the abdominal aorta: a comparison of in vitro and in vivo measurements. *Journal of Applied Physiology*. 1994;76(4):1520-7.

Moore JE Jr, Xu C, Glagov S, Zarins CK, Ku DN. Fluid wall shear stress measurements in a model of the human abdominal aorta: oscillatory behavior and relationship to atherosclerosis. *Atherosclerosis*. 1994; 110(2):225-40.

Nagel T, Resnick N, Atkinson WJ, Dewey CF Jr, Gimbrone MA Jr. Shear stress selectively upregulates intercellular adhesion molecule-1 expression in cultured human vascular endothelial cells. *Journal of Clinical Investigation*. 1994;94(2):885-91.

Ohno M, Cooke JP, Dzau VJ, Gibbons GH. Fluid shear stress induces endothelial transforming growth factor beta-1 transcription and production. Modulation by potassium channel blockade. *Journal of Clinical Investigation*. 1995;95(3):1363-9.

Oshinski JN, Ku DN, Mukundan S Jr, Loth F, Pettigrew RI. Determination of wall shear stress in the aorta with the use of MR phase velocity mapping. *Journal of Magnetic Resonance Imaging*. 1995;5(6):640-7.

Oshinski JN, Ku DN, Pettigrew RI. Turbulent fluctuation velocity: the most significant determinant of signal loss in stenotic vessels. *Magnetic Resonance in Medicine*. 1995;33(2):193-9.

Oyre S, Paaske WP, Ringgaard S, Kozerke S, Erlandsen M, Boesiger P, Pedersen EM. Automatic accurate non-invasive quantitation of blood flow, cross-sectional vessel area, and wall shear stress by modelling of magnetic resonance velocity data. *European Journal of Vascular & Endovascular Surgery*. 1998;16(6):517-24.

Oyre S, Pedersen EM, Ringgaard S, Boesiger P, Paaske WP. In vivo wall shear stress measured by magnetic resonance velocity mapping in the normal human abdominal aorta. *European Journal of Vascular & Endovascular Surgery*. 1997;13(3):263-71.

Oyre S, Ringgaard S, Kozerke S, Paaske WP, Erlandsen M, Boesiger P, Pedersen EM. Accurate noninvasive quantitation of blood flow, cross-sectional lumen vessel area and wall shear stress by three-dimensional paraboloid modeling of magnetic resonance imaging velocity data. *Journal of the American College of Cardiology.* 1998;32(1):128-34.

Oyre S, Ringgaard S, Kozerke S, Paaske WP, Scheidegger MB, Boesiger P, Pedersen EM. Quantitation of circumferential subpixel vessel wall position and wall shear stress by multiple sectored three-dimensional paraboloid modeling of velocity encoded cine MR. *Magnetic Resonance in Medicine.* 1998;40(5):645-55.

Pedersen EM, Oyre S, Agerbaek M, Kristensen IB, Ringgaard S, Boesiger P, Paaske WP. Distribution of early atherosclerotic lesions in the human abdominal aorta correlates with wall shear stresses measured in vivo. *European Journal of Vascular & Endovascular Surgery.* 1999;18(4):328-33.

Prakash S, Ethier CR. Requirements for mesh resolution in 3D computational hemodynamics. *Journal of Biomechanical Engineering.* 2001;123:134-144.

Reddy KS, Yusuf S. Emerging epidemic of cardiovascular disease in developing countries. *Circulation.* 1998;97(6):596-601.

Sato M, Levesque MJ, Nerem RM. Micropipette aspiration of cultured bovine aortic endothelial cells exposed to shear stress. *Arteriosclerosis.* 1987;7(3):276-86.

Shyy YJ, Hsieh HJ, Usami S, Chien S. Fluid shear stress induces a biphasic response of human monocyte chemotactic protein 1 gene expression in vascular endothelium. *Proceedings of the National Academy of Sciences of the United States of America.* 1994;91(11):4678-82.

Steinman DA, Ethier CR, Rutt BK. Combined analysis of spatial and velocity displacement artifacts in phase contrast measurements of complex flows. *Journal of Magnetic Resonance Imaging.* 1997;7(2):339-46.

Steinman DA, Frayne R, Zhang XD, Rutt BK, Ethier CR. MR measurement and numerical simulation of steady flow in an end-to-side anastomosis model. *Journal of Biomechanics.* 1996;29(4):537-42.

Stokholm R, Oyre S, Ringgaard S, Flaagoy H, Paaske WP, Pedersen EM. Determination of wall shear rate in the human carotid artery by magnetic resonance techniques. *European Journal of Vascular & Endovascular Surgery.* 2000;20(5):427-33.

Taylor WR, Nerem RM, Alexander RW. Polarized secretion of IGF-I and IGF-I binding protein activity by cultured aortic endothelial cells. *Journal of Cellular Physiology.* 1993;154(1):139-42.

Uematsu M, Ohara Y, Navas JP, Nishida K, Murphy TJ, Alexander RW, Nerem RM, Harrison DG. Regulation of endothelial cell nitric oxide synthase mRNA expression by shear stress. *American Journal of Physiology.* 1995;269(6 Pt 1):C1371-8.

Varner SE, Medford RM, Alexander RW, Nerem RM. Chronic laminar shear stress differentially inhibits inflammatory activation of vascular endothelial VCAM-1 and NF-κB. 1997 Bioengineering Conference Proceedings. New York: American Society of Mechanical Engineering; 1997;545-6.

Weston SJ, Wood NB, Tabor G, Gosman AD, Firmin DN. Combined MRI and CFD analysis of fully developed steady and pulsatile laminar flow through a bend. *Journal of Magnetic Resonance Imaging.* 1998; 8(5):1158-71.

Wood NB, Weston SJ, Kilner PJ, Gosman AD. Firmin DN. Combined MR imaging and CFD simulation of flow in the human descending aorta. *Journal of Magnetic Resonance Imaging.* 2001;13(5):699-713.

World Health Organization. The World Health Report 1997. Geneva: World Health Organization; 1997.

Young DF, Tsai FY. Flow characteristics in models of arterial stenoses. I. Steady flow. *Journal of Biomechanics.* 1973a;6(4):395-410.

Young DF, Tsai FY. Flow characteristics in models of arterial stenoses. II. Unsteady flow. *Journal of Biomechanics.* 1973b;6(5):547-59.

Zarins CK, Giddens DP, Bharadvaj BK, Sottiurai VS, Mabon RF, Glagov S. Carotid bifurcation atherosclerosis. Quantitative correlation of plaque localization with flow velocity profiles and wall shear stress. *Circulation Research.* 1983;53(4):502-14.

Zarins CK, Zatina MA, Giddens DP, Ku DN, Glagov S. Shear stress regulation of artery lumen diameter in experimental atherogenesis. *Journal of Vascular Surgery.* 1987;5(3):413-20.

VITA

Daniel Roberts Karolyi was born on July 31, 1974, in Birmingham, Alabama. He attended the Georgia Institute of Technology and graduated with a Bachelor of Science in Chemistry in June of 1996. He entered the Medical College of Georgia School of Medicine in Augusta, Georgia in August of 1996, where he was a student in the University System of Georgia MD/PhD program. After completing the first two years of the Medical Doctorate curriculum, he returned to the Georgia Institute of Technology to begin graduate studies at the Georgia Institute of Technology / Emory University Wallace H. Coulter School of Biomedical Engineering. While at Georgia Tech, he earned a Master of Science in Mechanical Engineering degree as well as a Doctorate of Philosophy. Dan will return to the Medical College of Georgia School of Medicine in June, 2002, to complete the requirements for the Medical Doctorate.